Performance of a flexible bioreactor for tendon tissue engineering

Nicole Dvorak

St. Anne's College

University of Oxford

A thesis submitted for the degree of

Doctor of Philosophy

Hilary 2023

This thesis is dedicated to everyone who thinks there is no space for them in research.

.

Whether it be due to ethnicity, skin color, socio-economic background, gender, sexual orientation or disability.

.

You belong here.

Acknowledgements

I don't believe I have ever done anything as difficult as staying committed to this DPhil.

.

My own diagnosis, Brexit, two life-altering breakups, two and a half years of global pandemic, three changes in medication, six different houses, eleven months of no labwork, my mother's diagnosis and everything that came with it...and one supervisory team that helped me through it all. It was of course your expertise, time and patience that made this work possible, but let me express my sincerest gratitude for things that may not have been obvious to you;

To Pierre-Alexis Mouthuy, your responsiveness, calm demeanour and unwavering understanding for my needs supported me in ways I cannot begin to express. I am also grateful for our conversations about my future career as a disabled woman in STEM.

To Sarah Waters, often we lose sense of what is meant to be easy or difficult in a DPhil, you always made me feel proud of my achievements. Thank you for believing in me and supporting the ludicrous idea of me using computational models.

To Cathy Ye, who knew how to make me snap out of a spiralling thought and make me think rationally. I knew I could always rely on your help, should I need it. That is an invaluable trait to have in a supervisor.

To Andy Carr, who saw my potential before I had started. I learned so much by watching you lead the Botnar and NDORMS so empathetically. This will stay with me forever.

Thank you also;

.

My transfer and confirmation assessors Timothy Denison and Philippa Hulley, for your invaluable input and for supporting my retrospective suspensions.

Samuel Burnell and Afsie Sabokbar, I have to keep it short, but simply put; I don't think I would have made it, if it wasn't for you.

The entire Carr group for all the small and big ways you supported me in. Roxanna Abhiri, Risto Martin, Edyta Augustiniyak, Jolet Mimpen, Luka Savic, Tonia Vincent, Joana Martin, Hayley Morris and Tyler Ferguson, Peter Johnson, Prof. Stephen Mullen, for either teaching me a technique, providing feedback on experimental plans or helping with coding. Sarah Salmon for your support in the lab. Jason Zekun for your input on soft sensors. Kalin Dragnevski, for your help on the SEM with my extra difficult samples. Michael Richard from 3D life-prints for providing parts so quickly. Alan Weinman from the Dunn School of Pathology, for teaching me (again and again) how to use the confocal. Rhodri Wilson and James Brown at the Wellcome Centre for Human Genetics. The Botnar facilities and IT teams. Maria Granell, for your work on topics that mean so much to me. George Booth and Amy Kent for their help with mathematical concepts and notation.

My dearest colleagues and friends who made this time in Oxford so so special. Rand Alkaissy, Iain Sander, Kevin Hurlbutt, Elena Porter, Jasper Fried, Jack Wrighton, Sarah Salmon, Tania Choreno Machain, Thales Ferreira, Rhydian Williams, for all the banter inside the office and out. To the St. Anne's Boatclub and all its members, especially Orly Welch. To James Maxwell, thank you for trying.

My friends and family from home. Sarah Zippusch, Marlene Polleres, Rolando Matos, Katrin Brandmair, for commiserating and always providing help and feedback. To the Borbelys, I love you. To my aunt for supporting me. To Kerstin for putting up with my absence, your loyalty is unmet. To my dad for believing in me. To my mum for enduring so much, I am so happy you will see me graduate.

And Wesley, you were my rock.

Abstract

Tendon tears caused by age, trauma or sports-related injuries are an increasing problem. Rotator cuff injuries in particular often have a poor outcome due to the state of the tear and surgeries leading to re-rupturing of the repaired tendon. Tissue engineering strategies aim to support the native tendon in its ability to self-repair through the application of cells and biomaterials. In recent years the importance of mechanical stimulation to tissue engineering constructs came into focus. In order to apply physiologically relevant stresses, new bioreactors capable of multiaxial stimulation need to be developed. One such bioreactor is presented in this work. The bioreactor consists of a filamentous electrospun scaffold, strongly resembling the native tendon structure. A flexible gas-permeable membrane encloses the system and maintains sterility. The aim of this thesis was to characterize the performance of this flexible bioreactor for tendon tissue engineering. The main objectives were to identify a seeding technique that would lead to an even cell distribution throughout the scaffold. Next a computational model was built and applied to investigate nutrient and metabolite distribution throughout the bioreactor, their influence on cell growth, and to gain insight in how different flow rates impact the system. The model was validated through a set of experiments. Lastly, factors that can improve cell retention on the scaffold needed to be identified. We identified that following seeding, the capillary effect was a greater determiner of cell distribution than seeding technique. The computational model was able to give us 3D spatial insight into the system that was otherwise not available. Furthermore it assessed the importance of the membrane being permeable to gasses, and it could assure us that stopping the media flow was not going to affect cell growth over a period of 20 hours. Through the validation experiment, superior outcomes were identified from higher flow rates, but shortcomings of the model were also highlighted. The sensors optimized for this set of experiments gave robust measurements with satisfying robustness which will be used in future work. Lastly, we could not identify the main reason for a lack of cell attachment to the scaffolds. Future work will include further investigations into the mechanisms behind poor cell retention on our scaffolds, and will see the expansion of the bioreactor as a mechanical stimulation platform.

Statement of Originality

I certify that this thesis is a true and honest account of my own research, which was conducted ethically, and the results obtained are genuine. Where I have drawn on the work, ideas, and results of others, this has been appropriately acknowledged in this thesis.

Nicole Dvorak

Abbreviations

MPa	Mega Pascal
PCL	Polycaprolactone
FDA	Food and Drug Association
DOF	Degrees of freedom
ECM	Extracellular matrix
TSPCs/TDSC	Tendon stem progenitor cells/Tendon derived stem cells
TGF	Transforming growth factor
Wnt	Wingless-related integration site
ERK	Extracellular signal-regulated kinase
mRNA	Messenger ribonucleic acid
IGF	Insulin-like growth factor
bFGF	Basic fibroblast growth factor
PDGF	Platelet-derived growth factor
VEGF	Vascular endothelial growth factor
BMPs	Bone morphogenic proteins
CTGF	Connective tissue growth factor
Scx	Scleraxis
NSAIDs	Non-steroidal anti-inflammatory drugs
CSIs	Corticosteroid injections
PRP	Platelet rich plasma
BMSCs	Bone-derived mysenchomal stem cells
ASCs	Adopose-derived
MRI	Magnetic resonance imaging
IPSCs	Induced pluripotent stem cells (iPSCs)
MHC	Major histocompatibility complex
PLA	Polylactic acid
PLLA	Poly-L-lactic acid
PGA	Polyglycolic acid
PLGA	Poly(DL-lactide-co-glycolide)
AA	Ascorbic acid

PDMS	Polydimethylsiloxane
CAD	Computer assisted drawing
CFD	Computational fluid dynamics
HFIP	Hexafluoroisopropanol
HFF-1	Human foreskin fibroblasts
DMEM	Dulbecco's Modified Eagle Medium
FBS	Fetal bovine serum
P/S	Penicillin/Streptomycin
RCF	Relative centrifugal force
aFLOT	Angled fluorescence laminar optical tomography
OsO_4	Osmium Tetroxide
VPSEM	Variable pressure scanning electron microscope
EDS	Elemental dispersed spectroscopy
keV	Kilo electronvolt
uCT	Micro computed tomography
TTE	Tendon Tissue Engineering
GLUTs	Independent glucose transporters
SGLTs	Sodium dependant glucose transporters
ATP	Adenosine Triphosphate
CLSI	Clinical and Laboratory Standards Institute
HLPC	High-performance liquid chromatography
GFP	Green Fluorescent Protein
DAPI	4',6-diamidino-2-phenylindole, DNA intercalating dye

Contents

List of Figures

List of Tables

List of Scripts and Codes

Chapter 1

Introduction

1.1 Rotator Cuff

1.1.1 Significance of Rotator Cuff Tendon Tears

Musculoskeletal problems are on the rise as the population grows older. The Rotator cuff attaches the humerus to the shoulder blade and helps to lift and rotate the arm. It is one of the most commonly injured soft tissues requiring surgery [1]. Rotator cuff tendon tears can be caused by age, trauma or sports-related injuries, often involving overhead arm rotations. They can lead to significant pain and loss of function of the damaged tissue. This can mean the loss of independence through the inability to perform daily tasks, and be a big threat to a professional athlete's career. Patients are advised to rest and exercise only to a small extent as this can be favorable in the healing process. If this fails, only surgical treatment can repair a tear. For this purpose, the tendon is re-anchored to the bone. According to a recent study, over 460,000 rotator cuff surgeries are performed in the the US every year. This number is expected to rise above 570,000 by 2023, making them the second most common orthopaedic soft tissue repair procedure [1]. Since 2001, the amount of surgeries conducted to repair rotator cuff injuries have increased by over 500% in the UK [2]. However, the re-tear rate in this kind of treatment is reported to lie between 5-90 %

[3, 4]. This large range is due to differences in the patients' age, bone mineral density and tear size amongst other factors [5, 6]. Furthermore successful rotator cuff repairs bear a big societal and economic value. A study from 2013 estimated the lifetime societal savings of rotator cuff repairs to 3.44 billion, based on the assumption that 250,000 repairs are performed in the U.S. each year [7]. If left unrepaired, tears can grow in size and lead to further complications such as joint failure or the development of osteoarthritis. Rotator cuff tears therefore pose a significant problem to society as a whole and better treatment options need to be investigated.

1.1.2 The Rotator Cuff Structure

The human shoulder consists of three bones: the humerus, the scapula and the clavicle. Joints form entities of two or more bones to enable movement between them. The main joint in the shoulder is a ball and socket, the glenohumeral joint. It connects the humerus to the shallow socket of the scapula (glenoid), which enables movement in three degrees of freedom: through an axial motion (or twist), and two spherical motions (or swing). These are also referred to as medial–lateral rotation, flexion–extension, and abduction–adduction. Other important joints in the shoulder include the acromioclavicular joint which connects the scapula at its bony tip (acromion) to the clavicle, the sternoclavicular joint which connects the clavicle to the sternum, and the scapulothoractic joint which connects the scapula to the thorax. The rotator cuff is responsible for shoulder movement and stability, and works together with the deltoid and pectoral muscles. It consists of four muscles; the supraspinatus (SS), infraspinatus, teres minor and subscapularis. These originate from the scapula and insert onto the proximal humerus. Their respective tendons pass over the glenohumeral joint and unite together with the coracohumeral ligament, the glenohumeral ligament complex and the articular capsule, forming a collar around the humeral head. A true rotator cuff is defined as individual flat tendons that blend

together to form a single insertion [8]. Humans are special in that most animals do not have a true rotator cuff, the exception being the Orangutans, Chimpanzees and the Tree Kangaroo, all animals requiring frequent overhead arm movements [9]. The SS muscle and tendon are responsible for initiating abduction (moving the arm sideways away from the body), up to about 15 degrees. The deltoid muscle abducts the arm beyond that point. The subscapularis is responsible for internal rotation of the shoulder. The infraspinatus and teres minor are responsible for external rotation of the shoulder [10, 11]. Damage to these muscles or tendons can therefore significantly impact daily activities. The bursa, a small fluid-filled sac, provides a cushion in the area between the rotator cuff tendons and the acromion and reduces friction to prevent damage [11]. Figure 1.1 gives an overview of the described structures in a posterior and anterior view.

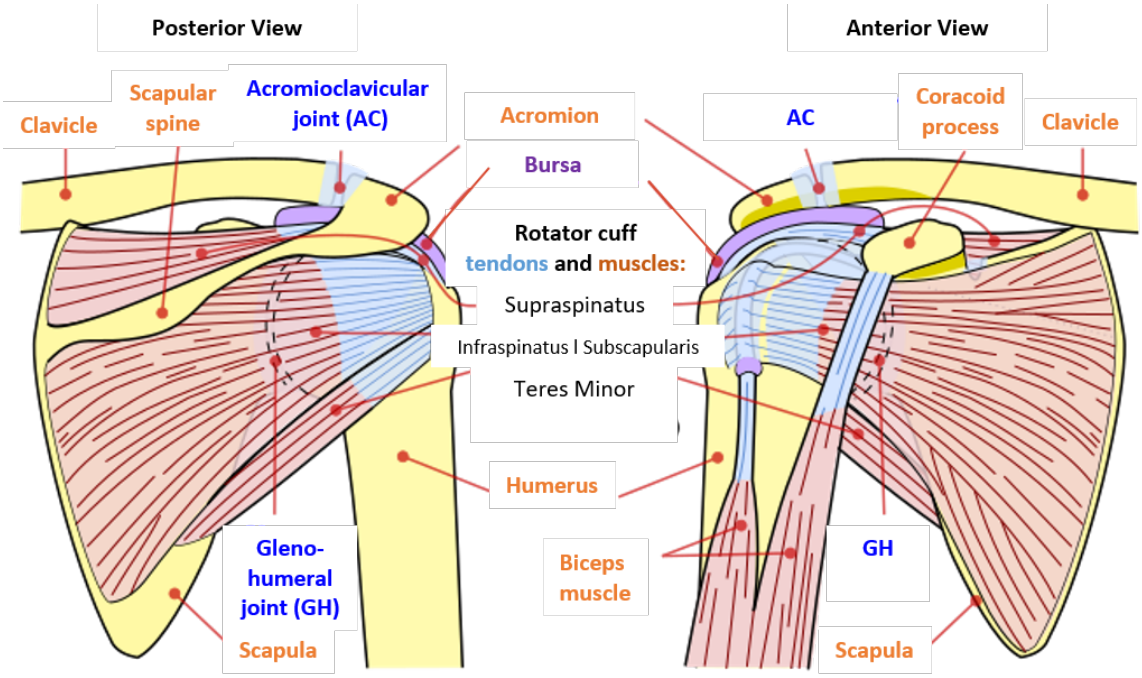

Figure 1.1: **Anatomy of the shoulder and rotator cuff.** The shoulder consists of 3 bones, the humerus, scapula and clavicle. The humerus is inserted into the scapula via the glenohumeral joint. This forms a ball and socket structure and enables movement in three degrees of freedom. Further structures of the shoulder include the acromioclavicular joint connecting the scapula to the clavicle (shown), the sternoclavicular joint connecting the clavicle to the sternum (not shown), and the scapulothoractic joint connecting the scapula to the thorax (not shown). The rotator cuff is responsible for shoulder movements and stability, and works together with the deltoid and pectoral muscles. It consists of the supraspinatus (SS), infraspinatus, subscapularis and teres minor muscles (light red) and their corresponding tendons (light blue). Also shown are the biceps muscles and long and short head tendons, connecting to the top of the socket (glenoid); and the coracoid process respectively. Original image on the left adapted from wikimedia.com and identified as being free of known restrictions under copyright law, including all related and neighboring rights. Image on the right adapted from Jmarchn, CC BY-SA 3.0 https://creativecommons.org/licenses/by-sa/3.0¿, via Wikimedia Commons

1.2 Tendons

1.2.1 Macroscopic Structure of Tendons

On a macroscopic level, tendons are structures connecting muscles to bones or other tissues such as the eyeball. Tendons therefore help force transmission, enable move-

ment, stabilize complex tissues and enable shock absorption. Adult tendons appear white in color. This is due to the relatively scarce circulation of blood within them [12, 13]. The tendons in the rotator cuff all express different degrees of vascularization [14, 15]. The SS tendon is unique in terms of its vascular bed. Previously a "critical zone" located proximal from the bony insertion site, was described as largely avascuar [16]. Later studies elucidated the presence of a vascular bed, where filling of the blood vessels depended on the positioning of the arm [14]. Other tendons such as the Achilles tendon have since been described to possess similar zones scarce in vasculature [17]. Degeneration and subsequent rupture of tendons has been associated with hypovascularity of specific regions within certain tendons [14, 18]. This stands in contrast to an increased angiogenic response in chronic tendinopathy and tendon healing [19]. The importance of the vasculature in tendon damage and repair has been reviewed elsewhere [20, 21]. The adult tendon vasculature must endure the mechanical forces exerted on the tendon. The vessels are therefore embedded in the endotenon tissue and form "curves" [22], which can be stretched accordingly. Tendons contain nerves and mechanoreceptors, through which they provide sensory feedback to muscles [23]. Activated mechanoreceptors in turn lead to a response via cells remodelling their ECM or changes in gene expression (section 1.2.3). This is the reason tendons in various locations of the body differ in size and make-up. Muscles responsible for high power and endurance, such as the quadriceps femoris and triceps surae, have short and robust tendons. While muscles of precise and delicate nature such as the finger flexors have elongated and thin tendons [24]. The tendon structure also differs within itself. Along the lengitudinal axis the tendon is attached to the bone via the enthesis, and to the muscle on the other end via the myotendinous junction (MTJ) (Figure 1.2). The enthesis consists of a continuous gradient from non-calcified tendon to calcified bone. This gradient is grouped into 4 distinct zones; pure dense fibrous connective tissue, uncalcified fibrocartilage, calcified fibrocartilage and bone [25]. The

myotendinous junction is an optimized tissue that transmits force through its unique architecture of the muscle fibers at the MTJ. Imaging techniques have shown that foldings of tendon protrude into invaginations of the muscle membrane. This leads to an increased contact area between muscle and tendon and a better contractile force transmission from myofibrils to the tendon [26]. Tendons are viscoelastic, meaning their mechanical behaviour is dependent on the rate of strain. Their viscoelasticity is likely a result of their microscopic makeup, explained in the next section [27, 28].

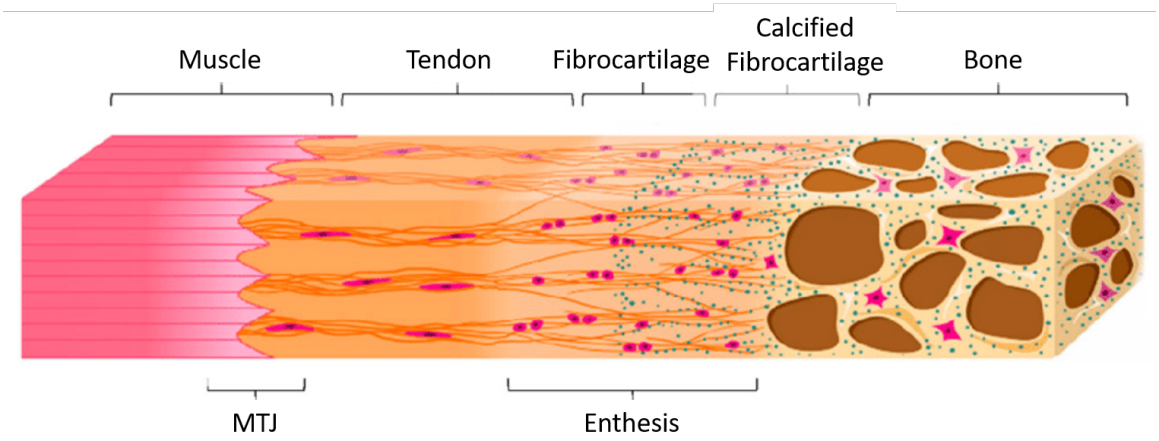

Figure 1.2: **Schematic image of the macroscopic structure of the Tendon, including myotendinous junction (MTJ) and the enthesis with its different zones: dense fibrous connective tissue, fibrocartilage, calcified fibrocartilage and bone.** The dense tendon zone consists of elongated tenocytes (pink), embedded in an extracellular matrix (ECM). It consists primarily of collagen type I (red lines) and proteoglycans such as aggrecan and fibromodulin, as well as glycoproteins like lubricin and elastin. The fibrous cartilage zone II contains rounded chondrocytes (pink), the surrounding ECM gradually changes from collagen type I to collagen type II and collagen type III (red lines), together with aggrecan. The mineralized fibrous cartilage zone (III) consists of Collagen type II and forms a mesh which anchors the tendon to the bone. The transition from non-calcified to calcified fibrocartilage (zone II and III), is called tidemark and is marked by dense calcification. Calcium phosphate driven mineralization (small turquoise-colored dots) is pronounced in the bone zone (zone IV). The main cell types resigning in the bone zone are Osteoblasts, osteocytes and osteoclasts (star-shaped, pink). The bone is highly vascularized and provides nutrients to the avascular enthesis [29] Individual collagen type I fibers in the bone zone are not shown here[30]. Picture adapted from Bianchi et al. under the Creative Commons Attributions License 4.0.[31]

1.2.2 Microscopic Structure of Tendons

On a microscopic level, tendons are highly hierarchical. It is this hierarchy that gives them their high mechanical strength and enables them to sustain repetitive loads. Tendons consist of cells, fibres and extracellular matrix. The cell portion of tendons is made up by 90% of tendon fibroblasts. The other 10% are (1) synovial cells which are found on the fibrous sheath enveloping the tendon (2) chondrocytes, residing in the enthesis, and (3) vascular cells found in blood vessels in the endotenon and epitenon network. Together, these cell types collaborate to maintain the tendon micro-environment. A new type of cells resident in tendons is now under investigation. A small portion of resident cells possess multi-potency and are called tendon stem/progenitor cells (TSPCs) which have the ability to self-renew and may play an important role in tendon healing and aging [32, 33]. Tendon healing is introduced in section 1.2.4

Fibres in tendons are mostly type 1 collagen. The primary amino acid sequence of collagen is glycine-proline-X or glycine-X-hydroxyproline, where X can be any of the other 17 amino acids, and every third amino acid is glycine [34]. Chains of these amino acids make up poly-peptide strands. A single collagen molecule, called tropocollagen, consists of three poly-peptide strands twisted together in a left-handed helix. Three of these strands are then twisted together and form a right-handed helix. The tropocollagen strands are arranged in a parallel manner and form collagen fibrils. Most fibrils are aligned along the long axis of the tendon, but a small number of fibrils are aligned across in order to resist rotational forces. Longitudinal fibrils aggregate into wavy fibres, leading to the typical crimp structure seen in tendons (figure 1.3).

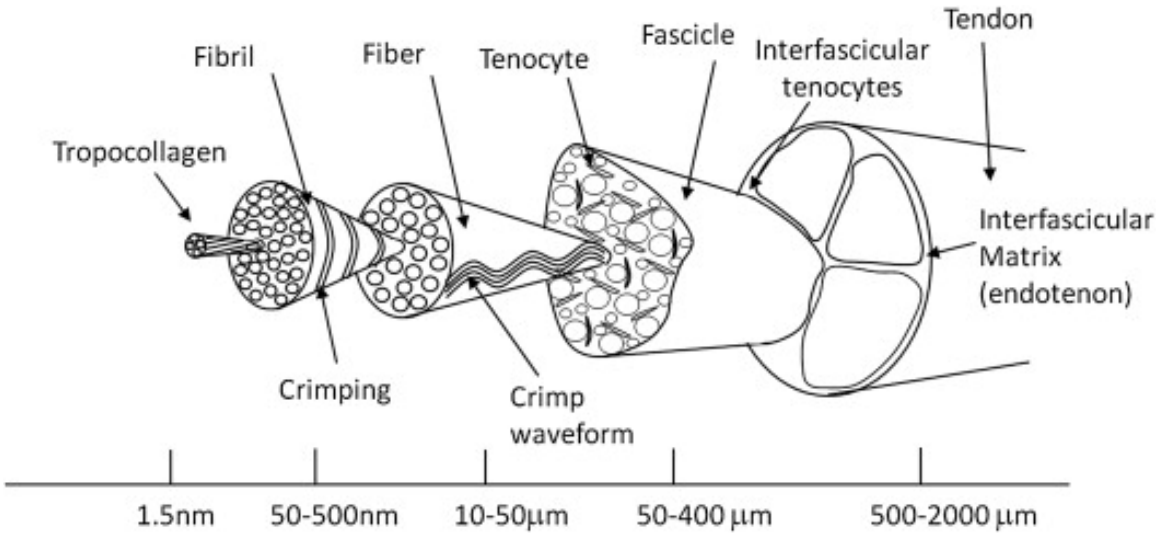

Figure 1.3: **Microscopic to Macroscopic hierarchical structure of tendons. Parallel tropocollagen strands form collagen fibrils along the long axis of the tendon.** Fibrils aggregate into wavy fibres leading to a force-absorbent crimp structure. Fibrils bound together form fascicles. A tube-shaped connective tissue called endodotenon encapsulates fibrils and fascicles for vascularization purposes. A tendon consists of several fascicles, the number of which depends on the load-bearing requirements of the anatomical site. Reprinted from Thorpe et al, with permission from Elsevier [35].

The crimp structure is responsible for the force-absorbent quality of tendons. Forces that lie within the physiological range will lead to an elastic deformation of fibres. Non-physiological loads exceed this deformation capability and lead to micro-tears in the fibres. We highlight this load-deformation response curve as found in Wang et al.[36] in figure 1.4.

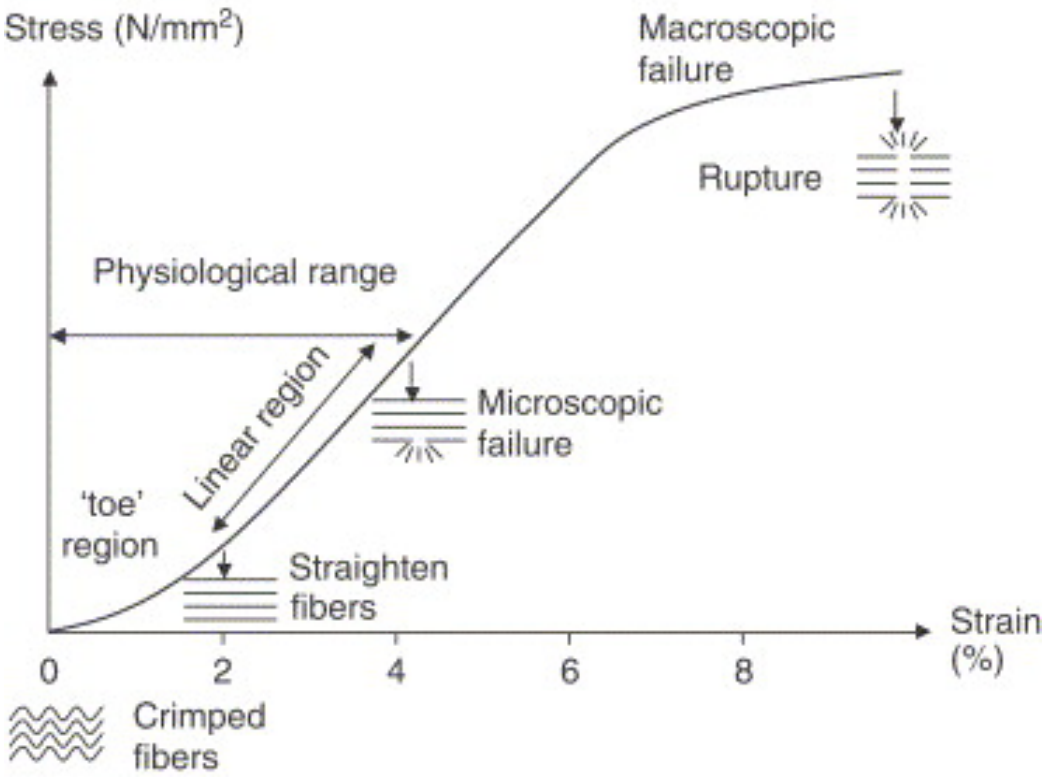

Figure 1.4: **Typical load-deformation curve of a tendon**. Graph indicates the physiological range in which tendons naturally deform. Past that point microscopic failures occur, until the point of macroscopic failure and ultimately rupture. Image adapted from Wang et al [36]. Permission granted.

Fibrils are bundled together into fascicles. Fascicles, as well as fibrils, are surrounded by a tube-like connective tissue called the inter fascicular matrix (IFM) or endotenon. [37]. The endotenon provides vascularization to cells located within. It is the number and diameter of fascicles that change from tendon to tendon. Even within the same tendon these parameters change. The microscopic structure depends on the forces the tendons experience. Some larger, higher load-bearing tendons have a synovial sheath around them, providing lubrication to avoid damage through friction. The reason we see differences in size and mechanical properties from tendon to tendon is their ability to adapt to stresses via their cells and ECM.

The ECM consists mainly of collagen, proteoglycans and glycoproteins. These provide a scaffold for cells, blood vessels and nerves. The ECM's main component is

collagen type 1, found throughout the whole ECM. Collagen type III is found in the endotenon and epitenon. Proteoglycans such as aggrecan, biglycan, decorin, perlecan, agrin, laminin, versican, lumican and fibromodulin are responsible for the viscoelastic properties of tendons, and their ability to retain water. Indeed tendons consist of 70% water [38], and collagen accounts for 65 to 80% of the dry mass of tendon tissue [32]. Glycoproteins such as tenascin C, fibronectin and thrombospondin are responsible for cell-cell interactions and cell-adhesion. Glycoproteins together with integrins link the cells' cytoskeleton to the ECM, ensuring the transduction of mechanical signals into the cells' cytoplasm. This process is called mechanotransduction [38].

1.2.3 Mechanotransduction and Development

Mechanotransduction refers to the ability of cells to respond to mechanical stimulation by releasing biochemical signals [39]. It plays a key role in the development and maintenance of biological tissues and is particularly evident with musculoskeletal tissues [40]. Tendon development in the limb is a two-stage process. The first stage does not involve mechanical stimulation and is driven by the transcription factor scleraxis (Scx). It leads to progenitor cell specification, organization and patterning into a densely packed fibrous tissue with a morphology ranging from broad sheets to highly elastic cables, and regulates Col1a1 expression. Scx is not a master regulator as Scx mutant mice are viable and mobile, but progenitors do fail to condense upon Scx loss [41, 42]. The second stage of tendon development in the limb, requires muscle presence and contraction. It leads to tendon differentiation, maturation and maintenance. Abnormalities in the musculoskeletal development can arise due to insufficient fetal movement [40]. This was first highlighted by Curt Herbest in 1901, who discovered that a calf born with no spinal cord below the cervical region had no muscle in the posterior half of the body. The skeletal parts were well developed but half as heavy as normal, and the joints were ankylosed [43]. Since then, a large

body of evidence has been compiled that strengthens these findings and expands on the molecular mechanisms leading to under-developed tendons. These were reviewed by others [40, 44, 45, 46]. The importance of movement for tendon development continues once baby is born. The presence of postnatal mechanical stimulation through spontaneous muscle activity is vital for enthesis maturation [47, 48].

Mechanotherapy [49, 50, 51], in-vivo [52, 53] and in-vitro [54, 55, 56, 57, 58] studies show also adult tendons rely on movement for tissue homeostasis and repair. Studies conducted on tendon cells suggest that mechanotransduction can be triggered in two ways; cytoskeleton deformation and cell-matrix interactions [59]. Cytoskeleton deformation, leads to a plethora of downstream effects. Mechanical stimulation is sensed through actin, intermediate filaments, and micro-tubules. Actin polymerizes and de-polymerizes rapidly, which in turn leads to the translocation of molecules into the nucleus, interacting with Wnt [60] and TGF-beta pathways [61]. These pathways influence cell differentiation, cell cycle regulation and migration. If the stress is large enough to deform the nucleus, DNA can undergo conformational changes, leading to transcriptional responses [62]. The second way for mechanotransduction to occur, cell-matrix interactions, is enabled by focal adhesions linking cells' intracellular actin bundles to the ECM via integrin-containing multi-protein structures. Integrins are trans-membrane receptors that can be activated upon mechanical load leading to further signal transduction involving pathways such as Erk1/2, TGF-beta and Wnt [59]. A cell will then either adjust its attachment to the local matrix or remodel itself. Mechanical signals can also reach neighbouring cells via gap junctions. Tenocytes have shown to remodel their gap junctions in response to mechanical stimulation; while levels of the key protein in gap-junctions, connexin 43, were decreased, connexin 43 mRNA levels were up-regulated. This mechanism of breakdown and remodelling shows that gap junction permeability relies on mechanical load [63]. It is suggested that there is a tipping point between functional remodelling and fibrotic scarring in

tendon homeostasis [64]. Today, it remains unclear which mechanism triggers gene expression first, whether it is direct deformation of the cytoskeleton and nucleus or indirect signalling through focal adhesion activation [59].

1.2.4 Injury and Healing with a focus on the Supraspinatus Tendon

Rotator cuff tears are among the most common soft tissue injuries. Rotator cuff tendon tears were reported to have a population prevalence of 22 % in 2022 [65]. The SS tendon is the most commonly injured tendon within the rotator cuff. Studies showed that age above 50 years, diabetes [66] and overhead activities significantly increase the risk of rotator cuff tendinopathy [67]. A meta analysis involving 3240 patients further showed that old age, smoking, male sex, diabetes and hypertension were among the risk factors for SS tendon tears, though the pathogenesis remained unclear [68]. Rotator cuff disease encompasses a number of symptoms starting with tendon impingement, partial tears to full-thickness tears [69]. Rotator cuff tears can be classified in several ways; by size (Cofield, or Bateman for full tears), shape (Ellman or Gartsman), structures affected (Snyder), level of retraction (Patte), topography (Patte, Habermayer), degree of muscle atrophy (Thomazeau), and fatty degeneration (Goutallier) [70]. Tears can not only cause significant pain to the patient, but also lead to loss of function, loss of independence and can mean the end of a professional athlete's career.

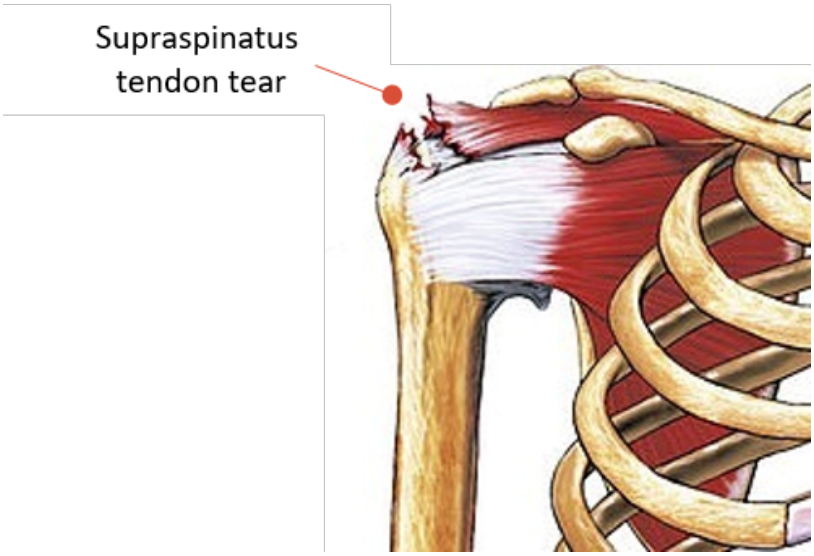

Figure 1.5: **Depiction of Rotator Cuff tear in the supraspinatus tendon.** Rotator cuff tears can have different causes, mainly grouped into degenerative and traumatic. They can be classified in several ways; by size (Cofield, or Bateman for full tears), shape (Ellman or Gartsman), structures affected (Snyder), level of retraction (Patte), topography (Patte, Habermayer), degree of muscle atrophy (Thomazeau), and fatty degeneration (Goutallier) [70]. This image shows a full tear in the supraspinatus tendon. Image adapted from Nucleus Communications www.nucleusinc.com, CC BY 4.0 https://creativecommons.org/licenses/by/4.0, via Wikimedia Commons

Rotator cuff tears can have different causes, mainly grouped into degenerative and traumatic. Trauma can be caused by external influences such as high impact or sports involving an overuse of overhead arm rotations. A typical load-deformation curve for a tendon is presented in figure 1.4. At about 4% strain, a non-physiological strain, the crimping pattern of the collagen fibres straightens and microscopic tears develop. Increasing the strain further will lead to macroscopic tears and eventual complete tendon rupture [38].

For degenerative causes of tendon tears the underlying mechanisms remain unclear. Recently 30 genes have been identified that might have an influence on tendinopathy and could serve as therapeutic targets. Of interest here were Mmp3, TGF-beta1, Col3a1 and TGF-beta2. Increased expression of these genes may indicate a remodeling process in the SS tendon, as a result of the ongoing micro-damage. Further-

more up-regulation of Mmp3 may promote the breakdown of the extracellular matrix (ECM), such as collagen fibers [71]. What makes tendon injuries so impactful is their poor ability to heal.

Healing of tendons is frequently studied in animal models via induced tendon rupture of otherwise healthy tendons. While acute traumatic tendon ruptures may appear to occur without previous tendinopathy, studies showed that there were large numbers of degenerative processes preceding spontaneous tendon ruptures [72]. We currently do not have a good understanding of tendon healing in adults. What we understand was summarized well by Schulze-Tanzil et al. [73]. Roughly, healing can be grouped into three stages; (1) inflammation, (2) proliferation/repair, and (3) remodeling [74]. Immediately after rupturing a tendon, a blood clot forms and chemo-attractants are released. These form a preliminary scaffold. During the inflammatory phase, cells such as neutrophils, monocytes and lymphocytes infiltrate the injured site from the surrounding tissue. Phagocytes digest necrotic debris while tenocyte recruitment begins. The next stage takes place around 2 days after injury. Fibroblasts migrate from the synovial sheat and paratenon to the epitenon [75]. Migrated tenocytes and fibroblasts proliferate, synthesize ECM and form neo-vasculature at their new site [76]. The ECM produced by tenocytes is mainly composed of collagen type III [77]. During this process, the number of neutrophils is reduced, macrophages release growth factors such as insulin-like growth factor (IGF), TGF-beta 1, basic fibroblast growth factor (bFGF), platelet derived growth factor (PDGF), vascular endothelial growth factor (VEGF), bone morphogenic proteins (BMPs) and connective tissue growth factor (CTGF), for a continuous recruitment of cells [78]. The tendon has an increased water content and glycosaminoglycan level at this point [79]. Neutrophhil levels decline while macrophages remain and release growth factors for continuous cell recruitment [78]. Around 1-2 months after the injury, the remodelling phase begins. During this phase tenocytes and collagen fibers align along the axis of stress and larger amounts

of collagen type I is produced [80]. The tendon becomes more and more acellular and type III collagen as well as glycoasminoglycan contents are reduced [79]. The newly formed tissue changes from fibrous to more and more scar-like tendon tissue. This leads to the repaired tissue never regaining the original mechanical properties [81]. Recent studies show that this is particularly true in adults. Comparing mouse neonatal tendon-healing to adult tendon-healing identified the recruitment of scleraxis (Scx)-lineage cells in the neonatal group, whereas adult Scx-lineage tenocytes trans-differentiated into ectopic cartilage instead. Scx is a transcription factor that plays a central role in promoting tenocyte proliferation and matrix synthesis during embryonic tendon development [82]. This strengthens the idea that tendon regeneration is driven by tenocyte proliferation and recruitment from within the original tendon. However in adult tissue the tenocytes are quiescent after injury and instead adult fibrotic healing is induced. Furthermore TDSCs/TSPCs may be involved in tendon healing [82]. TSCPs' healing capabilities have been shown to vary with age. Colony formation assays showed TSPCs numbers decreased in aged animals, and exhibited a decreased proliferation rate as well as delayed cell cycle progression with age. Importantly CD44 expression was elevated in aged TSCPs. High levels of CD44 have been shown to play a negative role in tendon healing [33]. TSPCs behave unlike their regenerative tissues pendant. Muscle and intestine healing is regulated by tissue specific stem cells, whereas tendon healing is marked by scar cartilage or bone formation. We can only speculate that some TSPCs don't behave as traditional stem cells do, but rather represent an early progenitor cell responsible for tendon growth during postnatal development, and subsequently lost once the tendon has matured [83]. The full extent in which TSPCs influence tendon healing is still unknown. Future studies will hopefully elucidate events that regulate tendon healing with the potential for the development of new therapies.

1.2.5 Treatment Strategies

Different treatment strategies to repair tendon injuries have been proposed: conservative treatments, surgical treatments, non-steroidal anti-inflammatory drugs (NSAIDs), cell-based therapy, growth factor delivery, and gene therapy [84]. While some of these are used frequently in the clinic, others are under development as their medical benefit is yet to be proven. Which approach is chosen depends on the individual and the tear characteristics. Patient-related parameters like activity level, degree of impairment, comorbidities, patient expectations and age should be considered. In terms of tears the classification (size, retraction level, fatty degeneration etc) plays an important role [85]. A treatment algorithm has been attempted by Tashjian et al [86]. Hereby patients are grouped into group I: chronic full-thickness tears and older than 60 years of age, irreparable tears, receiving initial conservative treatment. Group II: all chronic full thickness tears and younger than 60 years of age, all acute tears above 1cm, receiving early surgical repair. Group III: tendinopathy, partial thickness tears, small full thickness tears under 1cm, receiving prolonged conservative treatment.

1.2.5.1 Conservative/Non-Operative management

Conservative treatment strategies usually involve a combination of physiotherapy, pain relief, electrotherapy, acupuncture, and taping. It is most often chosen for atraumatic complications not requiring surgery. The aim of conservative therapy is to regain functional movement to complete daily tasks, and to prevent further long term adverse outcomes. Evidence-based exercise protocols consist of four phases; range of motion, flexibility, strengthening and advanced strengthening/proprioception. Exercises start by moving the arm passively (with the help of the healthy arm or a physiotherapist) and gradually move to active movements [87]. For rotator cuff tears evidence on whether surgery or conservative treatments are more effective is limited. Due to the higher risk involved in surgeries, a conservative approach as the

initial treatment is preferred [88]. This is especially true for patients above the age of 65, as the benefits are impeded by slow or no healing. The risk of surgery therefore outweighs the potential benefits. Should conservative treatment not lead to improvements, surgery can be performed in order to restore some of the functionality or turn a symptomatic into an asymptomatic rotator cuff tear [87].

There is also a question of whether physical therapy following surgery should be applied immediately (early rehabilitation) or some time after surgery (delayed therapy), with studies pointing into the direction of improved pain reduction and functionality in the early groups [89].

1.2.5.2 Non-Steroidal Anti-Inflammatory Drugs

NSAIDs can be part of a conservative approach. These aim to control the pain. There has been evidence that NSAIDs might impede healing [85]. A 2021 randomized, double-blind, placebo-controlled trial involving 100 patients showed ibuprofen did not lead to an increased risk of tendon re-tear one year post surgery [90]. However, a much larger systematic review on clinical outcomes on soft tissue healing using NSAIDs following surgery, involved 4451 patients. It was found celecoxib administration had a significantly higher rate of re-tear (37%), and might inhibit tendon-to-bone healing in rotator cuff repairs, compared to ibuprofen [91]. NSAIDs might be a double-edged sword as their use increases ranges of motion, enabling patients to complete their physiotherapy exercises better, despite a lack of histologic evidence of inflammation reduction [92, 93].

1.2.5.3 Injection-based therapy

Injection-based therapies such as corticosteroid injections (CSIs) or platelet-rich plasma (PRP) are used as part of the conservative approach to rotator cuff tears and tendinopathy. Corticosteroids are mainly used to reduce inflammation and suppress the immune

system. PRP treatment can help support wound healing in trauma and joint injury by introducing platelets and other proteins contained in blood-plasma. However there is debate whether or not these have an effect.

A multi-centre, pragmatic, 2x2 factorial, randomised controlled trial involving 2287 patients found that subacromial corticosteroid injection provided no long-term benefit in patients with rotator cuff disorders [94]. A Network meta-analysis of randomized controlled trials involving 18 studies showed that CSI lead to pain reduction and functional improvement in the short term (3-6 weeks) but not in long-term (over 24 weeks). The analysis also showed that other injection-based therapies such as platelet rich plasma and prolotherapy, may yield better outcomes in the long term [95].

Jo et al showed major improvements in 48 patients following PRP injection in SS tendon reconstruction. The re-rupture rate was at 55% without PRP treatment, as compared to 20% in patients treated with PRP [96]. A meta analysis comparing 11 studies with 597 patients found re-tear rates were only significantly decreased when PRPs were used for the treatment of large tears and using a double-row technique. There were no statistically significant differences overall and an increased risk for bias was found [97]. A more recent randomized control trial showed patients who received PRP experienced better pain relief and function at short-term follow-up (3 months), compared to patients that received CSI. However, the long-term (12 months) effect showed no difference between the PRP and CSI groups [98]. A recent randomized, placebo-controlled superiority trial also concluded no patient benefit of PRP treatment in the short or long term, following archilles tendon rupture [99, 100].

1.2.5.4 Surgical Treatment

Surgical treatment is needed when rotator cuff tears don't sufficiently heal due to age or the size of the tear. In small tears it is usually decided after a patient fails conservative treatment. The major aim of surgical repair strategies is to re-anchor the

tendon to the bone and stabilize the joint throughout the healing period, to restore function and mobility [101]. The open trans-osseous technique, inserting bone anchors into the head of the humerus and reattaching the remaining tendon via sutures, used to be the gold standard in rotator cuff repair surgeries. However, the outcome highly depended on the quality of the bone and the sutures often tore through the soft tissue. Today surgical techniques focus on arthroscopic suture-anchor fixations which can withstand cyclic load [102]. Suture-anchor systems need further evaluation as length of screws, thread length, suture material and eyelet location are variable and have led to different outcomes [89]. Not only the design of the materials but also the surgical technique itself is variable. Biomechanical studies were performed comparing single-row to double-row anchors, with the latter leading to improved initial fixation strength, ultimate tensile load, gap formation, and footprint area strain [103]. However, a more recent review concludes there is a lack of statistically significant differences between the two techniques. Furthermore the double-row technique should be applied strictly to selected patients, due to the high cost and surgical skill involved [104]. Re-rupture rates following arthroscopic rotator cuff surgery are high with values ranging from 11% to 94% [105, 4]. The success of these surgeries depend on tear size, age, muscle strength and prevalence. Tear sizes are roughly grouped into small, medium, large, and massive tears, corresponding to <1 cm, 1-3 cm, 3-5 cm, and >5 cm respectively [106]. The value of some rotator cuff surgeries have recently been questioned, as a recent study found no benefit of arthroscopic subacromial decompression versus a placebo arthroscopic surgery. The authors concluded that this should be communicated to patients during the shared treatment decision-making process.

New strategies have been developed to tackle issues around failing surgeries. Additional tissue grafts can be harvested from the patient (auto) [107], another individual (allo) [108], or a different species altogether (xeno) [109]. Where this is not possible

or feasible, synthetic patches are used to bridge larger gaps [110].

1.2.5.5 Patch Augmentation

The aim of patch augmentation in rotator cuff repair is to assist or induce native tissue growth and provide biomechanical support, particularly in large to massive or otherwise irreparable rotator cuff tears. Surgically there are two ways patch augmentations are used; suturing the patch on top of the tendon-to-bone repair, or suturing the patch into the exposed area as a bridge following a partial repair [111] Current patches can be classified into different categories: non-degradable structures, biological scaffolds such as ECM-based patches or tissue grafts (including auto-, allo-, and xenografts), and degradable synthetic scaffolds [2, 112]. Baldwin et al recently identified 28 different patches [112]. Cook et al identified 13 different patches currently in use in the UK [111].

Non-degradable structures have high compliance in terms of mechanical strength. They aim to permanently support the diseased tendon and disregard complete tissue healing [113]. Materials include polyester [114], polypropylene (Dacron or Marlex) [115, 116, 117], polycarbonate polyurethane [118, 119, 120], polyethylene (Mersilene Mesh, Ethicon, Somerville, NJ) [121] and polytetrafluoroethylene (Teflon) [122, 123]. There have been concerns that these patches can cause chronic infection and loss of integrity in the long-term [114]. The latter was highlighted in carbon-fibre implants which defragmented in the body and lead to systemic chronic inflammation [124, 125, 126]. Indeed most studies peaked between 2000 and 2010, although polypropelene [117] and polytetrafluoroetylene [122, 123] have recently resurfaced. An in-vivo model of polypropelene mesh showed to be biomechanically suitable as an interposition graft for large irreparable rotator cuff tears [117]. To bridge massive rotator cuff tears, a teflon patch was employed and showed improved range of passive motion and improved strength. Sadly there was no control-group reported [122]. A superior

capsule reconstruction study compared 1-layer to 3-layer teflon graft outcomes. The 3-layer teflon grafts significantly improved shoulder function and shoulder abduction strength, with pain relief and a lower rate of postoperative complications [123]. The lack of suitable controls make these studies difficult to interpret. Furthermore these non-degrading polymers can lead to long term disruption of mechanical loading, and therefore interfere with tendon healing and strength. Long-term follow-ups are therefore necessary to fully assess their effect.

Biological scaffolds aim to eliminate the defragmentation problem and allow natural tendon healing. They tend to have similar mechanical properties as native tissues, as the ECM is maintained. Biological patches include commercially available and FDA approved ones such as GraftJacket[127, 128, 129] (Wright Medical Technology, Arlington, Tennessee), CuffPatch (Organogenesis, Canton, MA), Permacol (Tissue Science Laboratories, Covington, Georgia), Arthroflex (Arthrex, Munich, Germany), Dermaspan (Zimmer Biomet, Warsaw, Indiana), and TissueMend (TEI Biosciences, Boston, Massachusetts) [130, 131]. Although some of these are animal derived, and originally caused concerns [132], modern complete DNA extracting procedures led to less and in most patients subclinical immune responses [133, 134]. Commonly these scaffolds are derived from porcine small intestinal submucosa [135], porcine dermal graft [136], porcine dermal ECM [133, 137] bovine pericardium–derived collagen patches [116] or bovine tendon patches [138]. Results showed a reduction in the structural failure rate compared to standard rotator cuff repair [133, 136], while others reported no superior outcomes in patients [135]. Grafts from human donors have also been investigated widely. Autografts from the fascia lata [139], quadriceps tendon [140], humeral periosteal flap [141, 142], and acellular dermal allografts [143] have been reported. Depending on tear size and graft type, some showed no healing improvement [141, 139], while others did show improvements [143, 140].

Synthetic degradable structures show potential for patch augmentation as they aim

to disintegrate at the same speed that the tissue takes to remodel itself. Thereby they are highly versatile, offering malleable mechanical strengths and structures. A PLLA synthetic patch was used to treat rotator cuff tears. It showed successful repair of large to massive rotator cuff tears in 83% of patients at 12 months after surgery and 78% of patients at 42 months after surgery, with substantial functional improvement [144]. Few have been used in the clinics, but many have been tested in tissue engineering studies (section 1.3.2). Further research is needed to assess whether tissue engineered synthetic degradable patches can keep what they promise.

Overall there are pros and cons for all types of patches. The literature is significantly lacking direct comparisons. A recent study has called for a randomized control trial assessing the effectiveness and cost-effectiveness of patch augmented rotator cuff repair [111]. The group noted that due to the large variation in the patches, it was unlikely that a single study would be sufficient to address all of the key research questions. It was also noted that, should a randomized control study be conducted, non-animal based patches were preferred and particularly porcine-based patches were to be excluded. Results showed no preference for a single type of patch, neither in terms of use nor favourable clinical evidence. Though too weak for conclusions, some evidence was collected in favor of allograft and synthetic patches for reducing re-tear rates, and synthetic patches for reducing pain.

1.2.5.6 Growth factor delivery

Growth factors have the potential to contribute to tendon healing by stimulating proliferation, differentiation, ECM synthesis, and remodeling, thereby presenting a way to complement treatment and improve the outcome [145]. We introduced the mechanisms in section 1.2.4. However, at this point in time there are unanswered questions regarding growth factor selection, optimum dose, duration and delivery method. For rotator cuff injuries there are currently no growth factors approved

by the FDA, and only very few growth factor formulations are approved overall for clinical use (BMP2, BMP7 and PDGF for bone fractures, PDGF for neuropathic ulcers) [146, 147].

1.2.5.7 Cell-based Therapy

Although growth factors and PRP have had some promising results, both have some unsolved problems. The idea of cell-based therapy is the introduction of autologous or allogous cells, to enhance repair and remodelling. Stem cells such as bone-derived mesenchymal stem cells (BMSCs), adipose-derived (ASCs) and tendon-derived stem cells (TDSCs) are promising for musculoskeletal repair approaches as they have the ability to differentiate into bone, cartilage and tendon. Alternatively, fully developed tenocytes could be used. Tennis elbow, a chronic over-use injury marked by micro-tears and the subsequent degeneration of the wrist extensor tendons [148], treated with the injection of laboratory grown dermal fibroblasts led to 11 out of 12 patients showing satisfactory results [149]. Autologous dermal fibroblasts were used in a different study involving 46 patients with patellar tendinopathy. The treatment led to a reduction in disability and improved pain [150]. Wang et al tested the injection of autologous tenocytes into a small number of patients with tennis elbow. This improved function and repair of the tendon tissue. However, while patient satisfaction was reported to be high, magnetic resonance imaging (MRI) results showed the need for further treatment [151]. In the same year, Wang reported an autologous tenocyte injection in a young athlete with partial-thickness rotator cuff tear and tendinopathy. After 1 year the the MRIs showed improved tendinopathy and healing of the partial-thickness tear. The patient reported substantial improvement of symptoms and was able to return to national-level competitions [152]. In order to bridge large defects, cell-seeded scaffolds seem to be a promising approach. These can be implanted into the defect and could then produce ECM from within. There are currently no clinical

studies for this approach. However, there is promising evidence resulting from in-vivo studies [153, 154].

In recent years the potential of tissue engineering strategies to enhance tendon regeneration and produce alternative rotator cuff repair strategies, taking biological healing into account has become evident. These involve combinations of different types of scaffolds [155], cells, and external stimulation.

1.3 Tendon Tissue Engineering

1.3.1 Cells

The main type of cells resident in tendons are tenocytes, also called tendon specific fibroblasts. These are fully developed tendon cells. In the literature we commonly see three types of cells used for tendon tissue engineering; MSCs, dermal fibroblasts, and tenocytes. A study compared the suitability of mouse muscle-derived cells, dermal fibroblasts, and tenocytes for tendon tissue engineering. The reasoning was that reciprocal muscle-tendon interactions are necessary for tendon formation during development. Given that the absence of muscle in tendon development will lead to tendon degeneration, muscle-derived cells could exert its regulatory effect by producing growth factors [40]. Therefore, muscle-derived cells were chosen as seed cells for engineered tendon, and the result showed that they not only had good proliferation potential, but could also form strong engineered tendon. The *in-vivo* results showed that muscle-derived cells proliferated faster, and lead to better alignment of cells along the collagen fibres. They also lead to more mature collagen fibrils and stronger mechanical properties. The paper concludes that tenocytes and fibroblasts are still promising candidates, but muscle-derived cells should be further investigated [156].

1.3.1.1 Mesenchymal Stem Cells

MSCs can be extracted from embryo, fetus or adults. In adults they can be extracted from several sites such as bone marrow, adipose tissue, synovium, peripheral blood, muscle, periosteum or tendon (also referred to as tendon-derived stem cells or tendon progenitor cells) [157, 158]. MSCs have shown to be phenotypically different depending on the tissue they originated from. Youngstrom tested MSCs derived from tendon, bone marrow and adipose tissue. The group did so including cyclic load and hypothesized that tendon-derived MSCs would differentiate better into a tenocyte phenotype. It was concluded that these MSCs were indeed the most suitable in treating tendinopathies. Bone marrow and adopise tissue derived MSCs could function as robust alternatives however [159]. Alternatively, MSCs can be obtained from induced pluripotent stem cells (iPSCs) [160]. MSCs require the correct conditions for proliferation and differentiation. They are believed to have higher levels of proliferation and collagen synthesis and have the advantage to replicate for longer compared to differentiated cells [158]. MSCs also have a lower risk of immune reaction in the host, whether autologous or allogenic, as they have been shown to express no class II major histocompatibility complex (MHC) [159], and have immunosuppresive properties [161]. As MSCs can differentiate and have a high proliferative capacity, they also pose the risk of tumorigenicity and differentiation into a different, unwanted cell types such as an osteogenic line [162]. Currently the lack of consensus on differentiation protocols is what is slowing down progress in the use of stem cells in tendon tissue engineering [163]

1.3.1.2 Tenocytes

Tenocytes can be extracted from donor tendons and cultured in-vitro. These have the advantage that they are fully developed and can be cultured without the need for a complex cocktail of growth factors. Studies conducted with this type of cells

will give the best insight into tendon-like behaviour. However, tenocytes pose several problems. They are more difficult to obtain due to rarity of donor tissue and requires an invasive procedure. Due to the scarceness of cells in tendons, the yield tends to be low. Once obtained, cell de-differentiation during expansion is a problem [151]. Due to their low doubling time they are also harder to grow and therefore less feasible for some labs [164].

1.3.1.3 Fibroblasts

Dermal fibroblasts are a more readily available cell source. These are derived from the mesoderm, like tenocytes, and have a similar cell morphology and characteristics [156]. Fibroblasts are a very important cell type in connective tissue, responsible for the production and maintenance of the ECM. A study testing their response to silk fibroin PCL scaffolds showed that these cells can upregulate gene expression of tendon-specific marker proteins such as collagen I and III, fibronectin and byclycan [165]. In a different study they were shown to take on a tenogenic phenotype and form organized neotendon in vitro, as well as tenogenic gene expression in-vivo [166]. In a different study, twelve patients diagnosed with tennis elbow were treated with laboratory-grown dermal fibroblasts. Eleven patients were healed to a satisfactory level. After 6 months, a reduction in the number of tears, angiogenesis, and tendon thickness was observed [149]. Elsewhere, forty-six patients were treated with autologous skin fibroblasts after suffering from patellar tendinopathy. Their disability scores, severity and pain all improved [150]. However, there remain concerns as these cells are not specific to the tissue in question [167]. Another common source of fibroblasts is human newborn foreskin tissue. It is estimated that one-third of the population with a penis worldwide is circumcised [168]. The skin removed during surgery is readily available and a by-product that would otherwise be discarded, which makes it an ideal cell source. Another advantage these fibroblasts bear is their highly proliferative

phenotype, which is the result of the donors generally being very young. In the human foreskin itself, 61 different clones of dermal fibroblasts have been isolated. A small population of these cells are multipotent, and two clones have the capacity to differentiate into neurons, adipocytes or hepatocytes under certain culture conditions [169], making this a highly versatile cell type applicable to a variety of research interests.

1.3.2 Scaffolds

Scaffolds for tissue engineering tendons are used in two ways. They are either investigated as model-systems in-vitro, or studied with a clinical setting in mind. In the clinics, scaffolds could be used to by-pass the problems of poor tendon state for repair, rare allografts and immune risks involving xenografts. Scaffolds can either be seeded with cells prior, or implanted without cells. Questions have been raised which approach was better. A study conducted for bone tissue engineering compared cell-seeded scaffolds and cell-free scaffolds. The latter group lead to better healing of the defect. Furthermore M2 macrophage activity was confined to the construct's periphery in seeded scaffolds, indicating the MSCs' matrix deposition might hinder remodeling and healing [170]. ECM-based scaffolds showed the same results. Acellular ECM scaffolds lead to an M2 macrophage response, leading to tissue healing and constructive remodeling as opposed to cell-seeded ECM scaffolds, leading to an M1 type response and scarring. This was the case even for autologous cells [171]. The outcome is not only dependent on the addition of cells, but also the material properties of the scaffold itself. Tissue engineering scaffolds can be grouped into synthetic and non-synthetic scaffolds. Scaffolds aim to provide a supportive structure for cells to adhere to, and to bridge the tendon tear. The goal is to mimic the structure and mechanical strength of the native tissue as closely as possible.

1.3.2.1 Natural scaffolds

As mentioned, natural scaffolds are decellularized tissues, or biological materials such as silk, or collagen. Overall, biological materials have a lower mechanical strength while decellularized tissues are meant to retain the mechanical strength and structure. There are a number of biological scaffolds approved for tendon repair by the FDA, outlined in section 1.2.5.5. Seeing as a tendon's structure is built mainly on collagen, it comes without surprise that collagen based hydrogels have been suggested. However, these have very low mechanical strength and are best used in combination with synthetic scaffolds [172].

1.3.2.2 Synthetic Degradable Scaffolds

Promising materials currently under investigation include poly-l-lactic acid (PLLA), polyglycolic acid (PGA), poly(lactic-co-glycolic acid) (PLGA), polycaprolactone (PCL), and polydioxanone (PDO) [113]. This is due to different manufacturing techniques such as extrusion or electrospinning, post processing such as weaving, braiding, or chemical alterations and adjusting properties such as hydrophilicity and speed of degradation [173]. Rapid prototyping has led to faster and faster advancements in scaffolds production in tissue engineering [174], resulting in fibrous structures, gels or sponges. MSC-seeded scaffolds have been used to regenerate fibrocartilaginous tendon-bone insertion sites in a rabbit model. The seeded PGA sheets were found to induce regeneration of the fibrocartilage with enhanced collagen deposition and improved mechanical properties compared to the non-seeded PGA sheets. However, the mechanical properties were not up to the standard of natural tissue [175]. Gniesmer et al compared a commercially available porous polymer patch (Biomerix) with electrospun PCL fiber mats and chitosan-graft-PCL coated electrospun PCL (CS-g-PCL) fiber mats in vivo. Results showed a lowers immune response and higher vascularization for the CS-g-PCL fiber mats [176]. However, degradation of synthetic scaffolds

tends to happen via hydrolysis, releasing acidic products into the body, which, in high concentrations, was found to be toxic to tenocytes [177]. More recently co-polymers have been explored to circumvent commonly occurring issues with single-polymer scaffolds. An electrospun nanofiber scaffold composed of PGA and poly-L-lactide-co-caprolactone (PLCL) was tested in an acute sheep model. Scaffold-treated sheep were compared to a scaffold-free group. Animals in the scaffold-treated group displayed an insertion in the humerus that was starting to resemble native fibrocartilaginous insertion of the ovine infraspinatus tendon. Furthermore perforating collagen fibers, similar to Sharpey fibers, were observed in this group. The study noted no complications in all 40 sheep [178]. Synthetic scaffolds tend to have greater mechanical properties over natural scaffolds, but are problematic due to their hydrophobicity, leading to cell-attachment issues [131]. Furthermore, molecules released during degradation may be toxic in high concentrations [113]. The ideal tissue engineering scaffold allows for strong cell attachment, ECM deposition, cell infiltration and proliferation with tailored degradation speed. Sometimes this is only achieved by blending polymers, or augmenting the surface [179].

1.3.2.3 Surface Modifications

Surface modifications include changes in hydrophobicity, charge and chemical composition of the material [113]. Cells have been shown to prefer positively charged polymers, but when cell attachment mechanisms were tested (electrostatic interaction, hydrophobic interaction, and biological interaction), results showed cells adhered irrespective of electrostatic force and protein adsorption [180]. Protein adsorption is influenced by surface charge which might in turn affect integrin binding and improve cell adhesion. Additionally, while each of these modifications can lead to improvements, hydrophobicity and charge are themselves dependent on the material chemistry, and so it is difficult to interpret some of these studies. Hydrophobicity is often

changed by plasma-treating scaffolds, though low efficiency on 3D structures needs to be considered [181]. Other surface modifications include dip coating scaffolds in minerals [181] surface etching [182] to increase surface roughness, or tethering growth factor proteins to the scaffolds [183]. The surface of the scaffolds plays another role in mechanotransduction and can be seen as an external stimulus to cells.

1.3.3 External Stimuli

Cells respond to external stimuli by altering their morphology or gene expression (section 1.2.3). This is of particular interest in tendon tissue engineering, as tenocytes have been shown to lose their tenogenic phenotype for the lack of adequate stimuli, and because we understand very little about these mechanisms. These stimuli form a natural part of the tendon micro-environment and include chemical cues and biophysical cues.

1.3.3.1 Chemical Cues

Chemical cues are molecules added to the cell media which will enhance tenogenic differentiation, such as growth factors. We talked about these in section 1.2.4 and 1.2.5. Other chemical cues could be Ascorbic Acid. Murine fibroblasts treated with Transforming Growth Factor Beta (TGF-beta) and Ascorbic Acid (AA) in combination with mechanical stimulation on a PEG-fibrinogen hydrlgel led to a type I collagen-rich ECM, and cells aligning along the stretching direction. Treatment with TGF-beta and AA alone was not able to significantly promote this differentiation [184].

1.3.3.2 Biophysical Cues

Providing biophysical cues is critical for tendon development in embryos and will lead to malformations if not received [185]. Biophysical cues are typically provided

through the scaffold structure itself or external mechanical stimulation. The scaffold can be designed to provide patterned topographies such as grooves or aligned structures which guide cell shape (figure 1.6. Nanopores on fibers, have lead to improved proliferation, cell adhesion and potentially higher viability of cells, compared to smooth fibre surface [186]. Low stiffness has led to lower cell alignment along strain, and a more spread-out cell morphology, likely sensed through the cytoskeleton [187]. Mechanical stimulation is provided via more elaborate tissue engineering bioreactors.

1.4 Tissue Engineering Bioreactors

1.4.1 Static Mechanical Stimulation Bioreactors

Static mechanical stimulation refers to non-repetitive tension or compression. Fibroblast-seeded collagen gels were anchored on two ends to create static tension in an approach to produce small tendons [188]. Cell-seeded hydrogel yarns were statically stretched by wrapping them between two pins (figure 1.6 A2) [189]. Magnetic tweezer technology was developed to apply static stretch to study complex membrane biomechanics (1.6 A3) [190]. For myotube formation studies, a cell-seeded collagen scaffold was clamped in suspension (figure 1.6 A4) [191]. Static compression was applied by placing a glass cover and metal weights on top of a ligament cell layer [192]. Physiologically, tendons experience repeated motions. To apply these, dynamic mechanical stimulation bioreactors were developed.

1.4.2 Dynamic Mechanical Stimulation Bioreactors

Dynamic stimulation bioreactors deliver cyclic mechanical stimulation such as tension, torsion or compression. Traditionally these bioreactors consist of rigid boxes, housing the media and construct, an external actuator to mechanically stimulate the

construct, and sensors like load cells, to track the forces applied. These bioreactors are used to study the responses of cells to the forces experienced, to test different materials, or in the future to prepare tendon grafts for transplantation.

1.4.2.1 Chambers

The bioreactor chambers are what we consider the outer component, holding the bulk material, scaffold, cells and media and ensuring sterility. Scaffolds and tissue constructs are usually clamped into place. At least one clamp is linked to the actuator. Materials and adhesives of these chambers must withstand sterilization, be non-leachable, bio-compatible and must not alter the culture media. This includes chamber housings, gaskets, parts of actuators that are in contact with cells or cell media, lids, clamps, tubing etc. While many manufacturers claim bio-compatibility of their materials, this should be tested in a separate cytotoxicity study in the full setup. The material must be permeable to gasses or be equipped with air vents and filters to enable gas-exchange. The size of these chamber varies, some groups use custom-built box structures [193], others have adapted existing petri-dishes [194], multi-well plates [192, 195] or single well chamber slides [191]. The chamber's size also depends on the application, culture duration and nutritional requirements. Larger chambers can hold several samples at once enabling technical and biological replicates and multiple stimulations in parallel [196]. Neglecting this has led to a potential source of confounding in the past [197]. The size also depends on the intended use; large scale whole tissue studies [198] require bigger chambers over scaffold testing, single-cell fluid shear stress or mechanotransduction studies [199].

1.4.2.2 Actuators

Dynamic stimulation aims to apply repeated tension, torsion or compression to a construct. This can be applied in precise amplitudes and frequencies and aim to resemble

repetitive movements in the body. The most common way to apply dynamic tension is via a stepper motor (figure 1.6 B1) [200]. Movement of a stepper motor can also be translated into radial displacement (figure 1.6 B2) [**?**], and scaled up to run several stimulations in parallel (figure 1.6 B3) [201].

Another type are perfused-, or shear-stress bioreactors (figure 1.6 C1). The term perfused in this field is not used to describe feeding strategies, but to indicate that media is purposefully used to create shear stress on cells. Shear stress in bioreactors can be created through high flow rates or manipulating the fluid in other ways, such as by introducing stirrers or using spinning or rotating flasks [202, 203].

To provide physiologically relevant stresses, combinations of different mechanical stimuli have been studied. Maeda et al built a chamber capable of stretch and shear stress application (Figure 1.6 C2) [204]. In a different study a pressure vessel was filled with distilled water and placed into a water bath at 37deg C. The vessel contained a cell-culture bag. The combination of Hyperbaric pressure and chondrogenic priming lead to faster osteogenesis in hMSC (figure 1.6 C3) [205]. More combinations and their effects were reviewed extensively [187]. What these studies highlight is the importance of multiaxial stimulation. True multiaxial stimulation however is difficult to achieve with current bioreactor systems.

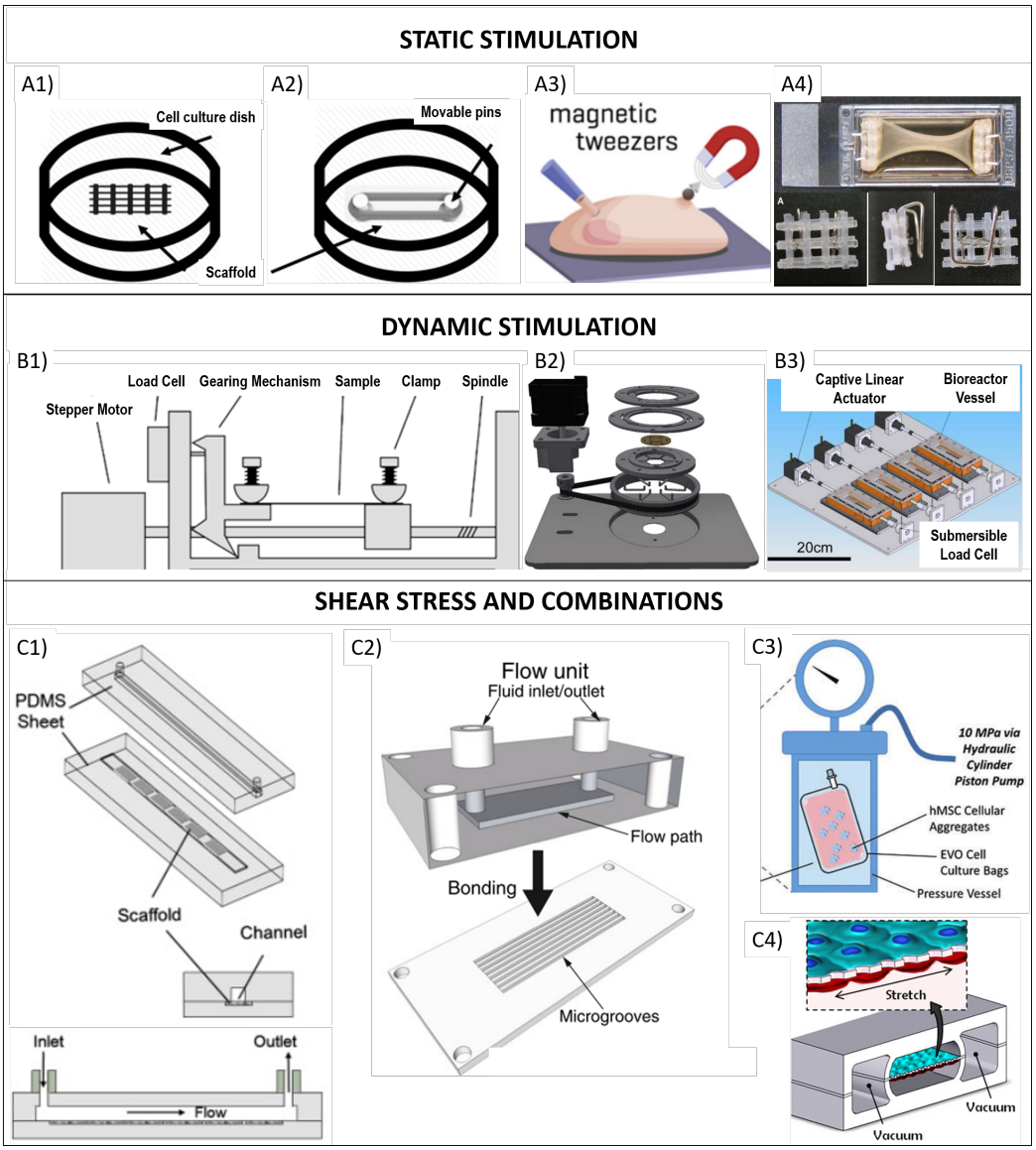

Figure 1.6: **Illustration of traditional stress bioreactors capable of static, dynamic and combinations of mechanical stimulation.** Static stimulation: A1) Cell culture on a scaffold with topographic mechanical cues. A2) Cell culture on a scaffold stretched between two Teflon pins. [189] Permission granted. A3) Magnetic tweezer technology used to apply a membrane pinch to individual cells [190]* Permission granted. A4) Static stretch through flotation bars [191]. Permission granted. Dynamic Stimulation: B1) Conventional setup of a stepper motor applying repetitive stretch to a clamped sample. [200] Permission granted. B2) Movement of a stepper motor translated into radial displacement. [**?**]. Permission granted. B3) Scale up for multiple stimulations in parallel [201]. Permission granted. Shear Stress and Combinations: C1) Shear stress bioreactor s, adapted image [206]. Permission granted. C2) Bioreactor chamber capable of stretch and shear stress application [204]. Permission granted. C3) A hydrostatic pressure vessel, containing a cell-culture bag with hMSC [205]. Permission pending. C4) Lung on a chip platform to study effect of mechanical stimulation and shear stress [207]. Permission not required. All images were adapted

1.4.2.3 Sensors

Sensors are used to get real time information about the culture conditions. Sensors most commonly used in cell culture measure temperature, gas mix, pH, glucose and metabolites. Typically sensors can be grouped into on-line/in-line or off-line sensors. As the name suggests, the latter work off-line, so away from the culturing system. These are usually bench top glucose measuring devices or could be colorimetric assays to assess contents in the cell culture medium. In-line sensors do not require sample-taking and are directly integrated into the culture system. These are most typically gas-mix or oxygen sensors, but can also be glucose/metabolite sensors. Tissue engineering bioreactors tend to be small and therefore fit into an incubator, where temperature and gas-mix are automatically measured, and the pH maintained stable via CO_2 addition. An important component of mechanical stimulation bioreactors, is the accurate measurement of the forces applied to the construct. Currently this is done by load cells or similar piezoelectric sensors. These are put in place between the construct and the actuator and can measure a pulling or compressing force applied to the sensor.

1.4.2.4 Shortcomings

Current approaches for tendon tissue engineering have shortcomings in that mechanical stimulation is mostly uniaxial and applies tension only. The missing piece is to accurately mimic movement. The inability to apply physiologically relevant multidimensional stimulation to rigid structures is a main concern for the advancement of tissue engineering. While combinations of different mechanical stimuli and multidirectional stimulation were attempted, they can only get so close while being attached to a rigid chamber. What is needed is a bioreactor that moves with the stimulation, or an actuator that moves with the bioreactor.

The traditional load-cell sensors can only deliver an approximation of the forces exhib-

ited to the construct. Since the sensors are usually bridging the connection between actuator and construct, it cannot measure local differences. Soft sensors, an emerging technology, can be inserted directly and measure forces applied locally.

Clamping is a crucial and often problematic step in mechanical stimulation. If not clamped into place correctly, a pulling actuator could pull more on one side of the construct than on the other,leading to an uneven strain distribution. The solution tends to be pivoting clamps, but this does not eliminate the possibility of the sample slipping. Moving toward constructs being permanently embedded in the chamber, or having the stimulation embedded in the carrier through soft actuators, would greatly improve sample gripping problems, and reduce the bioreactor size.

Unless the system has a built-in microscopy window, microscopic analyses of the constructs are hardly possible throughout the experiment and can only be conducted at the end, when the sample can be detached from the actuator. Bioreactor systems with a built-in microscopy window usually consist of a glass slide, making it rigid and therefore the application of multiaxial movement is limited. As these chambers tend to be permanently linked to the actuator, it is also limited in size, as the whole system would need to fit under the microscope.

1.4.3 Emergence of Soft Bioreactors

In order to overcome the issues mentioned above, researchers have worked on the development of a new class of bioreactors - soft bioreactors. These consist either of a soft chamber or a soft actuator. The parallel development of flexible soft sensor systems is an advantage we would also like to briefly highlight here. These systems aim to apply multiaxial stimulation.

1.4.3.1 Soft Chambers

Soft chambers are capable of multiaxial stimulation through their soft outer shell, which moves with the actuation. There are general requirements for flexible bioreactor chambers. The material must not crack, rupture, decompose or leach due to the force or friction resulting from the mechanical stimulation. The material must sit loosely enough as to not interfere with force translation and force measurements. If the latter is not possible, the material's role in bearing some of the force must be taken into account and reported accordingly. Materials such as Polydimethylsiloxane (PDMS) seem promising as they are malleable to different degrees of stiffness. The moulds can be drawn in computer assisted drawing (CAD) software and modelled in computational fluid dynamics (CFD) software. PDMS is also optically transparent, allowing microscopic observation and it is gas-permeable. The drawback is that moulding PDMS is not a trivial task and requires tweaking to obtain a mixture that resembles the mechanical properties of tissue. There are a few more material candidates commonly used in medicine, such as silicone, polyvinylchloride, polyethylene, polypropylene, polymethylmetacrylate ,and polyurethane [208]. These materials can be shaped and sealed into flexible membranes or bags through melting, ultrasonic welding, UV/LED curing systems or medical grade glues such as epoxies. Alternatively, to insure bioreactors with rigid and flexible parts are liquid- and airtight, the membrane can be fixed between two plates with O-rings in between (figure 1.7 A1) [209]. Secerovic et al developed a soft bioreactor chamber capable of movement in 6 degrees of freedom. It is aimed to stimulate invertebral discs (figure 1.7 A2). The chamber consists of a custom-made polycarbonate structure wrapped by a soft silicone membrane. The system is assembled with the mechanical interface and sealed with a nut [210].

1.4.3.2 Soft Actuators

Soft actuators are a novel approach to stimulate cells and tissues from within the construct. Fell et al developed a bio-hybrid soft robot capable of angular and radial actuation for vascular tissue stimulation. Movement is achieved via a pneumatic soft actuator pumping fluid into the structure. The centre is directly seeded with MSCs which are subsequently conditioned for 24 hrs (figure 1.7 B1) [211]. Paek et al developed a soft robotic constrictor for in vitro modelling of dynamic tissue compression (figure 1.7 B2) [212]. This elastomeric actuator is pneumatically regulated and capable of dynamic bending motion, mimicking the constriction of tubular organs. The system is compatible with a variety of human primary cells. The actuator is capable of organotypic modelling of complex tissues such as solid tumours and vascular networks and the effects of compressive forces on them. A hydraulic soft robotics approach to mimic index finger and thumb was developed by combining different materials and localized designs. These were designed with the help of mathematical models, and capable of bending, extending, expanding and twisting (figure 1.7 B3) [213]. While cells have not yet been incorporated, we highlight this approach as it has the potential to stimulate cells. Furthermore, the algorithm reported has the ability to produce designs for different tissues and streamline the production process. A soft robotic sleeve was developed to be implanted around the heart and actively compresses and twists to act as a cardiac ventricular assist device. The actuators were designed to stiffen when pressurized. It can be customized to patient-specific needs by adapting to the size of the heart and the pre-tensioning required. This system was controlled by the native cardiac cycle and adapted the actuation to deliver disease-specific assistance (figure 1.7 B4) [214].

The advantage in these actuators is that they can adapt to complex and dynamic environments. Their softness resembles that of biological tissue more than the rigid actuation systems detailed earlier. This makes them more capable of replicating shape

and functions of the biological tissue in question. Cells can typically be incorporated directly into the actuator, eliminating the need for a cell carrier and circumventing clamping/mounting problems. Because these systems do not rely on scaffolds or tissue constructs, most of their application is currently limited to mechanotransduction studies or the stimulation of whole tissues, rather than tissue engineering constructs. However, there is the potential to apply the same mechanism to stimulate scaffolds from within, or from around as seen in Roche et al's soft robotic sleeve, thereby creating the opportunity for more clinically relevant tissue constructs.

1.4.3.3 Soft Sensors

Soft sensors address the challenges of conventional sensors, which have limited deformation capacity and would interfere with multi-axial stimulation. By employing soft sensors, the mechanical stress and deformation, as well as changes to the micro-environment of cells are detected in real time. In one study, a stretchable and suturable fibre sensor based on capacitance changes was reported. It successfully measured strain in an *in-vivo model* (figure 1.7 C1) [215]. Another soft strain sensor was developed for neuromodulation in growing tissue (figure 1.7 C2) [216]. The device is capable of electrical stimulation and monitoring of tissue repair in a rapid-growth rat tissue model. A multi-functional soft sensor, capable of strain and pressure sensing, showed excellent biocompatibility and function in a rat model. This sensor was made of biodegradable materials, making it the ideal sensor to be transplanted (figure 1.7 C3) [217]. Flexible sensors should have high flexibility and biocompatibility as well as well-matched biodegradability with tissue growth to avoid a second surgery to remove the device. Research on soft sensors for soft bioreactors is scarce.

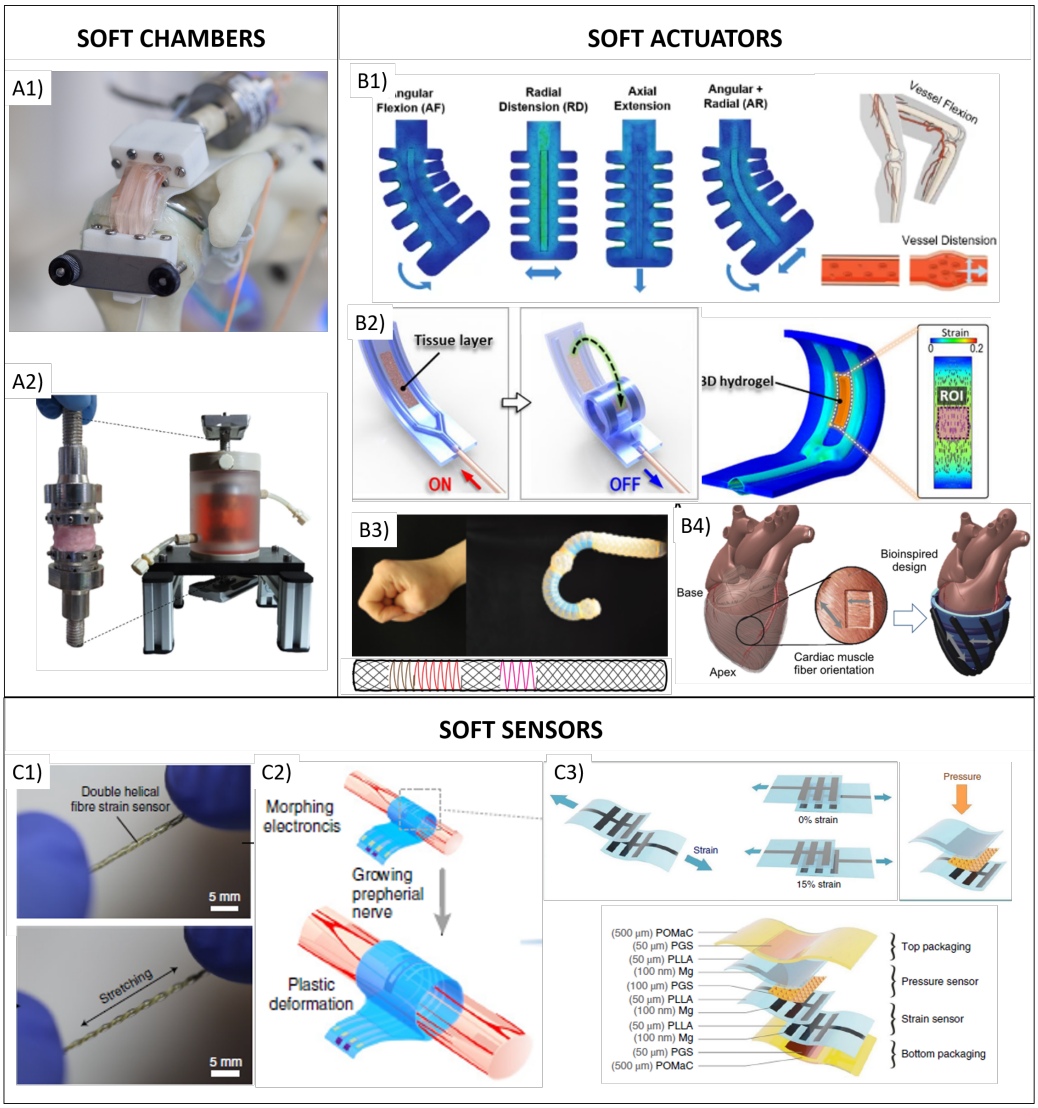

Figure 1.7: **Overview of soft bioreactors** Soft Chambers: A1) Humanoid bioreactor chamber developed in our group [209]. The chamber is mounted onto a robotic shoulder where it can be stimulated externally. A2) Invertebrate disc bioreactor capable of 6 degrees of freedom. Image adapted[210]. Permission granted*. Soft actuators: B1) Femoropopliteal artery soft actuator capable of angular and radial actuation for vascular tissue stimulation [211], permission granted. B2) Pneumatically actuated soft constrictor actuator mimicking the constriction of tubular organs [212]. Permission granted** B3) Finger soft actuator capable of bending, extending, expanding and twisting [213], permission not required. B4) Soft robotic implantable sleeve for heart stimulation [214]. Image adapted from Roche et al 2017. Reprinted with permission from AAAS. Soft Sensors: C1) photographs of a capacitive strain sensor made with double helical stretchable conductive fibers under initial and stretched conditions [215]. Permission granted. C2) Sensor for neuro-stimulation and sensing of strain [216]. Permission granted. C3) Soft capacitance sensor capable of strain and pressure sensing [218]. Permission granted. *https://creativecommons.org/licenses/by-nc-nd/4.0/. **http://creativecommons.org/licenses/by/4.0/

.

1.5 Humanoid Bioreactor System

Our group has developed a humanoid bioreactor system (HBR), consisting of a novel flexible cell culture chamber, housing a cell-seeded scaffold, supported by advanced robotic systems. It has the ability to replicate the human musculoskeletal motions and provide physiological forces to living cells. This system can provide multiaxial stresses and different loading regimes. Potentially, it could improve the formation of tissue grafts *in-vitro*, but also led to a better understanding of the importance of mechanical stresses in biology. Ultimately this could serve as a platform with the potential to treat musculoskeletal injuries such as tendon tears. It may also reduce the use of animal models in the translation of novel therapies into clinics [219, 209].

1.5.1 Chamber

The chamber consists of a thin tube of transparent polyurethane membrane. It is rolled and then heat-sealed along the long edge. To ensure air-tightness, the membrane is secured between two plates, a ring and two biocompatible rubber gaskets. The membrane is capable of holding media and maintain sterility. During mechanical stimulation, the membrane is loose enough to allow the media to be pushed against the walls and not burst through the applied pressure. Furthermore it does not interfere with force transmission onto the scaffold. In fact the membrane's Young's modulus was reported to be 10.3 ± 1.0 MPa, and therefore takes a negligible amount of the strain compared to the scaffold [209]. This soft chamber is independent from the actuation system. The group can run several chambers in parallel and attach them to the actuator ad-hoc. In traditional systems the chamber is directly linked to the actuator. The chambers can also be moved between different actuation systems, or different positions on the humanoid robot. Providing a platform to test different anatomical locations as well as directly comparing traditional uniaxial actuators to

the robotic arm with the same type of chamber. The group is currently exploring the use of this chamber under the microscope to track cell growth via live-cell imaging.

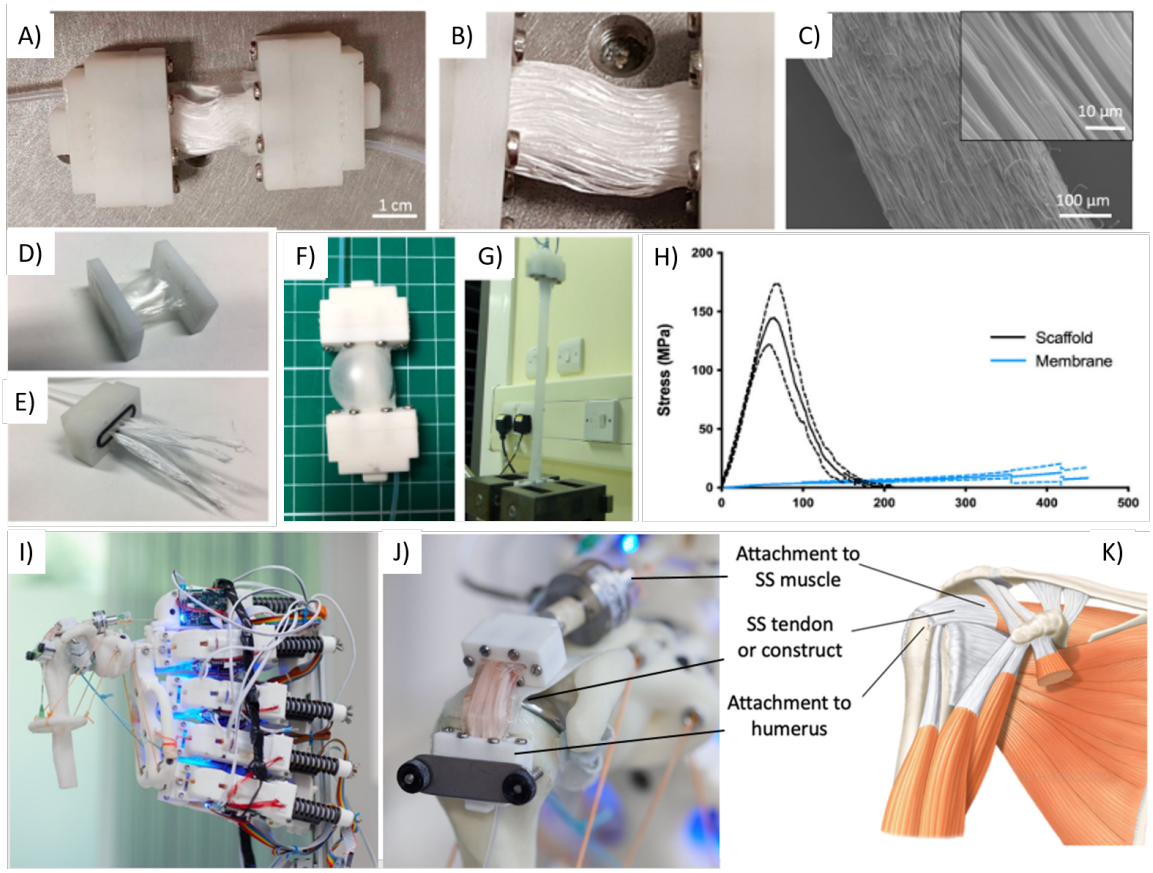

Figure 1.8: **Details of the starting point for this thesis. Flexible bioreactor chamber, scaffold and robotic shoulder**. A) Assembled bioreactor chamber, B) Multi-filament parallel scaffold, C) SEM images of a single filament at two different magnifications, D) The middle- section of the chamber consisting of polyurethane membrane and its 3D printed holders. The scaffold is slid into the membrane and resined into the main inserts. The 3D printed parts are screwed onto the main insert, E) filament bundles resined into the main insert, F) Expanded membrane upon filling the chamber with air G) Results of tensile tests to failure of a chamber. The membrane keeps its integrity at high strains, H) Stress-strain curves of the scaffold and membrane (measured separately). The dashed lines represent the standard deviation. Results suggest the membrane carries little stress at low strains, I) Robotic shoulder at the start of this thesis. Bioreactor chamber attached to the robotic shoulder at the SS location J) Close-up of the chamber in the SS location K) Comparison of SS tendon location on a human shoulder. Permission granted under the Open Access Creative Commons Attribution 4.0 International License. Figure adapted from Mouthuy et al 2022 [209]

1.5.2 Scaffold

The scaffolds are made from Polycaprolactone (PCL), an FDA-approved polyester fit for load-bearing tissue engineering. It is favourable for our applications as its degradation and mechanical strength can be controlled. PCL's contact angle is reported to be 130° [220] and therefore highly hydrophobic. Nonetheless, PCL is used in a variety of fields such as cardiac, tracheal, bone, skin, breast, vascular, dental, neural, skeletal and soft tissue engineering [179].

Briefly, PCL is electrospun into filaments and assembled into bundles of 40 filaments. The chamber contains 5 of these bundles, resulting in a 200-filament strong scaffold. The Young's modulus of the scaffold was reported to be 550.6 ± 63.4 MPa which reasonably matched values observed for human tendons [221, 222].

1.5.3 Humanoind Shoulder Actuator

The actuator responsible for the mechanical stimulation of the cells consists of a robotic humanoid shoulder. It was designed and manufactured by Devanthro. This shoulder was based on the biologically-inspired tendon-driven humanoid robot Roboy 2.019. The shoulder was based on a ball-and-socket joint actuated by up to nine artificial muscles, positioned on a trunk-like stand. Each muscle is represented by a DC motor [223]. The motors pull on inelastic strings, which are attached to 3D printed bones. The original shoulder was not intended to accurately mimic a human shoulder, and therefore was only capable of movements in 3 degrees of freedom (DOF). This was sufficient for the planned movements in this work. Several modifications were made to this setup, some of which were summarized in [209]. Figure 1.8 I) shows a photograph of the robot at the start of this thesis. These adaptations improved the clinical relevance, though quantitative measurements are needed to assess the degree of mimicry between a human shoulder and this humanoid shoulder robot.

1.6 The need to characterize the HBR

The data obtained before the start of this thesis, and work done by other members of the group alongside it, has shown that the humanoid bioreactor works as a proof-of-concept. It was shown that the platform can maintain cells in long term culture and deliver load that induces changes in gene expression and proliferation. However, a low cell viability in the high force regime, compared to the low force regime, and generally a slow proliferation were measured [209]. This is in contrast to traditional uniaxial loading regimes, which lead to proliferation at strains up to 10%. These regimes also lead to a higher variation in gene expression, particularly for genes associated with the extracellular matrix (ECM) [224, 225].

Little is known about the conditions inside the chamber. Monitoring the environment during culture with the help of sensors to measure nutrients and metabolites (oxygen, glucose, lactate, etc.) will help our understanding of the conditions the cells face. Furthermore operating parameters such as seeding technique and flow rate will have to be analyzed, in order to establish the system as an in-vitro culture model. Mathematical models have a strong potential to support this research [226, 227]. One potential reason for the high loss in cell numbers was the scaffold stiffness. Different materials will therefore be investigated. The timing of the loading regime was another concern mentioned which will be addressed.

1.7 Aims and Hypotheses

The overarching aim of this thesis is to characterize the performance of this novel flexible bioreactor system for mechanical stimulation. We hypothesize that we can seed cells evenly into the chamber, that the bioreactor system can successfully hold and proliferate cells, that the addition of sensors should lead to an improved understanding of the culture conditions, that mathematical models will greatly advance

our knowledge on spatial differences in nutrient concentration and culture conditions, as well as help us choose operating parameters, and that changes made to the scaffold will improve cell retention. We also hypothesize that the system is capable of supporting cell proliferation and of mechanically stimulating cells.

1.8 Thesis Structure

The thesis is grouped into five chapters. Chapter 1 sees the introduction of the topic, comprises a literature review on the state of the art in mechanical stimulation tissue engineering, with a focus on tendons and gives an overview of the starting point of this project as well as Thesis Aims and Hypotheses. Chapter 2 investigates the distribution of cells on our scaffold following different seeding techniques. The results from chapter 2 lead to one of the input parameters of a computational model, described in chapter 3. The model investigates nutrient distribution, metabolite accumulation and cell growth at different flow rates. The model is followed by a validation chapter 4 which aims to assess the accuracy of the model. A suitable flow rate is chosen from these results and used in chapter 5, where we investigate the role of different scaffold modifications, and mechanical stimulation. This thesis is structured in a scientific paper format, each of the experimental chapters have their own abstract, introduction, materials and methods, results, discussion and conclusion. The overall conclusion of the thesis is the final chapter 6.

Chapter 2

The Effect of Seeding Techniques on Cell Distribution

2.1 Abstract

Seeding cells effectively onto a tissue engineering scaffold will often determine the success of these. Many studies focus on the infiltration of cells rather than the effect the seeding technique, gravity and capillary action have on cell distribution. In this chapter we developed a fast, reproducible and semi-quantifiable method to identify cells within the scaffold. Cells were seeded in three ways - with the filaments within the scaffold aligned along gravity standing upright, perpendicular to gravity lying flat on the bench, and dynamically on a rocking plate. Upon leaving the cells to attach for an hour, they were fixed and stained with Osmium Tetroxide. The scaffolds were imaged with μCT and SEM together with a no-cell control. Seeding cells dynamically led to a slightly more even cell distribution. It was also shown that cells spread effectively from one bundle to the next via capillary action. This method provided useful information on which seeding technique to use going forward and under which circumstances cells would spread within the scaffold.

2.2 Introduction

Tissue engineering aims to regenerate tissue or build tissue constructs through the combination of scaffolds, cells and the appropriate environment. In any novel scaffold, cell distribution is important to be assessed. Uniform cell distribution through the entirety of the scaffold is crucial to enable cell-cell interaction and equal nutrient distribution. An even cell distribution also leads to a more uniform ECM deposition and therefore uniform tissue build up within the scaffold. Moreover, underpopulated areas can be the result for various reasons such as poor cell suspension, cluster formations, seeding technique, problematic scaffold design or nutrients not reaching the cells. In order to be able to trace the reason for uneven cell distribution it is important to establish where the cells land right upon seeding.

Cell distribution throughout scaffolds has been studied multiple times. Most studies use cryo-sectioning combined with microscopy imaging [228] followed by further analysis via mathematical models [229] and/or image analysis [230] or angled fluorescence laminar optical tomography (aFLOT), which allows in-depth molecular characterization of 100-200 μm resolution and penetration depths of 2-3mm [231]. In our case, these techniques were not an option as the scaffold material would not withstand cryo-sectioning. Furthermore, the scaffolds in the mentioned studies are much smaller. Our scaffold here would require a much larger amount of slices, ending up amounting to multiple hundreds to individually image and piece back together.

In the literature we see different seeding techniques being used. These can be grouped into two types - static and dynamic. Static seeding techniques include surface seeding and direct injection into the scaffold [229]. Dynamic seeding use tools such as orbital shakers [232, 229], spinner flasks [233], centrifuge [229], rotating wall vessels [234], and perfusion. However, these studies focused on the seeding density [233, 232] and seeding efficiency [234] rather than the seeding technique and cell distribution.

Due to the nature of the material we use, the unique make-up of our scaffolds and our

setup that allows seeding onto one bundle from one side only (1.8 A), we wanted to investigate not only the influence of the seeding technique per-se, but also the roles gravity and capillary action play on cell distribution throughout the scaffold and from one bundle to the next.

2.3 Aims and Hypotheses

The aim of this study is to investigate the effect of three different seeding techniques (Upright, Flat, Rocked) on cell distribution;

1. throughout the scaffold
2. from one bundle to the next

For the Upright sample it is hypothesized the seeded cell suspension runs along the bundles as it is pulled down by gravity. The suspension collected on the bottom of the insert is then channelled up through the second bundle via capillary effect. For the Flat sample it is hypothesized the seeded cell suspension runs from the top bundle to the bottom bundle. The suspension is also channelled through the entire bundle via capillary effect. For the Rocked sample it is hypothesized the seeded cell suspension runs evenly up and down the scaffold enabled by the rocking motion, and a more even cell distribution can be achieved.

The information obtained will influence the mathematical model described in chapter 3, as uniform vs non-uniform cell distribution has an effect on how many spatial variables we have to consider. It will also influence the way we seed cells going forward.

2.4 Materials and Methods

2.4.1 Scaffolds

Scaffolds are produced using electrospinning, a technique described in [235, 209]. Briefly, this technique uses electrostatic forces to pull thin charged polymer filaments onto a grounded collector (Figure 2.1 A). PCL granules were (lot 002-19, Inherent Viscosity 1.07dl/g, Ashland Specialities Ireland, Dublin) were dissolved in hexafluoroisopropanol (HFIP, Lot: AS479557, Apollo Scientific, Bradbury, Stockport) at a concentration of 17%. It was then electrospun into filaments using a stainless steel wire collector of 100μm diameter. We used a range of voltage between 7kV and 10kV, the wire speed was set to 0.5mm/s, the syringe pump was set to a flow rate of 1ml/hr. Filaments were manually stretched to around 7x their original length and were assembled into 3cm bundles of 40 parallel filaments (Figure 2.1 B). The bundles were stored in a desiccator prior to further use.

2.4.2 Bundle Inserts

Bundle inserts (figure 2.1 C) were designed in Solidworks (2018, Dassault Systemes, Tennessee) and printed in clear resin on a Formlab 2 SLA 3D-printer (Formlabs, Somerville, Massachusetts, United States) at the Institute for Biomedical Engineering (IBME). Each replicate consists of 2 bundles positioned behind each other. After printing, the inserts were washed in isopropyl alcohol for two minutes and cured for 20 minutes.

2.4.3 Assembly Stage

To facilitate the handling and positioning of the inserts and bundles, an aluminium assembly stage was drawn in Solidworks and manufactured at the workshop of the Institute for Biomedical Engineering (IBME). Two stainless steel bars and screws on

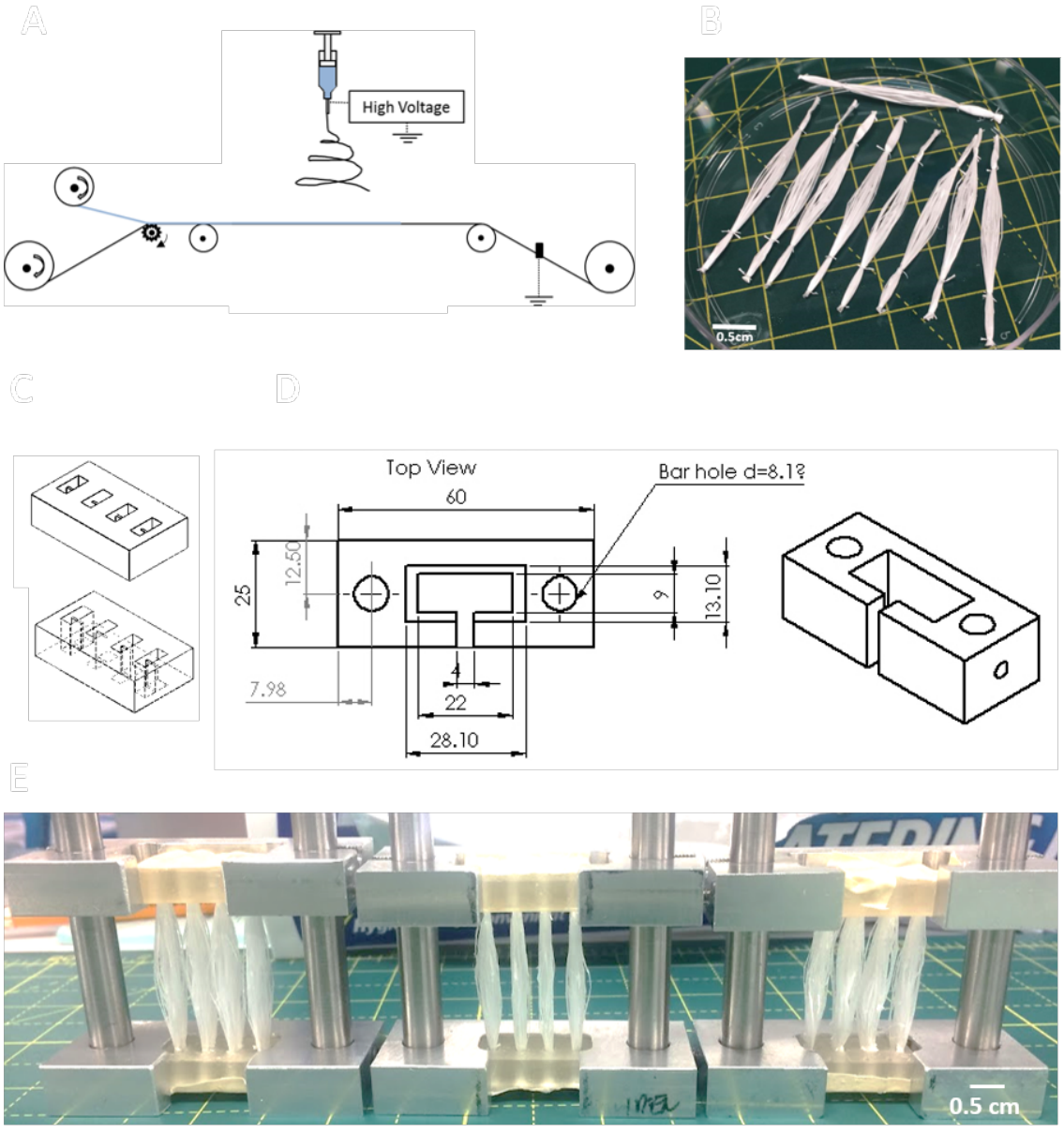

Figure 2.1: **Scaffold Preparation.** A) Electrospinning technique to obtain filaments. B) Stretched filaments assembled into bundles. C) Technical drawing of assembly stage. D) Technical drawings of 3D printed inserts. All dimensions are given in mm E) Full assembly ready for sterilization and seeding. Bundles are taped into the inserts and held in a stretched position through adjusting the distance between top and bottom of assembly stage.

each of the centre pieces enabled sliding of the parts to apply the same stretch across all bundles at assembly (figure 2.1 D and E).

2.4.4 Sterilization

Once assembled, bundles, inserts and stages were sprayed generously with 70% EtOH from all sides and left to dry off via evaporation in a petri-dish in a cell culture hood.

2.4.5 Cell Culture

Human foreskin fibroblasts (HFF-1, ATCC® SCRC-1041™) were expanded in T75 flasks in Dulbecco's Modified Eagle Medium (DMEM) F-12 HEPES (11330032, Thermo Fisher, Waltham, Massachusetts, USA) with 10% Fetal Bovine Serum (FBS), 1% Penicillin/Streptomycin (P/S). Media was changed every third day. Cells were passaged when approximately 80% confluence was reached. Cells were harvested using two TrypLE (12605-010, TripLE Express, Thermo Fisher, Waltham Massachusetts, USA) and one scraping step. The cell suspension was spun down for 5 minutes at 0.3 Relative Centrifugal Force (RCF). Viable cells were counted and resuspended in media to obtain a cell concentration of 40.000/100μL.

2.4.6 Seeding Methods

40.000 cells per scaffold were seeded in triplicates. Seeding was performed using a p200 pipette with 100 μl of cell suspension. One pair of bundles were seeded at a time. Care was taken to perform this slowly, to ensure media would not pearl off the scaffold and the filaments had time to soak up the suspension. We had n = 4 experimental repeats, and each repeat had 3 replicates so that each condition had a number of N = 12 samples. The no-cell control was seeded with pure medium only. Seeding techniques are highlighted in figure 2.2.

2.4.6.1 Upright

The scaffolds stand upright, so that the filaments are aligned in parallel along gravity.

2.4.6.2 Flat

The scaffolds lie flat on a surface, so that the filaments are aligned perpendicular to gravity.

2.4.6.3 Rocked

The scaffold lie flat on the surface. Upon seeding were transferred onto a rocking plate and rocked back and forth to ∼15° at 17rpm .

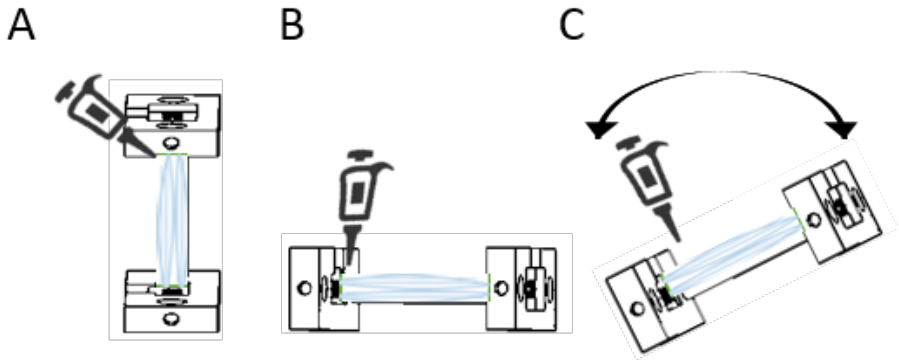

Figure 2.2: **Schematic of the three different seeding conditions.** A) Upright, B) Flat, C) Rocked

Cell-seeded scaffolds were left in the cell culture hood and on the rocking plate for 60 minutes, so that cells could attach. Subsequently, cells were fixed by pipetting 2.5% Glutaraldehyde (Grade II, 25% H_2O, Lot: STBH0868, Sigma-Aldrich Company Ltd., Gillingham, Dorset) onto the samples and left to soak for 30 minutes. Samples were washed and stored in PBS at 4°C for further analysis.

2.4.7 Osmium Tetroxide Staining

Samples were stained for 2 hrs with 300μL of Osmium Tetroxide (OsO_4 for electron microscopy, 4% in H_2O, Sigma-Aldrich Company Ltd., Gillingham, Dorset) per scaffold. During this time, the stain intercalates into the cells' lipid bi-layer and oxidises, causing the characteristic black color change. This did not happen in the no-cell controls (Figure 2.3. Next samples are flushed 3x with dH_2O, every time transferring them into a new petri dish. Then, samples were dehydrated in an Ethanol gradient of 40%, 70%, 90%, 95% and 100% for 10 minutes each. Lastly, 300μl of Hexamethyldisilazane (HMDS, electronic grade, 99%+, Alfa Aesar, Heysham, England) were pipetted on each replicate and left to evaporate in the fume hood overnight.

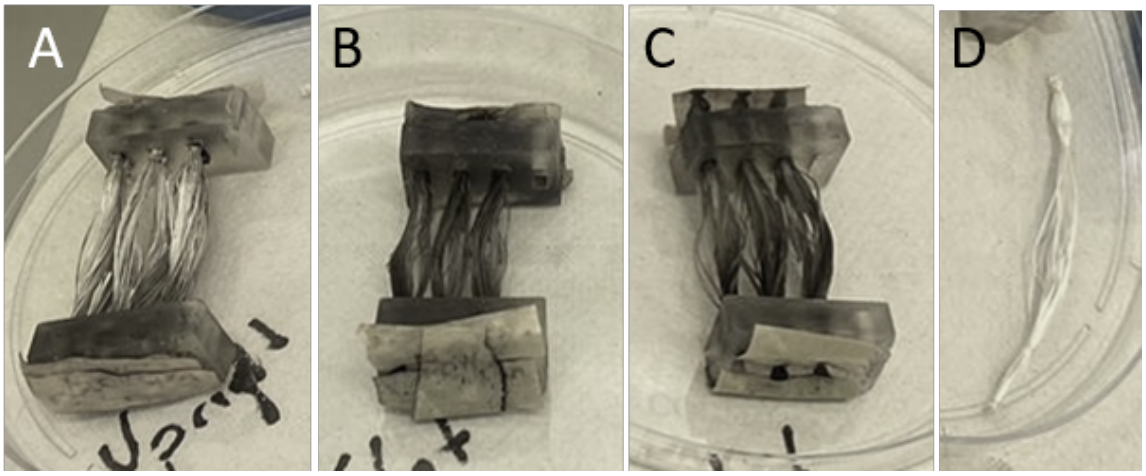

Figure 2.3: **Samples after osmiumtetroxide staining.** A) Upright, B) Flat C) Rocked, D) No-cell control. Cell-seeded samples take on characteristic black tone after staining, while the no-cell controls remain white

2.4.8 SEM and Elemental X-Ray Analysis

To inspect samples on the micron scale, a Variable Pressure Scanning Electron Microscope (VPSEM) was used at the Laboratory for in-situ Microscopy and Analysis at the Department for Engineering Sciences, University of Oxford (Carl Zeiss Evo LS15 INCA X-Act X-ray system, Oxford Instruments). Samples were not splutter coated,

as to not interfere with the visibility of the stain. Due to the size of the samples, carbon stickers could only conduct so much electricity. The machine was set to work in variable pressure, and the SE and VPSE detectors were used.

Elemental x-ray analysis or elemental dispersed spectroscopy (EDS) was used to confirm observations made under the SEM. This technique works in conjunction with SEM. When the SEM electron beams hit the surface of the sample, electrons are ejected. Missing electrons are replaced by electrons from a higher energy state, and an x-ray is emitted to balance the energy difference. When an x-ray hits the detector, a charge pulse is created and converted into a voltage pulse. This pulse is characteristic to individual elements. The system compares the sample's x-ray energy values to that of known elements.

2.4.9 Micro-CT scanning

The stained samples were scanned in a micro computed tomography machine (μCT) (Bruker Skyscan 1172, Kontich, Belgium). A no-cell negative control, also stained, was included in each scan. The medium camera setting was chosen with a voxel resolution of 13.5μm. Before scanning, a flat field correction was executed and the voltage adjusted to achieve the highest detailed image possible. The scans were over-size in two segments and later on stitched together with the built-in software NRECON. This software was also used to reconstruct the images.

2.4.10 Image post-processing

Once the μCT images were obtained, they were cleaned up in order to be run through a python script that would detect voxels above a threshold (Appendix A.2.1). These image post-processing steps were performed in CTan (Version 1.12.0, Bruker, Kontich, Belgium). First, we made sure all images showed a similar length of the scaffold. Samples that were slightly tilted would show the 3D printed inserts and would there-

fore give false positive signals. Therefore we defined an area that would exclude any 3D printed parts. Care was taken to ensure that the remaining images still showed a comparable length of the scaffold across all samples. Next, we drew a region of interest around all bundles. This was to exclude signal emitted from the support structures (plastic straws and bluetac). We additionally drew the region of interest around each bundle-pair. This means we ended up with 12 sets of front and rear bundles per seeding condition, to investigate the spreading of the cell suspension from one bundle to the next. Then, we manually set the threshold so that the control sample would disappear. This was different from sample to sample. These values were later fed into the python script. As a last step the region of interest was set to exclude the no-cell control to avoid any other signal interference. Appendix figure A.2 shows a flow chart of this process.

2.4.11 Image Analysis

The python script (Scripts and Codes A.2.1) was run through the individual cross-sectional images to count voxels above a threshold. This means we are analysing three replicates at the same time. The script asks the user for a threshold and converts all images into binary images, so that every pixel below that threshold is turned into black voxels, and every voxel above it into white voxels. The script then counts the number of white voxels in each slice of the μCT stack. The results are then transcribed into a .csv file ready to be analysed further. Taking the number of voxels above the threshold for each image, we separated the length of the scaffold into 10 sections (each 0.3cm long). For each section we took the average number of voxels and expressed it as a percentage relative to the total signal from 10 sections. Despite the mentioned post-processing steps, there were still some outliers. These images looked like filaments merged (Figure A.1). We had to exclude the following sections (Table 2.1):

Table 2.1: Excluded scaffold sections due to signal interference.

Seeding Technique	**Repeat Number**	**Sections affected [cm]**	
Upright	1	1.2-1.5	1.5-1.8
Upright	3	1.5-1.8	
Flat	1	0-0.3	2.7-3
Rocked	1	2.4-2.7	
Rocked	3	0-0.3	

We were unable to discern why this would happen, as it occurred at variable locations and across different seeding techniques and repeats. Where we had interference, we ignored the signal coming from these sections and assumed the rest of the signal added up to 100%.

2.4.12 Statistical Analysis

The three different seeding techniques were put into columns (n=4), and the 10 subsections into rows. A two-way ANOVA was conducted to identify whether there was a significant difference in cell distribution across the three seeding techniques. Then, a multiple comparisons analysis was conducted for each row, comparing columns, so that each of the 10 locations/subsections was compared between seeding techniques, answering the question of whether different seeding techniques lead to a significantly higher number of cells settled in location X (simple effects within rows). Another multiple comparisons study compared different rows within each column (simple effects within columns), so that we could compare the different locations within one seeding technique. Statistical significance was determined at $\alpha < 0.05$.

Another two-way ANOVA was conducted. The two factors were seeding technique (n=4) and location. The groups consisted of signal coming from the front and rear bundles. This was done for each seeding technique. Statistical significance was determined at $\alpha < 0.05$

2.5 Results

2.5.1 SEM and Elemental X-Ray Analysis

Cells stained with OsO_4 appeared brighter than their surrounding scaffold material under the SEM (figure 2.4). This could be observed without splutter coating the samples, enabling further analysis under the μCT. The cells seen and highlighted by red arrows in figure 2.4 appear flat, similar to plaques.

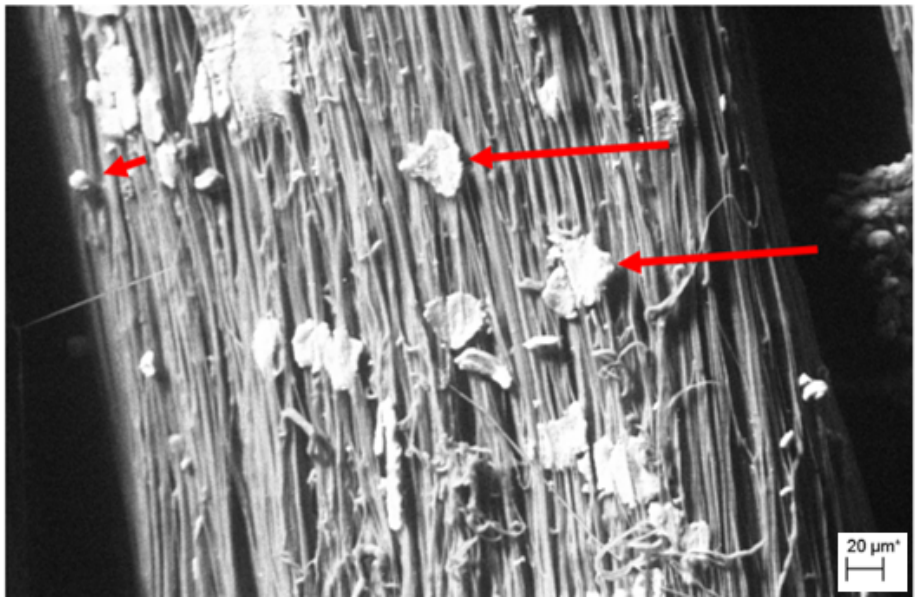

Figure 2.4: **SEM image of the Rocked sample.** The image contains one filament and visible are the sub-micron fibres. Red arrows indicate some of the characteristic cell-patches containing osmium. The cells appear brighter than the surrounding scaffold. Their shape is flat, likely due to the dehydration step post staining.

SEM images were taken at the top, middle and bottom section of each scaffold and an elemental x-ray analysis on each of them was also performed. The resulting SEM images and the corresponding elemental map and elemental spectra can be seen in figure 2.5. The electron images on the left show the sub-micron fibre structure of the OsO_4 stained scaffolds with bright patches of cells. The no-cell control showed no cells or other characteristic patches on the electron image. The elemental maps in the middle show areas of osmium, consistent with the location of the patches

observed. For the no-cell control an X indicates that no osmium was detected. The elemental spectra seen on the right were obtained from the same area of interest. The spectra show keV on the x-axis and relative x-ray counts on the y-axis, giving some quantitative information. We could confirm characteristic osmium peaks around 1.5keV. These are highlighted by white arrows in figure 2.5. The elemental spectra did not show peaks on the no-cell control.

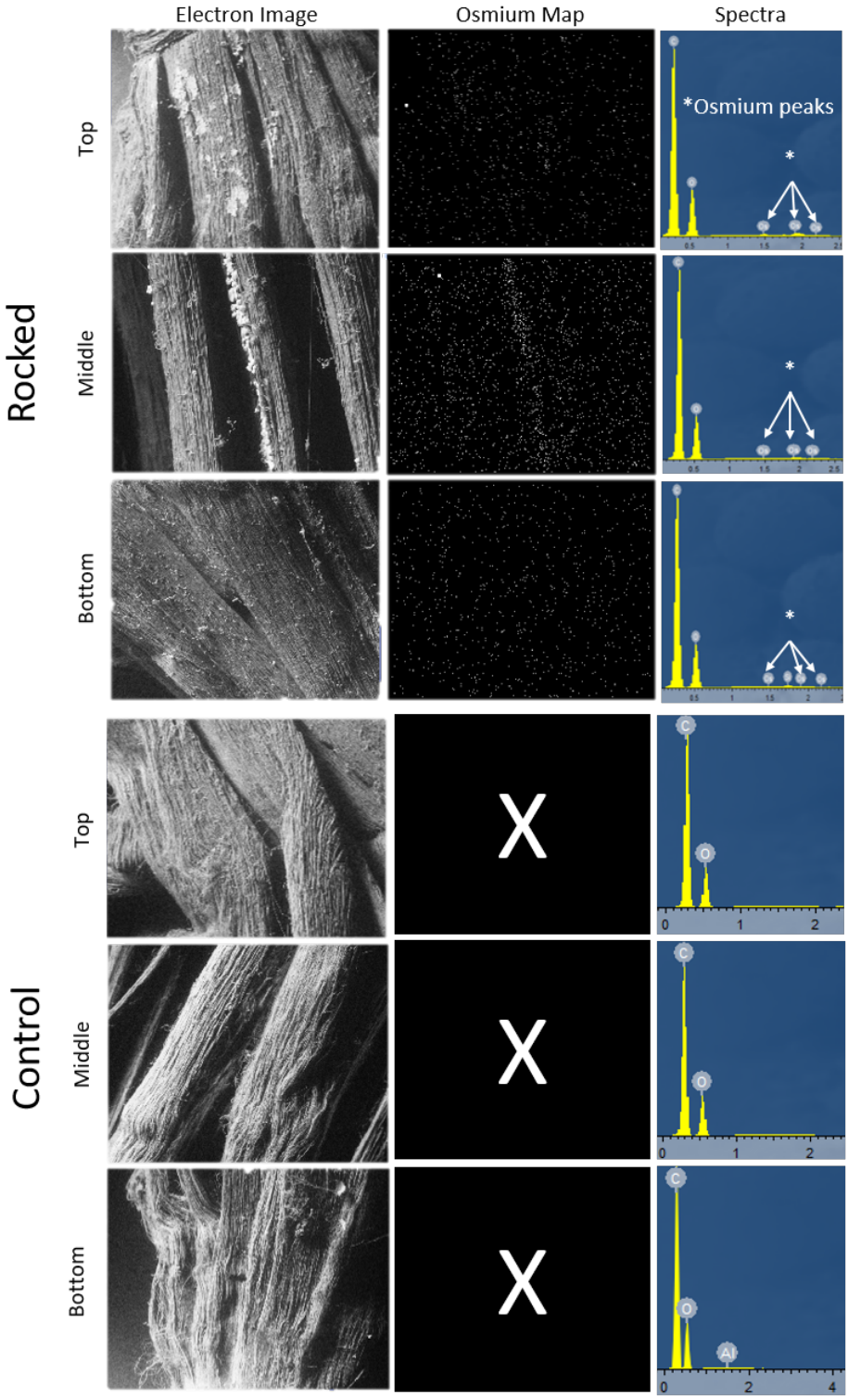

Figure 2.5: **Electron images, elemental maps and elemental spectra of osmium-stained scaffolds.** Electron images in the left column show patches of cells at top, middle and bottom for the rocked scaffold. The elemental maps in the middle column show Osmium detected on the same regions. No Osmium was found on the control samples, indicated with X. Characteristic Osmium peaks are shown in the elemental spectra on the right, indicated by white arrows. There were no osmium peaks for the no-cell control.

2.5.2 micro-CT analysis

As shown in figure 2.6, the scaffold structure was visible under μCT. Cell-seeded bundles, where OsO_4 intercalated into the cells' membrane, appeared much brighter than the no-cell control. Cells appear brighter on the cross-sectional images too and could be seen both on the surface of the scaffold and penetrating within the bundles of filaments, as shown in figure 2.6 B. Unfortunately it was outside of the scope of this chapter to quantify the degree of cell infiltration into the middle of the bundles.

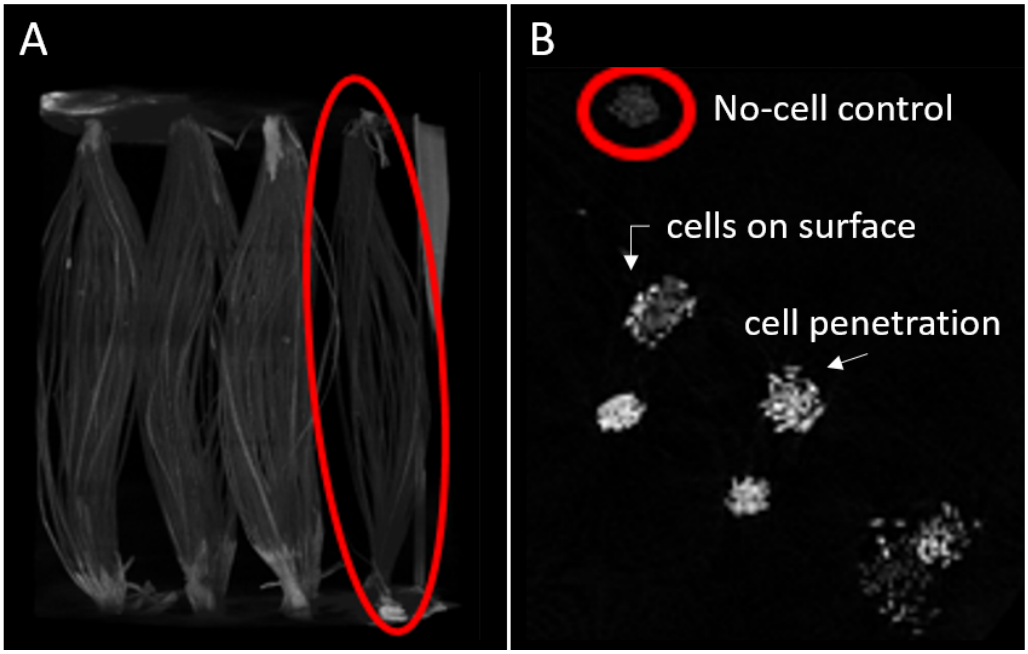

Figure 2.6: **μCT images of cell-seeded bundles and no-cell control** A) The μCT images of three cell-seeded repeats and one no-cell control, reconstructed into a 3D image. Individual filaments are clearly visible. The cell-seeded scaffolds appear brighter than the no-cell control due to the intercalation of the metal stain OsO_4 into the cell membrane. B) Cross-sectional images. The cross-section shows the bundle-pairs which are not visible at this angle on the 3D reconstructed image. We highlight cells that stay on the surface of the bundle and cells that have penetrated the bundle. The control bundle is highlighted in red and appears much more faint.

2.5.3 Effect of seeding technique on cell distribution

Figure 2.7 shows the distribution of OsO_4-containing cells across the scaffolds, for each seeding technique: upright, flat and rocked. The two-way ANOVA showed that across the average of 4 repeats, there was no significant difference in signal between the three seeding techniques (p=0.9981), meaning that cell distribution was not affected by the seeding technique. The multiple comparison of simple effects within rows showed no significant difference, meaning that cell distribution at a particular location was not significantly different between seeding techniques (lowest p = 0.3238).

2.5.3.1 Upright

The distribution of cells was fairly even with a slight increase in signal towards the bottom (around 20%). Although this increase was not significant across the 4 repeats. The multiple comparison analysis for the simple effects within columns showed no significant difference between locations. The lowest p-value stems from the difference between the bottom and top locations (p = 0.4459).

2.5.3.2 Flat

The results for the flat samples show a more scarce distribution in the middle. The multiple comparison analysis for the simple effects within columns showed no significant difference between locations. The lowest p-value here comes from comparing the sections 0.3 - 0.6cm and 0.9 - 1.2cm (lowest p = 0.7967).

2.5.3.3 Rocked

Results of the rocked sample show a fairly even distribution of cells. The multiple comparison analysis for the simple effects within columns showed no significant difference between locations, the lowest p-value comes from comparing the sections 0.7 - 0.9cm vs. 1.8 - 2.1cm (p = 0.6613)

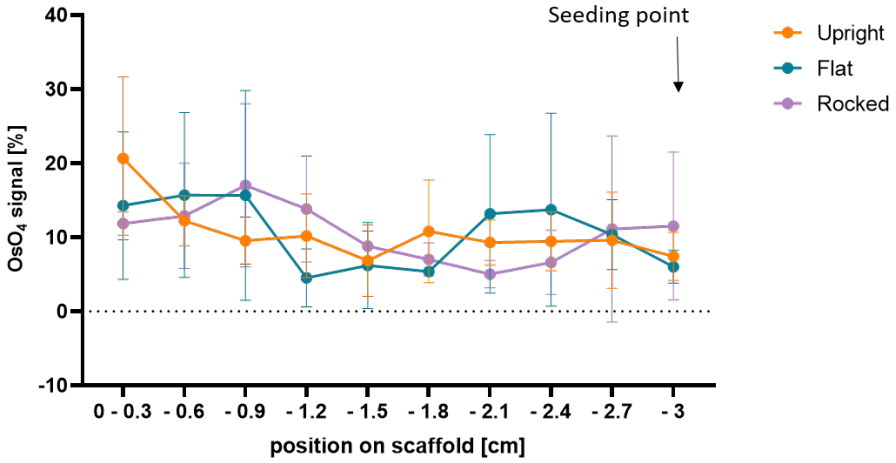

Figure 2.7: **Cell distribution upon different seeding techniques.** The point of seeding was at the 3cm mark, highlighted by a black arrow. Shown here are the results for each seeding technique across four repeats (n=4). Signal obtained from μCT images (y-axis) was divided into 10 sub-locations on the scaffold (x-axis). The graph shows what percentage of the overall detected signal corresponds to which section. In each category the sum of all sections will equal 100% of the signal. Orange = signal from the the Upright seeding technique, Blue = signal from the Flat seeding technique. Violet = signal from the Rocked seeding technique. Error bars indicate the stdev. The two-way ANOVA showed no significant difference between the seeding techniques (p=0.9981). Multiple comparisons of simple effects within rows showed no significant difference in cell distribution at a particular location across seeding techniques (lowest p = 0.3238). Multiple comparisons of simple effects within columns showed no significant difference in cell distribution within one seeding technique (Upright lowest p = 0.4459, Flat lowest p = 0.7967, Rocked lowest p = 0.06613)

2.5.4 Reaching of cell suspension from one bundle to the next

We investigated whether the cell suspension could reach from one bundle to the next. Figure 2.8 showed no significant difference between the front and the rear bundle for the Upright (p=0.1163, front $\approx$ 56%, rear $\approx$ 43%) and Flat (p=0.7411, front $\approx$ 51%, rear = $\approx$ 48%) seeding technique. The Rocked seeding technique did lead to a significant difference (p = 0.0008, front $\approx$ 61%, rear $\approx$ 38%).

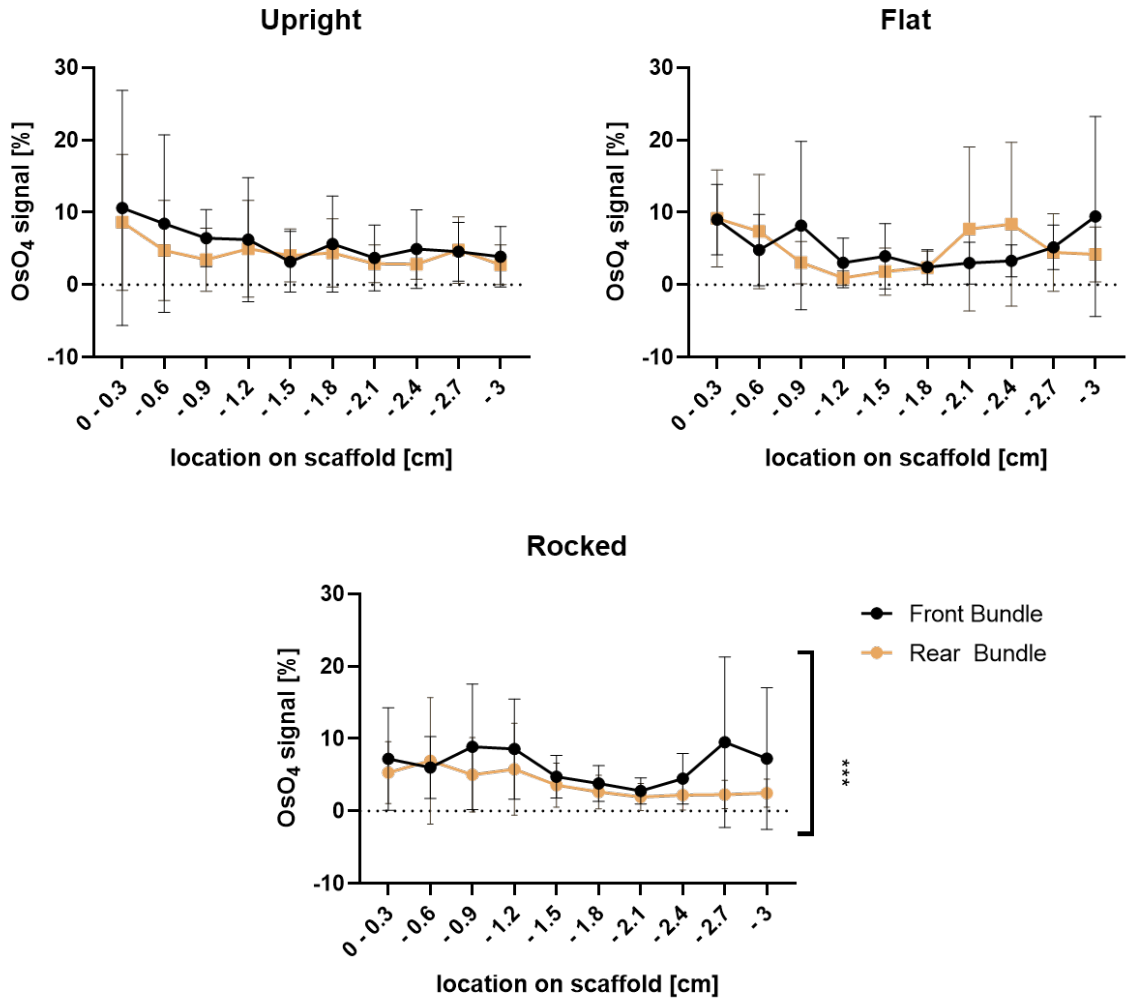

Figure 2.8: **Distribution of cells across and along two bundles.** The point of seeding was at the 3cm mark on the front bundle. Shown here are the results for each seeding technique across all replicates (N=12). Signal obtained from μCT images (y-axis) was divided into 10 sub-locations on the scaffold (x-axis). 100% of the signal came from front and rear bundle together. Black = signal from the front bundle, Orange = signal from the rear bundle. Error bars indicate the stdev. The two-way ANOVA showed a significant difference between front and rear bundle, only for the Rocked condition (*** p = 0.0008)

2.6 Discussion

In order to interpret the results, it is worth noting that untreated PCL is highly hydrophobic [236]. When seeding cells onto the Upright condition, the cell suspension would run along the filaments straight to the bottom of the scaffold. The scaffold would then visibly soak the suspension from the bottom up. While we see some accumulation of cells at the bottom, this was not significant, suggesting that the capillary effect pulls the cells up into the scaffold. However there could be cells stuck to the 3D printed inserts. A similar problem was encountered seeding in the Flat condition. The cell suspension would often roll off the bundles. We observed that a certain tension between the filaments lead to a better uptake of the suspension into the bundle. This tension needs to bring filaments close enough together to create a capillary effect, but far enough apart to allow the suspension to come in contact with several filaments. This observation corresponds well with all seeding techniques leading to a less populated middle-section, where the filaments are furthest away from each other (Figure 2.6). We observed this with the SEM and the μCT. This observation is likely a result of the discussed capillary effect between filaments and the hydrophobicity of PCL. We therefore aimed to adjust the tension between filaments accordingly on the assembly stages (section 2.4.3). The most even cell distribution, though not significant, was achieved with the dynamic seeding method. This is coherent with a study done on porous collagen and chitosan scaffolds. Following Subramanian et. al.'s static seeding method, the majority of the cells remained at the surface and did not penetrate the scaffold. Whereas with centrifugation-seeding cell distribution shifted from the top to the middle or bottom sections [230] We saw penetration into the centre of the bundle. Unfortunately it was not within the scope of this chapter to quantify this.

The results following the front vs rear bundle analysis are encouraging because it shows the cell suspension spreads successfully from bundle to bundle. However this was not true for the Rocked condition. What this means for us is that seeding from

one inlet only might be sufficient, as long as we seed enough volume. A combination of seeding cells in an upright position first, and then rocking the chamber is likely to give the best results.

2.7 Limitations and Future Directions

Several challenges were encountered along the way. First, setting the threshold for the analysis of the μCT images was subjective as this has to be done manually by increasing the threshold up to a point where no signal was found on the no-cell control. Furthermore, working with a pixel size of 13.5 μm, smaller cells may remain undetected. For the future a higher resolution could be used.

Since cells only had 1 hour to attach, these results do not inform about the cell's ability to migrate or their preference on the scaffold. Furthermore, only the cells that successfully attached to the scaffold within the time given could be analysed. Cells in the cell suspension that rolled off the hydrophobic PCL could have been lost. Furthermore cells located at the very ends of the scaffold, might have been outside the regions of interest. The python script detected variable numbers of voxels between repeats. We needed to convert the signal into a percentage to make it comparable between conditions and repeats. For these reasons it was not possible to relate the OsO_4 signal to a cell number. To reliably relate the results to a cell number, a combination of techniques such as SEM or confocal microscopy could give insights.

The use of OsO_4 for cell distribution analysis is not new. Bosworth et al investigated cell infiltration on a PCL electrospun yarn with OsO_4-staining and high resolution X-ray tomography [237]. Scheller et al suggest this method to map marrow adipose tissue [238]. However, those results were a qualitative yes/no, rather than a semi-quantitative one like we show here. It should be pointed out that OsO_4 is highly toxic and is to be handled with care and proper training. We used a simplified setup

compared to our whole chambers to make the staining process as straightforward as possible. Ideally we should stain a whole chamber, consisting of five bundles rather than two, and a fixed inlet from which we seed the cells.

Most studies use cryo-sectioning and subsequent confocal microscopy to assess cell distribution [228, 230]. However, for larger engineered tissue constructs this would result in hundreds of slides, time consuming analysis and the destruction of the scaffold. Recent studies have explored the use of a less toxic (however still hazardous) haemateinlead(II) acetate trihydrate-based contrast agents [239] or eosin-based stains [240]. Other methods which are non-toxic and quick such as IVIS technology have been suggested [241]. Unfortunately we did not have the time to do this.

2.8 Conclusion

Even though there was no significant difference between the seeding techniques, important details can be deducted from the results. Firstly, the different analysis techniques complement each other and show coherent results. The SEM and elemental x-ray analysis, in combination with a stained no-cell control were useful to establish that the signal detected in the μCT were cells. The methods used were straight forward, coherent and visualized cell distribution throughout a scaffold without the need of cryo-sectioning. Secondly, the capillary action played an important role, more so than gravity. Thirdly, rocking the sample immediately after seeding leads to better cell distribution throughout the scaffold, but keeping it steady will lead to improved spreading from one bundle to the next.

Going forward, we will seed the chambers in an upright position and manually rock them to help the fluid spread across the five bundles. We will keep some tension on the bundles during seeding.

These results will also serve as one input parameter for the following chapter 3.

Chapter 3

Investigating Flow Rates with a Computational Model

3.1 Abstract

Cells need oxygen and nutrients, such as glucose, to proliferate. In bioreactors these are provided with cell culture media and are usually fed into the system at a certain flow rate. Finding a flow rate that ensures the delivery of sufficient nutrients and clearance of metabolites is not straight forward, and can require a lot of experimental testing. In this chapter we developed a computational model of our bioreactor system, which can look at the effect of different flow rates on nutrient distribution, metabolite accumulation and cell proliferation. We model the bioreactor geometry as an inner and an outer cylinder, representing the scaffold and a free flow area around it. We determine the steady fluid flow through the system. Then, the resulting nutrient diffusion and advection, cell metabolism and cell growth are modelled in a time-dependent study. Additionally, a parametric sweep of different flow rates was performed. We highlighted three flow rates which were later tested to validate this model *in vitro*. The results showed no benefit on cell growth curves for flow rates

higher than 0.5ml/min. Glucose was present in abundance in all tested flow rates. For the low flow rate of 0.001ml/min, the accumulation of lactate lead to a halt in cell growth. We could also identify pockets of no flow, which did not have an impact on cell growth in flow rates of 0.293 and 1.5ml/min. The importance of using a permeable membrane material was highlighted by allowing oxygen to enter the system through the outer wall in the model. Removing such a permeable wall leads to critically low oxygen levels at 0.001ml/min and slightly affected those at 0.293ml/min. The model proved to be a useful tool. We can test a higher number of flow rates and initial cell seeding densities than would have been feasible in *in vitro* experiments. Furthermore it allows a more detailed look into the location of cells and nutrients, as well as information about flow paths and shear stress experienced by cells.

3.2 Introduction

The cultivation of cells in a newly developed bioreactor is a non-trivial task. Instead of investing a lot of time, money and effort into testing the most favourable input parameters in the laboratory, they can be modelled *in silico*. Computational models of complex systems, such as cell culture, require a good understanding of the problem at hand. There are several mechanisms we need to understand first.

3.2.1 Fluid Flow and Mass Transport

Delivering nutrients to cells is achieved by surrounding cells in the appropriate type and amount of medium. In continuously fed culture systems, fresh media is added as nutrient deprived media is removed through at least one in- and one outlet [199, 198]. This process is usually automated in bioreactor systems, and the media is fed via a syringe or peristaltic pump. In order for cells to survive and proliferate, the nutrients must also effectively reach the cells within the scaffold. Nutrients such as glucose and

oxygen will follow physical phenomena and diffuse from sites of high concentration to low concentration, according to the compounds' diffusivity properties. In perfusion bioreactors, nutrients are further transported through the system via advection. The permeability of the scaffold plays an additional role as the fluid needs to permeate through the structure to reach the cells. These nutrients are then taken up by cells, which further contributes to changes in local concentrations. While shortages in glucose are not likely to be an issue, and media can always be enriched with glucose, oxygen solubility in the media can only be influenced by changing the pressure or temperature, which would adversely affect the cells. It is therefore of crucial importance to achieve a well-mixed system. The geometry of the system, scaffold design and initial cell numbers play an important role in the resulting nutrient and cell distribution. Cells could starve, should there be any bottlenecks. It is possible that an accumulation of cells take up all the available oxygen and a create a state of local hypoxia. Furthermore, lactate can accumulate in pockets of low- or no flow. In this model we assume a homogeneous cell distribution to begin with. This will highlight conditions leading to uneven nutrient distribution, without the confounding factor of heterogeneous cell distribution.

3.2.2 Cell Metabolism and Growth

Metabolism is the conversion of nutrients into usable energy to run cellular processes. We differentiate between first- and zero-order kinetics in cell metabolism. If the metabolic rate R^i is equal to the maximum reaction rate, V_{max} and independent on the substrate concentration C^i, then the reaction is considered to follow zero-order kinetics. This means nutrients are taken up at a constant rate. This is the case when all uptake mechanisms are saturated and the uptake rate does not depend on the concentration anymore.

$$R^i = V^i_{max} \tag{3.1}$$

If the metabolic rate and the substrate concentration are dependent on each other, then the reaction follows first-order kinetics. This means the nutrient concentration and the uptake is linear. It is influenced by the Michaelis constant K_m [g/L] which describes the substrate concentration at which the reaction rate is half of V_{max} (Eqn. 3.2).

$$R^i = -\frac{V^i_{max} C^i}{K^i_m + C^i}. \tag{3.2}$$

The main source of energy for cells is adenosine triphosphate (ATP). Cells gain ATP through the uptake and breakdown of glucose. Glucose is hydrophilic and is taken up via glucose transporters. There are two types of glucose transporters; independent glucose transporters (GLUTs) and sodium dependent glucose transporters (SGLTs). GLUTS do not require ATP and are abundant in all cell types. SGLTs are sodium dependent and require ATP to form a sodium gradient which is later used to transport glucose into the cell. Once glucose has been transported into the cell, it can be stored as glycogen or used for energy gain. Glycolysis is necessary to break down the glucose molecules into workable smaller molecules called pyruvates. This process takes place in the cytoplasm and converts one glucose molecule into 2 pyruvates, 2 ATP and NADH molecules [242].

Next, if there is sufficient oxygen present, aerobic respiration/oxidative phosphorylation can take place. Hereby the pyruvates will move into the cell's mitochondria where they are carboxylated and enter the citric acid cycle and electron transport chain, where more ATP is produced. Aerobic respiration is highly efficient as one molecule of glucose will yield 30 to 32 ATPs.

When no oxygen is present, the cell will undergo anaerobic fermentation/non-oxidative phosphorylation, and two pyruvates are further processed into lactate. Pyruvic-acid and lactate can both be turned back into glucose via gluconeogenesis. Since non-oxidative metabolism takes place when oxygen is depleted, lactate could be an indi-

cator of hypoxia. However, evidence suggests that proliferating cells favour anaerobic over aerobic metabolism, despite the latter being energetically more efficient, and regardless of sufficient oxygen being present. Rapid cell growth leads to a partial oxidation of glucose into CO_2 and H_2O in all ATP producing mammalian cells [243]. This is called the Warburg effect and will result in glucose being converted into lactate. Cells undergo this effect when nutrients need to be rapidly consumed to fulfill high ATP demands despite the presence of enough oxygen. As an example, experimental flux measurements showed fibroblasts metabolize about one-half of their glucose uptake aerobically (producing 30 ATP/glucose) and the other half anaerobically (producing lactate and 2 ATP/glucose) [244]. Lactate can therefore be considered a by-product of glucose metabolism and can indicate proliferation, but not necessarily oxygen deprivation. In a study with cell-stressors such as amiodarone, diclofenac, troglitazone, cadmium chloride, cephaloridine, cidofovir, cyclosporine A and buflomedi, lactate was identified as a marker for mitochondrial and oxidative disturbances [245]. Once lactate accumulates as a result of these mechanisms, it can have devastating consequences. In a study conducted on fibroblasts, low *in vitro* lactate levels (10mM) were tolerated well, but cell viability was severely compromised by high lactate concentrations (=20 mM). Scratch assays for wound healing experiments showed that cell migration was affected earlier than viability in response to increasing lactate levels [246].

The reason we monitor lactate in cell culture therefore is two-fold:

1. Increased lactate production might be the result of hypoxia, tissue repair (proliferation), oxidative stress and mitochondrial disturbances. Lactate levels can therefore tell the operator a lot about the system.

2. High lactate concentrations can severely compromise cell viability and stress cells. It is therefore a parameter that needs to be controlled.

Some accumulation of lactate can be avoided by controlling the oxygen levels. However, what exactly enough oxygen means is a non-trivial question. Typically the literature distinguishes between anoxia, hypoxia and normoxia. However *in vivo*, oxygen levels are influenced by a number of mechanisms such as vasodilation and constriction, changes in vascularization and adjustment of respiration/metabolic rates. These are conditions currently not considered *in vitro*. Typically the atmosphere for cell culture in an incubator is set to $20\%O_2$ and $5\%CO_2$. This is referred to as normoxia, while anything lower than that is considered hypoxia. However, this refers to incubator conditions and does not account for the oxygen levels that are effectively reaching the cells. Furthermore different tissues have different vascularization and physiological oxygen levels. For this reason the term physoxia has been coined to describe the normal oxygen concentrations a particular type of cell would encounter in their corresponding tissue in vivo [247]. Anoxia, a state of no or very little oxygen present, will lead to apoptosis for most cells [248], whereas hypoxia, a state of low oxygen, has distinctly different effects such as increased angiogenesis, collagen synthesis and entire phenotype shifts [249, 250].

In this model we simplified some of these mechanisms to model fluid flow, mass transport, nutrient uptake, metabolite production and cell growth.

3.2.3 Mathematical and Computational Modelling

Tissue engineering encompasses complex multi-cellular, multi-scale biological systems that are difficult to understand experimentally or through conventional logic-driven thinking alone. Mathematics uses a concise language to describe these problems. Mathematical models can be much faster and cheaper than performing numerous time consuming and expensive laboratory experiments [251]. The key steps of developing a mathematical model are summarized excellently in Waters et al's reivew [252]. Briefly these are a repeating cycle of, model construction, calibration, pre-

diction and refinement. During development, models aim to describe the system's mechanics and phenomena. We calibrate models through comparing its outputs with experimental data. Enlacing a model with data obtained experimentally can make it much more powerful, though this is a non-trivial task as data tend to be complex, contain noise and are often incompletely observed. Another aim of model calibration is to identify which parameters are most likely producing a certain outcome/data, called parameter inference. Considering experimental data also serves us in determining the model's complexity and choosing from competing hypotheses [252]. Next the model needs to be validated (Chapter 4). Discrepancies between model predictions and experimental data can then indicate model refinements. Models for tissue engineering can be grouped into mechanistic, discrete, continuum and hybrid models. The first tries to encompass all components and their interactions on a large scale, such as cell growth of tendons and their response to mechanical stimulation, considering cell number, fluid flow, nutrients and the dependence on space and time. The second studies a much smaller scale, such as an individual cell and its interaction with the surrounding. A full picture can then be drawn by applying this model a lot of times. Continuum models particularly focus on a larger system's dependence on space and time. Hybrid discrete-continuum models deal with discrete models combined with continuum models, such as discrete cell behaviour and their surrounding micro-environment. Statistical models aim to understand the relationship of input variables, to output variables, so that experimental input variables can predict the experimental data. A review of the literature showed that perfused bioreactors are most commonly modelled as follows: A bioreactor geometry modelled in either 2D, 3D or axisymmetric, and has at least one in- and outlet. Flow inside the bioreactor is modelled through a Navier-Stokes equation [253, 254, 255, 256], assuming incompressible fluids and negligible terms of inertia, or Poiseuille's equation for long tube-like bioreactors [254]. Scaffolds are often modelled as porous structures and the govern-

ing fluid flow equations here are Darcy [257, 255] with the potential for a Binkman extension [256]. Mass transport of nutrients and metabolites is described through advection-diffusion equations. Nutrient uptake is modelled as Michaelis-Menten kinetics and Cell Growth via Monod [255] or Contois equations [256]. From there, different study aims are pursued such as highlighting issues with scaffold design, cell distribution, flow velocity or inlet and outlet locations [257], optimizing chamber design [254], predicting concentration gradients [258] or maximizing mass transfer while controlling shear stress levels [259]. Other studies focus on multiphase problems such as the effect of flow on tissue growth [253] or investigate the effect of shear stress on cell yield and distribution within hollow-fibre bioreactors [260].

Models of bioreactors are developed to give a better insight into the system. Furthermore they can strengthen the experimental results and influence decision making for future experiments by giving a more in depth insight into the system. We can model culture times far beyond what is currently feasible in the lab and get a much higher spatial resolution of nutrient and metabolite concentrations.

3.3 Aims and Hypotheses

The aim is to develop and solve a theoretical model that can predict nutrient distribution under different flow rates and determine candidate flow rates that promote cell growth. Furthermore the influence of a membrane that is permeable to gases is explored. We also aim to investigate the impact of stopping perfusion for a period of time. It is hypothesized that low flow rates lead to poor nutrient distribution and therefore lower cell numbers. They would also lead to an accumulation of lactate and a lack of fresh nutrients. Higher flow rates should ensure even nutrient delivery and increased cell growth rates.

3.4 Materials and Methods

3.4.1 Mathematical Model

As a first step, steady fluid flow through a porous cylinder and a free flow cylinder is solved at steady state. Next, mass transport of nutrients and metabolites is modeled via advection-diffusion-reaction equations. The reaction terms describe glucose and oxygen consumption, as well as lactate production and cell growth. Metabolic rates obtained from the literature serve as input for these. Finally we model nutrient and metabolite transport, as well as cell growth via a reaction-diffusion equation. The multiphysics software COMSOL [261] is used to solve this model. The predictive character of the model is tested in a set of validation experiments in chapter 4.

3.4.2 Model Setup

We consider fluid flow, mass transport and cell growth in a bioreactor chamber. A schematic of the geometry is shown in Figure 3.1. The geometry consists of an inner and an outer cylinder. The inner cylinder represents a porous structure and has a radius R_1, permeability κ and porosity ϵ. The outer cylinder represents a free flow region with radius R_2, surrounded by a rigid wall. We use subscripts j to denote the scaffold s and pure fluid regions w. The bioreactor has a length l. We consider a cylindrical coordinate system r, Θ, z with corresponding coordinate directions $\mathbf{r}$, Θ, $\mathbf{z}$. We assume axisymmetry, so that quantities do not vary with Θ, and there is no flow in the azimuthal direction. The outer wall where $\mathrm{r} = R_2$ is permeable to oxygen but impermeable to fluid, glucose and lactate. There are solid walls where $0 < \mathrm{r} < R_1$ at $\mathrm{z} = 0$ and $\mathrm{z} = \mathrm{L}$. The fluid (cell culture media) enters the bioreactor from the inlet at a volumetric flow rate Q_{in}, carrying glucose and oxygen, and leaves at the outlet. The inlet and outlet are both located at opposite ends of the pure fluid region.

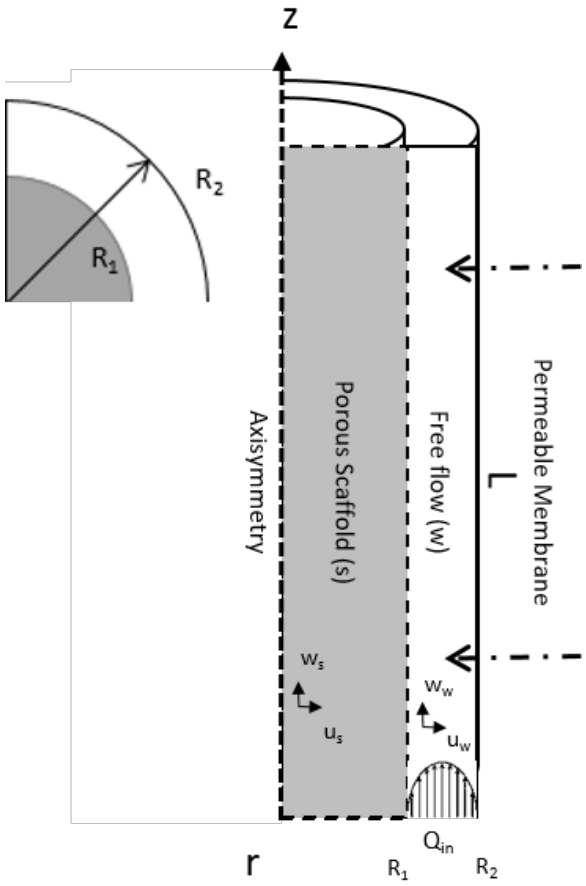

Figure 3.1: **Schematic of the bioreactor axisymmetric geometry with a gas permeable membrane.** Oxygen is allowed to diffuse radially into the bioreactor across the permeable membrane. R_1 is the outer radius of the scaffold, R_2 is the radius of the pure fluid region, and L is the bioreactor length. The radial coordinate is denoted by r and the axial coordinate by z. Velocity components in the radial and axial direction are denoted by u and w respectively and subscripts s and w are used to distinguish scaffold and free flow area.

The fluid is modelled as incompressible Newtonian of viscosity η and density ρ. Steady fluid velocity $\mathbf{u}_j$ has components $u_j\hat{\mathbf{r}} + w_j\hat{\mathbf{z}}$. Pressure is denoted as p_j.
The nutrients enter the system at the inlet, are taken up by cells in the scaffold region, where the metabolite lactate is produced by the cells, and leave the system at the outlet. The concentrations C_j^i of the individual nutrients are governed by diffusion-advection-reaction equation. The superscript i stands for glucose G, oxygen O_2 or lactate L. The nutrients diffuse through the pure fluid region and the scaffold region

at different rates respectively. These are given by their individual diffusivity D_j^i. The reaction term R^i describes nutrient uptake/production. These only take place in the scaffold region. In terms of nutrients, $R^i > 0$, corresponds to metabolite production by cells and $R^i < 0$ is nutrient consumption by cells. Nutrient consumption/production is governed by Michaelis-Menten kinetics where V_{max} is the maximum rate at which a reaction can take place and the Michaelis constant K_m [g/L] describes the substrate concentration at which the reaction rate is half of V_{max}.

Cells N are located on the scaffold domain only. Initially we assume the cells are homogeneously seeded throughout the scaffold. Cell growth μ is governed by a Monod-type kinetic equation dependent on the local nutrient concentrations C_s^i, the maximum growth rate μ_{max} and the Michaelis-Menten growth constant K^i. Oxygen and glucose concentrations contribute to cell growth, whereas lactate limits growth. A maximum cell number N_{max} is used to model contact inhibition. Furthermore, cells spread from areas of high cell density to low density, with a diffusion coefficient D^N.

3.4.3 Fluid Flow

We consider fluid flow at steady state. In the free flow domain, we assume inertial forces are negligible in comparison to the viscous forces so that the governing flow is Stokes Flow (Eqn. 3.3).

$$\nabla \cdot \mathbf{u}_w = 0, \quad \mathbf{0} = \nabla \cdot (-p_w \mathbf{I} + \mathbf{K}_w), \tag{3.3}$$

where $\mathbf{I}$ is the identity tensor and and $\mathbf{K}_w$ is the viscous stress tensor given by

$$\mathbf{K}_w = \eta \left(\boldsymbol{\nabla} \mathbf{u}_w + (\boldsymbol{\nabla} \mathbf{u}_w)^T \right). \tag{3.4}$$

In the scaffold domain, we assume that fluid flow is governed by the Brinkman equation as follows:

$$\nabla \cdot \mathbf{u}_s = 0, \;\; \mathbf{0} = \boldsymbol{\nabla} \cdot (-p_s \mathbf{I} + \mathbf{K}_s) - \eta \kappa^{-1} \mathbf{u}_s, \tag{3.5}$$

where K_s is the stress tensor defined as:

$$\mathbf{K}_s = \frac{\eta}{\epsilon} \left(\boldsymbol{\nabla} \mathbf{u}_s + (\boldsymbol{\nabla} \mathbf{u}_s)^T \right). \tag{3.6}$$

Boundary Conditions

We impose symmetry conditions along the line centre. We impose continuity of velocity and stress at the interface between the two domains. The fluid flows in at the inflow boundary with flux Q_{in} and flows out with zero back-pressure. At r = R_2 we applied no slip and no flux conditions. The parabolic velocity profile is imposed at the inlet. These conditions can be written mathematically as follows:

Axisymmetry

$$\text{at r} = 0, \frac{\partial w_s}{\partial r} = 0, u_s = 0. \tag{3.7}$$

Continuity of Velocity

$$\text{at r} = R_1, \mathbf{u}_s = \mathbf{u}_w. \tag{3.8}$$

Continuity of Stress

$$\text{at r} = R_1, (-p_s \mathbf{I} + \mathbf{K}_s)\hat{\mathbf{r}} = (-p_w \mathbf{I} + \mathbf{K}_w)\hat{\mathbf{r}}. \tag{3.9}$$

Inflow

$$\text{at z} = 0, \; R_1 < r < R_2, u_w = 0 \text{ and } w_w = \alpha(r - R_1)(r - R_2). \tag{3.10}$$

Where α is found by imposing:

$$\alpha = f(Q_{in}), \rightarrow Q_{in} = 2\pi \int_{R_1}^{R_2} w_w r dr. \tag{3.11}$$

Outflow

$$\text{at z} = L,\ R_1 < r < R_2,\ \mathbf{n} \cdot (-p\mathbf{I} + \mathbf{K}_w)\hat{\mathbf{z}} = \mathbf{0},\ \mathbf{u} \cdot \hat{\mathbf{r}} = 0 \tag{3.12}$$

Non-slip and no-flux conditions

$$\text{at r} = R_2,\ 0 < z < L, u_w = w_w = 0, \tag{3.13}$$

$$\text{at z} = L,\ \text{and}\ z = 0,\ 0 < r < R_1, u_s = \mathbf{0} \tag{3.14}$$

3.4.4 Mass Transport

Nutrients and Metabolic Products

We consider the transport of nutrients (glucose and oxygen) and metabolic products (lactate). We assume diffusivity to be different in both domains. The governing equation for the free flow domain is the following, where the first term on the right hand side describes diffusion and the second term describes advection by the fluid velocity $\mathbf{u}_w$

$$\frac{\partial C_w^i}{\partial t} = D_w^i \nabla^2 C_w^i - \mathbf{u}_w \cdot \nabla C_w^i \tag{3.15}$$

The free diffusion coefficient in media D_w^i needs to be adjusted in the scaffold domain. To find D_s^i we consider porosity ϵ of the scaffold and, tortuosity τ. Tortuosity is usually a function of porosity and sphericity of particles. However, because the scaffold is made of long filaments rather then round particles, we assume tortuosity to be equal to 1 and let

$$D_s^i = \frac{\epsilon}{\tau} D_w^i. \tag{3.16}$$

The advection-reaction equation for the scaffold domain is then:

$$\frac{\partial C_s^i}{\partial t} = D_s^i \nabla^2 C_s^i - \mathbf{u}_s \cdot \nabla C_s^i + R^i. \tag{3.17}$$

Reaction Term

The reaction term R^i represents consumption of glucose/oxygen or production of lactate. We assume nutrient uptake not to be affected by lactate production. The reaction rate is then given by first order Michaelis-Menten kinetics:

$$R^G = -\frac{V_{max}^G N C^G}{K_m^G + C^G}. \tag{3.18}$$

The lactate production is directly correlated with glucose uptake by a factor $Y_{L,G}$, describing the lactate yield from glucose, its production can be linked as follows:

$$R^L = Y^{L,G} \frac{V_{max}^G N C^G}{K_m^G + C^G}. \tag{3.19}$$

The oxygen uptake is as follows

$$R^{O_2} = -\frac{V_{max}^{O_2} N C^{O_2}}{K_m^{O_2} + C^{O_2}}. \tag{3.20}$$

Boundary and Initial Conditions

We assume that initially the glucose concentration is that of fresh media S^G, lactate concentration due to FBS in the cell culture media is estimated to be S^L [262], and oxygen concentration is assumed to have reached equilibrium with the surrounding atmosphere, so that the concentration is equal to the solubility of oxygen in water

S^{O_2} [263].

The symmetry at the center line corresponds to zero radial flux. We impose continuity of concentrations and continuity of flux at the interface between the two domains (r = R_1). Glucose, lactate and oxygen enter the system via media through the inlet, so that C_w^i is equal to S^i. As glucose and lactate cannot leave or enter the system in the radial direction, at the outer membrane of the bioreactor, we impose zero diffusive flux (noting that advective flux is zero as the flow velocity is zero). We assume that at equilibrium, the concentration of oxygen passing through the wall is equal to the solubility of oxygen in water, as the polyurethane membrane is highly permeable to gases. This leads to a new boundary condition setting the concentration of oxygen to the solubility of oxygen S^{O_2} in water at the wall.

Initial Conditions

$$\text{at t} = 0, C_j^G = S^G,\ C_j^L = S^L,\ C_j^{0_2} = S^{O_2}. \tag{3.21}$$

Axisymmetry

$$\text{at r} = 0, \frac{\partial C^i}{\partial r} = 0. \tag{3.22}$$

Continuity of Concentrations

$$\text{at r} = R_1, C_w^i = C_s^i. \tag{3.23}$$

Continuity of Flux

$$\text{at r} = R_1,\ u_w C_w^i - D_w^i \frac{\partial C_w^i}{\partial r} = u_s C_s^i - D_s^i \frac{\partial C_s^i}{\partial r}. \tag{3.24}$$

Inlet

$$\text{at z} = 0,\ R_1 < r < R_2, C_w^i = S^i. \tag{3.25}$$

Outlet

$$\text{at z} = L,\ R_1 < r < R_2, \frac{\partial C_w^i}{\partial z} = 0. \tag{3.26}$$

Walls

$$\text{at r} = R_2,\ 0 < z < L, \frac{\partial C_s^{G,L}}{\partial r} = 0. \tag{3.27}$$

$$\text{at z} = L \text{ and z} = 0,\ 0 < r < R_1, \frac{\partial C_s^{G,L,O_2}}{\partial z} = 0. \tag{3.28}$$

$$\text{at r} = R_2, 0 < z < L, C_s^{O_2} = S^{O_2}. \tag{3.29}$$

3.4.5 Cell Behaviour

Cell growth is modelled as follows:

$$\frac{\partial N}{\partial t} = \begin{cases} \mu N \left(1 - \frac{N}{N_{max}}\right) + D_N \nabla^2 N, & 0 \leq C^L < C_{crit}^L \text{ and } C^{O_2} \geq C_{crit}^{O_2} \\ 0, & C^L \geq C_{crit}^L \\ 0, & C^{O_2} \leq C_{crit}^{O_2} \end{cases} \tag{3.30}$$

where μ describes cell growth rate via:

$$\mu = \mu_{max} \left(\frac{C^G}{K^G + C^G} \frac{C^{O_2}}{K^{O_2} + C^{O_2}} \frac{K^L}{K^L + C^L} \right). \tag{3.31}$$

This is a Monod-type kinetic equation consisting of a maximal specific growth rate μ_{max}, a half-velocity constant K^i, and a yield coefficient μ dependent on nutrient and metabolite concentration. Glucose and oxygen contribute to cell growth whereas lactate concentration decelerates cell growth. Contact inhibition is given by the maximum number of cells that can fit onto the scaffold N_{max}. The diffusion term describes cell's natural movement from regions of high cell concentration to low cell concentration. The conditions state that cell growth is halted once the critical lactate con-

centration C_{crit}^{L} or the critical oxygen concentration $C_{crit}^{O_2}$ is reached. Critical oxygen concentration was set to 0.097mM, the concentration of oxygen where cytochrome C oxydase is at half its speed [263].

Boundary Conditions

Initially, the cell number is equal to the number of cells seeded onto the scaffold (N_0). The axisymmetry condition along the centreline corresponds to zero radial diffusion of N. Cells are only found on the scaffold domain, there is no change in cell number at r = R_1. Cells cannot leave the system through the walls.

Initial Condition

$$\text{at t} = 0, N_{t=0} = N_0. \tag{3.32}$$

Axisymmetry

$$\text{at r} = 0, \frac{\partial N}{\partial r} = 0. \tag{3.33}$$

Scaffold Domain Boundary

$$\text{at r} = R_1 \text{ where } 0 < z < L, \frac{\partial N}{\partial r} = 0. \tag{3.34}$$

Walls

$$\text{at z} = 0 \text{ and z } = L \text{ where } 0 < r < R_1, \frac{\partial N}{\partial z} = 0. \tag{3.35}$$

3.4.6 Input Parameters

Input variables for the bioreactor dimensions, the fluid flow as well as the mass transport and rate terms are collected in table 3.1. The volumetric inlet flow rate, Q_{in} is later set on the peristaltic pump for the experimental validation of this model (Chapter 4). Some geometrical input data were extracted from earlier obtained μCT images (Chapter 2) using Fiji image analysis software [264].

Table 3.1: Model input parameters and their source.

Variable	Value	Units	Description	Source/Reference
Scaffold				
L	3	cm	length of chamber	Experimental
R_1	3.60	mm	Radius Scaffold	micro-CT measurements
R_2	5.75	mm	Radius Chamber	CAD
κ	3.00E-06	m^2	Permeability of Scaffold	$5.19e-8m^2$
Filaments				
F	200		No. of filaments	Experimental
a	261.53	μm	Length of ellipse shaped filament	micro-CT measurements
b	110.38	μm	Width of ellipse shaped filament	micro-CT measurements
A_{fc}	22673	μm^2	Crossectional area of one filament	micro-CT measurements
A_{afc}	$A_{fc} * F$	μm^2	Crossectional area of all filaments	micro-CT measurements
e	$1-(A_{afc}/A_{R1})$	%	Porosity	micro-CT measurements
t	1		Turtuosity	Assumption
Fluid Flow				
M_{water}	18.01528	g/mol	Molecular Weight Water	
SMDW	RMMW/ρT	m^3/mol	Std Molar Volume	
T	273.15+35	K	Temperature Conversion	
ρ	993.37	kg/m^3	Density of water at 37°C	[265]
η	0.00692	kg/ms	Viscosity of water at 37°C	[265]
Q_{in}	1.5	ml/min	Volumetric Flow Rate	Set Value
Glucose				
D_w^G	5.40E-06	cm^2/s	Diffusivity of Glucose in Medium	[266]
D_t^G	$D_w^G * \frac{e}{t}$	m^2/s	Diffusivity of Glucose in Scaffold	Derived Value [255]
S^G	15	mmol/L	Initial Glucose Concentration	Experimental
R_{max}^G	272	fmol/h/cell	Max Glucose Uptake Rate	[267]
Km^G	3.5x10^{-7}	mol/cm^3	Michaelis-Menten Constant	[268]
Lactate				
D_w^L	1.10E-05	cm^2/s	Diffusivity Lactate in Medium	[269]
D_s^L	$D_w^L * \frac{e}{t}$	cm^2/s	Diffusivity of Lactate in Scaffold	Derived Value [255]
S^L	2.5	mM	Initial Lactate Concentration	Experimental
y_l	2		Lactate Yield from Glucose	[269]
C_{crit}^L	4	mM	Critical Lactate Concentration	[270]
Oxygen				
$D_w^{O_2}$	3.29E-05	cm^2/s	Diffusivity of Oxygen in medium	[271]
S^{O_2}	0.2	mM	Initial Oxygen Concentration	Experimental
$R_{max}^{O_2}$	1.00E+02	fmol/h/cell	Max OUR	[267]
Km^{O_2}	4.05E-09	mol/cm^3	Michaelis-Menten Constant	[272]
$C_{crit}^{O_2}$	0.097	mM	Critical Oxygen Concentration	[263]
Cell Growth				
D^N	D^{Ncc}/sf	cm^2/s	Cell Migration Fibroblasts (14x slower than cancer cells)	[273]
D_{Ncc}	1.38E-10	cm^2/s	Cell Migration Cancer Cells	[274]
sf	14.6		speed factor Osiecki's cancer cells to fibroblasts	
μ_{max}	ln(2)/dt	h^{-1}	Max growth rate	[275]
dt	48	h	Doubling Time	[275]
N_0	N_{in}/V_{R1}	cm^{-3}	Initial Cell Concentration	Set Value
N_{in}	500000		Initial Cell Number	Experimental
N_{tf}	5.67E+06		No. of Cells that fit on Scaffold	μCT measurements
N_{max}	N_tf/V_R1	cm^{-3}	Maximum Possible Cell Concentration	μCT measurements
K^G	0.006	mM	Growth Constant Glucose	[276]
K^L	43	mM	Growth Constant Lactate	[277]
K^{O_2}	0.001	mM	Growth Constant Oxygen	[276]

3.5 Results

3.5.1 Fluid Flow at steady state

We present three input flow rates, which were later tested in a validation experiment (Chapter 4). The flow velocity heatmaps in figure 3.2 A) show similar flow paths at all flow rates. The fluid takes the path of least resistance. The highest flow rates are found in the free flow area. The flow rate is much slower in the scaffold region but evenly distributed through it. There were high fluid velocities at the in- and outlet, and lower velocities at the wall boundaries. The images in figure 3.2 B) show the flow profile at the inlet (B1) and a defined cutline (B2) for the three flow rates of interest. We can see a fully developed parabolic flow profile. Importantly we can see that the flow in the scaffold region is slower than in the free flow region, but not zero. The model did not identify pockets of no flow.

The pressure profile in figure 3.3 shows gradually decreasing pressures from the inlet to the outlet. The flow rates lead to maximum pressures of 0.01 mPa, 3mPa and 20 mPa in increasing order of flow rates.

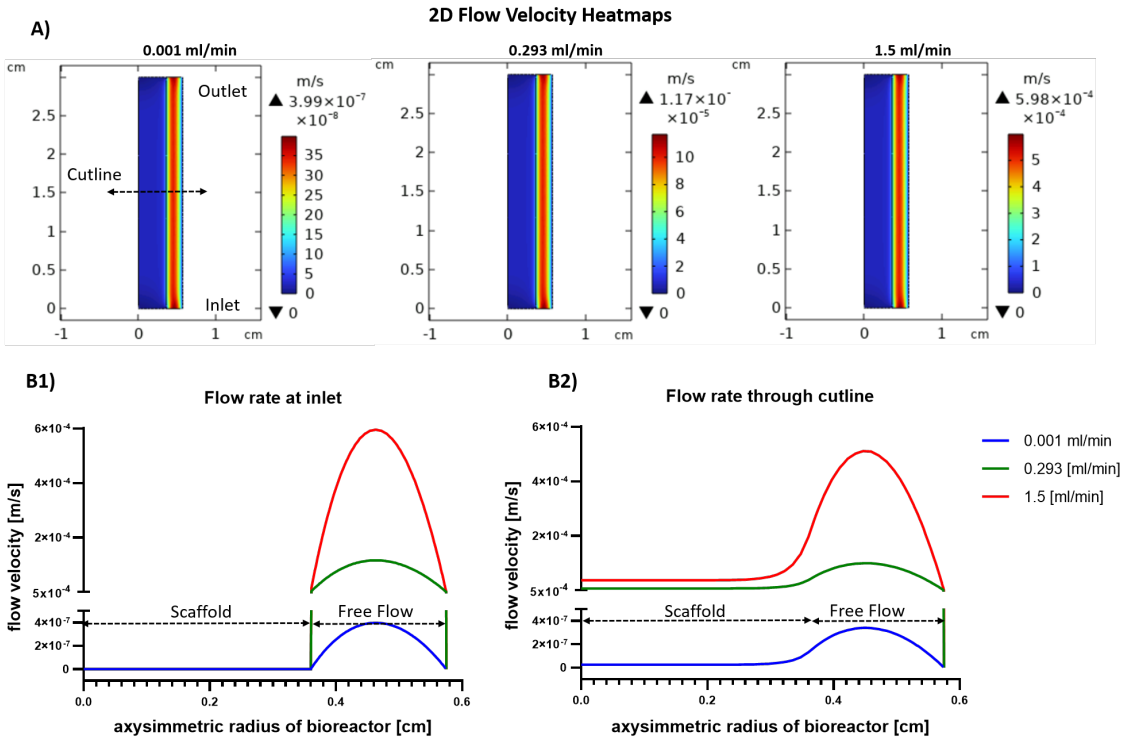

Figure 3.2: **Fluid flow velocity profiles.** A) Surface velocity heatmaps of fluid velocities [m/s]. The flow paths are identical in all three flow rates. The flow velocities are equal to zero at the walls (dark blue) and comparably low in the scaffold domain. Fluid velocities are high (red) in the free-flow domains. B1) Flow profile at the inlet. The x-axis shows the radius of the bioreactor with the centre (r=0) at x=0. Y-axes show the fluid velocity and are broken into two segments in order to visualize all three flow rates in one graph. he results are shown for three inlet flow rates of interest. Results are in blue for the low flow rate, red for the medium flow rate and green for the high flow rate. All flow rates show a parabolic flow profile of varying height at the inlet. There is no flow at the wall boundary. B2) Flow profile at the cutline. The cutline was drawn across the scaffold and free flow region at L =1.5cm. The flow profiles are slightly tilted to the left indicating the deceleration of fluid velocity in the scaffold domain.

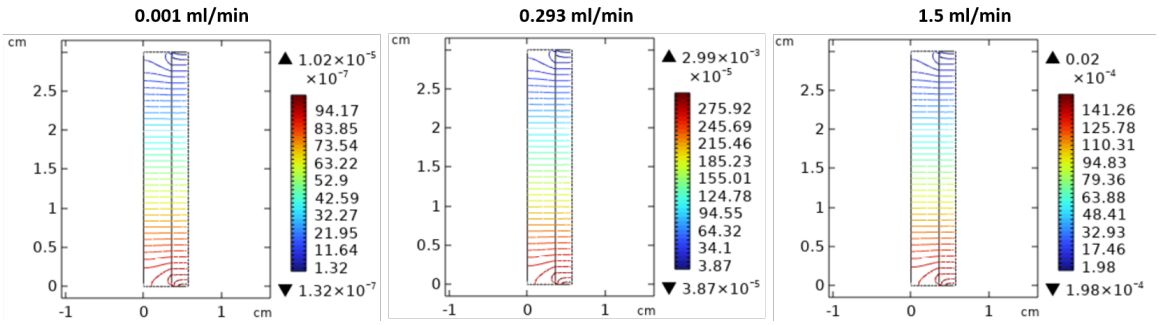

Figure 3.3: **Pressure distribution throughout the bioreactor [Pa].** Results shown at the input flow rates of interest. High pressures are indicated with a red color and low pressures in blue. The small black arrows indicate the maximum and minimum pressure values. The pressure gradually decreases along the length of the bioreactor and is distributed evenly across the free-flow and scaffold domain.

3.5.2 Mass Transport

Next we solve the time-dependent mass transport equations. We consider a culture duration of 10 days. Figure 3.4 shows the distribution of nutrients locally at day 10 of culture. The heatmaps highlight local differences in concentrations of glucose, lactate and oxygen for all three flow rates.

Glucose rich medium enters at the inlet, and the concentration gradually decreases towards the outlet. The lowest flow rate shows the most local differences. The medium flow rate shows slightly lowered glucose levels in the scaffold region. The high flow rate equilibrates glucose concentrations throughout the bioreactor.

Lactate accumulates towards the outlet and is lower at the inlet where fresh, lactate-free medium is brought in. The low flow rate leads to a gradual accumulation of lactate. The medium flow rate leads to elevated lactate levels in the scaffold region. In the high flow rate lactate levels are equilibrated throughout the bioreactor.

Oxygen enters the system at its maximum concentration at the inlet and the permeable membrane. For the low flow rate the lowest oxygen concentration is found next to the inlet, in the scaffold region. The medium flow rate has lower oxygen levels across most of the scaffold region. The high flow rate equilibrates oxygen most

successfully, though levels reach a concerningly low level next to the outlet.

Figure (3.5) displays the nutrient concentration over time at different flow rates.

In the lowest flow rate glucose levels drop from the first day on wards. The two higher flow rates have almost identical glucose concentrations over time. There is no sharp drop because glucose is replenished quicker.

As for lactate, the lowest flow rate does not replenish fresh media quickly enough, and levels of lactate double within the first four days. In the higher flow rates lactate levels increase very slightly, but never reach a critical point, as fresh media is replenished.

Oxygen levels drop instantly in the lowest flow rate and more gradually in the other two. Despite this sharp drop, the system does not reach a critical oxygen concentration, even looking beyond the 10 days of interest.

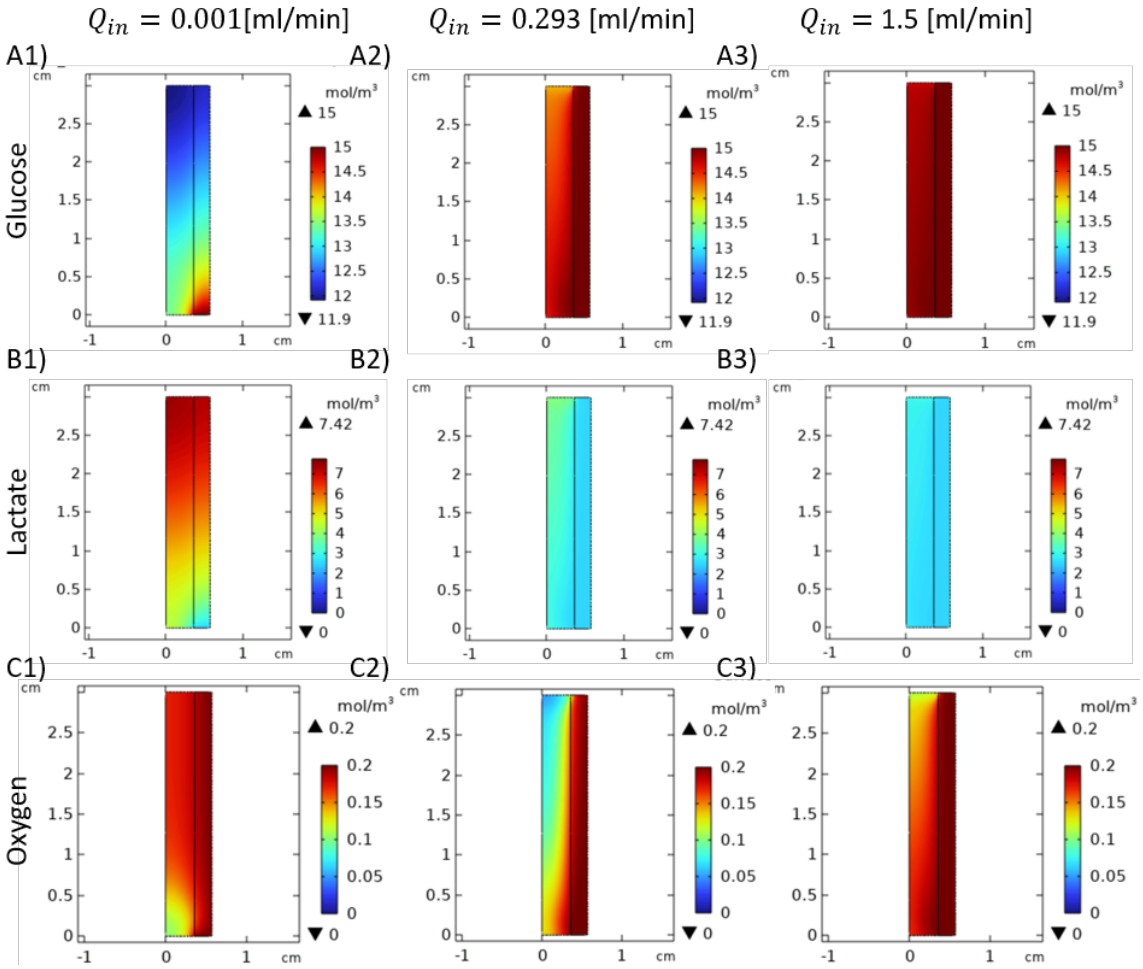

Figure 3.4: **Heatmap of Nutrient and Metabolite Concentrations on day 10.** We depict spatiotemporal concentrations of Glucose, Lactate and Oxygen in the bioreactor on day 10 of culture. High concentrations are depicted in dark red, low concentrations in dark blue. Results are shown for the three flow rates of interest. A1-3) Glucose concentration is found highest near the fluid inlet for the low flow rate. It decreases gradually along the long axis of the bioreactor, and slightly less so in the scaffold domain. The medium and high flow rates both lead to an even distribution of glucose, though glucose concentrations are slightly lower in the scaffold than the free flow domain. B1-3) Lactate concentration is lowest near the fluid inlet for the low flow rate. It gradually increases along the long axis of the bioreactor and reaches almost double its inetlet concentration near the outlet. The medium flow rate shows a low accumulation of lactate in the scaffold domain, and more so towards long end of the bioreactor. The high flow rate shows the least accumulation of lactate. It is only slightly elevated in the scaffold region nearest the outlet. C1-3) Oxygen concentration in the low flow rate is the lowest in the scaffold region near the inlet. The rest of the bioreactor shows high concentrations of oxygen, though slightly lower in the scaffold region. The medium flow rate has the most uneven oxygen distribution. The concentration is high near the inlet and the walls and gradually falls toward the centre of the scaffold. The high flow rate leads to the most evenly distributed concentration of oxygen. The concentration is half its maximum in the scaffold region closest to the outlet and towards the centre.

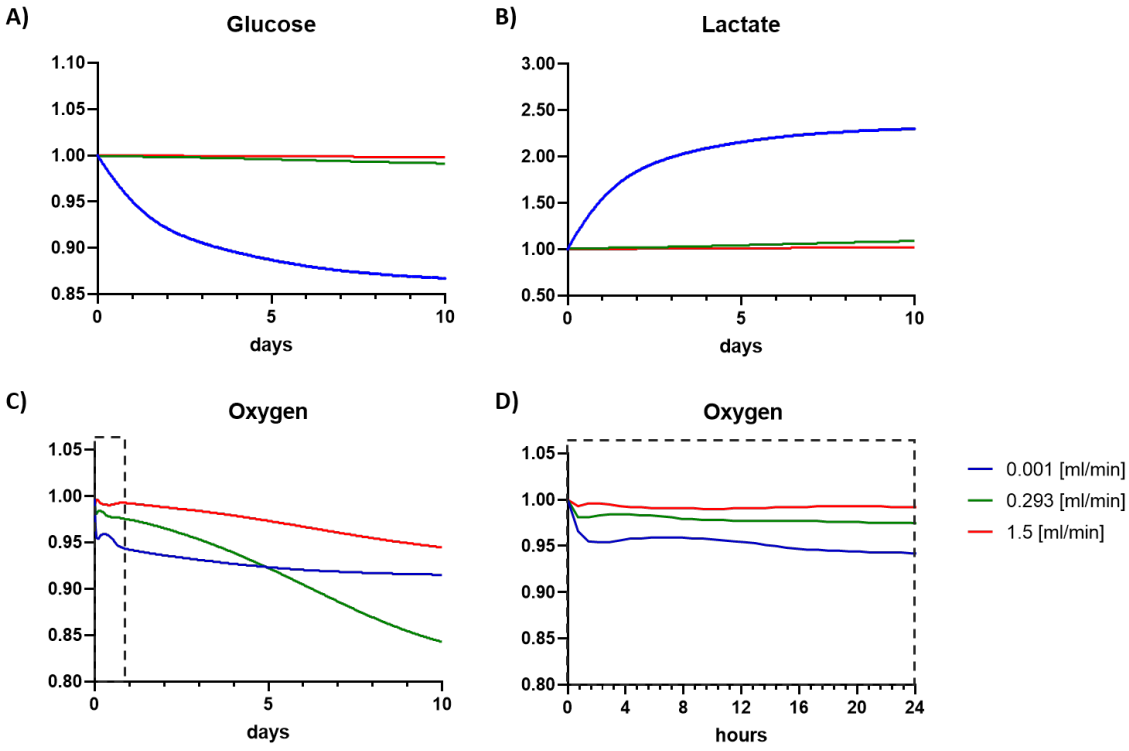

Figure 3.5: **Fold changes of nutrients and metabolites in the bioreactor chamber from day 0 to day 10 at different flow rates.** The graph shows integrated quantities across the whole bioreactor. A) shows glucose over time. B) shows lactate. C) shows oxygen. D) shows oxygen in the first 24 hours. For glucose and lactate the lines depicting inlet flow rates of 1.5ml/min and 0.293ml/min are almost identical and hide behind one another.

3.5.3 Cell Behaviour

We are interested in how the differences in nutrient distribution, caused by different flow rates, affect cell growth. Figure 3.6 shows local differences in cell concentration on the scaffold, resulting from the three flow rates of interest. Pictured are time points at which cell viability was measured in the validation experiments. The lowest number of cells in dark blue is equal to the number of cells seeded (500.000). While we can observe uniform cell distribution in the higher flow rates, the low flow rate shows a drastic lack of cells growing throughout the scaffold. Cells appear to accumulate near the fluid inlet at the bottom of the scaffold. This would be where lactate is

cleared most efficiently, as lactate-free media comes in. Figure 3.4 shows that regions where lactate accumulates and glucose concentrations are low, correlate with regions of low cell concentration in figure 3.6. Conversely, oxygen levels are low where cell concentrations are high.

In addition, we conducted a parametric sweep to identify whether higher flow rates lead to a higher cell growth. As shown in figure 3.7, increasing the flow rate beyond 0.05ml/min has no great benefit in terms of cell growth. For flow rates higher than 0.05ml/min the graph resembles expected Monod-Type growth curves consisting of a lag phase, log phase, and plateau phase where the nutrient uptake and cell growth come to an equilibrium. The phases start at different time points for different flow rates and are indicated as an approximation only. Growth curves overlap initially. Flow rates lower than 0.05ml/min start having a negative effect on cell growth. Flow rates lower than 0.001ml/min cannot sustain cell growth. The three flow rates of interest are underlined in the legend.

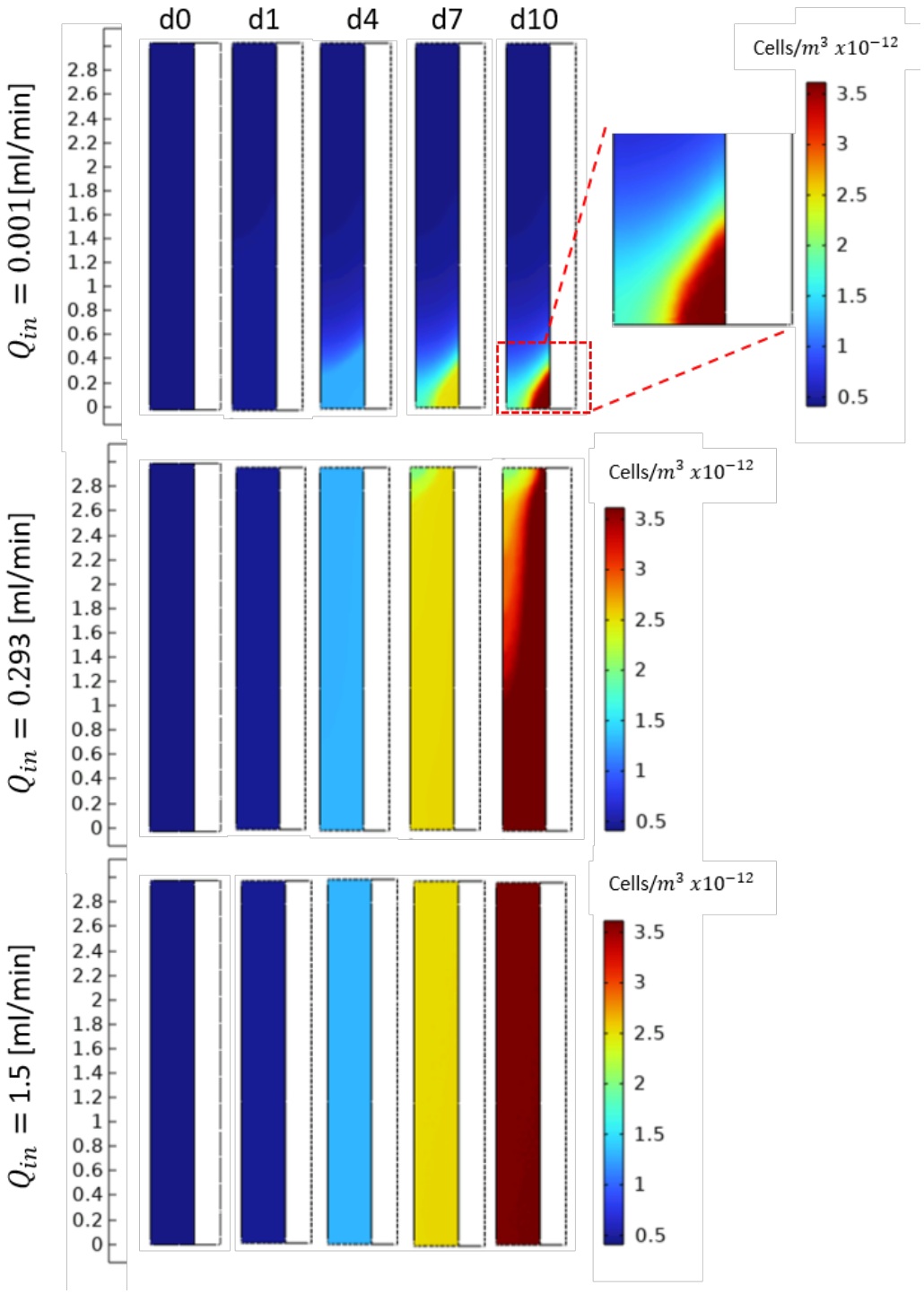

Figure 3.6: **Heatmaps showing cell concentration throughout the scaffold**. Each row shows a different input flow rate, and each column represents a different day. Cells accumulate near the inlet for the 0.001ml/min flow rate whereas cells distribute evenly throughout for the other two flow rates.

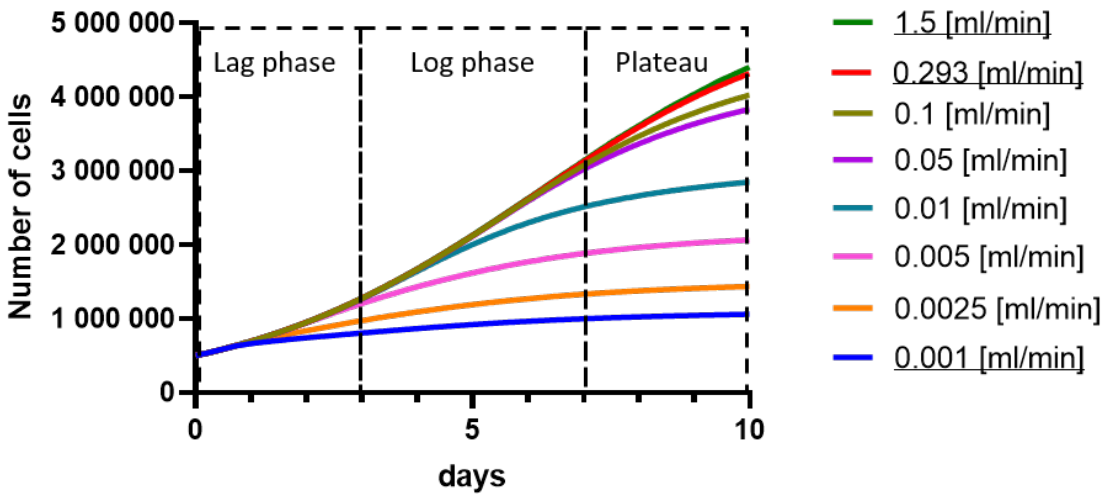

Figure 3.7: **Cell growth curves at different flow rates over 10 days of culture.** We depict the change in cell numbers from day 0. Numbers were obtained by integrating across the scaffold domain. The three flow rates of interest are underlined in the legend. The cell growth phases are approximations for reference.

We highlight the negative effect of the low flow rate further in figure 3.8. We depict lactate levels in red and cell growth in blue. Cell growth is slowed down drastically after a day, due to the critical lactate concentration being reached after 28 hours (highlighted by a vertical solid grey line). Cells keep growing in very small numbers near the inlet (figure 3.6) as lactate-free media comes in. Within a 10 day culture period, a critical lactate concentration is not reached for the other flow rates.

In the *in vitro* experiments, the bioreactors need to be disconnected from the media flow circulation for approximately one hour or more at a time. This is done either to move the chambers onto the robotic shoulder to apply mechanical stimulation, to conduct viability assays, or to move them under a microscope. We are therefore interested in the effect of no flow. The results depicted with dotted lines in figure 3.8 show this effect. Initially we assume a well mixed system supplied with plenty of nutrients and the starting concentration for lactate. There is no flow and no nutrient transport due to advection. Cells grow through uptake of glucose and oxygen, and produce lactate. The critical lactate concentration (highlighted by a vertical dotted

grey line) is reached after around 22 hours. At this point cells stop growing locally, as lactate cannot be removed without perfusion. Stopping the flow for this amount of time did not have a significant effect on glucose or oxygen concentrations.

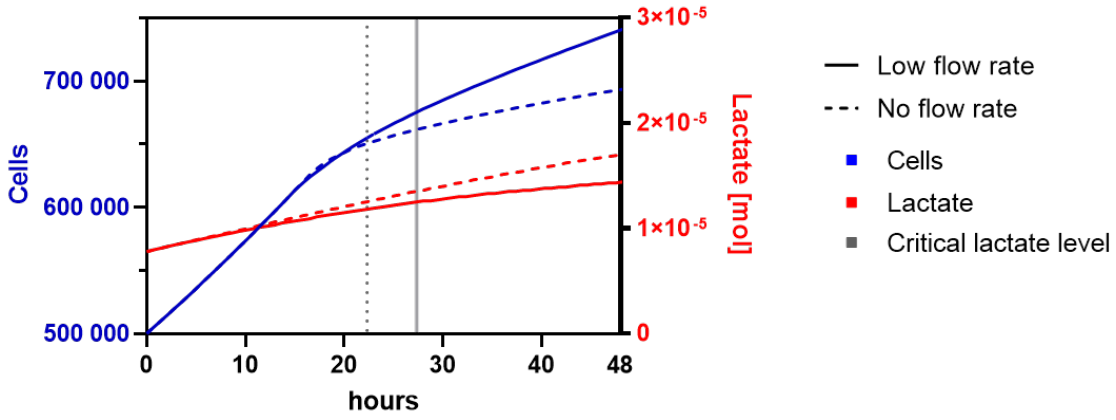

Figure 3.8: **Effect of lactate accumulation and cell growth in flow and no-flow conditions.** The no flow condition mimics the state of the bioreactor during mechanical stimulation, proliferation assays or microscopy. The solid lines show the results from the low flow rate, and the dotted lines show no flow rate. The number of cells are shown in red and the lactate levels in blue. The critical lactate concentration is reached after 22 hours for the no-flow condition and 28 hours for the low flow condition. This point is highlighted with vertical gray bands.

3.5.4 The influence of a permeable membrane on oxygen levels

Oxygenation in bioreactors can be achieved through high perfusion rates or artificial aeration in combination with impellers or other ways of agitating the fluid. To omit cell responses to shear stress that these techniques would cause, our bioreactor uses an outer membrane that is permeable to oxygen instead. In this section we investigate its effect compared to an outer membrane impermeable to oxygen. To model the permeable membrane, we set the oxygen concentration at the wall to 0.2mM, based on the solubility of oxygen in water. To model the impermeable membrane, we remove this concentration.

Figure 3.9 shows the oxygen concentrations on the time points of interest in a 2D axisymmetric view of the bioreactor, with the two different membranes. There is little oxygen present in the chamber with the impermeable membrane. The permeable membrane however leads to a more even and concentrated oxygen distribution. In the impermeable chamber, oxygen is only present near the inlet. Figure 3.10 shows the change in cell numbers (blue) and oxygen concentration (red) over time for the permeable membrane (solid lines) and impermeable membrane (dotted lines). Oxygen levels stay consistent in the permeable condition, and drop down to a critical oxygen concentration after less than 6 hours in the impermeable chamber. Cell growth consequently thrives in the permeable condition and comes to a halt once the critical oxygen concentration is reached (highlighted by a vertical dotted grey line).

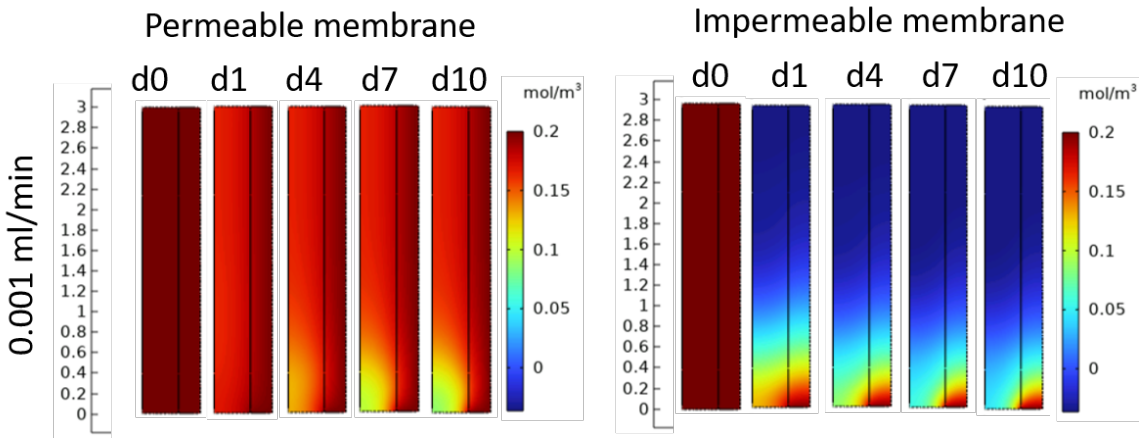

Figure 3.9: **Heatmaps of oxygen concentration with permeable and impermeable membrane.** The graphs show the distribution of oxygen at a flow rate of 0.001ml/min. Higher flow rates did not show a significant difference between the two membranes.

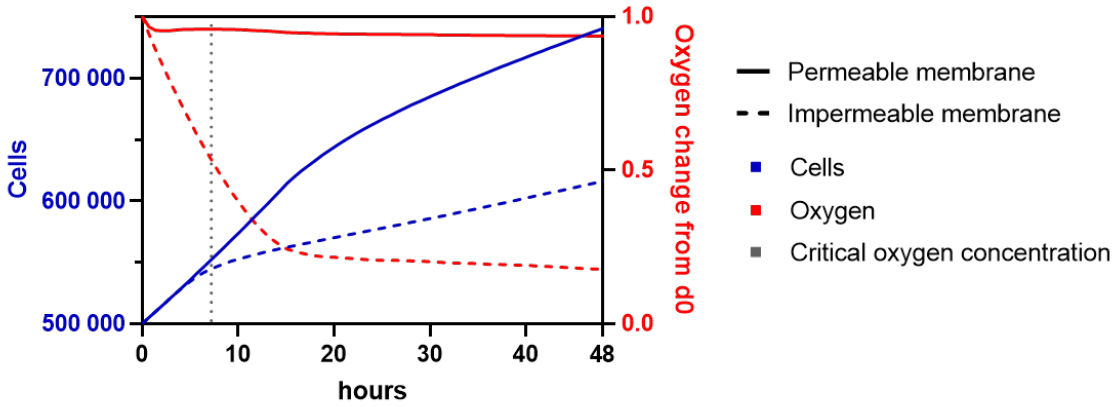

Figure 3.10: **Influence of membrane permeability on oxygen concentration and cell growth over time at an input flow rate of 0.001ml/min.** The solid lines show the results from the permeable membrane, and the dotted lines show the impermeable membrane. The number of cells are shown in red and the oxygen levels in blue. The critical oxygen concentration is reached after around 6 hours in the impermeable membrane. This point is highlighted with vertical gray bands. Higher flow rates do not cause oxygen to be depleted in either scenario.

3.6 Discussion

The flow paths within the bioreactor give a good insight into how the geometry and scaffold characteristics influence the fluid flow. The overall design leads to lower flow rates in the scaffold region than the free-flow region. Within the scaffold, the fluid spreads evenly. There are pockets of no flow at both ends of the scaffold. Fluid flow is slowed down near the walls, which was expected due to the non-slip condition.

A point of concern is the pressure acting on the cells as a result of the flow velocities. The maximum pressures for the three flow rates were 0.01mPa, 3mPa and 20 mPa. The level of fluid-induced shear stress on native tendons is unknown, but estimated to lie between 54nm/s and 10μm/s, resulting in 15 and 65mPa [278, 279]. Cyclic strain induced shear stress was predicted to be between 0.15mPa and 0.46mPa [280]. A shear stress term (as suggested below) should therefore be introduced in this model. The nutrient distribution does not appear to correspond to the flow profiles alone.

Mass transport must therefore be affected by both, advection and diffusion. This is an important detail as diffusion effects could be lost in very high flow rates, leading to much poorer nutrient distribution in no flow pockets. Nutrients could have a harder time passing through the permeable scaffold without diffusion.

Glucose concentrations remain sufficiently high throughout the culture period of 10 days. As highlighted, lactate levels do reach a critical level in the low flow rate. The reduced oxygen concentration is concerning and generally oxygen transfer is an underappreciated problem in cell culture [263]. It should be controlled via sensors or additional oxygenators. Our results show that the permeable membrane is hugely important for the distribution of oxygen. The ability of oxygen to diffuse is partially dependent on the depth of the media, meaning at larger depths, the nutrients don't diffuse fast enough to reach cells and sustain necessary levels. It is encouraging to see that, in the current setup, this is not an issue. We could also deduce that a flow rate of 1.5ml/min and 0.293ml/min lead to sufficient oxygen delivery, without the need for a permeable membrane. The result that no-flow does not affect cell growth up until around 22 hours of culture, is greatly encouraging as it allows us to run cultures without media feed for this time.

There are some limitations to this model and we should take these into account when judging the results.

3.7 Model Limitations and Refinements

3.7.1 Scaffold and Geometry

The geometry of the bioreactor is simplified as a 2D axisymmetric model and could be improved as follows. The in- and outlets are currently located at each end of the bioreactor and reach all around the scaffold. In reality, they are located at each end on opposing sides next to the scaffold (Figure 1.8 A). A more accurate model would

take the true location into account. To keep this simple, it could be drawn as a 2D- rather than axisymmetric model. With one inlet on the bottom right side and one outlet on the top left. However, because this is also a simplified model, we recommend it be used as an addition to the existing model, rather than a replacement.

3.7.2 Diffusivity and Permeability

The current diffusivity values of glucose, lactate and oxygen through the scaffold (D_s^i) are given by the scaffold's porosity (e) and turtuosity (t). Porosity is obtained by calculating the cross sectional area occupied by filaments, and the area the scaffold and the liquid occupy. In order to more accurately model these values, experimental data should be obtained.

3.7.3 Flexible Walls

The current model assumes the outer membrane to be rigid. In reality we are dealing with a flexible, soft bioreactor, capable of bending, twisting and stretching. The membrane can therefore expand or shrink depending on the pressure the fluid is exerting onto it. We have neglected this at this stage. Furthermore we have made the assumption that the membrane is at its full capacity given the length and radius of it. This means that in reality the media volume held my the membrane could be smaller and therefore less nutrients are present.

3.7.4 Fluid Shear Stress and Pressure

As mentioned, the pressure experienced by cells in the high and medium flow rate is not negligible. Perfusion can greatly aid nutrient distribution but it can also mechanically stimulate cells through shear stresses. High fluid shear can negatively influence cells and even lead to their detachment. For tenocytes, some shear stress is benefi-

cial as it is known that loading and unloading of the tendon causes fluids to flow in and out of the tissue [281]. Shear stress is something we have not considered in this model and it should be included in the next iteration. Furthermore, the chambers lay at a slight angle to create back pressure at the outlet and ensure the chambers are properly filled with media. Future iterations of the model should include back pressure at the outlet.

3.7.5 Media Feed

In the current model, we made the assumption that media is being recirculated in a media reservoir big enough to replenish all nutrients. This decision was made after experimental data showed that glucose, lactate and oxygen levels remained fairly stable. However, should the operator decide to use a smaller reservoir volume, the results might change and the model should be adapted accordingly so that $C^i_{out} = C^i_{in}$. Furthermore we have not considered oxygen exchange of the media reservoir. This is only a shortcoming of the non-permeable membrane model.

3.7.6 Metabolism

There are several avenues in which we could build on the metabolism model. The current model considers first-order kinetics only. This means the substrate concentration is much smaller than the Michaelis-Menten constant K^i_m.However, when the substrate concentration is much higher than K^i_m, it might be more accurate to model zero-order kinetics (Eqn. 3.1). Furthermore, this model uses glucose and oxygen uptake rates obtained from mysenchymal stem cells, rather than fibroblasts or tenocytes. What we are lacking in literature are uptake rates specific to our cells. In addition, glucose is often metabolized in different amounts depending on the local glucose concentration [282]. The production of Lactate as a result of glycolytic reactions is more complex than currently modeled. In high glucose environments, more lactate is produced as

a result of glucose uptake than in lower glucose environments. It has been observed that cells can grow at the same growth rate under different glucose uptake and lactate production rates [282].

It was challenging to find a critical oxygen concentration specific to tenocytes. This is not only due to the poor definition of normoxia, hypoxia and physoxia (Section 3.2.2). More generally there is a lack of communication of key parameters such as cell type, media depth or cell specific oxygen uptake rates in the literature [283]. This goes hand in hand with oxygenation being an underappreciated problem [263]. In the model we set the critical oxygen concentration to 0.097mM, the concentration of oxygen where cytochrome C oxidase is at half its speed [263]. Cytochrome C oxidase is the last enzyme in the electron transport chain in the cells' membrane. It is responsible for receiving electrons from each of four cytochrome c molecules, and transferring them to one oxygen molecule and four protons. This leads to the formation of two molecules of water. In addition to binding the four protons from the inner aqueous phase, it transports another four protons across the membrane, increasing the transmembrane difference of proton electrochemical potential, which is then used by the ATP synthase to synthesize ATP. However, there are Oxygen sensing enzymes that have a lower affinity for oxygen. Hypoxia-inducible factor prolyl-hydroxylases (HIF-PHDs) and Factor Inhibiting HIF (FIH) enzymes need oxygen during hydroxylation of proline and asparagine residues on HIF transcription factors [284]. Their K_m values lie between 0.100 and 0.240 mM [285, 286, 287]. The role of hypoxia in tenocytes is not entirely clear. Total hypoxia leads to apoptosis. Tenocytes respond to hypoxia of $1\%O_2$ *in vitro* by activating classical HIF-1 α-driven pathways. Interestingly hypoxia led to the activation of some, but not all, hypoxia-induced apoptosis factors, as well as VEGF. However, treatment with VEGF could not save tenocytes from apoptosis. This is interesting as VEGF is known for starting the growth of blood vessels, and tendons are known to be relatively avascular [288]. Looking further in the literature,

another typical critical oxygen concentration groups have used for mammalian cells is $2x10^{-2}$ mM [272] , and reported that there exists a critical concentration at 1% of air saturation.

Ideally, we would assess hypoxia in-house. However, this would go beyond the scope of this project.

3.7.7 Cell Growth

In the current model, cell growth is slowed down by lactate concentrations in accordance with Michaelis-Menten kinetics. Cell growth is also halted by a set critical concentrations for lactate and oxygen. However, cell concentrations never fall, and are kept at a minimum of 500.000 cells, given by the initial seeding number. A useful extension to this model is a death rate μ_d. A simple approach can be included as follows:

$$\frac{\partial N}{\partial t} = \mu N \left(1 - \frac{N}{N_{max}}\right) - \mu_d N + D^N \nabla^2 N. \tag{3.36}$$

Where μ_d is the death rate $[h^-1]$ and given by

$$\mu_d = \frac{\mu_{d,max}}{1 + \left(\frac{K_{d,lac}}{C_{lac}}\right)}. \tag{3.37}$$

Where $\mu_{d,max}$ is the inherent maximum cell death rate $[h^{-1}]$ and $K_{d,lac}$ is the Michaelis-Menten constan for cell death by lactate [mM]. Cell death could also be linked to ammonium $K_{d,amm}$ concentrations or anoxia levels, given these values can be found in the literature.

3.7.8 Cell Location

An intriguing feature Comsol offers is to include spatial coordinates of objects. We obtained cell locations in a 3D space in chapter 2 and could include these as an

input parameter in a later iteration of the model. These locations could also be obtained at later days into the culture and give a better insight into cell migration and accumulation in particular locations on the scaffold. Including this data in the model would lead to a model more closely resembling the experimental data.

3.8 Conclusion

When designing a new bioreactor there are many considerations to make, including how the design will affect fluid flow, what flow rate is needed to provide enough mass transfer, how many cells should be seeded and how these parameters will affect cell growth. It would be time-consuming and expensive to test them all. The model presented in this chapter takes the current design of the bioreactor chamber into account and tests a variety of input parameters. We have not presented all of them, as the possibilities are near infinite, but we presented the most important ones.

The model can determine nutrient concentrations under different flow rates and their influence on cell growth. It is able to show 3D nutrient and cell distributions. We were able to assess the influence of a permeable membrane and its effect on oxygen levels. We could also conclude that stopping perfusion over a period of 20 hours will not affect cell growth, for the number of cells and volume of media considered. Though using a membrane impermeable to oxygen would be detrimental to cell viability. This model highlights potential design flaws and risk factors such as an accumulation of lactate in low flow rates. As the current setup might lead to areas of no flow and an accumulation of lactate in those areas, the model has highlighted some room for improvement with the design.

Model input values specific to our system were challenging to find and implemented to the best of our knowledge. In order to make a more educated decision about the results of this model, a validation experiment needs to be conducted.

Chapter 4

Experimental Validation of the Computational Model

4.1 Abstract

In this chapter we conducted a set of experiments to investigate how well the computational model performs. Cells cultured in the bioreactor chamber were perfused at three different flow rates, and glucose, lactate and oxygen levels were measured frequently. Cell viability was assessed via PrestoBlue analysis. The results are discussed and compared to the model. We found that the model could predict cell growth trends for the different flow rates, but not cell numbers. Metabolite analysis showed comparable trends for the higher flow rates in the model and the validation. In this experiment we could not see the large increase in lactate, predicted by the model. Finally we discuss which model improvements suggested earlier could lead to a more powerful model.

4.2 Introduction

Designing new bioreactor systems comes with challenges. *In silico* models can aid the design and characterization of these systems. However, in order to assess how well a model performs, we need to validate it. Model validation can be done in two ways: through comparing the results with existing literature, and through in-house experimental testing. When validating through the literature, it is of utmost importance that the system modelled in the literature and the system used in the lab are comparable. It can be tricky to judge whether the system described in papers is similar enough to the system at hand. In our case this was not very feasible. Experimentally, models can be validated against existing results, or by retrospectively conducting experiments. In a study performed by Bai et al, a model for gas to liquid sided mass transfer of oxygen was validated against existing experimental data and showed a $\pm 20\%$ match. It lead to an improved understanding of the system [289]. In our case the model was tested alongside experiments. A challenge in validating computational models is making sure values of interest are accurately measured in the experiment. This was done through the use of glucose, lactate and oxygen sensors, as well as cell viability assays.

4.2.1 Metabolite Sensors

Metabolite sensors are tools that can determine the concentration of certain molecules such as glucose, lactate or oxygen. They tend to consist of three main components.

1. A portion that interacts with the metabolite of interest such as an enzyme, receptors, nucleic acids, antibodies or microorganisms which readily bind and lead to a signal,

2. a transducer able to convert this signal into something measurable, and

3. a computer to process the signal into something that can be interpreted by the user.

Transducers can be based on magnetic, optical, piezoelectric, thermoresponsive, or electrochemical physical phenomena. Though nowadays most sensors use electrochemical principals as they have better sensitivity, reliability, reproducibility, shelf-life stability and calibration procedures. They also tend to be cheaper and therefore more accessible for smaller labs [290].
Indeed bench top industrial sensors start at around 7000£ upwards. For our application electrochemical flow-through sensors were identified as most suitable, as they deliver in-line results, can be employed for long periods of time and come at a reasonable cost.

4.2.2 Cell Viability Assays

Cell viability assays use a variety of indicators of metabolically active cells, and relate the amount of these indicators to the number of viable cells present. Commonly measured indicators are a cell's energy source; Adenosine Triphosphate (ATP), the ability to reduce a substrate metabolically, or enzyme activities. For this experiment we identified the resazurin-based metabolic assays as the most suitable method to determine cell numbers. Resazurin is a nontoxic water soluble molecule. This assay makes use of the cells' mitochondrial activity to reduce the nonfluorescent blue resazurin to the fluorescent pink resorufin. The cells do not have to be lysed in order for this to happen. The reagent PrestoBlue uses this principle. We chose this reagent as it shows a quantitative correlation between its conversion rate and the cell number with no influence of the flow rate and shear stress [291].

4.3 Aims and Hypotheses

The aim of this chapter is to validate the computational model presented in chapter 3, using three flow rates: 0.001, 0.293 and 1.5 ml/min.

We hypothesize that the model can predict some of the outcomes observed in these experiments, such as higher flow rates leading to a better outcome on cell growth and a speedier removal of lactate. Based on the model, all flow rates are expected to deliver sufficient levels of glucose and oxygen.

4.4 Materials and Methods

4.4.1 Experimental Setup

Three chambers were perfused in parallel at three different flow rates (0.001, 0.293 and 1.5ml/min) each. This was repeated 4 times (n = 4 per condition). The pumps were housed in a 37°C heating chamber and the rest of the setup inside a cell incubator at 5%CO_2.

Low Flow Rate Setup:

For the low flow rate we used a single-pass setup (figure 4.1 A) with a syringe pump (NE-1000, New Era pump systems, Farmingdale, NY). The pump was loaded with a 20ml syringe filled with DMEM-F12 HEPES cell culture media supplemented with 15% FBS and 1% P/S (11330032, Thermo Fisher, Waltham, Massachusetts, USA). The pump was set to a syringe diameter of 20.1mm and a flow rate of 0.001ml/min. This was the lowest achievable flow rate. The media was pumped into the chamber, followed by an in-line oxygen sensor (section 4.4.6) and a waste bottle equipped with filters for aeration.

Medium and High Flow Rate Setup:

For the higher flow rates we used a peristaltic pump (ISMATEC 12 channel IPC peristaltic pump, Cole-Parmer Instrument Company, 9 Orion Court, St. Neots, UK) and a closed loop media feed (figure 4.1 B). On the pump, the operator can set a tubing diameter, and a desired flow rate. These two input parameters govern the work (=rotation speed per minute) the pump will put in to achieve the required flow rate. We set the input values (tubing diameter and desired flow rate), and mounted a tube with a different diameter, so that the flow rate was affected according to the continuity equation (Appendix B)

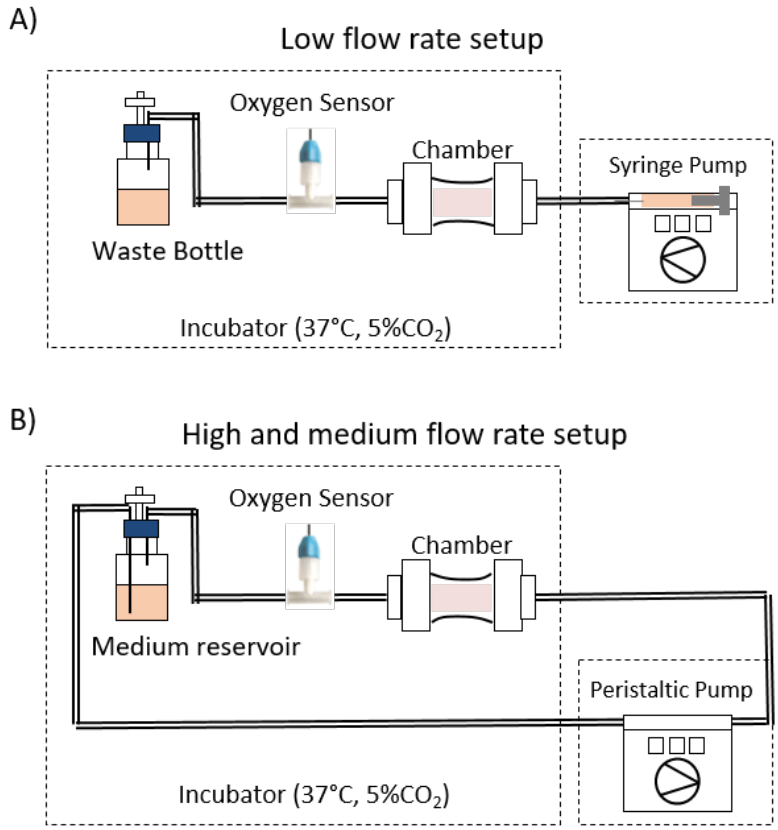

Figure 4.1: **Experimental setup with syringe pump and peristaltic pump** for A) low flow rate and B) medium and high flow rates. The pumps were encased by a heating chamber at 37°C to keep the medium at an adequate temperature. The rest was housed by the cell incubator. The media was circulated from the pump into the chamber, followed by an in-line oxygen sensor and into the waste bottle or medium reservoir. In the medium and high flow rate setup, the media is recirculated from there.

To confirm the pump could do this, it was set up with a 0.64mm inner diameter (ID) tube and set to various flow rates. We then fitted the pump with another tube of 1.6mm ID, keeping the previous input parameters. The pump was turned on for 2 minutes and water pumped through the tubes was collected and measured. We tested flow rates of 0.5, 0.1 and 0.25ml/min. This was conducted three times for each input flow rate. The results of this calibration can be found in the appendix table B.1. Following the calibration, the pump was equipped with a 0.64mm ID tubing and set to a flow rate of 0.293 ml/min. In order to achieve a flow rate of 1.5 ml/min, the tubing for this had an inner diameter of 1.51mm. The media is pumped into the chamber and the in-line oxygen sensor, followed by the medium reservoir. From there, the media is re-circulated.

The glucose/lactate sensors did not form part of the circuits as it was easiest to perform the measurements on the bench. Chambers were resting at a 15° angle to stop air bubbles from accumulating during perfusion. Cells were cultured in the chambers for 10 days post seeding.

On day 10 the chambers were opened and the scaffolds cut into two pieces. One half of the scaffold was put in TRIzol (15596018, Ambion life technologies, Carisbad California) for RNA extraction, the other half was fixed in 10% formalin for 30 minutes and subsequently stored in PBS in the fridge for confocal analysis.

4.4.2 Chamber Assembly

Bioreactor chambers were assembled as follows. Electrospun bundles were produced and assembled as decsribed in section 2.4.1. The bundle ends were covered in 1:10 epoxy resin (Epotek 301, Epoxy Technology Inc., Billerica, USA) and left to dry over night. Chamber parts were 3D printed by 3D-Life Prints (Nuffield Orthopaedics Centre, Oxford, UK). The obtained inserts were tapped and subsequently five bundles were inserted up to their knot, forming the scaffold. To fix the scaffold in place,

bundles were glued in with epoxy resin. The flexible, gas-permeable membranes (polyether-based thermoplastic polyurethane film, TFL-2EA, thickness: 50μm, kindly donated by Permali Gloucester Limited, Goucester, UK) were cut to size, heat sealed (Cole-Palmer, Illinois, USA) and then wrapped around the 3D-printed rings to assemble the rest of the chamber. Inlets and outlets were resined into place. Once the chambers were assembled completely, they were tested for air-tightness and sterilized. Sterilization took place in the biosafety cabinets. For this, chambers were filled with 70% ethanol and left for 2 hours. After this, the ethanol was drained and the chambers washed 3x with PBS. For drying, the chambers were left in the biosafety cabinet for at least 2 nights and equipped with filters on each end. Once chambers had completely dried they were either used immediately for seeding, or closed and stored for future use.

4.4.3 Cell Culture

As extracted Tenocytes have shown to grow rather slow and lead to long waiting times, we used an alternative cell source. This would lead to more pronounced results for shorter culture periods. Human foreskin fibroblasts (HFF-1, American Type Culture Collection, SCRC-1041^{TM}) were expanded in T75 flasks in DMEM F-12 HEPES, 15%, FBS 1% P/S media. Media was changed every third day. Flasks were split when approximately 80% confluence was reached. Cells were harvested using two TrypLE (12605-010, TripLE Express, Thermo Fisher, Waltham Massachusetts, USA) and one scraping step. The cell suspension was spun down for 5 minutes at 0.3 RCF. Subsequently cells were seeded at a concentration of 500.000 per chamber. This was done in a 250μl cell suspension drawn into a 1mL syringe and fed through the inlet of the chamber. The chambers were held upright at a slight angle during seeding, and rocked back and forth thereafter to enable the cell suspension to reach all parts of the scaffolds. The seeded chambers were then transferred to the incubator and after

15 minutes, the chambers were topped up with 50μl media to avoid drying of the scaffold. Once the cell attachment period of one hour had passed, the chambers were filled with 1mL of media and further incubated for 1 hour. After this, the media was replaced by 1mL of PrestoBlue solution, giving a day 0 time point. Once this was done, the chambers were connected to their respective circuits and the pumps were switched on, starting the experiment.

4.4.4 Cell Viability Assay

Cell viability was assessed on day 0, 1, 4, 7 and 10 using PrestoBlue assays (LOT 2103456, Thermo Fisher, Waltham, Massachusetts, United States). PrestoBlue solution was mixed with media to make a 1:10 mix. The pumps were stopped and chambers were disconnected from the media feed, media was gently drained from the chamber and stored for glucose/lactate measurements. The chambers were then filled with 1mL of PrestoBlue mix. The whole procedure is done in a tissue culture hood with the lights turned off to shield the solution from light. Chambers and a non-cell control containing only PrestoBlue mix were then incubated for 1hr at 37°C and 5% CO_2. Following incubation, the PrestoBlue mix is collected and 100μl were dispensed into white 96-well plates in triplicates. The non-cell control was included in triplicates as background subtraction value. The plates were read at excitation 544nm, emission 590nm, with 500 gain on a fluorescence plate reader (BMG FLUOstar Omega Microplate Reade, BMG Labtech, Ortenberg, Germany). The following blank-corrected triplicates are then averaged. We normalized data to improve inter-chamber variability. For this, we looked at the change in signal over time. Cell retention was measured by setting day 0 as a reference value equal to 1. To analyze cell proliferation day 1 was set equal to 1. Both raw and normalized data were analysed with a multiple comparison two-way ANOVA in Graphpad Prism 9. The two-way ANOVA showed statistical significance when the p-value was < 0.05.

4.4.5 Glucose and Lactate Measurements

Glucose and lactate measurements were taken on day 0, 1, 4, 7 and 10. For day 0, a sample was taken straight from the media bottle, before seeing any cells. For all subsequent days, approximately 1mL of media was drained directly from the chambers into eppendorf tubes. From there, the media was drawn up into a 1mL syringe and fed into the glucose/lactate sensors B.LV5.GL (Jobst Technologies GmbH, Freiburg, Germany) via a syringe pump. Media was fed at 0.006ml/min and read for a minimum of 5 minutes and until a stable curve was seen on the BioMon software. The instrument (potentiostat) delivers a measurement point every 1.6 to 2 seconds. The software then averages the last 10 seconds worth of data (moving average). These values were gathered and then averaged again across the 5+ minutes. In order to compare this data to the mathematical model results, we normalized to the change in concentration over time from day 0. Before each time point, the sensor is re-calibrated to a glucose and lactate standard of 18.5mM and 4mM respectively.

In order to test how well these new sensors perform, we compared the same samples with an established glucose/lactate sensor located at the John Radcliffe Hospital, Clinical Biochemistry Department. The machine used was an ARCHITECT cSystems glucose and lactate sensor (Abbott, Abbott Park, Illinois, U.S.A.).

The raw as well as normalized glucose and lactate measurements were analyzed with a two-way ANOVA with repeat measures. Statistical significance was determined wtih a p-value of < 0.05. The results of the two glucose sensors were analyzed with a paired two-tailed t-test and a Bland-Altman % Difference test.

4.4.6 Oxygen Measurements

The concentration of oxygen was measured using a Presens Oxygen Measurement System for Perfusion Monitoring, consisting of a multi-channel oxygen meter (OXY-4 SMA G3), polymer optic fibre cables, and O2 Flow-Through Cells (FTC-PSt7,

PreSens Precision Sensing GmbH, Am Biopark 11, 95053 Regensburg Germany). As the incubator is opened and closed frequently on day 0 and the O2 levels affected by this, we did not include day 0 in our analysis. The measurements were taken on day 1, 4, 7 and 10. For these time points the incubator was closed for at least 24 hours before taking the measurement. The sensors were left to acquire oxygen concentration data for 10 minutes, taking a measurement every 3 seconds. The average of these values is taken and data normalized as change over time from day 1. This was done due to a high inter-sensor variation. The results were analyzed with a two-way ANOVA repeated measures and multiple comparison analysis. A p-value < 0.05 was considered significant.

4.5 Results

4.5.1 Cell Proliferation Assay

The cell proliferation results are presented in figure 4.2, together with the results of the mathematical model. Data is shown as change over time in order to make these results more comparable with the model, as this assay does not provide exact cell numbers. Due to the large drop in cell numbers between day 0 and day 1, we plot the change from day 0 onward for the model, and change from day 1 onward for the experiments. On average, the experimental results showed that the higher the flow rate, the higher the PrestoBlue signal. Cell numbers doubled in the high flow rate, increased by 1.5 times in the medium flow rate, and stayed constant in the low flow rate. A two-way ANOVA with repeated measures on the experimental raw data showed that overall there was no significant difference between the three flow rates ($p = 0.1656$). The multiple comparisons showed there was a significant difference on day 1 ($p = 0.0203$) and day 7 ($p = 0.0323$) between the low and medium flow rate . Normalized data did not show statistical significance.

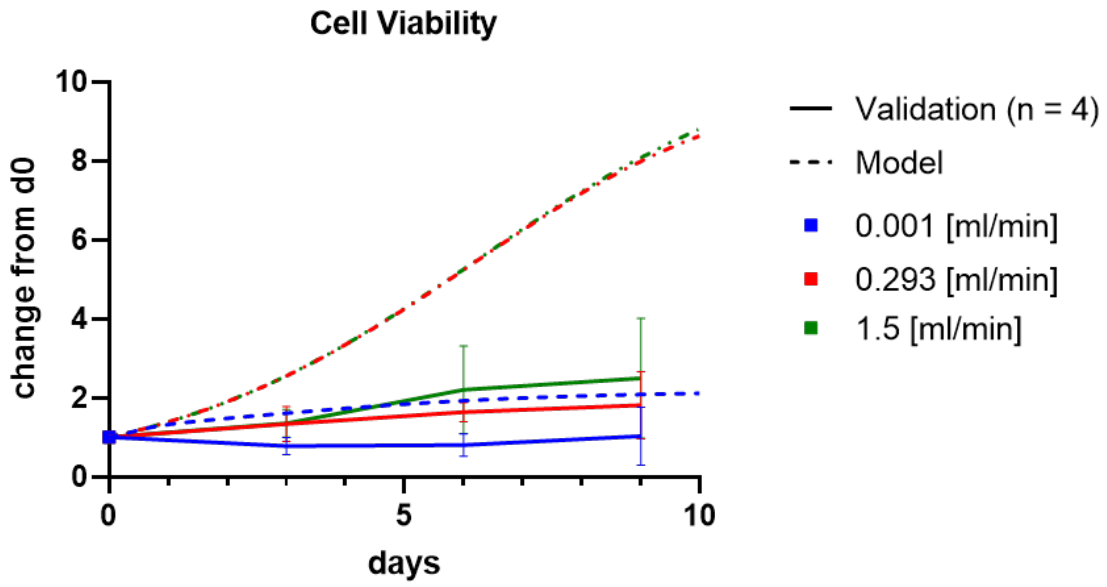

Figure 4.2: **Cell viability at three different input flow rates.** The experimental results are shown from day 1 onward to take into account the time it takes for cells to settle. Results are in blue for the low flow rate, red for the medium flow rate and green for the high flow rate. The solid lines indicate the experimental results, dotted lines indicate the respective modelling results. A two-way ANOVA with repeated measures on the experimental raw data showed that overall there was no significant difference between the three flow rates ($p = 0.1656$). The multiple comparisons showed there was a significant difference in signal on day 1 between the low and medium flow rate ($p = 0.0203$). Day 7 showed a significant difference between the low and medium flow rate ($p = 0.0323$). Normalized data did not show statistical significance. Error bars indicate the standard deviation of $n = 4$

4.5.2 Cell retention upon seeding

In our experiments there was an initial drop in the cell viability from day 0 to day 1. This is depicted in figure 4.3. We can see similar drops for all three flow rates. The two-way ANOVA on raw values with repeated measures and multiple comparisons showed that there was a significant effect between flow rates ($p = 0.0132$). If we normalize day 0 across flow rates, this effect disappears as half of the data set is now equal to 1. The loss of signal from day 0 to day 1 is further investigated in chapter 5.

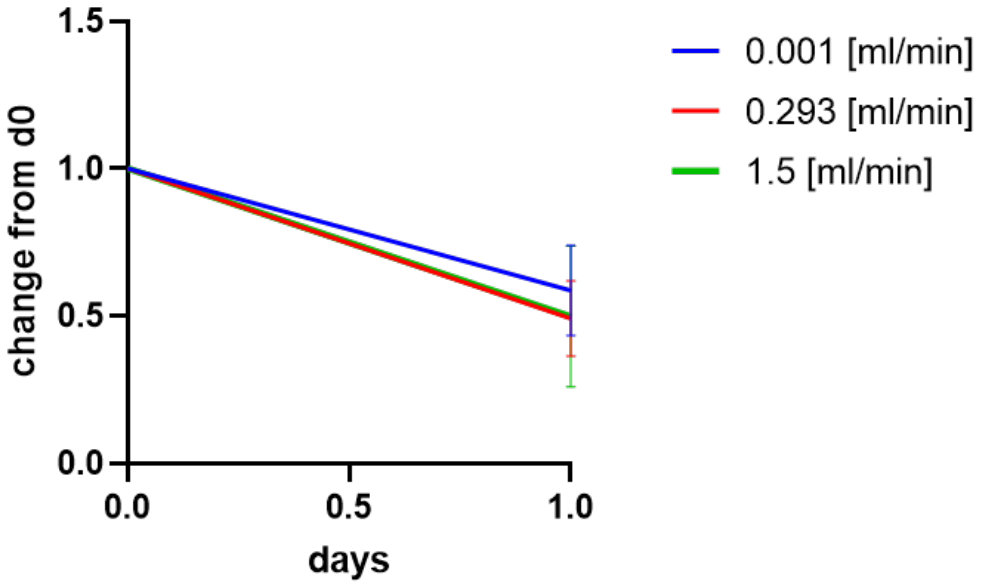

Figure 4.3: **Drop in Presto Blue signal from day 0 to day 1 at the three flow rates of interest.** Depicted are the change in signal from day 0 to day 1. Blue = low flow rate, red = medium flow rate, green = high flow rate. The two-way ANOVA on raw values with repeated measures and multiple comparisons showed that there was a significant effect between flow rates ($p = 0.0132$). Error bars indicate the standard deviation of $n = 4$. The results for 0.293ml/min and 1.5ml/min are very similar and partially overlap.

4.5.3 Glucose and Lactate Concentration

These results are plotted in figure 4.4. The sensor detected slight variations of glucose concentrations over time. According to the raw data, the different flow rates did not have a significant impact on glucose concentration ($p = 0.8284$), and neither in normalized data ($p = 0.9824$).

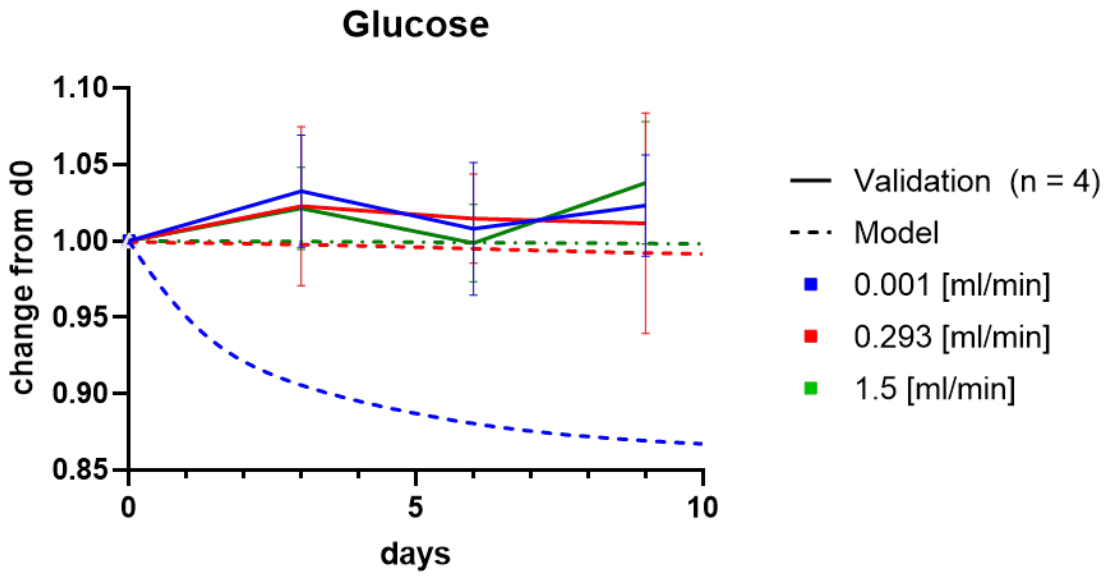

Figure 4.4: **Change in glucose concentration over time.** Blue = low flow rate, red = medium flow rate, green = high flow rate. Solid lines = experimental results, dotted lines = respective modelling results. According to the raw data, the different flow rates did not have a significant impact on glucose concentration ($p = 0.8284$), and neither in normalized data ($p = 0.9824$). Error bars indicate the standard deviation of $n = 4$

The lactate concentrations measured are plotted in figure 4.5. On average the lactate was slightly elevated for the low flow rate. Taking the raw data, there was no significant difference for the different flow rates ($p = 0.0828$), but indeed a significant difference for time ($p = 0.0484$). In particular, time played a significant role on day four between the low and medium flow rate ($p = 0.0211$). There was no other significant difference between the flow rates. Taking the normalized data, there was no significant difference observed.

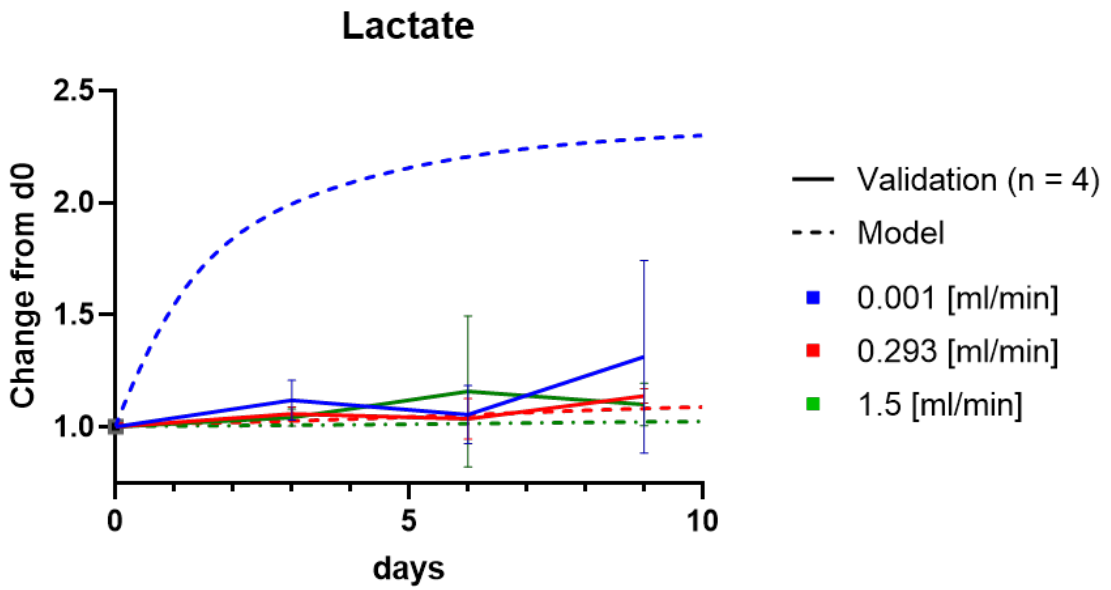

Figure 4.5: **Change in lactate concentration over time.** Blue = low flow rate, red = medium flow rate, green = high flow rate. Solid lines = experimental results, dotted lines = respective modelling results. The raw data showed no significant difference between the different flow rates ($p = 0.0828$), but indeed a significant difference for time ($p = 0.0484$). In particular, time played a significant role on day four between the low and medium flow rate ($p = 0.0211$). There was no other significant difference between the flow rates. Error bars indicate the standard deviation of $n = 4$

Due to the day-to-day sensor variation and the initial inexperience with this type of glucose/lactate sensors, we investigated how these sensors compared to a more established measuring tool. Data obtained through this comparison can be found in figure 4.6. The two plots on the left show box plots of $n = 27$ measurements obtained from the Architect sensors located at the John Radcliffe Hospital, and the in-house sensors. The boxes represent values within the upper and lower quartile. The line within the boxes shows the median. The whiskers extend to the minimum and maximum value measured. The concentrations for glucose obtained on the Architect have a much smaller min/max range than the ones obtained in-house. The range of 50% of the data is also smaller.

For lactate there was a slightly wider range of values obtained on the Architect compared to the in-house sensors. The two medians are much closer together.

On the right side of the graph, all data points for glucose and lactate on the two different sensors are plotted. The Architect tends to measure higher values than the in-house sensors. For lactate both sensors follow very similar trends, as the lactate levels increase on the Architect sensor, so do the values on the in-house sensor. We cannot see the same effect for the glucose values. An identify outliers test conducted in GraphPad Prism 9 did not identify any outliers. A paired two-tailed t-test showed a significant difference between Architect vs in-house measurements for both glucose and lactate (n=27, p=<0.0001), and the Bland-Altman analysis shows that they consistently deliver different results (bias=17.16%).

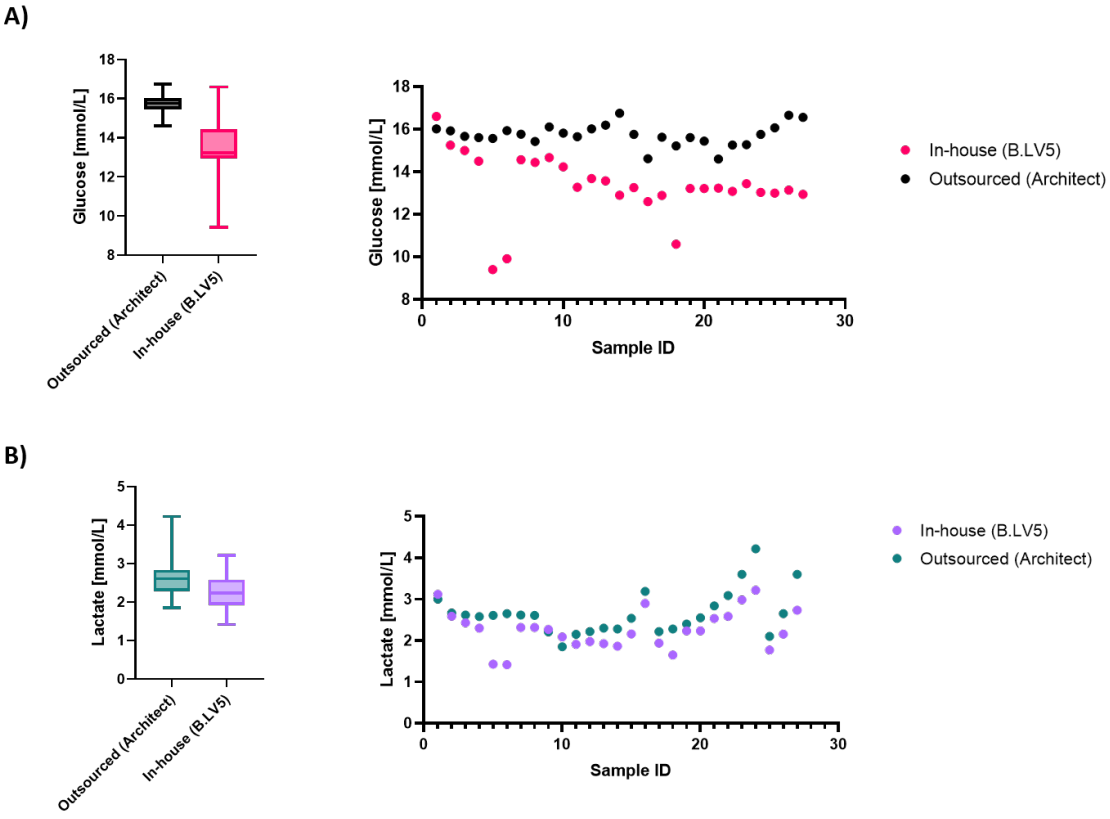

Figure 4.6: **Glucose and lactate measurements taken on outsourced (Architect) and in-house sensors (B.LV5).** A) Glucose concentrations of 27 samples presented in box plots and detailed scatter plot. B) Lactate concentrations of the same 27 samples presented in box plots and detailed scatter plot. The boxes represent values within the upper and lower quartile. The line within the boxes shows the median. The whiskers extend to the minimum and maximum value measured. A paired two-tailed t-test showed a significant difference between Architect vs in-house measurements for both glucose and lactate (n=27, p=<0.0001), and the Bland-Altman analysis shows that they consistently deliver different results (bias = 17.16%)

4.5.4 Oxygen Concentration

The results for the oxygen concentration measurements are plotted in figure 4.7. Throughout the culture period, oxygen levels dropped by a few percent for all three flow rates. For the lowest flow rate, a more pronounced drop can be seen, especially from day 1 to day 4. Overall, all three flow rates lead to similar oxygen level outcomes. Importantly, the levels did not drop to a critical level.

Looking at the normalized data, the flow rates made no significant difference. The time factor did play a significant role ($p = 0.0061$) and the matching was very effective ($p = 0.0032$).

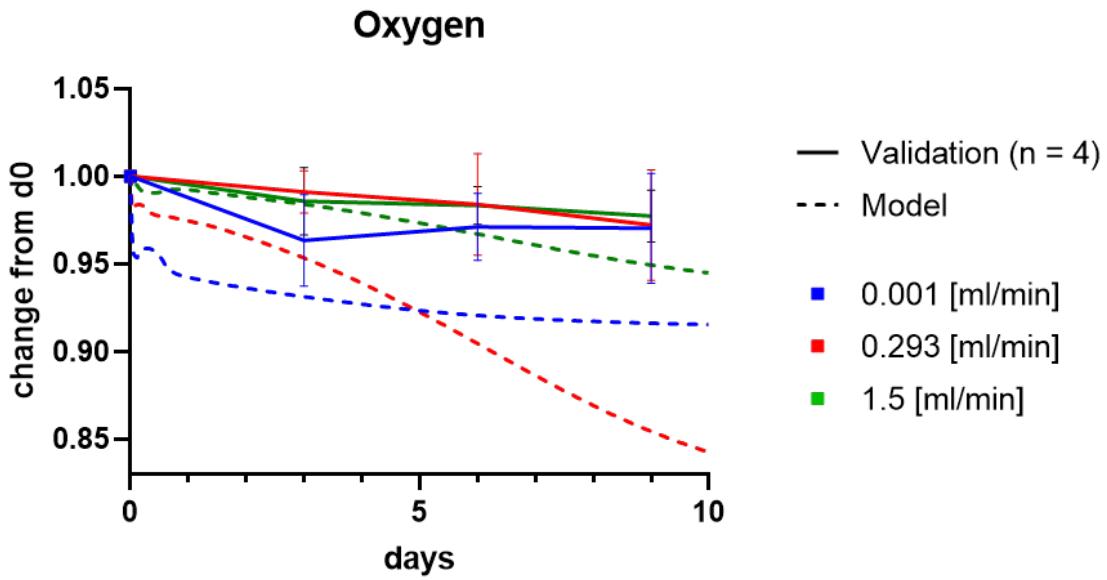

Figure 4.7: **Change in oxygen concentration over time.** Blue = low flow rate, red = medium flow rate, green = high flow rate. Solid lines = experimental results, dotted lines = respective modelling results. Error bars = standard deviation of n = 4. Analysis of the normalized data indicated that the flow rates made no significant difference. The time factor did play a significant role ($p = 0.0061$) and the matching was very effective ($p = 0.0032$). A closer view on time points between day 0 and day 1 for the modelling results can be found in the previous chapter.

4.6 Discussion

4.6.1 Validation Experiments

In this set of experiments, we explored the effect of three different flow rates on cell growth and the concentration of key nutrients and metabolites. We were able to observe small differences in cell growth for the three different flow rates. However, these were not significant and can only be treated as trends. The PrestoBlue signal dropped significantly from day 0 to day 1. The PrestoBlue signal then rises slowly but is not restored to what it was like on day 0. Indeed the problem of seemingly losing large numbers of cells from day 0 to day 1 needs further investigation, which is attempted in the next chapter.

Selecting appropriate sensors was challenging. The glucose values seem to fluctuate throughout the 10 days of culture (figure 4.4). This was irrespective of flow rates and leads us to think the variable results stem from day-to-day variations of the sensor. The manufacturer states a daily variation of up to 5% in sensitivity. This happened despite re-calibrating the sensors before every time point. It seems that there was less day-to-day variation for the Lactate measurements (figure 4.5). We can also observe this when looking at the difference between our in-house sensor's performance and the measurements taken on the Architect (figure 4.6). This does not mean that either sensor is unsuitable, but could be an indication that sensitivities for the two sensors are different, especially given the bigger range of values we obtained with the in-house sensors. It is challenging to say which one delivers better results without testing them both against a media-specific standard of known concentration. This is essentially how the calibration for our in-house sensors work, though we have not tested the same solution on the Architect. In either case both sensors seem to deliver acceptably consistent results that can be deemed good enough for our application. The Architect cSystem has been tested following Clinical and Laboratory Standards

Institute (CLSI) guidelines [292] . Measuring similar glucose levels to this sensor's measurements is therefore to be interpreted as a positive result.

Pontius et al compared the same in-house sensors (B.LV5) to a High-performance liquid chromatography (HPLC) glucose analysis among others [293]. In their study the B.LV5 sensors detected between 10 and 20mM more glucose than the HPLC did, and there was an even greater difference when the samples contained cells grown in suspension. We should note here that the group worked with much higher glucose concentrations of up to 150mM, compared to our measured 15mM. The study also found a similar time for their B.LV5 sensors' signal to settle as we did in our experiments (around 5 minutes). Overall, the study showed the B.LV5 had outstanding mechanical stability in direct contact with medium and accurate glucose quantification in the presence of various electroactive species up to 150mM glucose. We are therefore encouraged to be satisfied with the results our sensors achieved.

The oxygen measurements were challenging in that the saturation of oxygen was influenced every time the incubator door was opened. This was a necessary step to check the chambers were functioning as intended, and for taking PrestoBlue and metabolite measurements. We aimed to minimize this phenomenon by keeping the incubator door shut for a least 24 hours before the next oxygen measurement. The sensors performed well, although the inter-sensor difference was a challenge. Upon contacting the manufacturer we were assured these differences were within the specifications. We had to overcome this with data post-processing, which is never ideal. It was encouraging that in the current setup oxygen concentrations do not reach a critical level. What we did not show in this thesis is that the sensor was tested to its extremes when contamination lead to anoxic levels of oxygen, which it was able to detect. With this set of experiments we were also able to show that an oxygenation unit, which was previously used in our group, was in fact not necessary. This was also shown with the model.

4.6.2 Model's Prediction Capabilities

In the results section for the model and validation chapters we have focused on the results as stand-alone chapters so far. Now we will discuss the predictive capabilities of the model and how the results of the two compare.

The cell growth in our model is an ideal-case simplified version of a Monod-type/Michaelis-Menten kinetic equation, taking a maximal specific growth rate, a saturation constant and a yield coefficient dependent on nutrient and metabolite concentration. It therefore consists of the phases typically seen in cell growth curves; an initial lag phase, a logarithmic phase, and a plateau at which fresh nutrients and new cells enter an equilibrium. In our experiments we see a prolonged lag phase, and a more time-consuming growth phase. There were similar trends of improved cell growth for the higher flow rates and less cell growth in the low flow rates. Indeed the growth curves for the low flow rates in the model and the experiment are close together. Cell growth in the low flow rate seem to come to a halt early on in the model as well as the experiment. However, we were not able to predict the growth curves for the higher flow rates. This may have been due to the fact that;

1. the model does not consider the suitability of the matrix that cells are grown on, and other factors such as the quality of the culture medium. This has two effects; First, the model likely starts out with more cells than the experiment does. This becomes clear when looking at the data in figure 4.3. We minimized this issue by comparing the change in cell numbers over time, rather than total cell numbers. However, cells tend to grow better in the proximity of other cells. The experimental results could therefore be improved once we understand why we lose cells from day 0 to day 1, and therefore start with a more similar number of cells in the model and the experiment. Second, cells might generally

grow slower in the experiments due to their environment not being optimized, whereas the model assumes the perfect environment, regardless of the seeding efficiency.

2. the model does not consider shear stress. This will have an effect not only on cell numbers but also on cell metabolism and therefore influence the metabolic results.

3. more generally speaking, the model could benefit from several improvements discussed earlier such as a lag phase or the consideration of further metabolites such as ammonium and glutamate, which in turn will influence the shape of the cell growth curves. Nonetheless the two higher flow rates follow similar trends in the experiment and the model.

Looking at the glucose concentrations in figure 4.4, we see strong differences between the predicted outcome at the low flow rate and the one observed in the experiments. This might again be due to the fact that in reality much less cells attach than we anticipated. As a result, the cell numbers are lower from the start and consume less. The point where cell numbers rise and glucose is consumed quicker than it is delivered does not come into effect in the experiment. The model nicely predicted a steady glucose concentration for the higher flow rates.

The same principal can be applied for the poor prediction of lactate. As less cells were present to consume glucose and produce lactate, the large accumulation of lactate failed to manifest. Nonetheless, we saw the highest levels of lactate in the low flow rate for both the model and the experiment.

As mentioned, it was challenging to measure oxygen without outer influences affecting the delicate gas-mix inside the incubator. However, there was a drop over time for all flow rates. It is most pronounced in the low flow rate, less so in the medium flow rate and least so in the high flow rate. The model shows the same trend as a result of the

three flow rates. It is likely that the experimental setup was artificially being aerated through the opening of the incubator. It remains to be seen whether with a strictly closed incubator we could reach similar oxygen levels as the model. Furthermore, the error bars reach their modeling pendant. It would therefore be useful to repeat this experiment, with a larger sample size. In order to assess the predictive character of the model better, considering the drop in cell numbers *in vitro*, a parametric sweep of different cell numbers could be attempted.

4.7 Conclusions

The experiment showed that the sensors can give us a good idea of what is going on. We can also conclude that sufficient oxygen and glucose is available at all times, and that lactate accumulation is not a problem as it only starts accumulating at day 10 in the low flow rate.

The model is capable of predicting better cell growth at higher flow rates. It correctly predicted that all flow rates would lead to sufficient nutrient delivery. Furthermore it can give spatial insights over local differences in cell number as well as nutrient distribution, which we are simply not able to assess experimentally. However, the drop in cell numbers from day 0 to day 1 needs to be further investigated, as this is something we have seen across operators, different flow rates and even batch culture systems without perfusion. Once this problem is solved, this experiment could be repeated with more consistent cell numbers. Only then can we make a proper judgement over the model's prediction capabilities.

Chapter 5

Investigating the effect of scaffold design and operating parameters on cell retention, proliferation and distribution

5.1 Abstract

We have studied cell distribution following different seeding techniques in chapter 2 and noted an even cell distribution straight after seeding. In chapter 4 we have noted a sharp drop in metabolic activity from day 0 to day 1. In this chapter we investigated the reason for this drop by studying the effect of scaffold design, operating parameters and mechanical stimulation on cell retention. We found that none of the parameters investigated lead to an improvement in initial cell retention or cell proliferation over longer culture periods. RNA quantification and confocal microscopy suggested that cells detach or die between day 0 and day 1, but the reason for this detachment remains undetermined. Future work might shed more light on this phenomenon.

5.2 Introduction

Designing a scaffold for tissue engineering applications is a non-trivial task. There are a number of key requirements that need to be fulfilled by the scaffold.

The first criterion is biocompatibility of the material. This means cells must be able to adhere firmly and proliferate effectively. Cell adhesion is greatly influenced by the choice of material. On a systemic level, the construct must not elicit an immune response in the host. A strong immune response can lead to poor wound healing or ultimately rejection of the graft.

Next, the material should be biodegradable. The goal of tissue engineering is to support the body in its own regenerative powers and offer the possibility for cells to lay down their own support structures, thereby gradually replacing the scaffold. Good scaffold design aims to time the degradation with the regeneration speed, so that the tissue can heal as the scaffold is broken down. The break-down of these scaffolds has to be non-toxic and be secreted from the body without further influencing cells down the line.

In order to ensure cells adhere well to the scaffold and proliferate as expected, the scaffold's structure and topography need to be optimized. Studies have shown superior cellular responses on submicron fibrous scaffolds rather than microfibrous scaffolds. This is likely because submicron fibers mimic the structure of collagen fibers. These scaffolds also have a higher surface area and can adsorb proteins better [294]. The structure of scaffolds must allow cell penetration and even cell distribution. It also has to enable the diffusion of nutrients to the cells, and waste removal from metabolic by-products.

Mimicking not only the structure, but also the mechanical properties of the native tissue is of utmost importance, especially looking at high load bearing tissues like tendons. Scaffolds must not only withstand high forces but also stay intact during repetitive loading.

The manufacturing technique needs to be chosen wisely, as it can greatly influence the properties of a scaffold. Techniques can range from 3D printing porous cylinders, over casting flat surfaces, to electrospinning aligned filaments. Cells have shown to respond to different topographical cues by changing expression levels of proteins. The expression of type II collagen and aggrecan mRNA changed considerably following surface treatment of PCL scaffolds, compared to untreated ones where no gene expression was detected [295]. A more recent study showed differenciation of ADSCs into tenocytes was possible through topography only, without the need for growth factors or other supplements. A tenocyte shaped topography mould was produced by casting a layer of PDMS onto fixed tenocytes. The mould later served as scaffold for ADSC and lead to the expression of tenogenic markers tenomodulin and scleraxis [296]. Topographical studies however need to be interpreted carefully, as a review in 2022 highlighted large experimental biases and low quality evidence. The most challenging feature of these studies is the isolation of topography as an inducer of gene expression, while excluding other confounding factors such as changes in hydrophilicity or surface area [297].

5.3 Aims and Hypotheses

The aim of this chapter was to investigate the effect of scaffold design, media flow and mechanical stimulation on cell retention, proliferation and distribution. We hypothesize that the drop in metabolic activity is due to a drop in cell numbers, rather than a quieting of their metabolic activity. We also hypothesize that hydrophobiciy and hydrogel content of the scaffold, perfusion and mechanical stimulation have a direct influence on cell retention.

5.4 Materials and Methods

5.4.1 Interventions overview

The interventions made to the scaffold are summarized in table 5.1. These included changes to the material, structure and surface-coating. In this chapter we mainly worked with PCL. All interventions were compared to the previously used parallel PCL filamentous scaffolds described in section 2.4.1. First we modified the surface by coating the scaffolds in either TrueGel or MaxGel. Next we made changes to the topography and tested a braided structure from the same material. The next set of interventions consisted of changes to operating parameters, such as perfusion and mechanical stimulation. Uncoated and coated parallel PCL scaffolds were tested under perfused and non-perfused conditions. Additionally, uncoated parallel and braided PCL scaffolds were tested under mechanical stimulation.

Some preliminary work was also done with a different scaffold material - PDO, presented in the appendix C. That work also included mechanical stimulation.

Each intervention was tested in their effect on cell retention and cell proliferation. The mechanical stimulation was additionally analyzed in its effect on cell distribution and morphology.

Table 5.1: **An overview of the scaffolds and interventions investigated in this chapter.** It details material, structure, type of coating, media flow and mechanical stimulation

Material	Structure	Coating	Perfusion	Mechanical Stimulation	Ref
PCL	Parallel	None	x	x	Figure 5.1 A
		TrueGel	x		
		Maxgel			
PCL	Braided	None	x	x	Figure 5.1 B
			x		
PDO (Appendix)	Parallel	None	x	x	Figure 5.1 C
			x		

5.4.2 Scaffolds

Scaffolds were produced by Electrospinning. PCL solution was prepared as described in 2.4.1. PDO solution was prepared by dissolving PDO granules (Riverpoint Medical, USA) at 7% in HFIP. PCL and PDO were electrospun as described in section 2.4.1. The resulting PCL filaments were stretched to around 7x their length, while PDO filaments were stretched to around 3x their length. PCL and PDO Filaments were assembled into parallel scaffolds as described earlier (section 2.4.1). For the braided PCL scaffold we used a braiding machine [235] with 24 yarns made of 9 filament each. A short section of each of these different scaffolds is shown in figure 5.1.

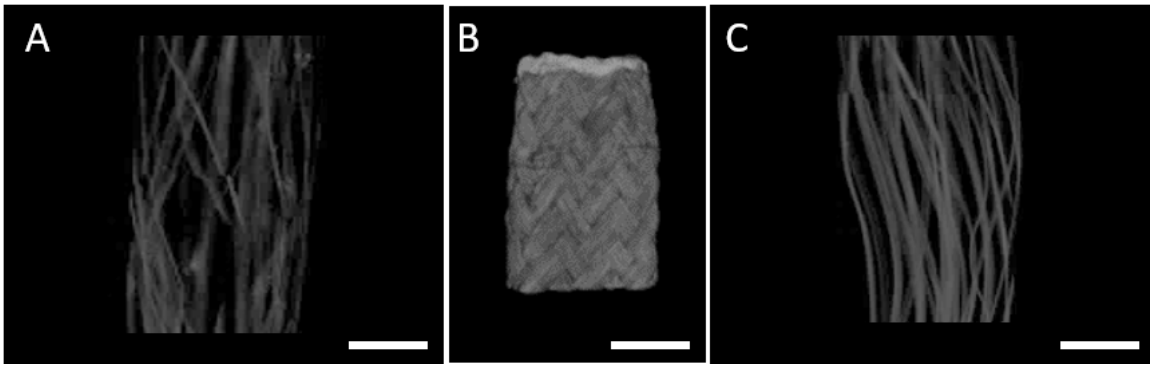

Figure 5.1: **microCT images of three different structures.** The scale bars indicate 0.5cm. A) the middle section of one bundle of parallel PCL scaffold B) the middle section of a braided PCL scaffold C) the middle section of one bundle of parallel PDO scaffold. Inside the chambers we house 5 bundles or one 3cm long braided scaffold. The parallel scaffold consist of 200 filaments knotted together at each end. The braided scaffold consists of 216 filaments tightly packed together into a braid.

5.4.3 Hydrogel Coating

PCL bundles were coated in two different hydrogels. At the cell-seeding step, the cell suspension was mixed with TrueGel (TRUE1-1KT, Sigma Aldrich, UK) or MaxGel (E0282, Sigma Aldrich, UK). Truegel is a biochemically defined hydrogel formed by mixing polymers with crosslinkers and therefore does not contain any products of animal origin that could interfere with or contaminate experiments. Maxgel is an in

vitro derived human basement membrane extracts to promote cellular proliferation. It contains ECM components such as collagens, laminin, fibronectin, tenascin, elastin, a number of proteoglycans and glycosaminoglycans.

5.4.4 Sterilization

The scaffolds were sterilized by either filling the chambers, or submerging them in 70% EtOH for 1hr, and subsequent washing in PBS.

5.4.5 Cell Culture

Cells on gel-coated scaffolds

We tested gel-coated scaffolds in chambers and well-plates. HFF-1 cells were cultured to confluency as previously described (section 4.4.3). For the chambers, cell suspensions of 250μl containing 500.000 HFF-1 cells (P17-24) were seeded together with TrueGel. For the multi-well samples we seeded 100.000 HFF-1 cells (P17) per bundle into 6-well plates. Cells were left to attach for 20 minutes, then 3mL cell culture media was added to submerge the bundles in the wells. After 1 hour, the media was refreshed and the culture period began.

Cells on different scaffold structures

HFF-1 cells were cultured to confluency as previously described (section 4.4.3).

Cell suspensions of 250ul containing 500.000 HFF-1 cells (P17-24) were seeded by injecting the chamber using 1 mL syringes with blunted needles (G18, Temuro Ltd, Surrey, UK).

Cells to analyze effect of perfusion

We used GFP-expressing mesenchymal stem cells, received by colleagues at the Institute for Biomedical Engineering to test cell retention in perfused and non-perfused chambers. Cells were thawed from a frozen vial and gently pipetted up and down before transferring them to a Falcon tube with 9 mL pre-warmed complete growth

media (DMEM (low Glucose 1 g/L)-Pyruvate-L-Glutamate (Life technologies; Cat No: 21885108), 10% FBS, 1% P/S). After centrifugation at 500 rcf x 5 min at room temperature cells were resuspended in 10mL media. Cells were plated into T75 flasks and media was changed every 2-3 days. This was work conducted by Victor Chan and Jinrong Li.

5.4.6 Cell Viability

Cell viability was measured via PrestoBlue analysis on days 0, 1, 4, 5, 6, 7 and 8 unless stated otherwise. For the chambers, this was done the same way as described previously (section 4.4.4.

For samples receiving mechanical stimulation, PrestoBlue analysis was conducted immediately before applying the loading regime.

For experiments conducted in well plates the bundles were moved into a new well first. Then 3ml of PrestoBlue mix was added and the protocol was followed as before.

5.4.7 Mechanical stimulation

Since the starting point described in chapter 1.5 we have further modified the robotic shoulder to make the movement smoother, more repeatable and consistent. The changes included a more stable base and structural changes to enable higher degrees of movement. The arm was equipped with a slot for weights, so that the forces could be adjusted more accurately.

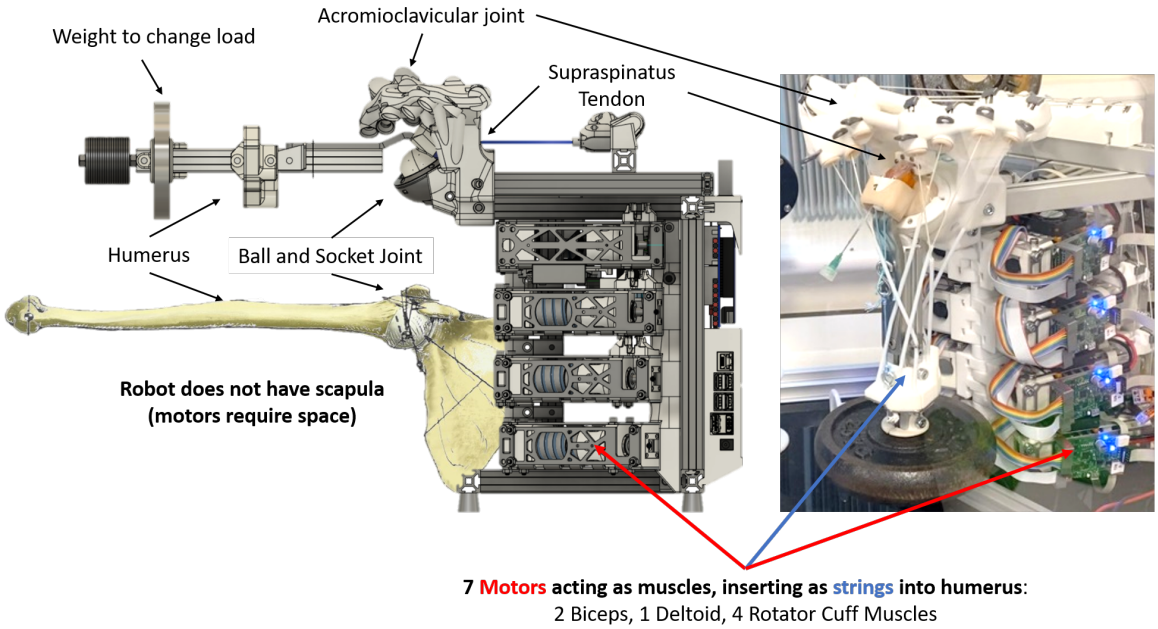

Figure 5.2: **Comparative image between human shoulder and adapted shoulder robot.** The humanoid shoulder robot was improved several times over the course of this project. The technical drawing is seen on the left, underlain with an anatomical representation of the shoulder skeleton for in full abduction of the arm comparison. To the right we show a picture of the robot with its arm in the 0-position (no abduction, no extension, no rotation). This robot has a stronger, more stable base and an adapted acromioclavicular joint. These structures ensure repeatability and smooth running of the motions applied. The robot consists of 7 motors representing 2 biceps, 1 deltoid and 4 rotator cuff muscles. Each muscle (red arrows) drives a string (blue arrow), acting as tendons, which insert into the humerus structure (pictured along the humerus in white). The ball and socket joint enables movement in 3 DOF. The SS tendon runs over the top of the ball and socket joint and inserts into the humerus. The string representing the SS tendon originates in the SS muscle/motor and is equipped with a load cell, followed by a slot for the bioreactor chamber to be tied into position, directly translating movement of these structures into the scaffold inside the chamber. The load is adjustable through the addition of weights at the end of the humerus. The robot lacks a scapula, as the anatomical location is occupied by the motors.

The parallel and braided PCL scaffolds were tested statically and dynamically. The dynamic group was put under mechanical stimulation on day 5 of culture. The loading regime consisted of a 60 degree adduction-abduction exercise (Figure 5.3. Two up-and-down movements are followed by a 5 second pause. The stimulation lasted

for 30 minutes at a frequency of 0.066Hz. This regime was developed by our PostDoc Tania Choreno Machain and is based on a number of studies analysing effectiveness and harms of exercise doses following rotator cuff injury [298, 299, 300, 301, 302], as well as previous studies conducted with the bioreactor chamber [209]. We chose this regime over others as it more closely resembles the commonly used uni-axial loading regimes.

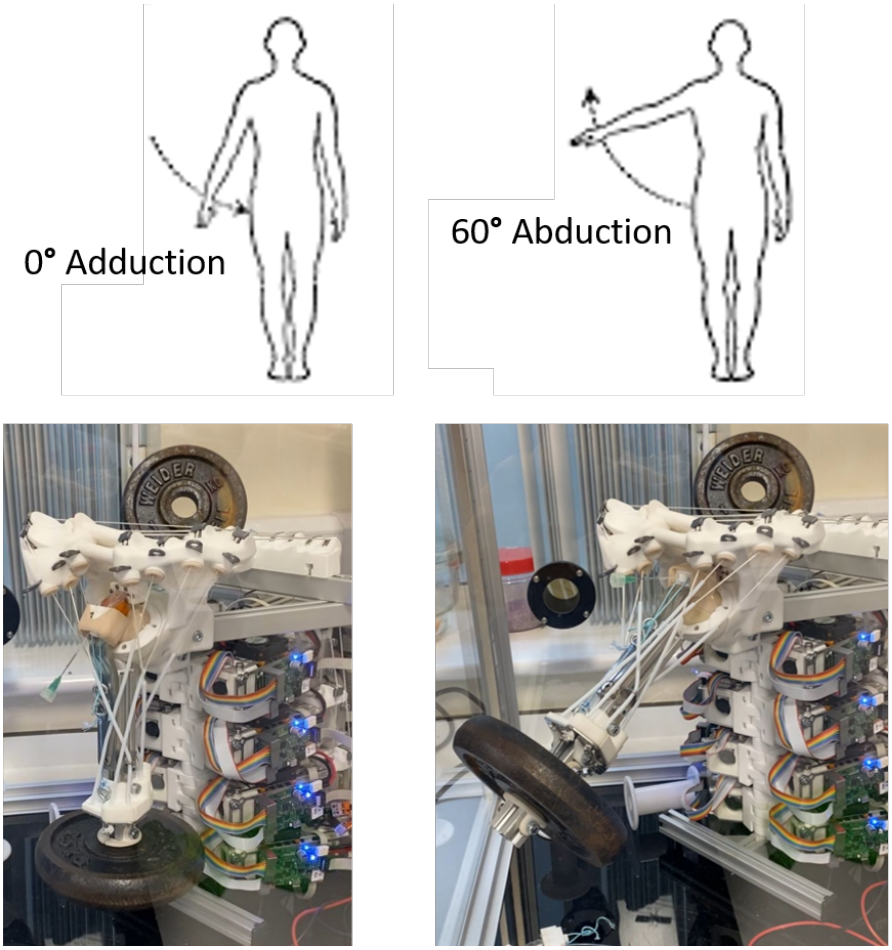

Figure 5.3: **Loading Regime applied to a chamber.** The robot lifts the arm and moves from the 0 position (no adduction) to 60° abduction. The chamber is mounted at the SS tendon location.

The chambers, equipped with needles and stoppers at the inlet and outlet, were mounted onto the robotic shoulder in the location of the SS tendon, as seen in figure 5.3. The ends of the chambers are 3D-printed and designed with a loop hole to pass

a string through. The strings were then attached to a hook on the lower end, which was connected to the humerus, and to the load cell on the upper end. The load cell itself was attached to the SS motor on the robot. The robotic arm was initialized in the 0 position, pulling all strings tight into the same position, and subsequently the regime was started.

5.4.8 Force data recording and analysis

The load cell attached to the motor and chamber measured forces every 0.1 seconds on average. Once the force data was recorded, a Matlab script with the function *findpeaks* was run to identify height, width and prominence of force peaks (Codes and Scripts C.1.5). We then calculated the average across these peaks to determine the force experienced across each repeat.

5.4.9 Cell-Scaffold harvesting

On day 8 of culture, chambers were opened and the scaffolds cut into sections. We cut along the long axis to have one half to analyze under the confocal microscope and one half for μCT analysis.

5.4.10 Confocal imaging

Samples were fixed in 2.5% gluteraldehyde for 1 hour and stored in PBS at 4°C for further use. Excess PBS was dabbed onto a paper towel and 100μl of 0.1% Triton X-100 was added to scaffolds to permeabilize the cells for 3 minutes. Samples were then washed 2x in PBS by submerging them in 6-well plates and shaking them for 2 minutes. Meanwhile Alexa Fluor 488 (A12379, Invitrogen, Waltham, Massachusetts, USA) is mixed 1:1000 in PBS. Excess PBS was dabbed off again and 100μl stain was added and incubated at room temperature for 20 minutes in the dark. The samples

were again washed 2x in PBS. Then 100μl of 1 in 1000 4',6-diamidino-2-phenylindole (DAPI) (62248, 1mg/ml, ThermoScientific, Rockford, IL, USA) stain was added per scaffold and incubated for 10 minutes. After two final washing steps in PBS, samples could be stored in PBS for further use. Samples were imaged on a Zeiss 880 Airyscan with lasers for DAPI and Alexa Fluor 488, as well as a red channel to capture auto-fluorescence of the scaffolds.

In order to further understand what causes the drop in PrestoBlue signal, I supervised two undergraduate students, Yuan (Dylan) Yeo and Victor Chan, who investigated this alongside me. This work was later continued by a visiting PhD student Jinrong Li. Chambers containing GFP-expressing MSCs were imaged on day 0 and day 1. One chamber was perfused and one was cultured without perfusion.

5.4.11 μCT analysis

We analyzed the distribution of cells following a similar protocol as described in Chapter 2. In order to avoid false positive signals through different material densities, we included control samples of the same structure and material as the different scaffolds. The threshold is then set according to the signal coming from the matching control sample.

5.4.12 RNA extraction

RNA extraction was performed using a RNA Clean and Concentrator-5 kit with DNAse treatment (Zymo Research, USA) following the manufacturer's protocol [303]. This protocol was adapted through work done previously in this group [209]. Samples previously stored frozen in TRIzol were thawed, topped up with 400μL of TRIzol and the centrifuge pre-cooled to 4°C. The sample was spun at 13000 RPM for 7.5 minutes. The supernatant was then transferred into a new 1.5ml tube, and 400 μL of 1-Bromo-3-chloropropane (BCP, Sigma-Aldrich, US) was added. Next the solution

was vortexed until it appearance was milky pink. After 5 minutes incubation at room temperature, it was centrifuged again at 13000 RPM for 20 minutes. The aqueos phase was transferred into a new tube and care was taken not to aspirate any of tthe intermediate/lower phase. If that happened, the solution was spun down again. An equal volume of 100%Ethanol was added to the new tube containing the aqueous phase. The solution is vortexed and transferred into a Zymo-Spin^{TM} IC column within a collection tube, and centrifuged for 30 seconds to discard the follow through in the collection tube. Next 400μL RNA Wash buffer is added to the Zymo-Spin column. This is centrifuged for another 30 seconds, and the follow through discarded. This process is followed by a DNAse 1 treatment. For each sample, we prepared 5μL DMAse 1 mixed with 35μL DNA Digestion Buffer in a 1.5mL tube. The DNAse mix was added directly to the column matrix and incubated for 15 minutes. Next the RNA was eluted by adding 400 μL of RNA prep buffer and ceintrifuged for 30 seconds. The follow through was discarded and 700 μL of RNA wash buffer added before another 30 second step of centrifugation. This is followed by a 2 minute cintrogugation with 400μL RNA wash buffer. Lastly the Zymo-Spin column is transferred to a 1.5mL tube and 15 μL of RNAse free water is added to the Zymo-spin tube, and centrifuged for 2 minutes to elute the RNA. RNA concentration was measured on a Nanodrop 10000 Spectrophotometer (ThermoFisher Scientific, USA). Prior to taking these measurements, a blank sample consisting of nuclease-free water was measured.

5.4.13 Statistical Analysis

For all cell proliferation analyses, data are presented as mean and standard deviation. For statistical comparison, two-way ANOVAs were performed to identify significance between each group. Statistical significance was determined at $p < 0.05$.

5.5 Results

5.5.1 The effect of gel-coating

5.5.1.1 Cell retention

Cell retention data from gel-coated scaffolds is summarized in figure 5.4. Raw data was normalized to day 0 and the change from day 0 to day 1 plotted. Cell numbers dropped by almost 50%.

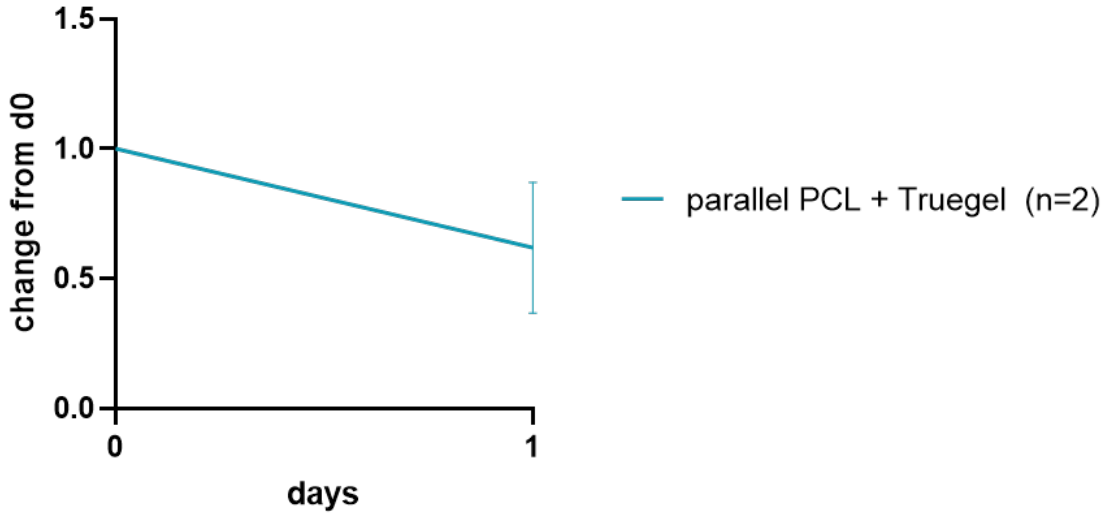

Figure 5.4: **Cell retention from day 0 to day 1 in chambers containing different scaffolds** Data is shown in change in signal over time. The error bars show the standard deviation. The flow rate was set to 1.5ml/min.

5.5.1.2 Cell proliferation

In figure 5.5 we summarize the cell proliferation data on bundles cultured in well-plates without perfusion. Cell numbers increased from day 1 and kept rising until day 14 of culture. The shape is reminiscent of the four phases of cell growth referred to in section 3.5.3. The lag phase lasts around 6 days, after which cells enter the log-phase. The stationary phase or death phase is reached around day 11. We observed no significant difference between the differently-coated samples ($p = 0.9234$).

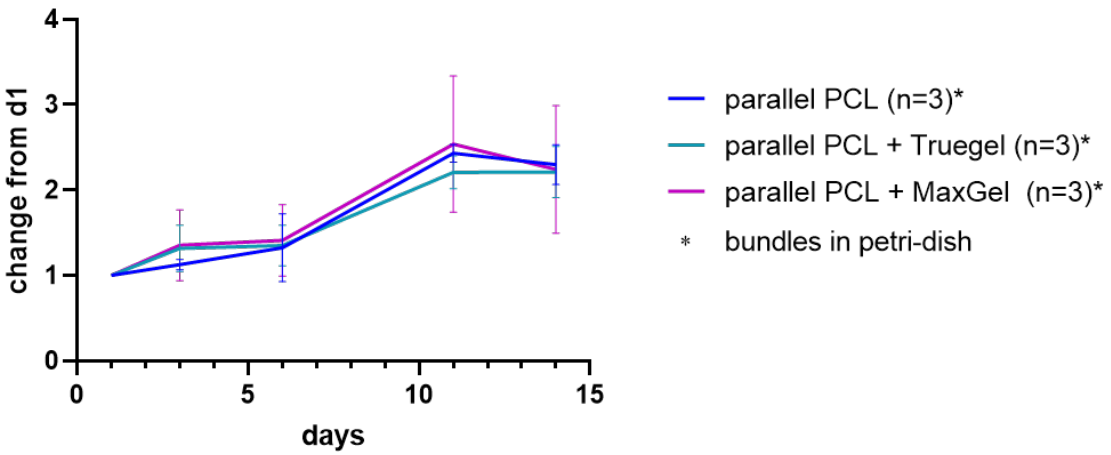

Figure 5.5: **Cell viability on hydrogel-coated scaffolds in petri-dish** We depict the change in PrestoBlue fluorescent signal from day 1, over 14 days of culture. The shape follows typical cell growth phases of lag-, log- and stationary/death phase. The error bars show the standard deviation. These samples were cultured statically (without perfusion) in petri-dishes. We observed no significant difference between the differently-coated samples ($p = 0.9234$)

5.5.2 The effect of scaffold structure

5.5.2.1 Cell retention

Parallel and braided PCL scaffolds were analyzed in their effect on cell retention from day 0 to day 1. Results are pictured in figure 5.6. Both conditions lead to a drop in cell numbers by around 50%. There was no significant difference between the two types of structures ($p = 0.1995$).

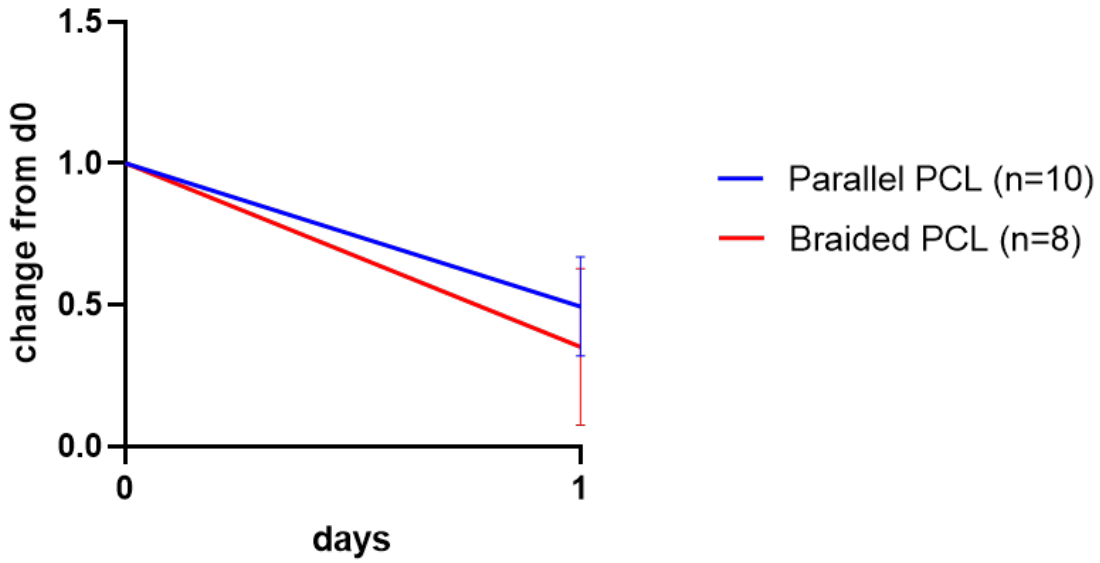

Figure 5.6: **Cell retention from day 0 to day 1 in chambers containing different structured scaffolds.** Data is shown in change in signal over time. The error bars show the standard deviation. The flow rate was set to 1.5ml/min. There was no significant difference between the two types of structures (p = 0.1995)

5.5.2.2 Effect on cell proliferation

Next we tested cell proliferation over 8 days of culture. Figure 5.7 summarizes data obtained from the PrestoBlue analysis. Here the cell numbers first dropped and started rising from day 5. This is in contrast to static samples where cells started growing from day 1 onwards. The log-phase appears to start around the same time (day 5). Culture times were not long enough to reach a stationary phase. There was no significant difference between the parallel and braided sample (p = 0.1950). We compared these results with preliminary data obtained from PDO scaffolds (Appendix C). The PDO scaffolds lead to an increase in cell numbers from day 1, but dipped again after that. At the end of culture we found more metabolic activity on the PCL scaffolds than on the PDO scaffolds. These results are statistically not significant (p = 0.9972).

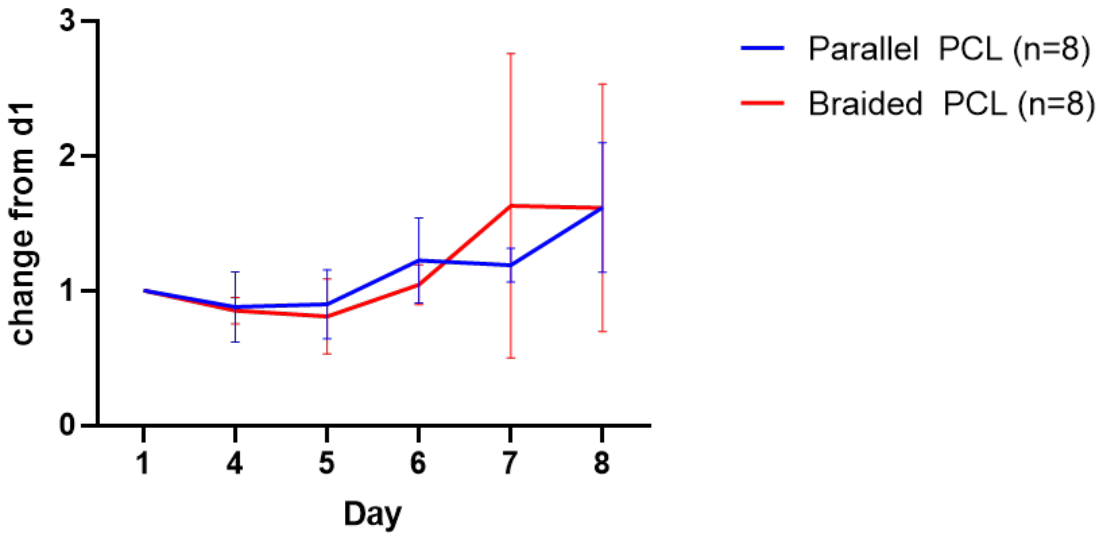

Figure 5.7: **Cell proliferation on two different scaffolds.** Data is shown in change in signal over time, from day 1, on the y-axis. PrestoBlue analysis was conducted on the timepoints shown on the x-axis. The error bars indicate the standard deviation. The flow rate was set to 1.5ml/min. There was no significant difference between the parallel and braided sample ($p = 0.1950$).

5.5.2.3 Effect on cell distribution

Figure 5.8 shows the distribution of cells along the scaffolds. Around 50% of the cells were found on one end. Cell numbers were elevated again towards the other end of the scaffolds. Barely any cells were located in the centre. Unfortunately we were not able to track the point of seeding for these samples. There was no significant difference in cell distribution between the two types of structures ($p > 0.9999$). Comparing each cell mean with each row mean (multiple comparison) showed cells accumulated in similar locations on both scaffolds (smallest $p = 0.9891$). Within a scaffold, there was a highly significant difference in the location, due to cells accumulating on one end of the scaffolds ($p < 0.0001$).

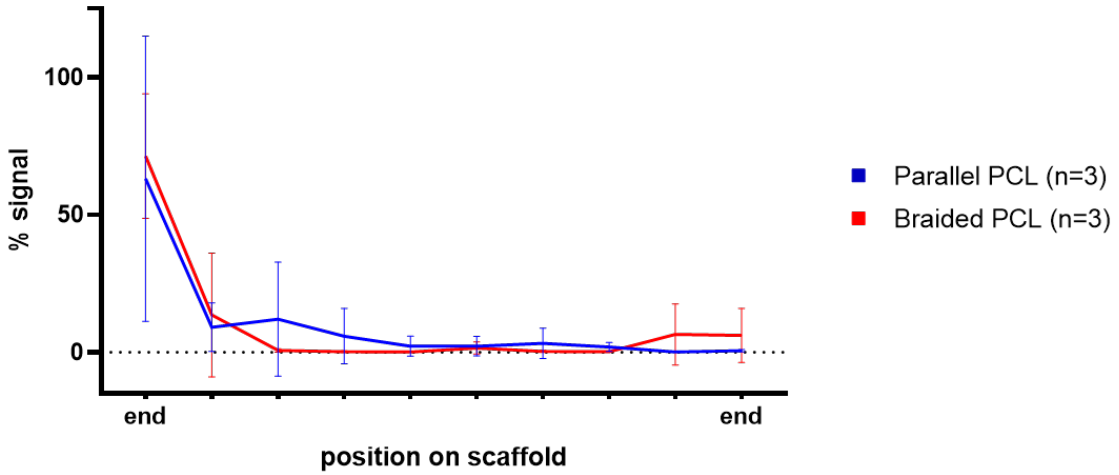

Figure 5.8: **Cell distribution in different scaffolds following μCT analysis on day 8.** The graph shows the average percentage of signal coming from 10 subsections of the scaffolds (see chapter 2). Due to the amount of samples we were not able to track which side we seeded on. We analyzed n = 3 scaffolds per condition. There was no significant difference in cell distribution between the two types of structures ($p > 0.9999$). Comparing each cell mean with each row mean (multiple comparison) showed cells accumulated in similar locations on both scaffolds (smallest $p = 0.9891$). Within a scaffold, there was a highly significant difference in the location, due to cells accumulating on one end of the scaffolds ($p < 0.0001$).

5.5.3 Effect of mechanical stimulation

5.5.3.1 Consistency of the loading regime

In figure 5.9 we depict an example of the load applied during 30 minutes of mechanical stimulation. The graph shows how the load increases and decreases as the arm moves through the different stages of the regime. During the 5 second pause, the load stays at around 4N, resulting from the resting weight of the arm. This force is highly compatible with what has been modelled for a SS tendon at rest [304, 305]. As can be seen, the load varies slightly from cycle to cycle.

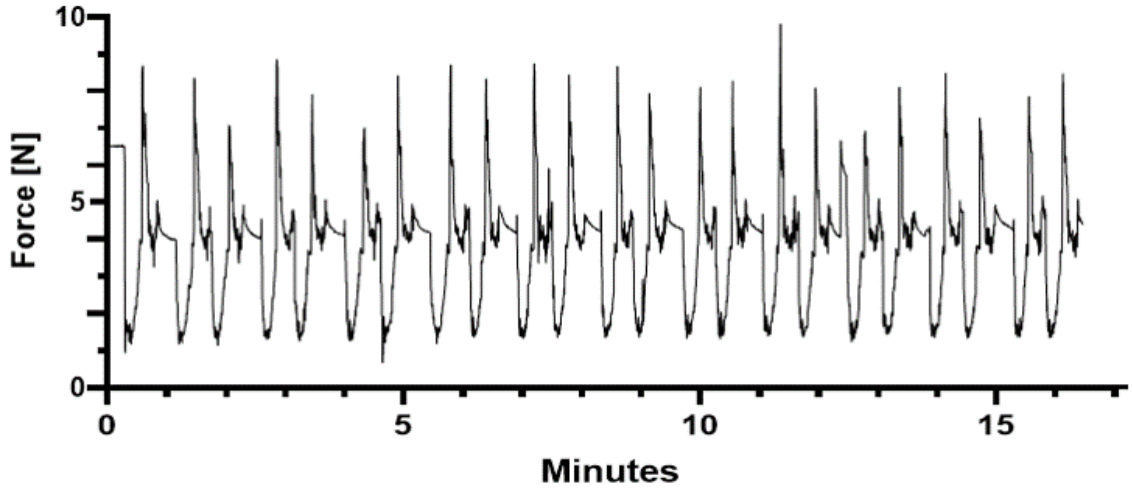

Figure 5.9: **Representative graph of load frequency resulting from loading regime.** The regime consisted of 2 up-down movements, each creating a peak, followed by a 5 second pause. The force was measured via a load cell and recorded in real time. The graph shows load applied [N] to the scaffold over the 30 minute mechanical stimulation. The force peaks at around 10 Newton.

The force also varies from day to day due to slight differences in mounting of the chamber to the arm. We analyzed the average peak force experienced across the five days of stimulation and summarized them in figure 5.10. Overall the forces applied were comparable between the two structures. A paired t-test showed no significant difference ($p = 0.2529$).

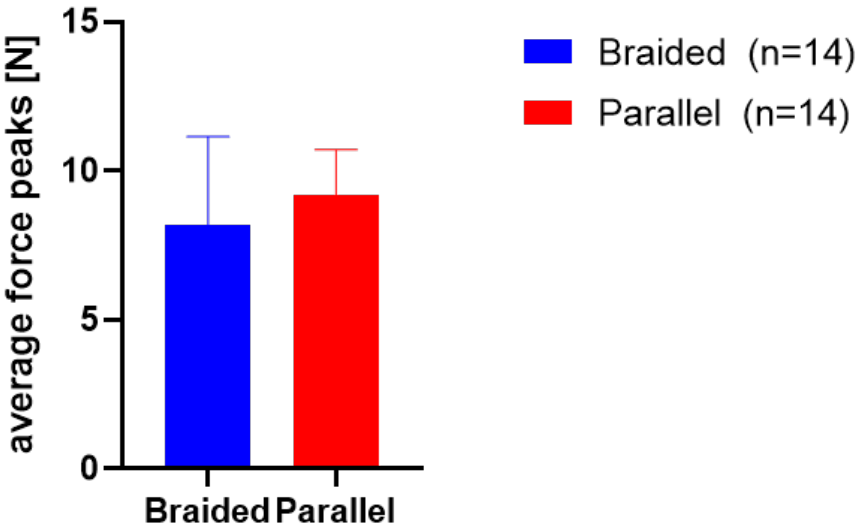

Figure 5.10: **Average force applied to the two different scaffold structures.** Samples were mechanically stimulated for 30 minutes a day over 5 days. The n = 14 is a result of 3 repeats with one day of recording missing. A paired t-test showed no significant difference in force between the two scaffolds (p = 0.2529)

5.5.3.2 Cell proliferation

Figure 5.11 shows the cell proliferation in perfused chambers following mechanical stimulation. Cell numbers start rising after the mechanical stimulation is first applied on day 5. We analyzed the difference between static (figure 5.7) and dynamic conditions. There was a short-lived significant difference between the braided dynamic sample and the static parallel sample on day 5 only (p = 0.0231). There was no significant difference between static and dynamic conditions otherwise.

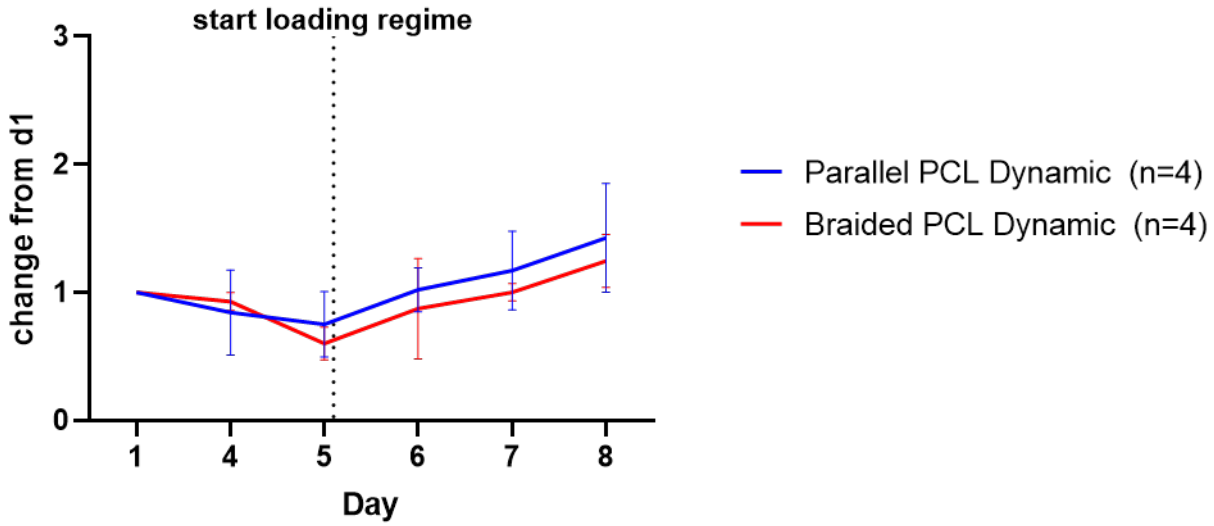

Figure 5.11: **Cell proliferation on different scaffolds following mechanical stimulation.** Mechanical stimulation was started after PrestoBlue readings for day 5 were taken. Data is presented as fold change from day 1.

5.5.3.3 Effect on cell distribution

Figure 5.12 shows the distribution of cells on scaffolds following mechanical stimulation (dynamic). Very few cells were located in the centre. The majority of cells was found at the ends. There was no significant difference in cell distribution between the scaffolds. This data was obtained from one repeat only.

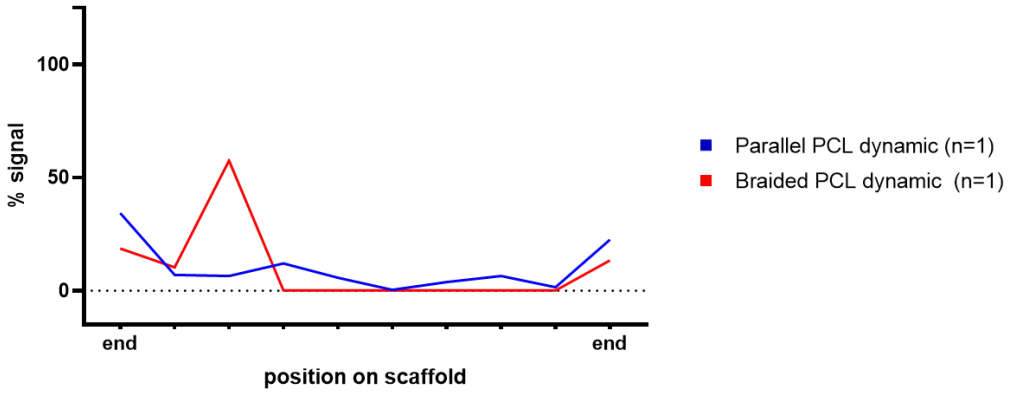

Figure 5.12: **Cell distribution in mechanically stimulated scaffolds following μCT analysis on day 8.** The graph shows the average percentage of signal coming from 10 subsections of the scaffolds. The results stem from parallel PCL scaffolds and braided PCL scaffolds. We analyzed one sample per type of scaffold in the dynamic group.

5.5.3.4 Effect on cell morphology and cell numbers

Figure 5.13 shows confocal images of cells on parallel and braided PCL scaffolds on day 8 of culture. The top row pictures the static condition and the bottom row the dynamic condition. The cytoskeleton appears in green, the nucleus in blue and some auto-fluorescence was captured in red. The cells are elongated and aligned along the scaffold's structure in all conditions. Cells on the braided PCL samples appear to grow in different directions, but follow along the braids (B1 and B2).

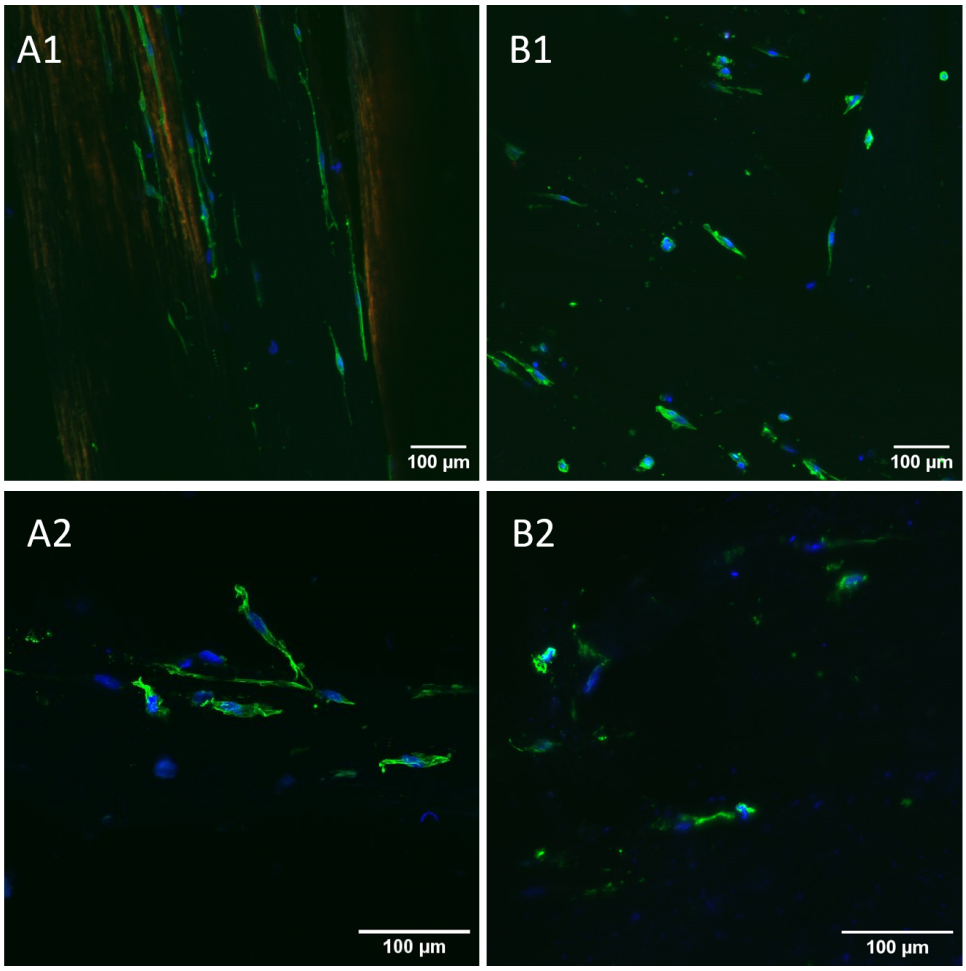

Figure 5.13: **Confocal images of cell morphology and cell numbers on three different scaffolds.** Green phalloidin = Cytoskeleton, Blue DAPI = Nucleus, Red = autofluorescence scaffold. All images were taken on day 8 of culture. Not all scaffolds showed autofluorescence. The first row represents the static condition and the second row the dynamic condition. Cell numbers were scarce with a majority of cells accumulating at the ends. Cells appear aligned along the filaments in all images. The morphology looks less uniform on the samples that were mechanically stimulated. The scale bars in the bottom right corner of each image show 100 μm. A1) Parallel PCL scaffold, not stimulated. A2) Parallel PCL scaffold, stimulated. B1) Braided PCL scaffold, not stimulated. B2) Braided PCL scaffold, stimulated

Subjectively, more cells were observed on the static samples, compared to the dynamic samples, and cells appeared more elongated on the static samples. However, it was not within the scope to quantify this. We must note that cells accumulated at the ends in all scaffolds and were low in numbers overall.

5.5.4 Effect of medium perfusion

Figure 5.14 shows GFP-expressing MSCs on day 0 and day 1, seeded onto parallel PCL scaffolds in non-perfused (A) and perfused chambers (B). The chambers contained parallel PCL. The images show cell numbers dropped regardless of perfusion. It was not within the scope to quantify this drop.

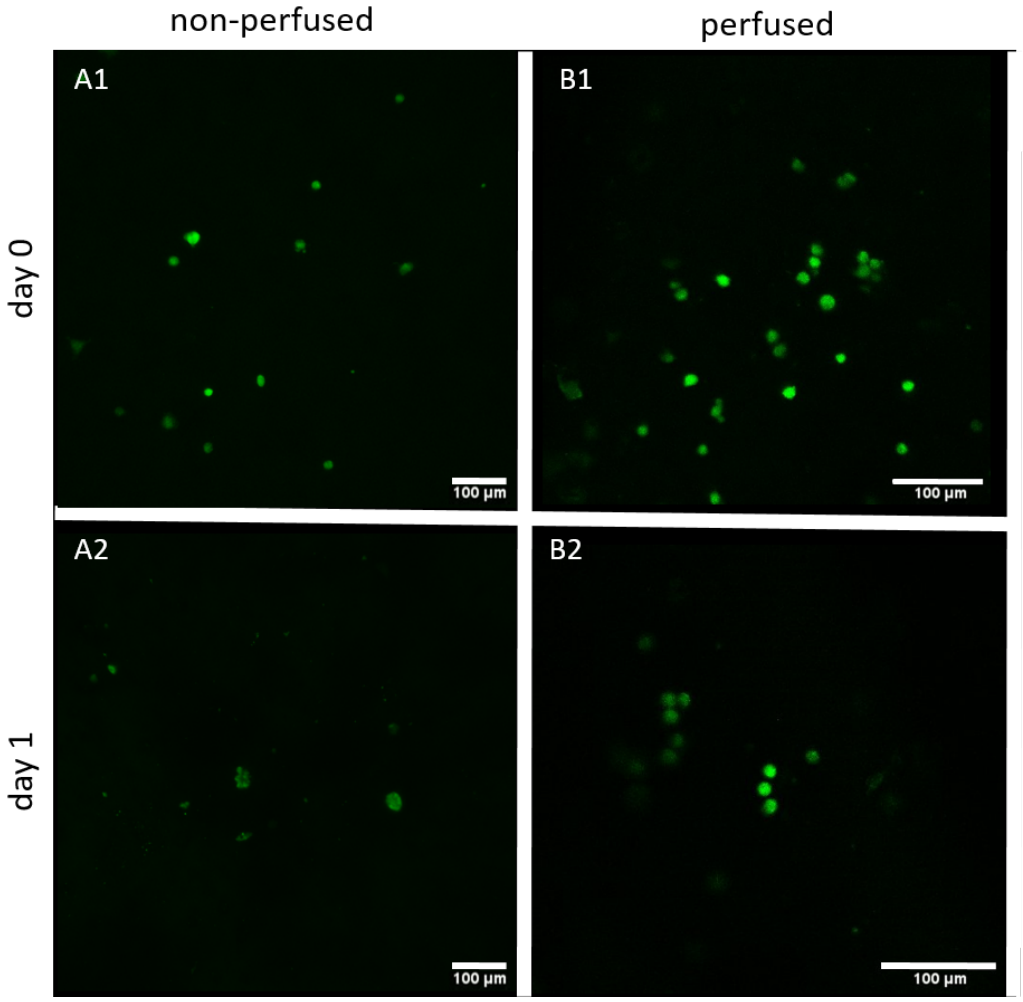

Figure 5.14: **Confocal images of cell numbers from day 0 to day 1 in perfused and non-perfused chambers.** Green = GFP expressing MSCs. The morphology does not appear elongated. Later timepoints are needed to conclude whether it takes cells longer to elongate or the cell type behaves differently. A1) day 0, non-perfused chamber. A2) day 1, non-perfused chamber. B1) day 0, perfused chamber. B2) day 1, perfused chamber. Images A1 and A2 obtained by Victor Chan. Images B1 and B2 obtained by Jinrong Lin.

5.5.5 RNA extraction

The RNA extraction results are summarized in figure 5.15. The minimum quantity of RNA required for bulk RNA sequencing was considered 50ng/μl. We were not able to extract enough RNA to analyze it further. The amount of RNA extracted, correlated well with the PrestoBlue Fluorescence values.

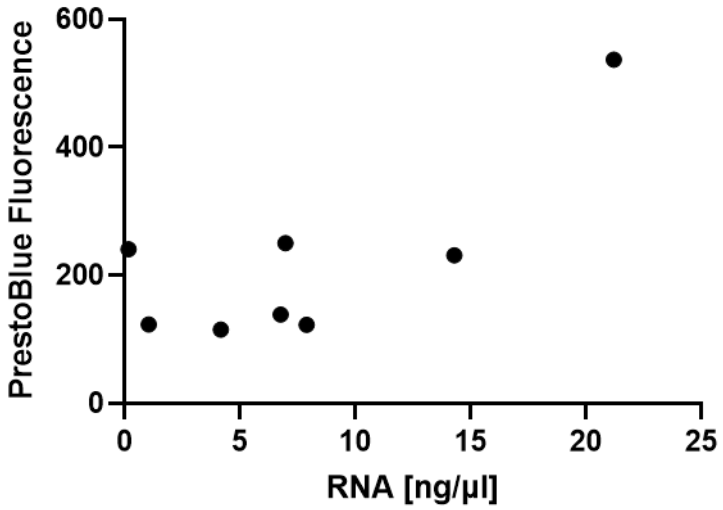

Figure 5.15: **Correlation of PrestoBlue fluorescence signal and RNA content** This graph shows there is a positive correlation between the number of cells and RNA extracted. The data for this graph was taken from a number of samples grown on paralle PCL scaffolds in chambers from the previous chapter and this chapter. r = 0.7644, p = 0.0272

5.6 Discussion

In chapter 4 we highlighted a drop in metabolic activity by around 50% in our chambers from day 0 to day 1. In this chapter we investigated the reasons behind this. According to the results from chapter 3 and measurements taken in chapter 4, we could exclude nutrient depletion and metabolite build-up as a cause.

We started with surface modifications to PCL by coating the scaffolds with hydrogels. There is some evidence that the combination of PCL and hydrogels could lead to im-

proved mechanical support while the hydrogel provided cell adhesion, proliferation and osteogenesis differentiation of BMSCs [306]. In a different study the incorporation of gelatin in a poly(l-lactic acid-co-caprolactone) (PLCL) nanofiber scaffold lead to improved adhesion and osteogenic differentiation of hMSCs [307]. A third study showed that water contact angle measurements for PCL/gelatin scaffolds indicated they were more hydrophilic [308] than PCL alone, and otherwise comparable with PLCL/gelatin scaffolds. In our experiments the addition of hydrogels had no significant advantage on cell retention, neither on bundles cultured in non-perfused petri-dishes nor inside perfused chambers. A problem for comparing our results to the literature is that not many groups report testing cell viability on day 0.

As a next step we changed the surface topography of our scaffolds from parallel filaments to braided filaments. Braided yarns have been shown to support tenogenic differentiation of human mesenchymal stem cells (hMSCs) and displayed similar mechanical behavior to native tendons [309, 310]. Our results showed the cell retention from day 0 to day 1 was similar on both topographies and had no effect on cell growth over 8 days of culture compared to the parallel scaffolds.

We mechanically stimulated both structures to see whether this would further influence cell viability, but saw no significant difference. The confocal images showed a similar elongation of cells on both types, though slightly more so in the static samples. The more elongated cells on the static samples could be an indication that cells are starting to detach and lose their aligned shape along the filaments following mechanical stimulation. Seeing as both structurally different scaffolds lead to very similar outcomes, we could argue that not structure but material was the reason for cells detaching. Studies have shown that PLLA braided scaffolds better supported ihPSC cell adhesion, elongation and tenogenic gene expression compared to braided scaffolds made from PCL. The authors put this down to the hydrophobicity of PCL and the fact that less adhesion proteins can be deposited [309]. We have highlighted the hy-

drophobicity of PCL in section 2.6. PCL's contact angle is reported to be 130° [220]. Many groups therefore blend PCL with natural polymers, thereby increasing cell adhesion, proliferation and differentiation of the seeded cells [311, 312, 313]. Another way to decrease hydrophobicity are surface modifications such as plasma-chemical etching to induce oxygen containing groups on PCL. Fibroblast cell attachment and proliferation were found to increase on plasma coated scaffolds [314]. Hydrophilicity is also improved by incorporating graphene oxide. This combination enhanced cell viability, proliferation and differentiation in a study looking at myoblast differentiation [315]. Collagen-modified PCL lead to an improved hydrophilicity of the scaffolds and an increase in the proliferation of smooth muscle cells [316]. We have not made any surface modifications that would affect hydrphobicity.

As an alternative, we tested whether a less hyrophobic material would lead to an improvement. For this we added a scaffold made from PDO, and kept the same structure of parallel filaments. PDO was first commercialized as a biodegradable suture by Ethicon in 1981 [317], and has resurfaced as electrospinning techniques were improved. It is currently used as sutures, commercial implants and in tissue engineering [318]. Tendon derived cells were reported to adhere and proliferate well on electrospun PDO mats for a period of up to 21 days [177].

Our preliminary analysis of n = 1 dynamic and n = 2 static PDO samples showed that this material lead to very similar outcomes compared to our PCL scaffolds. It did not improve cell retention, cell viability or cell distribution. This is interesting as PDO's contact angle is 32.1° and therefore hydrophilic, according to ASTM-D7334.

Next we had to look at the method we used for assessing cell viability. It is dependant on the metabolic activity of the cells. It was possible that cells were stressed and needed to adjust to the new environment, and therefore slowed down their metabolic activity. Another possibility was that we physically lose cells. The small amount of RNA extracted was the first indicator that this was true, as there was a strong cor-

relation between the PrestoBlue signal intensity and the amount of RNA extracted. Cells detaching could be due to the perfusion applied which could wash off the cells. Results presented here showed that whether perfused or not, both conditions lost cells in comparable amounts. We are however limited by the small sample size of n = 1 per condition. We can therefore not make an educated conclusion on this and further investigation is required. Other members of the group have run experiments without perfusion and observed a better cell retention. However this was conducted on MSCs and can therefore not be directly translated to fibroblasts.

We cannot exclude apoptosis as a reason for detachment either. For this, more tests are necessary. What we can deduct from the obtained images is that it is not the metabolic activity that affects the cell viability readings, but the cells detaching from the tested scaffolds.

The cell distribution data could give some insight into why cells detach. We observed the majority of cells accumulating at one end of the scaffolds. It could be that cells don't distribute evenly upon seeding, indicating that the seeding technique we use is not efficient enough after all. As full chambers are time consuming to make and come at a cost, we have looked at cell distribution upon seeding on day 0 on bundled scaffolds only. An uneven distribution upon seeding can lead to cells detaching. As discussed in chapter 2, in order for cells to thrive, they need to be able to communicate with each other. Cell density is important for cell proliferation, differentiation, and ECM synthesis. Studies have shown that a higher cell density leads to higher levels of collagen expression, invaluable for ECM generation [233, 232]. higher seeding densities also showed more aligned and elongated cell nuclei, which can lead to mechanotransduction and differentiation pathways for fibroblasts [319]. However, simply increasing the seeding density can have negative effects, such as ECM degradation, nutrient transport limitations and poorer mechanical properties [320]. Cell accumulation at one end can also be an indication of poor nutrient distribution, al-

though the model suggests otherwise and our sensors show sufficient oxygen, glucose and lactate levels. Alternatively shear stress could be acting stronger on end of the scaffold than the other, and wash cells off. We have tested eluted media straight after seeding and found no cells. However, this could mean cells detach at a later stage, between day 0 and 1. We have also repeatedly and sporadically imaged the chamber membrane, and found no cells. We have run cyto-toxicity assays on all chamber materials, and none of the materials used in this thesis were positive for cyto-toxicity.

5.7 Future Work

Future work will have to focus on understanding why cells detach from the scaffold and how to prevent it. This can be done in several ways.

1. More repeats are needed. Several interventions saw a low number of repeats, making the interpretation of this data challenging. This is especially true for perfused gel-coated samples and mechanically stimulated samples. Furthermore we have not been able to test non-perfused, gel-coated samples for their cell retention at all.

2. Further investigation into the role of perfusion is needed. A preliminary study that is not shown here investigated the effect of no perfusion on cell growth in our chambers. There was a significant difference between data obtained from perfused and not-perfused chambers. However, different cell types (fibroblasts, MSCs) were used for perfused and not-perfused chambers respectively. These cell types have different sizes, affecting the seeding outcome event at equal seeding densities. It is not unlikely they also respond differently to scaffolds. A study with the same type of cells for both conditions should be conducted. Another operating parameter to investigate is the timepoint of perfusion. Cells could be left to attach for a lot longer than the current 3 hours, potentially

enabling cells to form stronger attachments with the material. Perhaps the handling of the chambers upon seeding could be reduced. Cells are left to attach for one hour before being topped up with media, followed by a presto blue reading, followed by connection to the media circuit. The removal of the first media top-up could greatly reduce stress on cells and therefore lead to a firmer attachment.

3. The surface of the scaffold could be modified further. PCL scaffolds could be plasma-coated to enhance hydrophilicity and therefore make cells more likely to attach firmly. This could also make it easier for the cell suspension to enter the filaments at the point of seeding. Though the efficiency of the plasma treatment should be tested as plasma is known to have a low penetration and therefore low efficiency on 3D structures [181]. Other surface modifications could include dip coating [181] , etching [182], or tethering growth factor proteins to the scaffolds [183]. The electropsinning process could also be influenced by mixing self-assembling peptides (SAPs) with polymers before electrospinning [321] or blending polymer solutions [179].

4. Testing of different cell types. As introduced in the literature review section 1.3.1, different cells are being used in tendon tissue engineering. Tendons consist of fibroblast-like tenocytes, differentiated tenocytes and mesenchymal stem cells [32] which are encountered at different anatomic locations within the tendon. The fibroblasts we used in our experiments were derived from the skin. The literature suggests the same cell types derived from different tissues will behave differently in culture [159]. Preliminary results of our own experiments showed an increased cell retention for MSCs compared to fibroblasts. Stem cells have the advantage that they tend to proliferate well and have the ability to differentiate, giving us a direct insight into how they perceive their environment.

Tenocytes are fully developed and can be employed without differentiating them. However, they can still lose their phenotypic differentiation. Tenocytes can for example increase their expression of collagen type II indicating cartilage-like formations. Tenocytes have been shown to better maintain their phenotype in mechanical stimulation [322]. Cells could also be grown in co-culture. Tenocyes have been shown to promote tenogenesis of allogenic MSCs via paracrine signaling or cell–cell contact [323].

5. A different scaffold altogether. Preliminary work by colleagues have shown mixed results for decellularized pig trotter tendons. Some results showed major improvements in cell retention from day 0 to day 1, with PrestoBlue signal increasing further over time. Others showed a similar trend to what we have observed. This could be down to either the decellularization protocol, as it is non-trivial, or the quality of the obtained tendons. The group has also started work on Poly-tape, a polyester based tissue graft for ligament reconstruction.

6. The cell culture medium could be enhanced beyond the addition of FBS. Tendon differentiation markers Scx, Tenomodulin (Tnmd), Col-I and Decorin-null (Dcn) were significantly upregulated in media containing IGF-1 and TGF-beta$_3$ [324]. Whereas TGF-beta$_2$ was shown to improve TSPCs and BMCs' tenogenic differentiation [325, 326]. Ascorbic acid is a vitamin that prevents free radical formation and was shown to protect tenocytes from oxidative stress [327]. Media containing lower levels of glucose was shown to promote tenogenic marker expression and help cells cope with oxidative stress better [328]. Several proteins of the bone morphogenic protein family (BMPs) were found to be involved in tendon repair, as reviewed by Ryan et al[329]. BMP-12 is an especially promising candidate as it was the only one not involved in osteoconduction. Other growth factors such as connective tissue GF, platelet derived GF and vascu-

lar endotheial cell GF are involved in tendon healing and promising candidates [329]. The addition of growth factors will have an even greater effect in combination with mechanical loading as cells seem to really thrive in combinations of stimuli [325]. This was evidenced again by BMP-2, growth differentiation factor (GDF-5) and FGF-2 enhanced medium in combination with mechanical stimulation, leading to hMSCs' differentiation into the tenogenic lineage [310].

5.8 Conclusion

Through the various methods used in this chapter we could conclude that the decreased cell viability signal on day 1 of culture was due to cells detaching from the scaffold. The complimentary confocal images showed that this happened between day 0 and day 1. Taking what we've learned from chapter 3 and applying it to what we know from chapter 5 it looks like cells attach well in the first hour after seeding and detach anytime between then and day 1. At this point we cannot say whether cells detach due to perfusion or apoptosis. We tested several changes to our parallel PCL scaffold to improve cell retention, including surface modifications via gel-coating, topography changes by braiding PCL filaments, using a different material altogether and mechanically stimulating cells. None of these changes lead to a significant improvement in cell retention or proliferation. We suspect handling of the chamber around 1 hour post-seeding as the culprit. More work is needed and currently investigated by Jinrong Li.

Chapter 6

Conclusion and Prospects

6.1 Summary

A review of the literature identified rotator cuff tears as a debilitating problem for patients of old age and professional sportspeople. The success rate of repair strategies highly depends on the state the tendon and surrounding tissues are in. Tendon tissue engineering approaches offer the opportunity to improve the outcome of rotator cuff tears. Importantly, we identified the need for soft bioreactors to better stimulate tissues and study mechanotransduction. Soft chambers, in combination with humanoid robotic systems in particular, offer the possibility of anatomically and physiologically relevant movement. The development of such systems is a newly emerging feature which we are yet to see more of. This body of work characterized such a system and its working parts. Chapter 2 investigated seeding techniques to enable even cell distribution on our tendon-like fibrous scaffolds. This was achieved in our experiments, though should be revisited as more recent data showed that over a period of 8 days, cells distribute very differently inside the bioreactor chamber. In Chapter 3 we investigated flow rates and their impact on nutrient distribution and cell growth in a computational model. This model provides great insight into the 3D environment the

cells are exposed to and indicates sufficient nutrient delivery and metabolite transport out of the system. We identified a favourable flow rate and could confirm its effect in Chapter 4. Through the set of validation experiments we identified several shortcomings and ways to improve the presented model. Future work will implement a few of the suggested changes to the model and improve our understanding further. Chapter 5 dealt with the challenge of low cell viability on day 1. This chapter would particularly benefit from a higher number of repeats, to draw a full conclusion. The results showed, cells likely detach in between the first hour and the first day, indicating handling of the chamber post-seeding as the culprit. This is currently being investigated.

6.2 Scientific Contributions

This thesis contributes to the newly evolving field of soft bioreactors for multiaxial mechanical stimulation, and in a wider context to tissue engineering and regenerative medicine. The potential future of these bioreactors is multi-faceted and highly promising. The main implication of this work consists in highlighting the bioreactor's current shortcomings and the identification of next steps necessary to improve its performance. The conducted experiments have contributed in the following ways:

1. Cell seeding on untreated filamentous PCL scaffolds is driven by the capillary effect rather than the cell seeding method. We established Osmium tetroxide staining and subsequent image analysis as an effective tool to determine cell location in 3D on large scaffolds.

2. The computational model provides insight into a myriad of matters. It can determine nutrient concentrations under many different flow rates and their influence on cell growth. It is able to show 3D nutrient and cell distributions. The influence of a permeable membrane, as well as stopping the media flow

and the effect of these on oxygen levels can be determined, without the need for expensive and time-consuming experiments. The validation experiments confirm that the model performs well, but could be improved with the work suggested.

3. Sensors for nutrient and metabolite monitoring can affordably be integrated into our system and deliver robust results without the need for external measurements or large scale, costly equipment.

4. Low values in cell viability on day 1 post seeding are not due to cells undergoing a state of metabolic quiescence, but physically detaching from the scaffold. The reason remains undetermined though gel-coating, changes to PCL topography changing the material altogether and mechanically stimulating them does not lead to improvements.

6.3 Advantages and Future Opportunities created by the HBR

6.3.1 Independence from external actuation system

Our soft chambers can be detached from the actuation system, increasing their versatility. Being able to remove the chamber from the actuation system has several advantages. Handling of the chamber and construct is much easier and enables non-invasive monitoring of the cells such as viability assays or microscopy. The whole system is much smaller, the actuator can stay outside the incubator and the chambers can stay inside during rest periods, taking up minimal space, allowing for more repeats or other experiments to take place in the same incubator. Removing the chamber from the actuator makes it compatible with commercially available actuation systems, making this a highly customisable platform.

6.3.2 Reduced volume of medium

As the largest part of the system is usually the actuator, and because traditional rigid systems cannot be detached as easily, the volume of media required to fill that space is proportionally larger. Soft chambers can greatly reduce the amount of media needed and therefore reduce the cost.

6.3.3 Oxygen transfer through soft walls

A challenge greatly underestimated is the adequate delivery of oxygen [263]. The materials used in hard shell bioreactors are rarely permeable to oxygen and therefore rely on a layer of air above the media to enable gas exchange, or a media reservoir open to the environment. Unless properly filtered, this is a source of contamination. The materials suggested for soft chambers are variably permeable to oxygen and therefore passively enable gas exchange without the need for ventilation systems or alike. This provides a more sterile surrounding and creates more opportunity for oxygen to be circulated. Furthermore, perfusion through flexible chambers has lead to wave-flow, resulting in higher oxygen transfer. This effect was more efficient than commonly observed oxygen diffusion through whirlpool flows in shaker flasks [330].

6.3.4 Real time monitoring of cell growth

Mechanical stress bioreactor system capable of non-invasively imaging cells have been developed [201, 204]. In these systems, microscopy was a feature that had to be built-in via viewing windows, while not interfering with the actuator. This made multiaxial stimulation impossible. Soft chambers as presented here, offer the opportunity for real time monitoring of cell growth through the transparent membrane.

6.3.5 Future Opportunities

The humanoid bioreactor platform can serve different purposes in the future. It can be used as a material testing platform to test newly developed biomimetic patches for shoulder augmentation. Different structures, such as woven or braided, as well as different materials, such a synthetic, decellularized or ECM-based, can feasibly be mounted in the bioreactor chamber and tested regarding their mechanical strength, cell viability and infiltration as well as their suitability for ECM remodelling and tissue regeneration following mechanical stimulation. This is currently investigated by Hanif Nadhif, a DPhil student in our group. The implication of the HBR as a materials-testing platform is that we will be able to screen a large variety of potential patches a lot faster. Furthermore, animal studies often fall short in replicating the human anatomical environment. Specifically regarding the shoulder, as bipeds' rotator cuffs differ significantly from quadripeds' and even most bipedal primates [9]. Despite this fact and due to ethical issues and high feeding costs of suitable primate models, the majority of animal models for patch testing are conducted in rat, while biomechanical, performance and rehabilitation tests are performed in rabbit, canine, sheep and goat [331]. The HBR providing much greater human anatomical relevance, could not only bridge the gap in suitable models but also reduce the number of animal studies.

Our soft chamber differs fundamentally from traditional hard-shell bioreactors, which enables the construct to be stimulated in multiple directions. Complex motions such as torsion, compression and multiaxial tension can be applied. This is vital as more and more evidence shows that multiaxial stimulation leads to different outcomes over uniaxial stimulation. Multiaxial stimulation will also lead to the fluid being pushed around the construct, a phenomenon observed *in vivo* in tendons and synovial fluid. This enables us to mimic physiological conditions better. Platforms to apply multiaxial stimulation have been scarce. An important question that needs to be answered

is whether multiaxial stimulation affects cells differently than uniaxial stimulation, and how. Current literature suggests it does, but due to the lack of suitable platforms has insufficiently been studied. Applying this type of stimulation will help further our understanding of cells responding to mechanical stimulation, making it a great platform for mechanotransduction studies of different cell types. Dr Tania Choreno Machain, a Postdoc, in our group is currently investigating this. The implications of better mechanotransduction studies are plentifull and highly promising. The identification of new drug targets for muskuleskeletal diseases requires a profound understanding of the pathways involved in stress-sensing. Furthermore, additional knowledge in this field has a potential knock-on effect to other force-sensing organs such as the ear/auditory system [39]. Mechanotransduction studies can improve our understanding of developmental biology and related birth defects. Our ability to sense mechanical forces on the cellular level is a direct manifestation of how our bodies are constructed [39]. We will better understand healing and pathology in an architectural context. Conditions of the joints such as Ehlers Danlos Syndrome, Osteoarthritis and Rheumatic diseases will greatly benefit from this as well. Mechanotransduction highlights the ability of tissues to adapt, but the HBR platform will also enable us to study fibrotic mechanisms and responses to pathological load. What are they, how are they triggered, how to avoid them and how to best support the body in its natural responses. Along those lines our platform enables the direct investigation of healthy and diseased tissue, to get a better understanding of disease mechanisms of conditions such as tendinopathy or frozen shoulder. Furthermore we can study healing mechanisms through mounting partially teared tendons. Another implication is the testing of existing or emerging drugs under more physiologically relevant conditions of multiaxial stimulation.

As we envision this platform, it is a useful tool for physiotherapy, providing the potential to improve our understanding of different movement and loading regimes on

a healing tendon. The robot has adjustable weights, making it a more personalized platform for patients of different sizes. It could also informs about the benefits or drawbacks of weight-exercises versus body-weight only exercises. There is still debate about the time point at which physiotherapy should start post-surgery. This is another question that can easily be addressed by the HBR.

The application of the soft chamber presented in this work has the potential to be expanded onto other tendons in the shoulder. The chamber will straight forwardly be mounted in a different location matching the anatomical site of the tendon of interest. The same way the shoulder robot could be used with ligaments in mind. The shoulder robot used here is part of a whole-body humanoid robot. With different parts of the robot, the chamber could explore other locations in the body altogether such as the foot, fingers or the knee. The system could also easily be modified for cartilage/meniscus tissue engineering approaches.

The expansion from one soft component to several is a truly exciting feature currently under development in our group. Soft sensors which can be integrated into the scaffold and measure strain from within are being developed and tested by Dr Zekun Liu, another Postdoc in the team. This will lead to ever improving sensors capable of capturing accurate force measurements localized in the tissue or scaffold.

Soft chambers could function without external actuation systems altogether by further combining them with soft actuators, making the system entirely independent of rigid structures. There are potential complications in detaching the tissue construct from the soft actuator, and other unforeseen ones, and soft actuators need to be further developed to enable more physiologically relevant movements. Humanoid robots are one step ahead in this case.

6.4 Conclusion

The aim of this thesis was to characterize the performance of a novel flexible bioreactor system for mechanical stimulation. Traditionally bioreactors focus on uni-axial or bi-axial stimulation only, and cannot currently replicate the micro-environment of the tissue in question. The HBR has the ability to stimulate cells in a multiaxial fashion. Its soft flexible membrane leads to a more natural movement of the fluid/media around the construct. We have characterized this system in terms of cell distribution, nutrient delivery, distribution of nutrients and waste-product removal, cell proliferation, cell retention and mechanical stimulation. We have shown that the bioreactor chamber is capable of sustaining cell growth over 10 days and providing mechanical stimulation. This work demonstrates the proof of concept of the bioreactor chamber and identified a plethora of future work. Overall, we have further characterized the bioreactor chamber, improving our understanding of it, leading to its further development as a platform to study mechanotransduction, patch/graft development, disease and healing mechanisms and further tissue engineering opportunities.

Appendix A

Chapter 2

A.1 Micro-CT signal interference

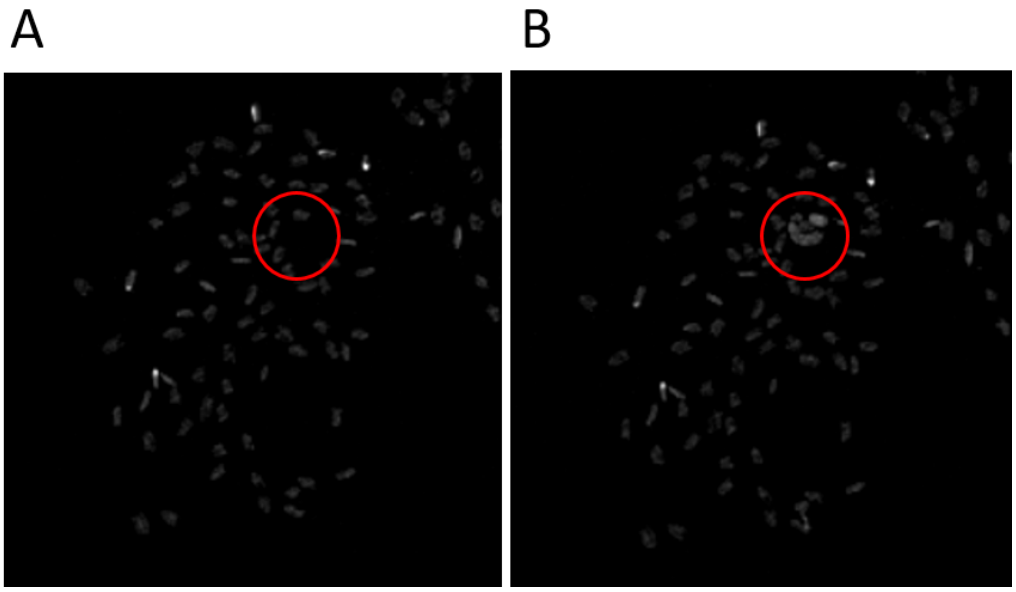

Figure A.1: **Example of signal interference on μCT.** A) shows a cross-section of filaments. B) shows the cross-section a few images down where filaments appear to have merged in higher intensity. The images were taken from Upright repeat 3 section 1.5-1.8 as referenced in Table 2.1

A.2 Micro-CT image post-processing

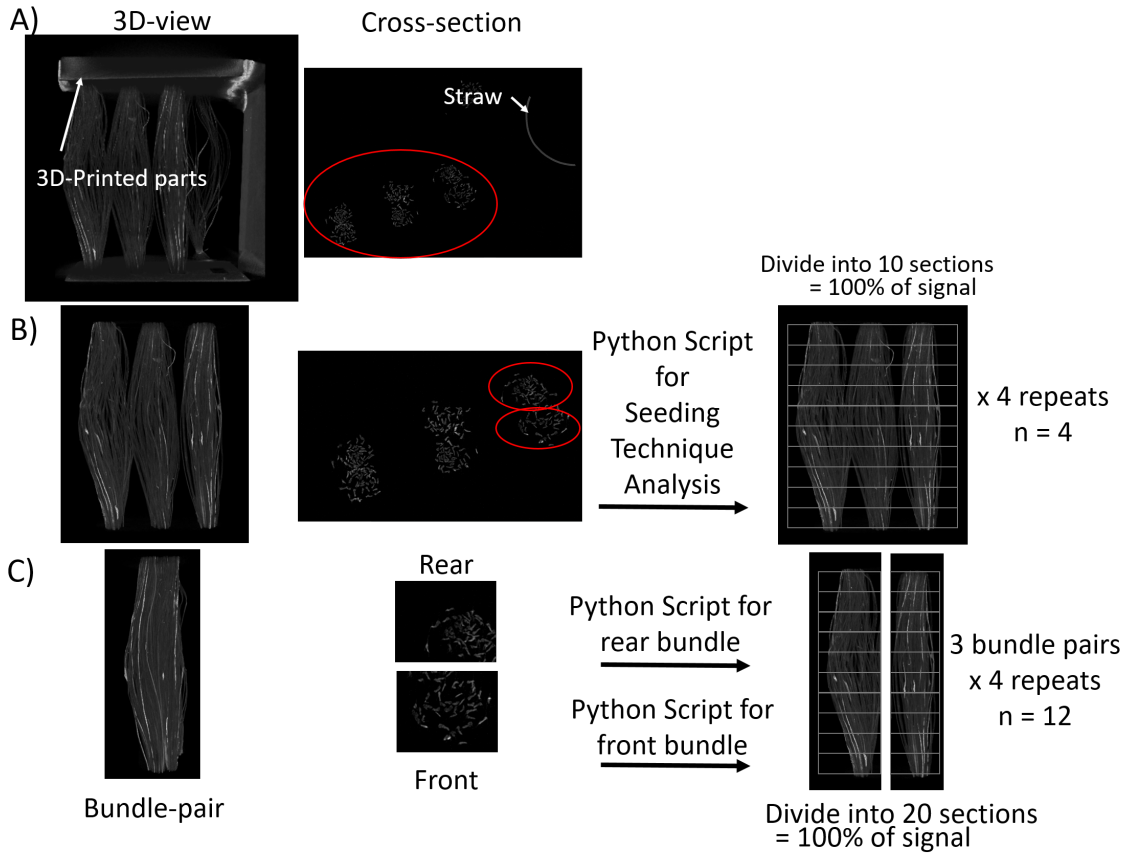

Figure A.2: **Flow chart of μCT image post-processing.** A) 3D-view and cross-section of the obtained images. Potential obstructions and signal interference is removed by drawing a region of interest (red circle) around bundles only. 3D printed parts and support structures such as a straw are therefore removed. B) Resulting images after the first post-processing step. From here, images can be fed into the python script to analyze all six bundles (triplicates) at once. The results are grouped into 10 sections. C) New regions of interest are drawn to analyze cell distribution between the front and rear bundles. Both sets of images are fed into the python script and the results grouped into 20 sections.

A.2.1 Python Script

```
from PIL import Image
import numpy as np
import csv
# ----- EDIT ME PLEASE ----------------
results_file = 'PvB_4_P2.csv' # title of .csv file for data
filename_base = 'PvB_5_P2_VOI_'# filename base of images
filename_ext = '.tif'   # file extension of images
start = 189 # number of image (following VOI_), in case of 0541, the
    0 is added by the script
end = 2189
threshold =106 #threshold found manually is added here
# -------------------------------------------------
def make_cell_count_csv(filename_base, filename_ext, start, end,
   threshold):
    results = []
    for i in range(start, end + 1):
        image_name= filename_base + str(i).zfill(4) + filename_ext
        try:
            image_tiff = Image.open(image_name)
        except:
            continue
        imarray = np.array(image_tiff)
        cells = np.where(imarray >= threshold, 255, 0)
        unique, counts = np.unique(cells, return_counts=True)
        counts_map = dict(zip(unique, counts))
        results_dict = {}
        results_dict['Filename'] = image_name
        results_dict['Number of Voxels'] = counts_map.get(255, 0)
        results_dict['Percentage above threshold'] = counts_map.get
   (255, 0) / cells.size * 100
        results.append(results_dict)
```

```
29      with open(results_file, mode='w',  newline='') as csv_file:
30          fieldnames = ['Filename', 'Number of Voxels', "Percentage
    above threshold", '', 'Threshold']
31          writer = csv.DictWriter(csv_file, fieldnames=fieldnames)
32
33          writer.writeheader()
34          writer.writerow({'Threshold': threshold})
35          for result in results:
36              writer.writerow(result)
37  if __name__ == '__main__':
38      print('running...')
39      make_cell_count_csv(filename_base, filename_ext, start, end,
    threshold)
```

Macros and Codes A.1: Python script used to identify pixels above a threshold.

Appendix B

Chapter 4

B.1 Pump Calibration

The governing equation for the peristaltic pump looks as follows:

$$Q = VNR \tag{B.1}$$

where: Q is the Volumetric flow rate, V is the pillow Volume, N is the Number of rotors and R is the Rotation speed per minute. The pillow volume depends on many things but can be approximated as a cylinder.

$$V = \pi r^2 h \tag{B.2}$$

therefore

$$Q = \pi r^2 hNR \tag{B.3}$$

The variables π, h and and N are constant. Once the two input variables Q and r are set, rotation speed per minute R is also constant.

It follows

$$Q = Cr^2 \tag{B.4}$$

On the pump in use, it is not possible to set different flow rates to run in parallel. However, if we set the input values (tubing diameter and desired flow rate), and mount tubes with different diameters, the flow rate will be affected according to the continuity equation:

$$\frac{Q_1}{r_1^2} = C = \frac{Q_2}{r_2^2} \tag{B.5}$$

If the pump is set to a certain flow rate Q_1 and tubing radius r_1, mounting a tube with a different radius r_2 will have the following effect on the resulting flow rate Q_2

$$Q_2 = \frac{r_2^2 Q_1}{r_1^2} \tag{B.6}$$

In order to test this, the pump was equipped with different size tubings, namely 1.6 and 0.64mm inner diameter (ID). We then set the ID on the pump to 0.64mm, set the flow rate to 0.5, 0.1 and 0.25ml/min.measured the volume of both tubes after two minutes(B.1. The resulting water was collected and measured. This was done three times for each input flow rate. The smaller tube over-performed and delivered more volume than predicted, The larger tube under-performed and delivered slightly less volume. The results are collected in B.1. Overall we were happy with these results and continued.

Table B.1: Pump and tubing diameter calibration. Predicted and measured volumes at different flow rates in two different sized tubes

Q_1 [ml/min]	0.5		0.1		0.25	
ID [mm]	1.6	0.64	1.6	0.64	1.6	0.64
measured volume [ml]	3.00	0.54	0.62	0.13	1.50	0.31
predicted volume [ml]	3.13	0.50	0.63	0.10	1.56	0.25
% difference	4%	-7%	1%	-21%	4%	-19%

Appendix C

Chapter 5

C.1 Effect of PDO

C.1.1 Effect on Cell Retention

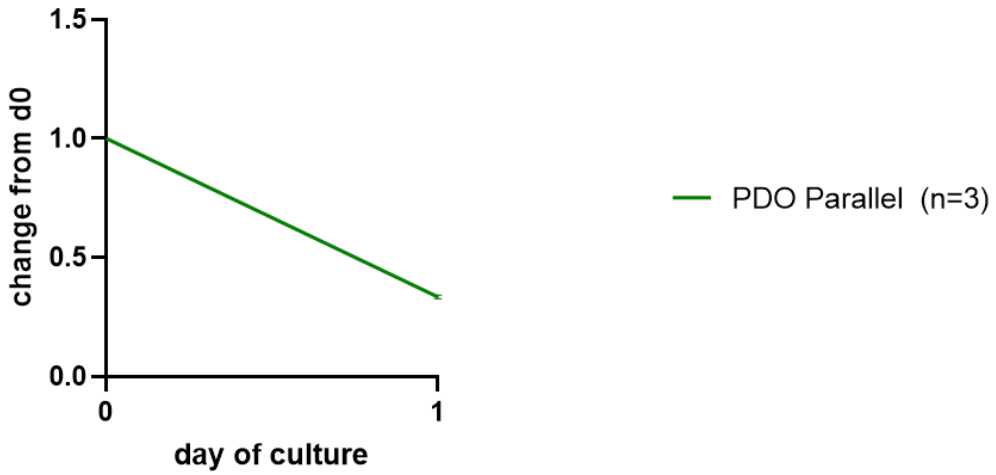

Figure C.1: **Cell retention from day 0 to day 1 in chambers containing PDO scaffolds** Data is shown in change in signal over time. The flow rate was set to 1.5ml/min. The error bars show the standard deviation

C.1.2 Effect on Cell Proliferation

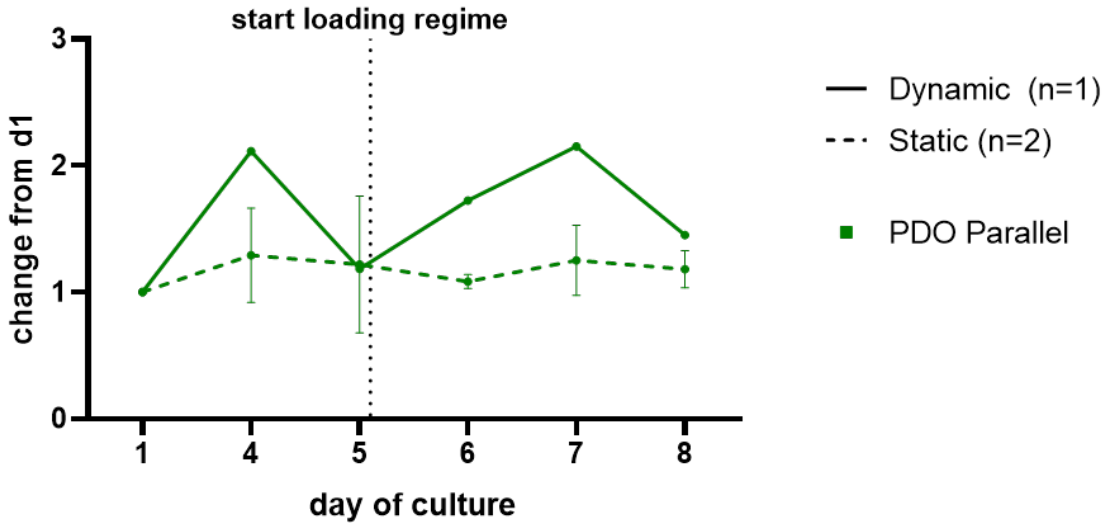

Figure C.2: **Cell proliferation on PDO scaffolds.** PrestoBlue analysis were conducted on the time points shown on the x-axis. Data are shown as fold-change from day 1 on the y-axis.

C.1.3 Effect on Cell Distribution

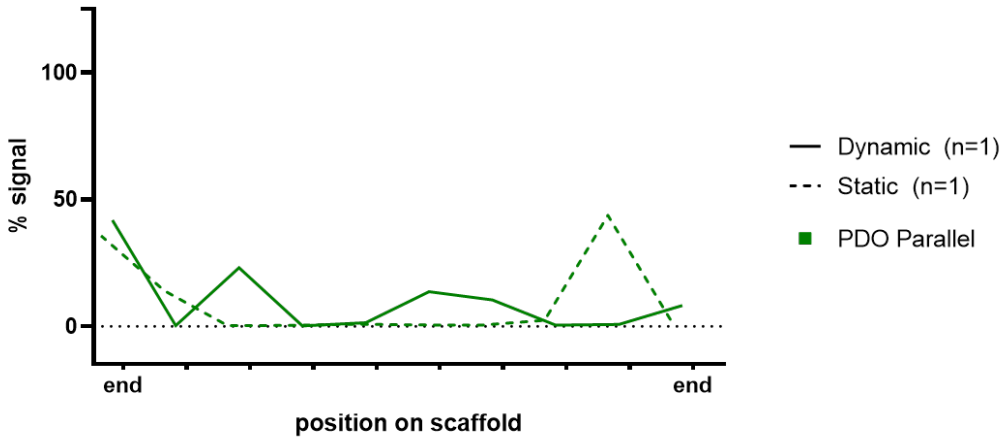

Figure C.3: **Cell distribution in different scaffolds following μCT analysis on day 8.** The graph shows the average percentage of signal coming from 10 subsections of the scaffolds. The results stem from parallel PDO scaffolds. Due to the amount of samples we were not able to track which side we seeded on

C.1.4 Effect on Cell Morphology

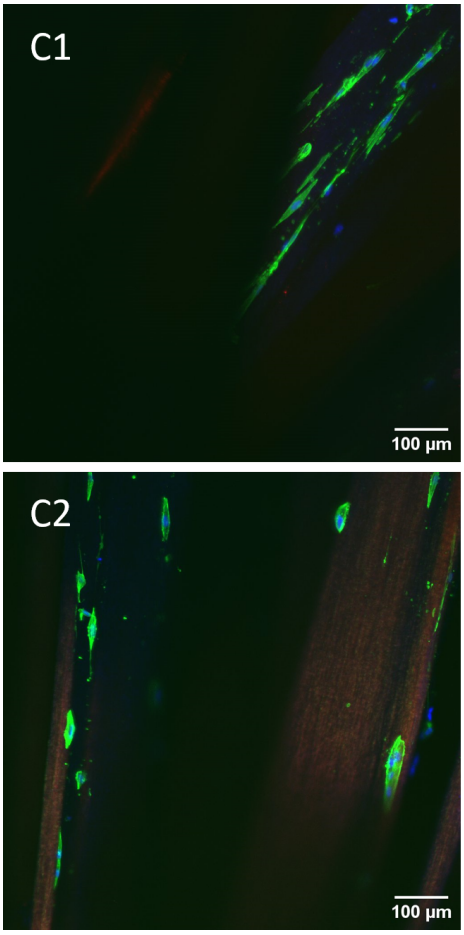

Figure C.4: **Cell morphology on day 8 on PDO scaffolds following no stimulation and mechanical stimulation** Mechanical stimulation as described in section 5.4.7 started on day 5 of culture and consisted of 30 minutes of adduction abduction movement up to 60°. The cytoskeleton was stained in green with phalloidin and the nucleus was stained in blue with DAPI. Cells appear elongated along the PDO fibres. C1) Samples that did not undergo mechanical stimulation. C2) Samples that underwent mechanical stimulation. Subjectively cells look slightly more rounded on the dynamic samples

C.1.5 Findpeaks Script

```
% To create output files automatically (ty Peter Johnson):
mfilePath = mfilename('fullpath');
folderPath = fileparts(mfilePath);
outputFolderPath = strrep(folderPath,'input','output');
allFiles = dir(fullfile(folderPath,'*.csv'));
fileNumber = size(allFiles,1);
outCell = cell(1, fileNumber*4);
%% Set up the Import Options and import the data
for i = 1:12 %reads alphabetically the first file and all files, 1:3
    would read the first three
    outStr = strcat("Calculating file: ", num2str(i));
    disp(outStr);
    fName = allFiles(i,1).name;
    datatable = readtable(fName, 'ReadVariableNames', false);
    numRows = height(datatable);

    opts = spreadsheetImportOptions("NumVariables", 5);
    % Specify sheet and range
    opts.Sheet = '';
    % opts.Sheet = "pnB4G0Ae";
    dataRangeStr = strcat("A2:E",num2str(numRows));
    opts.DataRange = dataRangeStr;
    % Specify column names and types
    opts.VariableNames = ["timestamp", "axis1_pos", "axis0_pos", "
   force", "axis2_pos"];
    opts.VariableTypes = ["string", "double", "double", "double", "
   double"];
    % Specify variable properties
    %opts = setvaropts(opts, "timestamp", "WhitespaceRule", "
   preserve");
    %opts = setvaropts(opts, "timestamp", "EmptyFieldRule", "auto");
```

```
28      opts.VariableOptions(1,1).WhitespaceRule = "preserve";
29      opts.VariableOptions(1,1).EmptyFieldRule = "auto";
30      %[file,path] = uigetfile({'*.csv';'*.slx';'*.ods';'*.*'},...
31       %                          'File Selector');
32      % Import the data
33      cmdstr = sprintf('tdata = readtable("%s%s", opts, "UseExcel",
    true);',strcat(folderPath,"\"),fName);
34      eval(cmdstr)
35
36      %% Clear temporary variables
37      clear opts
38      [pks,locs,w,p] = findpeaks(tdata.force,'MinPeakProminence',2);
39      %outArr = [pks;locs;w;p];
40      if i==1
41          outCell{1,1} =  pks;
42          outCell{1,2} =  locs;
43          outCell{1,3} =  w;
44          outCell{1,4} =  p;
45      else
46          outCell{1,(4*(i-1)+1)} =  pks;
47          outCell{1,(4*(i-1)+2)} =  locs;
48          outCell{1,(4*(i-1)+3)} =  w;
49          outCell{1,(4*(i-1)+4)} =  p;
50      end
51  end
52  %make table to export
53  outTable = cell2table(outCell');
54  writetable(outTable,"matlabOutput.csv")
```

Macros and Codes C.1: Matlab script used to identify peaks in force data.

References

[1] iData Research. Over 460,000 Rotator Cuff Surgeries per Year Reported in the United States by iData Research, 2018.

[2] Osnat Hakimi, Pierre Alexis Mouthuy, and Andrew Carr. Synthetic and degradable patches: An emerging solution for rotator cuff repair. *International Journal of Experimental Pathology*, 94(4):287–292, 2013.

[3] Hiroyuki Sugaya, Kazuhiko Maeda, Keisuke Matsuki, and Joji Moriishi. Repair integrity and functional outcome after arthroscopic double-row rotator cuff repair: A prospective outcome study. *Journal of Bone and Joint Surgery*, 89(5):953–960, 2007.

[4] Leesa M. Galatz, Craig M. Ball, Sharlene A. Teefey, William D. Middleton, and Ken Yamaguchi. The Outcome and Repair Integrity of Completely Arthroscopically Repaired Large and Massive Rotator Cuff Tears. *Journal of Bone and Joint Surgery*, 86(2):219–224, 2004.

[5] D T Harryman, L A Mack, K Y Wang, S E Jackins, M L Richardson, and F A Matsen. Repairs of the rotator cuff. Correlation of functional results with integrity of the cuff. *Journal of Bone and Joint Surgery - Series A*, 73(7):982–989, aug 1991.

[6] Avanthi Mandaleson. Re-tears after rotator cuff repair: Current concepts review. *Journal of Clinical Orthopaedics and Trauma*, 19:168–174, aug 2021.

[7] Richard C. Mather, Lane Koenig, Daniel Acevedo, Timothy M. Dall, Paul Gallo, Anthony Romeo, John Tongue, and Gerald Williams. The societal and economic value of rotator cuff repair. *Journal of Bone and Joint Surgery*, 95(22):1993–2000, nov 2013.

[8] Gabrielle Deprés-tremblay, Anik Chevrier, Martyn Snow, Mark B. Hurtig, Scott Rodeo, and Michael D. Buschmann. Rotator cuff repair: a review of surgical techniques, animal models, and new technologies under development. *Journal of Shoulder and Elbow Surgery*, 25(12):2078–2085, 2016.

[9] D. H. Sonnabend and A. A. Young. Comparative anatomy of the rotator cuff. *Journal of Bone and Joint Surgery - Series B*, 91(12):1631–1637, dec 2009.

[10] Iou-Ren Chang and Eman Elzeftawy. *Anatomy, Shoulder and Upper Limb, Glenohumeral Joint*. StatPearls Publishing, aug 2018.

[11] Smita Maruvada and Matthew Varacallo. *Anatomy, Rotator Cuff*. StatPearls Publishing, mar 2019.

[12] S. C. Ling, C. F. Chen, and R. X. Wan. A study on the vascular supply of the supraspinatus tendon. *Surgical and Radiologic Anatomy*, 12(3):161–165, 1990.

[13] I. M. Ahmed, M. Lagopoulos, P. McConnell, R. W. Soames, and G. K. Sefton. Blood supply of the achilles tendon. *Journal of Orthopaedic Research*, 16(5):591–596, sep 1998.

[14] James B Rathbun and Ian Macnab. the Microvascular Pattern of the Rotator Cuff the Journal of Bone and Joint Surgery. *The Journal of bone and joint surgery*, 52 B(3):540–553, 1970.

[15] D Determe, M. Rongières, J Kany, J M Glasson, Y Bellumore, M Mansat, and J Becue. Anatomic study of the tendinous rotator cuff of the shoulder. *Surgical and Radiologic Anatomy*, 18(3):195–200, 1996.

[16] Knut Lindblom. On pathogenesis of ruptures of the tendon aponeurosis of the shoulder joint. *Acta Radiologica*, 20(6):563–577, 1939.

[17] Volker Stein, Heinz Laprell, Stefan Tinnemeyer, and Wolf Petersen. Quantitative assessment of intravascular volume of the human Achilles tendon. *Acta Orthopaedica Scandinavica*, 71(1):60–63, 2000.

[18] C. Frey, M. Shereff, and N. Greenidge. Vascularity of the posterior tibial tendon. *Journal of Bone and Joint Surgery - Series A*, 72(6):884–888, 1990.

[19] Xueli Liu, Bin Zhu, Yujie Li, Xinyue Liu, Sheng Guo, Chenglong Wang, Sen Li, and Dingxuan Wang. The Role of Vascular Endothelial Growth Factor in Tendon Healing. *Frontiers in Physiology*, 12:766080–766080, oct 2021.

[20] Steven A. Fenwick, Brian L. Hazleman, and Graham P. Riley. The vasculature and its role in the damaged and healing tendon. *Arthritis Research*, 4(4):252–260, 2002.

[21] Herbert Tempfer and Andreas Traweger. Tendon vasculature in health and disease. *Frontiers in Physiology*, 6:330, 2015.

[22] Pekka Kannus. Structure of the tendon connective tissue. *Scandinavian Journal of Medicine and Science in Sports*, 10(6):312–320, 2000.

[23] Marco Franchi, Alessandra Trirè, Marilisa Quaranta, Ester Orsini, and Vittoria Ottani. Collagen structure of tendon relates to function. *The Scientific World*, 7:404–420, 2007.

[24] Bruno Bordoni and Matthew Varacallo. *Anatomy, Tendons*. StatPearls Publishing, apr 2019.

[25] John Apostolakos, Thomas J S Durant, Corey R. Dwyer, Ryan P. Russell, Jeffrey H. Weinreb, Farhang Alaee, Knut Beitzel, Mary Beth McCarthy, Mark P. Cote, and Augustus D. Mazzocca. The enthesis: A review of the tendon-to-bone insertion. *Muscles, Ligaments and Tendons Journal*, 4(3):333–342, 2014.

[26] A. B. Knudsen, M. Larsen, A. L. Mackey, M. Hjort, K. K. Hansen, K. Qvortrup, M. Kjær, and M. R. Krogsgaard. The human myotendinous junction: An ultrastructural and 3D analysis study. *Scandinavian Journal of Medicine and Science in Sports*, 25(1):e116–e123, feb 2015.

[27] Peter P. Purslow, Tim J. Wess, and David W.L. Hukins. Collagen orientation and molecular spacing during creep and stress-relaxation in soft connective tissues. *Journal of Experimental Biology*, 201(1):135–142, jan 1998.

[28] Dawn M. Elliott, Paul S. Robinson, Jonathan A. Gimbel, Joseph J. Sarver, Joseph A. Abboud, Renato V. Iozzo, and Louis J. Soslowsky. Effect of altered matrix proteins on quasilinear viscoelastic properties in transgenic mouse tail tendons. *Annals of Biomedical Engineering*, 31(5):599–605, 2003.

[29] M. Benjamin, B. Moriggl, E. Brenner, P. Emery, D. McGonagle, and S. Redman. The "enthesis organ" concept: Why enthesopathies may not present as focal insertional disorders. *Arthritis and Rheumatism*, 50(10):3306–3313, oct 2004.

[30] Nina Friese, Mattis Benno Gierschner, Patrik Schadzek, Yvonne Roger, and Andrea Hoffmann. Regeneration of damaged tendon-bone junctions (Entheses)—tak1 as a potential node factor. *International Journal of Molecular Sciences*, 21(15):1–21, aug 2020.

[31] Eleonora Bianchi, Marco Ruggeri, Silvia Rossi, Barbara Vigani, Dalila Miele, Maria Cristina Bonferoni, Giuseppina Sandri, and Franca Ferrari. Innovative strategies in tendon tissue engineering. *Pharmaceutics*, 13(1):1–24, 2021.

[32] Benjamin B. Rothrauff, Guang Yang, and Rocky S. Tuan. Tendon Resident Cells-Functions and Features in Section I-Developmental Biology and Physiology of Tendons. *Tendon Regeneration: Understanding Tissue Physiology and Development to Engineer Functional Substitutes*, pages 41–76, 2015.

[33] Zuping Zhou, Takintope Akinbiyi, Lili Xu, Melissa Ramcharan, Daniel J. Leong, Stephen J. Ros, Alexis C. Colvin, Mitchell B. Schaffler, Robert J. Majeska, Evan L. Flatow, and Hui B. Sun. Tendon-derived stem/progenitor cell aging: Defective self-renewal and altered fate. *Aging Cell*, 9(5):911–915, oct 2010.

[34] Barbara Brodsky, Geetha Thiagarajan, Balaraman Madhan, and Karunakar Kar. Triple-helical peptides: An approach to collagen conformation, stability, and self-association. *Biopolymers*, 89(5):345–353, may 2008.

[35] Chavaunne T. Thorpe, Helen L. Birch, Peter D. Clegg, and Hazel R.C. Screen. Tendon Physiology and Mechanical Behavior: Structure-Function Relationships. In *Tendon Regeneration: Understanding Tissue Physiology and Development to Engineer Functional Substitutes*, pages 3–39. Academic Press, jan 2015.

[36] James H.C. Wang. Mechanobiology of tendon. *Journal of Biomechanics*, 39(9):1563–1582, 2006.

[37] Chavaunne T. Thorpe, Marta S.C. Godinho, Graham P. Riley, Helen L. Birch, Peter D. Clegg, and Hazel R.C. Screen. The interfascicular matrix enables fascicle sliding and recovery in tendon, and behaves more elastically in energy

storing tendons. *Journal of the Mechanical Behavior of Biomedical Materials*, 52:85–94, dec 2015.

[38] J. Zabrzyński, Łapaj, Paczesny, A. Zabrzyńska, and D. Grzanka. Tendon — function-related structure, simple healing process and mysterious ageing. *Folia Morphologica (Poland)*, 77(3):416–427, 2018.

[39] Donald E Ingber. Cellular mechanotransduction: putting all the pieces together again. *The FASEB Journal*, 20(7):811–827, 2006.

[40] Neta Felsenthal and Elazar Zelzer. Mechanical regulation of musculoskeletal system development. *Development (Cambridge)*, 144(23):4271–4283, 2017.

[41] Ronen Schweitzer, Jay H Chyung, Lewis C Murtaugh, Ava E Brent, Vicki Rosen, Eric N Olson, Andrew Lassar, Clifford J Tabin, Joy Lincoln, Christina M. Alfieri, and Katherine E. Yutzey. Analysis of the tendon cell fate using Scleraxis, a specific marker for tendons and ligaments. *Developmental Biology*, 3866(2):3855–3866, 2001.

[42] Jessica W. Chen and Jenna L. Galloway. The development of zebrafish tendon and ligament progenitors. *Development (Cambridge)*, 141(10):2035–2045, may 2014.

[43] C Herbst. *Formative Reize in der Tierischen Ontogenese*. 1901.

[44] Ludovic Gaut and Delphine Duprez. Tendon development and diseases. *Wiley Interdisciplinary Reviews: Developmental Biology*, 5(1):5–23, 2016.

[45] Huanhuan Liu, Shouan Zhu, Can Zhang, Ping Lu, Jiajie Hu, Zi Yin, Yue Ma, Xiao Chen, and Hongwei OuYang. Crucial transcription factors in tendon development and differentiation: Their potential for tendon regeneration. *Cell and Tissue Research*, 356(2):287–298, 2014.

[46] Ronen Schweitzer, Elazar Zelzer, and Talila Volk. Connecting muscles to tendons: Tendons and musculoskeletal development in flies and vertebrates (Development 137 (2807-2817)). *Development*, 137(19):3347, 2010.

[47] Stavros Thomopoulos, Hyun Min Kim, Stefan Y. Rothermich, Carrie Biederstadt, Rosalina Das, and Leesa M. Galatz. Decreased muscle loading delays maturation of the tendon enthesis during postnatal development. *Journal of Orthopaedic Research*, 25(9):1154–1163, 2007.

[48] Alexander M. Tatara, Justin H. Lipner, Rosalina Das, H. Mike Kim, Nikunj Patel, Eleni Ntouvali, Matthew J. Silva, and Stavros Thomopoulos. The role of muscle loading on bone (re)modeling at the developing enthesis. *PLoS ONE*, 9(5), may 2014.

[49] L. Öhberg, R. Lorentzon, and H. Alfredson. Eccentric training in patients with chronic Achilles tendinosis: Normalised tendon structure and decreased thickness at follow up. *British Journal of Sports Medicine*, 38(1):8–11, feb 2004.

[50] Martin I. Boyer, Charles A. Goldfarb, and Richard H. Gelberman. Recent progress in flexor tendon healing: The modulation of tendon healing with rehabilitation variables. *Journal of Hand Therapy*, 18(2):80–85, 2005.

[51] Narender Saini, Vishal Kundnani, Purnima Patni, and S. P. Gupta. Outcome of early active mobilization after flexor tendons repair in zones II-V in hand. *Indian Journal of Orthopaedics*, 44(3):314–321, jul 2010.

[52] Alexander Scott, Jill L. Cook, David A. Hart, David C. Walker, Vincent Duronio, and Karim M. Khan. Tenocyte responses to mechanical loading in vivo: A role for local insulin-like growth factor 1 signaling in early tendinosis in rats. *Arthritis and Rheumatism*, 56(3):871–881, mar 2007.

[53] K. M. Heinemeier, J. L. Olesen, P. Schjerling, F. Haddad, H. Langberg, K. M. Baldwin, and M. Kjaer. Short-term strength training and the expression of myostatin and IGF-I isoforms in rat muscle and tendon: Differential effects of specific contraction types. *Journal of Applied Physiology*, 102(2):573–581, feb 2007.

[54] Jo A. Hannafin, Steven P. Arnoczky, Amardeep Hoonjan, and Peter A. Torzilli. Effect of stress deprivation and cyclic tensile loading on the material and morphologic properties of canine flexor digitorum profundus tendon: An in vitro study. *Journal of Orthopaedic Research*, 13(6):907–914, nov 1995.

[55] Tao Wang, Zhen Lin, Ming Ni, Christine Thien, Robert E. Day, Bruce Gardiner, Jonas Rubenson, Thomas B. Kirk, David W. Smith, Allan Wang, David G. Lloyd, Yan Wang, Qiujian Zheng, and Ming H. Zheng. Cyclic mechanical stimulation rescues achilles tendon from degeneration in a bioreactor system. *Journal of Orthopaedic Research*, 33(12):1888–1896, dec 2015.

[56] Jung Joo Kim, David S. Musson, Brya G. Matthews, Jillian Cornish, Iain A. Anderson, and Vickie B. Shim. Applying Physiologically Relevant Strains to Tenocytes in an in Vitro Cell Device Induces in Vivo Like Behaviors. *Journal of Biomechanical Engineering*, 138(12):121003, nov 2016.

[57] Shaohua Wu, Ying Wang, Philipp N. Streubel, and Bin Duan. Living nanofiber yarn-based woven biotextiles for tendon tissue engineering using cell tri-culture and mechanical stimulation. *Acta Biomaterialia*, 62:102–115, 2017.

[58] Cvetan Popov, Martina Burggraf, Ludwika Kreja, Anita Ignatius, Matthias Schieker, and Denitsa Docheva. Mechanical stimulation of human tendon stem/progenitor cells results in upregulation of matrix proteins, integrins and

MMPs, and activation of p38 and ERK1/2 kinases. *BMC Molecular Biology*, 16(1):1–11, mar 2015.

[59] Tao Wang, Peilin Chen, Monica Zheng, Allan Wang, David Lloyd, Toby Leys, Qiujian Zheng, and Ming H. Zheng. In vitro loading models for tendon mechanobiology. *Journal of Orthopaedic Research*, 36(2):566–575, 2018.

[60] Hans Clevers. Wnt/β-Catenin Signaling in Development and Disease. *Cell*, 127(3):469–480, nov 2006.

[61] Mary Y. Wu and Caroline S. Hill. TGF-β Superfamily Signaling in Embryonic Development and Homeostasis. *Developmental Cell*, 16(3):329–343, mar 2009.

[62] Arash Tajik, Yuejin Zhang, Fuxiang Wei, Jian Sun, Qiong Jia, Wenwen Zhou, Rishi Singh, Nimish Khanna, Andrew S. Belmont, and Ning Wang. Transcription upregulation via force-induced direct stretching of chromatin. *Nature Materials*, 15(12):1287–1296, dec 2016.

[63] Eijiro Maeda, Shangjun Ye, Wen Wang, Dan L. Bader, Martin M. Knight, and David A. Lee. Gap junction permeability between tenocytes within tendon fascicles is suppressed by tensile loading. *Biomechanics and Modeling in Mechanobiology*, 11(3-4):439–447, mar 2012.

[64] Jess G. Snedeker and Jasper Foolen. Tendon injury and repair – A perspective on the basic mechanisms of tendon disease and future clinical therapy. *Acta Biomaterialia*, 63:18–36, nov 2017.

[65] Hannah Hinsley, Charlotte Ganderton, Nigel K. Arden, and Andrew J. Carr. Prevalence of rotator cuff tendon tears and symptoms in a Chingford general population cohort, and the resultant impact on UK health services: a cross-sectional observational study. *BMJ Open*, 12(9):1–8, 2022.

[66] Jonathan Rees, Jamie E. Gaida, Karin Grävare Silbernagel, Johannes Zwerver, Joseph S. Anthony, and Alex Scott. Rehabilitation of tendon problems in patients with diabetes mellitus. In *Advances in Experimental Medicine and Biology*, volume 920, pages 199–208. Springer, Cham, 2016.

[67] Hio Teng Leong, Sai Chuen Fu, Xin He, Joo Han Oh, Nobuyuki Yamamoto, and Shu Hang Patrick Yung. Risk factors for rotator cuff tendinopathy: A systematic review and meta-analysis. *Journal of Rehabilitation Medicine*, 51(9):627–637, 2019.

[68] Jinlong Zhao, Mingui Luo, Guihong Liang, Ming Wu, Jianke Pan, Ling-feng Zeng, Weiyi Yang, and Jun Liu. Risk Factors for Supraspinatus Tears. *The Orthopaedic Journal of Sports Medicine*, 9:1–10, 2021.

[69] Alexis Dang and Michael Davies. Rotator Cuff Disease: Treatment Options and Considerations. *Sports Medicine and Arthroscopy Review*, 26(3):129–133, 2018.

[70] Rotator Cuff Classifications — ShoulderDoc. https://www.shoulderdoc.co.uk/article/1456. Last accessed 20/07/2023.

[71] Claire D. Eliasberg, Susumu Wada, Camila B. Carballo, Yusuke Nakagawa, Daniel A. Nemirov, Reyna Bhandari, Miguel Otero, Xiang-Hua Deng, and Scott A. Rodeo. Identification of Inflammatory Mediators in Tendinopathy Using a Murine Subacromial Impingement Model. *Journal of Orthopaedic Research*, (ii):1–8, 2019.

[72] P. Kannus and L. Jozsa. Histopathological changes preceding spontaneous rupture of a tendon: A controlled study of 891 patients. *Journal of Bone and Joint Surgery - Series A*, 73(10):1507–1525, 1991.

[73] G. G. Schulze-Tanzil, M. Delgado Cáceres, R. Stange, B. Wildemann, and D. Docheva. Tendon healing: a concise review on cellular and molecular mechanisms with a particular focus on the Achilles tendon. *Bone and Joint Research*, 11(8):561–574, 2022.

[74] Matthew Hope and Terry S. Saxby. Tendon Healing. *Foot and Ankle Clinics*, 12(4):553–567, dec 2007.

[75] W. L. Garner, J. A. McDonald, M. Koo, C. Kuhn, and P. M. Weeks. Identification of the collagen-producing cells in healing flexor tendons. *Plastic and Reconstructive Surgery*, 83(5):875–879, 1989.

[76] Roshan James, Girish Kesturu, Gary Balian, and A. Bobby Chhabra. Tendon: Biology, Biomechanics, Repair, Growth Factors, and Evolving Treatment Options. *Journal of Hand Surgery*, 33(1):102–112, jan 2008.

[77] Subhash C. Juneja, Edward M. Schwarz, Regis J. O'Keefe, and Hani A. Awad. Cellular and molecular factors in flexor tendon repair and adhesions: A histological and gene expression analysis. *Connective Tissue Research*, 54(3):218–226, 2013.

[78] Pramod B Voleti, Mark R Buckley, and Louis J Soslowsky. Tendon healing: Repair and regeneration. *Annual Review of Biomedical Engineering*, 14:47–71, 2012.

[79] Pankaj Sharma and Nicola Maffulli. Biology of tendon injury: healing, modeling and remodeling. *J Musculoskelet Neuronal Interact*, 6:181–190, 2006.

[80] Sven-Olof -O Abrahamsson, Göran Lundborg, and L. Stefan Lohmander. Recombinant human insulin-like growth factor-I stimulates in vitro matrix synthesis and cell proliferation in rabbit flexor tendon. *Journal of Orthopaedic Research*, 9(4):495–502, 1991.

[81] Guang Yang, Benjamin B. Rothrauff, and Rocky S. Tuan. Tendon and ligament regeneration and repair: Clinical relevance and developmental paradigm. *Birth Defects Research Part C - Embryo Today: Reviews*, 99(3):203–222, 2013.

[82] Kristen Howell, Chun Chien, Rebecca Bell, Damien Laudier, Sara F. Tufa, Douglas R. Keene, Nelly Andarawis-Puri, and Alice H. Huang. Novel Model of Tendon Regeneration Reveals Distinct Cell Mechanisms Underlying Regenerative and Fibrotic Tendon Healing. *Scientific Reports*, 7(1):1–14, mar 2017.

[83] Bhavita Walia and Alice H. Huang. Tendon stem progenitor cells: Understanding the biology to inform therapeutic strategies for tendon repair, jun 2019.

[84] Sandra Ruiz-Alonso, Markel Lafuente-Merchan, Jesús Ciriza, Laura Saenz-del Burgo, and Jose Luis Pedraz. Tendon tissue engineering: Cells, growth factors, scaffolds and production techniques. *Journal of Controlled Release*, 333:448–486, may 2021.

[85] Jeffrey D Osborne, Ashok L Gowda, Brett Wiater, and J Michael Wiater. Rotator cuff rehabilitation: Current theories and practice. *Physician and Sportsmedicine*, 44(1):85–92, 2016.

[86] Robert Z. Tashjian. Epidemiology, Natural History, and Indications for Treatment of Rotator Cuff Tears. *Clinics in Sports Medicine*, 31(4):589–604, oct 2012.

[87] Peter Edwards, Jay Ebert, Brendan Joss, Gev Bhabra, Tim Ackland, and Allan Wang. Exercise rehabilitation in the non-operative management of rotator cuff tears: A review of the literature. *International journal of sports physical therapy*, 11(2):279–301, 2016.

[88] Anssi Ryösä, Katri Laimi, Ville Äärimaa, Kaisa Lehtimäki, Juha Kukkonen, and Mikhail Saltychev. Surgery or conservative treatment for rotator cuff tear: a meta-analysis. *Disability and Rehabilitation*, 39(14):1357–1363, 2017.

[89] Kelms Amoo-Achampong, Michael K Krill, Derrick Acheampong, Benedict U Nwachukwu, and Frank McCormick. Evaluating strategies and outcomes following rotator cuff tears. *Shoulder and Elbow*, 11(1_suppl):4–18, 2019.

[90] Jennifer Tangtiphaiboontana, Andrew M. Figoni, Anthony Luke, Alan L. Zhang, Brian T. Feeley, and C. Benjamin Ma. The effects of nonsteroidal anti-inflammatory medications after rotator cuff surgery: a randomized, double-blind, placebo-controlled trial. *Journal of Shoulder and Elbow Surgery*, 30(9):1990–1997, sep 2021.

[91] David S. Constantinescu, Michael P. Campbell, Gilbert Moatshe, and Alexander R. Vap. Effects of Perioperative Nonsteroidal Anti-inflammatory Drug Administration on Soft Tissue Healing: A Systematic Review of Clinical Outcomes After Sports Medicine Orthopaedic Surgery Procedures. *Orthopaedic Journal of Sports Medicine*, 7(4), apr 2019.

[92] S. Gumina, G. Di Giorgio, A. Bertino, C. Della Rocca, B. Sardella, and F. Postacchini. Inflammatory infiltrate of the edges of a torn rotator cuff. *International Orthopaedics*, 30(5):371–374, oct 2006.

[93] Marc A. Childress and Anthony Beutler. Management of chronic tendon injuries. *American Family Physician*, 87(7):486–490, mar 2013.

[94] Sally Hopewell, David J Keene, Ioana R Marian, Melina Dritsaki, Peter Heine, Lucy Cureton, Susan J Dutton, Helen Dakin, Andrew Carr, Willie Hamilton, Zara Hansen, Anju Jaggi, Chris Littlewood, Karen L Barker, Alastair Gray, Sarah E Lamb, Marcus Bateman, Alison Hallett, Helen Thompson, Elaine

Willmore, Lucy McCann, Jonathan Price, Neil Smith, Harry Kardamilas, Matt Hurst, Tim Andrews, Lori Wells, Chloe De Matas, Arun Jaykumar, Sean Grove, Corinne Birch, Julie Bury, James Blacknall, Sally Jessop, Llewelyn Boucher, Robert Sandbach, Stacey Lalande, Gill Dickson, Treena Larkin, and Carole Cummings. Progressive exercise compared with best practice advice, with or without corticosteroid injection, for the treatment of patients with rotator cuff disorders (GRASP): a multicentre, pragmatic, 2 × 2 factorial, randomised controlled trial. *The Lancet*, 398(10298):416–428, jul 2021.

[95] Meng Ting Lin, Ching Fang Chiang, Chueh Hung Wu, Yi Ting Huang, Yu Kang Tu, and Tyng Guey Wang. Comparative Effectiveness of Injection Therapies in Rotator Cuff Tendinopathy: A Systematic Review, Pairwise and Network Meta-analysis of Randomized Controlled Trials. *Archives of Physical Medicine and Rehabilitation*, 100(2):336–349.e15, feb 2019.

[96] Chris Hyunchul Jo, Ji Sun Shin, Young Gil Lee, Won Hyoung Shin, Hyang Kim, Seung Yeon Lee, Kang Sup Yoon, and Sue Shin. Platelet-rich plasma for arthroscopic repair of large to massive rotator cuff tears: a randomized, single-blind, parallel-group trial. *The American journal of sports medicine*, 41(10):2240–2248, oct 2013.

[97] Ryan J. Warth, Grant J. Dornan, Evan W. James, Marilee P. Horan, and Peter J. Millett. Clinical and structural outcomes after arthroscopic repair of full-thickness rotator cuff tears with and without platelet-rich product supplementation: a meta-analysis and meta-regression. *Arthroscopy : the journal of arthroscopic & related surgery : official publication of the Arthroscopy Association of North America and the International Arthroscopy Association*, 31(2):306–320, 2015.

[98] Cory A. Kwong, Jarret M. Woodmass, Eva M. Gusnowski, Aaron J. Bois, Justin Leblanc, Kristie D. More, and Ian K.Y. Lo. Platelet-Rich Plasma in Patients With Partial-Thickness Rotator Cuff Tears or Tendinopathy Leads to Significantly Improved Short-Term Pain Relief and Function Compared With Corticosteroid Injection: A Double-Blind Randomized Controlled Trial. *Arthroscopy - Journal of Arthroscopic and Related Surgery*, 37(2):510–517, feb 2021.

[99] Joseph Alsousou, David J Keene, Paul Harrison, Philippa Hulley, Susan Wagland, Jacqueline Y Thompson, Scott R Parsons, Christopher Byrne, Michael M Schlüssel, Heather M O'Connor, Susan J Dutton, Sarah E Lamb, and Keith Willett. Platelet-rich plasma injection for adults with acute Achilles tendon rupture: the PATH-2 RCT. *Efficacy and Mechanism Evaluation*, 6(12):1–98, dec 2019.

[100] D. J. Keene, J. Alsousou, P. Harrison, H. M. O'Connor, S. Wagland, S. J. Dutton, P. Hulley, S. E. Lamb, and K. Willett. Platelet-rich plasma injection for acute Achilles tendon rupture. *Bone and Joint Journal*, 104B(11):1256–1265, nov 2022.

[101] Matthew T. Provencher, James S. Kercher, Leesa M. Galatz, Neal S. Elattrache, Rachel M. Frank, and Brian J. Cole. Evolution of rotator cuff repair techniques: are our patients really benefiting? *Instructional course lectures*, 60:123–136, 2011.

[102] Patrick J. Denard and Stephen S. Burkhart. The evolution of suture anchors in arthroscopic rotator cuff repair. *Arthroscopy - Journal of Arthroscopic and Related Surgery*, 29(9):1589–1595, 2013.

[103] David H. Kim, Neal S. ElAttrache, James E. Tibone, Bong Jae Jun, Sergai N. DeLaMora, Ronald S. Kvitne, and Thay Q. Lee. Biomechanical comparison of

a single-row versus double-row suture anchor technique for rotator cuff repair. *American Journal of Sports Medicine*, 34(3):407–414, mar 2006.

[104] Rocco Papalia, Francesco Franceschi, Sebastiano Vasta, Biagio Zampogna, Nicola Maffulli, and Vincenzo Denaro. Single- and double-row repair for rotator cuff tears - Biology and mechanics. *Medicine and Sport Science*, 57:122–141, 2012.

[105] Laurent Lafosse, Roman Brzoska, Bruno Toussaint, and Reuben Gobezie. The outcome and structural integrity of arthroscopic rotator cuff repair with use of the double-row suture anchor technique: Surgical technique. *Journal of Bone and Joint Surgery*, 90(Suppl. 2 part 2):275–286, oct 2008.

[106] Matthew R. Lewington, Devin P. Ferguson, T. Duncan Smith, Robert Burks, Catherine Coady, and Ivan Ho Bun Wong. Graft Utilization in the Bridging Reconstruction of Irreparable Rotator Cuff Tears: A Systematic Review. *American Journal of Sports Medicine*, 45(13):3149–3157, nov 2017.

[107] John M. Tokish, James S. Shaha, Patrick J. Denard, Jeremy J. Mercuri, and Gregory Colbath. Compressed Biceps Autograft Augmentation of Arthroscopic Rotator Cuff Repair. *Arthroscopy Techniques*, 11(11):e2113–e2118, nov 2022.

[108] Ignacio Pasqualini, Mariano E. Menendez, Javier Ardebol, and Patrick J. Denard. Dermal Allograft Augmentation for Rotator Cuff Tears. *Arthroscopy - Journal of Arthroscopic and Related Surgery*, 38(11):2957–2959, nov 2022.

[109] Raffaele Garofalo, Alberto Fontanarosa, Angelo De Crescenzo, Marco Conti, Roberto Calbi, and Alessandro Castagna. Does arthroscopic superior capsule reconstruction using porcine dermal xenograft represent a viable option in case of massive irreparable posterosuperior rotator cuff tear? *Archives of Orthopaedic and Trauma Surgery*, 143(1):439–445, 2022.

[110] Henry M. Shepherd, Patrick H. Lam, and George A.C. Murrell. Synthetic Patch Rotator Cuff Repair: A 10-year Follow-Up. *Shoulder and Elbow*, 6(1):35–39, jan 2014.

[111] Jonathan A. Cook, Mathew Baldwin, Cushla Cooper, Navraj S. Nagra, Joanna C. Crocker, Molly Glaze, Gemma Greenall, Amar Rangan, Lucksy Kottam, Jonathan L. Rees, Dair Farrar-Hockley, Naomi Merritt, Sally Hopewell, David Beard, Michael Thomas, Melina Dritsaki, and Andrew J. Carr. Findings from the patch augmented rotator cuff surgery (PARCS) feasibility study. *Pilot and Feasibility Studies*, 7(1):1–10, dec 2021.

[112] Mathew Baldwin, N. S. Nagra, Gemma Greenall, Andrew J. Carr, David Beard, J. L. Rees, Amar Rangan, Naomi Merritt, Melina Dritsaki, Sally Hopewell, and Jonathan Alistair Cook. Use of implantable meshes for augmented rotator cuff repair: A systematic review and meta-Analysis, dec 2020.

[113] Mathew Baldwin, Sarah Snelling, Stephanie Dakin, and Andrew Carr. Augmenting endogenous repair of soft tissues with nanofibre scaffolds. *The Royal Society Publishing*, 15(141), 2018.

[114] A. M. Nada, U. K. Debnath, D. A. Robinson, and C. Jordan. Treatment of massive rotator-cuff tears with a polyester ligament (Dacron) augmentation: Clinical outcome. *Journal of Bone and Joint Surgery - Series B*, 92(10):1397–1402, oct 2010.

[115] R. Russo, L. Vernaglia Lombardi, V. Visconti, and G. Della Rotonda. Massive rotator cuff tear treated with a synthetic patch: A case report 16 years after surgery. *Musculoskeletal Surgery*, 95(Suppl 1):83–87, apr 2011.

[116] Pietro Ciampi, Celeste Scotti, Alessandro Nonis, Matteo Vitali, Clelia Di Serio, Giuseppe M. Peretti, and Gianfranco Fraschini. The benefit of synthetic versus

biological patch augmentation in the repair of posterosuperior massive rotator cuff tears: A 3-year follow-up study. *American Journal of Sports Medicine*, 42(5):1169–1175, mar 2014.

[117] Winston Shang Rong Lim, Andy Khye Soon Yew, Hannah Lie, Siaw Meng Chou, and Denny Tijauw Tjoen Lie. Rotator cuff repair with an interposition polypropylene mesh: A biomechanical ovine study. *World Journal of Orthopedics*, 14(5):319–327, may 2023.

[118] Ivan Encalada-Diaz, Brian J. Cole, John D. MacGillivray, Michell Ruiz-Suarez, James S. Kercher, Nicole A. Friel, and Fernando Valero-Gonzalez. Rotator cuff repair augmentation using a novel polycarbonate polyurethane patch: Preliminary results at 12 months' follow-up. *Journal of Shoulder and Elbow Surgery*, 20(5):788–794, jul 2011.

[119] Brian J. Cole, Andreas H. Gomoll, Adam Yanke, Tamara Pylawka, Paul Lewis, John D. MacGillivray, and James M. Williams. Biocompatibility of a polymer patch for rotator cuff repair. *Knee Surgery, Sports Traumatology, Arthroscopy*, 15(5):632–637, may 2007.

[120] Brandon G. Santoni, Kirk C. McGilvray, Amy S. Lyons, Manjula Bansal, A. Simon Turner, John D. MacGillivray, Struan H. Coleman, and Christian M. Puttlitz. Biomechanical Analysis of an Ovine Rotator Cuff Repair via Porous Patch Augmentation in a Chronic Rupture Model. *American Journal of Sports Medicine*, 38(4):679–686, apr 2010.

[121] E. Audenaert, J. VanNuffel, A. Schepens, M. Verhelst, and R. Verdonk. Reconstruction of massive rotator cuff lesions with a synthetic interposition graft: A prospective study of 41 patients. *Knee Surgery, Sports Traumatology, Arthroscopy*, 14(4):360–364, apr 2006.

[122] Vasanth Seker, Lisa Hackett, Patrick H. Lam, and George A.C. Murrell. Evaluating the Outcomes of Rotator Cuff Repairs With Polytetrafluoroethylene Patches for Massive and Irreparable Rotator Cuff Tears With a Minimum 2-Year Follow-up. *American Journal of Sports Medicine*, 46(13):3155–3164, nov 2018.

[123] Kenji Okamura, Masayuki Abe, Yuichiro Yamada, Takeshi Makihara, Takaki Yoshimizu, Yoshinari Sakaki, Yuki Suzumori, and Teruhisa Mihata. Arthroscopic superior capsule reconstruction with Teflon felt synthetic graft for irreparable massive rotator cuff tears: clinical and radiographic results at minimum 2-year follow-up. *Journal of Shoulder and Elbow Surgery*, 30(3):625–634, mar 2021.

[124] J. B. King and C. Bulstrode. Polylactate-coated carbon fiber in extra-articular reconstruction of the unstable knee. *Clinical Orthopaedics and Related Research*, 196:139–142, 1985.

[125] A. A. Amis, S. A. Kempson, J. R. Campbell, and J. H. Miller. Anterior cruciate ligament replacement. Biocompatibility and biomechanics of polyester and carbon fibre in rabbits. *Journal of Bone and Joint Surgery - Series B*, 70(4):628–634, aug 1988.

[126] György Szabó, József Barabás, Sándor Bogdán, Zsolt Németh, Béla Sebők, and Gábor Kiss. Long-term clinical and experimental/surface analytical studies of carbon/carbon maxillofacial implants. *Maxillofacial Plastic and Reconstructive Surgery*, 37(1):1–14, dec 2015.

[127] Simon M. Johnson, Jennifer V. Cherry, Naveena Thomas, Mansoor Jafri, Arpit Jariwala, and Gordon G. McLeod. Clinical outcomes and ultrasonographic viability of GraftJacket® augmented rotator cuff repair: a prospective follow-up

study with mean follow-up of forty-one months. *Journal of Clinical Orthopaedics and Trauma*, 11(Suppl 3):S372–S377, may 2020.

[128] Jan Leuzinger, C. Sternberg, D. Smolen, and R. Jakob. Patch-Augmentation in der Re-Insertionschirurgie der Rotatorenmanschette bei älteren Patienten. *Zeitschrift fur Orthopadie und Unfallchirurgie*, 154(5):504–512, oct 2016.

[129] F. Alan Barber, Joseph P. Burns, Allen Deutsch, Marc R. Labbé, and Robert B. Litchfield. A prospective, randomized evaluation of acellular human dermal matrix augmentation for arthroscopic rotator cuff repair. *Arthroscopy - Journal of Arthroscopic and Related Surgery*, 28(1):8–15, jan 2012.

[130] Anthony Ratcliffe, David L. Butler, Nathaniel A. Dyment, Paul J. Cagle, Christopher S. Proctor, Seena S. Ratcliffe, and Evan L. Flatow. Scaffolds for Tendon and Ligament Repair and Regeneration. *Annals of Biomedical Engineering*, 43(3):819–831, mar 2015.

[131] Angelo V Vasiliadis and Konstantinos Katakalos. The role of scaffolds in tendon tissue engineering. *Journal of Functional Biomaterials*, 11(4):78, 2020.

[132] Judie R. Walton, Nicholas K. Bowman, Yasser Khatib, James Linklater, and George A.C. Murrell. Restore orthobiologic implant: Not recommended for augmentation of rotator cuff repairs. *Journal of Bone and Joint Surgery*, 89(4):786–791, 2007.

[133] Paolo Consigliere, Alessio Bernasconi, Richard Dimock, and A. Ali Narvani. Clinical outcomes and structural integrity rate of arthroscopic augmented rotator cuff repairs using extracellular porcine matrix patch. *Shoulder and Elbow*, 14(1):38–51, jul 2022.

[134] Timothy E. Cobb, Richard A.C. Dimock, Sahib D. Memon, Paolo Consigliere, Sam Ajami, Mohamed Imam, and A. Ali Narvani. Rotator Cuff Repair With

Patch Augmentation: What Do We Know? *Archives of Bone and Joint Surgery*, 10(10):833, 2022.

[135] Dianne Bryant, Richard Holtby, Kevin Willits, Robert Litchfield, Darren Drosdowech, Alison Spouge, David White, and Gordon Guyatt. A randomized clinical trial to compare the effectiveness of rotator cuff repair with or without augmentation using porcine small intestine submucosa for patients with moderate to large rotator cuff tears: a pilot study. *Journal of Shoulder and Elbow Surgery*, 25(10):1623–1633, oct 2016.

[136] Paolo Avanzi, Luca dei Giudici, Antonio Capone, Gaia Cardoni, Gianluigi Lunardi, Giovanni Foti, and Claudio Zorzi. Prospective randomized controlled trial for patch augmentation in rotator cuff repair: 24-month outcomes. *Journal of Shoulder and Elbow Surgery*, 28(10):1918–1927, oct 2019.

[137] Engineering a tendon extracellular matrix-functionalized elastomer scaffold for effective repair of large-to-massive tendon defects Shuting.

[138] Desmond John Bokor, David Sonnabend, Luke Deady, Ben Cass, Allan Young, Craig Van Kampen, and Steven Arnoczky. Preliminary investigation of a biological augmentation of rotator cuff repairs using a collagen implant: A 2-year MRI follow-up. *Muscles, Ligaments and Tendons Journal*, 5(3):144–150, jul 2015.

[139] Daisuke Mori, Noboru Funakoshi, Fumiharu Yamashita, and Tsuguru Wakabayashi. Effect of fatty degeneration of the infraspinatus on the efficacy of arthroscopic patch autograft procedure for large to massive rotator cuff tears. *American Journal of Sports Medicine*, 43(5):1108–1117, may 2015.

[140] C. Tempelaere, P. Desmoineaux, F. Lespagnol, J. Pierrart, P. Beaufils, and N. Pujol. Surgical repair of massive rotator cuff tendon tears: Autologous

quadriceps tendon graft versus arthroscopic repair. *Orthopaedics and Traumatology: Surgery and Research*, 103(3):435–440, may 2017.

[141] C. Holwein, B. von Bibra, P. M. Jungmann, D. C. Karampinos, K. Wörtler, M. Scheibel, A. B. Imhoff, and S. Buchmann. No healing improvement after rotator cuff reconstruction augmented with an autologous periosteal flap. *Knee Surgery, Sports Traumatology, Arthroscopy*, 27(10):3212–3221, oct 2019.

[142] Markus Scheibel, Anna Brown, Klaus Woertler, and Andreas B. Imhoff. Preliminary results after rotator cuff reconstruction augmented with an autologous periosteal flap. *Knee Surgery, Sports Traumatology, Arthroscopy*, 15(3):305–314, mar 2007.

[143] Eric A. Hohn, Blake P. Gillette, and Joseph P. Burns. Outcomes of arthroscopic revision rotator cuff repair with acellular human dermal matrix allograft augmentation. *Journal of Shoulder and Elbow Surgery*, 27(5):816–823, may 2018.

[144] Christopher S. Proctor. Long-term successful arthroscopic repair of large and massive rotator cuff tears with a functional and degradable reinforcement device. *Journal of Shoulder and Elbow Surgery*, 23(10):1508–1513, oct 2014.

[145] Anupama Prabhath, Varadraj N. Vernekar, Enid Sanchez, and Cato T. Laurencin. Growth factor delivery strategies for rotator cuff repair and regeneration. *International Journal of Pharmaceutics*, 544(2):358–371, 2018.

[146] Vítor E. Santo, Manuela E. Gomes, João F. Mano, and Rui L. Reis. Controlled release strategies for bone, cartilage, and osteochondral engineering-part i: Recapitulation of native tissue healing and variables for the design of delivery systems. *Tissue Engineering - Part B: Reviews*, 19(4):308–326, feb 2013.

[147] Caitlin Berry-Kilgour, Jaydee Cabral, and Lyn Wise. Advancements in the Delivery of Growth Factors and Cytokines for the Treatment of Cutaneous Wound Indications. *Advances in Wound Care*, 10(11):596–622, nov 2021.

[148] Alfonso Vaquero-Picado, Raul Barco, and Samuel A. Antuña. Lateral epicondylitis of the elbow. *EFORT Open Reviews*, 1(11):391–397, nov 2016.

[149] D. Connell, A. Datir, F. Alyas, and M. Curtis. Treatment of lateral epicondylitis using skin-derived tenocyte-like cells. *British Journal of Sports Medicine*, 43(4):293–298, apr 2009.

[150] Andrew W. Clarke, Faisal Alyas, Tim Morris, Claire J. Robertson, Jonathan Bell, and David A. Connell. Skin-derived tenocyte-like cells for the treatment of patellar tendinopathy. *American Journal of Sports Medicine*, 39(3):614–623, mar 2011.

[151] Allan Wang, William Breidahl, Katherine E. Mackie, Zhen Lin, An Qin, Jimin Chen, and Ming H. Zheng. Autologous tenocyte injection for the treatment of severe, chronic resistant lateral epicondylitis: A pilot study. *American Journal of Sports Medicine*, 41(12):2925–2932, dec 2013.

[152] Allan W. Wang, Stefan Bauer, Matthew Goonatillake, William Breidahl, and Ming Hao Zheng. Autologous tenocyte implantation, a novel treatment for partial-thickness rotator cuff tear and tendinopathy in an elite athlete. *BMJ Case Reports*, page bcr2012007899, 2013.

[153] Björn P. Roßbach, Mehmet F. Gülecyüz, Lena Kempfert, Matthias F. Pietschmann, Tina Ullamann, Andreas Ficklscherer, Thomas R. Niethammer, Anja Zhang, Roland M. Klar, and Peter E. Müller. Rotator Cuff Repair With Autologous Tenocytes and Biodegradable Collagen Scaffold: A Histological

and Biomechanical Study in Sheep. *American Journal of Sports Medicine*, 48(2):450–459, dec 2020.

[154] Pilar Tornero-Esteban, José Antonio Hoyas, Esther Villafuertes, Cruz Rodríguez-Bobada, Yamila López-Gordillo, Francisco J. Rojo, Gustavo V. Guinea, Anna Paleczny, Yaiza Lópiz-Morales, Luis Rodriguez-Rodriguez, Fernando Marco, and Benjamín Fernández-Gutiérrez. Efficacy of supraspinatus tendon repair using mesenchymal stem cells along with a collagen I scaffold. *Journal of Orthopaedic Surgery and Research*, 10(1):1–7, aug 2015.

[155] Song Zhao, Wei Su, Vishva Shah, Divia Hobson, Lara Yildirimer, Kelvin W.K. Yeung, Jinzhong Zhao, Wenguo Cui, and Xin Zhao. Biomaterials based strategies for rotator cuff repair. *Colloids and Surfaces B: Biointerfaces*, 157:407–416, 2017.

[156] Bo Chen, Jinping Ding, Wenjie Zhang, Guangdong Zhou, Yilin Cao, Wei Liu, and Bin Wang. Tissue Engineering of Tendons: A Comparison of Muscle-Derived Cells, Tenocytes, and Dermal Fibroblasts as Cell Sources. *Plastic and Reconstructive Surgery*, 137(3):536e–544e, 2016.

[157] Yanming Bi, Driss Ehirchiou, Tina M. Kilts, Colette A. Inkson, Mildred C. Embree, Wataru Sonoyama, Li Li, Arabella I. Leet, Byoung Moo Seo, Li Zhang, Songtao Shi, and Marian F. Young. Identification of tendon stem/progenitor cells and the role of the extracellular matrix in their niche. *Nature Medicine*, 13(10):1219–1227, sep 2007.

[158] Dilip S. Pillai, Baljinder S. Dhinsa, and Wasim S. Khan. Tissue Engineering in Achilles Tendon Reconstruction; The Role of Stem Cells, Growth Factors and Scaffolds. *Current Stem Cell Research & Therapy*, 12(6):506–512, may 2017.

[159] Daniel W. Youngstrom, Jade E. LaDow, and Jennifer G. Barrett. Tenogenesis of bone marrow-, adipose-, and tendon-derived stem cells in a dynamic bioreactor. *Connective Tissue Research*, 57(6):454–465, 2016.

[160] Hiroki Tsutsumi, Ryota Kurimoto, Ryo Nakamichi, Tomoki Chiba, Takahide Matsushima, Yuta Fujii, Risa Sanada, Tomomi Kato, Kana Shishido, Yuriko Sakamaki, Tsuyoshi Kimura, Akio Kishida, and Hiroshi Asahara. Generation of a tendon-like tissue from human iPS cells. *Journal of Tissue Engineering*, 13, 2022.

[161] Ratti Ram Sharma, Kathryn Pollock, Allison Hubel, and David McKenna. Mesenchymal stem or stromal cells: A review of clinical applications and manufacturing practices. *Transfusion*, 54(5):1418–1437, 2014.

[162] Ilias G. Petrou, Anthony Grognuz, Nathalie Hirt-Burri, Wassim Raffoul, and Lee Ann Laurent-Applegate. Cell therapies for tendons: Old cell choice for modern innovation. *Swiss Medical Weekly*, 144(3132):w13989–w13989, jul 2014.

[163] Ilze Donderwinkel, Rocky S. Tuan, Neil R. Cameron, and Jessica E. Frith. Tendon tissue engineering: Current progress towards an optimized tenogenic differentiation protocol for human stem cells. *Acta Biomaterialia*, 145:25–42, 2022.

[164] Megane Beldjilali-Labro, Alejandro Garcia Garcia, Firas Farhat, Fahmi Bedoui, Jean François Grosset, Murielle Dufresne, and Cécile Legallais. Biomaterials in tendon and skeletal muscle tissue engineering: Current trends and challenges. *Materials*, 11(7):1116, jun 2018.

[165] Chih Hao Chen, Shih Hsien Chen, Chang Yi Kuo, Meng Lun Li, and Jyh Ping Chen. Response of dermal fibroblasts to biochemical and physical cues in aligned

polycaprolactone/silk fibroin nanofiber scaffolds for application in tendon tissue engineering. *Nanomaterials*, 7(8), aug 2017.

[166] Wenbo Wang, Jing He, Bei Feng, Zhiyong Zhang, Wenjie Zhang, Guangdong Zhou, Yilin Cao, Wei Fu, and Wei Liu. Aligned nanofibers direct human dermal fibroblasts to tenogenic phenotype in vitro and enhance tendon regeneration in vivo. *Future Medicine*, 11(9):1055–1072, apr 2016.

[167] Grace Walden, Xin Liao, Simon Donell, Mike J. Raxworthy, Graham P. Riley, and Aram Saeed. A Clinical, Biological, and Biomaterials Perspective into Tendon Injuries and Regeneration. *Tissue Engineering Part B: Reviews*, 23(1):44–58, 2017.

[168] Abdullah Alkhenizan and Kossay Elabd. Non-therapeutic infant male circumcision: Evidence, ethics, and international law perspectives. *Saudi Medical Journal*, 37(9):941–947, sep 2016.

[169] Hsing I. Huang, Shao Kuan Chen, Robert Y.L. Wang, Chia Rui Shen, and Yu Che Cheng. Human foreskin fibroblast-like stromal cells can differentiate into functional hepatocytic cells. *Cell Biology International*, 37(12):1308–1319, dec 2013.

[170] Frank G. Lyons, Amir A. Al-Munajjed, Stephen M. Kieran, Mary E. Toner, Ciara M. Murphy, Garry P. Duffy, and Fergal J. O'Brien. The healing of bony defects by cell-free collagen-based scaffolds compared to stem cell-seeded tissue engineered constructs. *Biomaterials*, 31(35):9232–9243, dec 2010.

[171] Bryan N. Brown, Jolene E. Valentin, Ann M. Stewart-Akers, George P. McCabe, and Stephen F. Badylak. Macrophage phenotype and remodeling outcomes in response to biologic scaffolds with and without a cellular component. *Biomaterials*, 30(8):1482–1491, mar 2009.

[172] S. Van Vlierberghe, P. Dubruel, and E. Schacht. Biopolymer-based hydrogels as scaffolds for tissue engineering applications: A review. *Biomacromolecules*, 12(5):1387–1408, 2011.

[173] Ferry P.W. Melchels, Marco A.N. Domingos, Travis J. Klein, Jos Malda, Paulo J. Bartolo, and Dietmar W. Hutmacher. Additive manufacturing of tissues and organs. *Progress in Polymer Science*, 37(8):1079–1104, 2012.

[174] Shoufeng Yang, Kah-Fai E Leong, Zhaohui M E Du, and Chee-Kai Chua. The Design of Scaffolds for Use in Tissue Engineering. Part II. Rapid Prototyping Techniques. *Tissue Engineering*, 8(1), 2002.

[175] Shin Yokoya, Yu Mochizuki, Koji Natsu, Hiromichi Omae, Yoshihiko Nagata, and Mitsuo Ochi. Rotator cuff regeneration using a bioabsorbable material with bone marrow-derived mesenchymal stem cells in a rabbit model. *American Journal of Sports Medicine*, 40(6):1259–1268, jun 2012.

[176] Sarah Gniesmer, Ralph Brehm, Andrea Hoffmann, Dominik de Cassan, Henning Menzel, Anna Lena Hoheisel, Birgit Glasmacher, Elmar Willbold, Janin Reifenrath, Nils Ludwig, Ruediger Zimmerer, Frank Tavassol, Nils Claudius Gellrich, and Andreas Kampmann. Vascularization and biocompatibility of poly(ϵ-caprolactone) fiber mats for rotator cuff tear repair. *PLoS ONE*, 15(1), jan 2020.

[177] O. Hakimi, R. Murphy, U. Stachewicz, S. Hislop, and A. J. Carr. An electrospun polydioxanone patch for the localisation of biological therapies during tendon repair. *European Cells and Materials*, 24:344–357, 2012.

[178] Anthony Romeo, Jeremiah Easley, Dan Regan, Eileen Hackett, James Johnson, Jed Johnson, Christian Puttlitz, and Kirk McGilvray. Rotator cuff repair using a bioresorbable nanofiber interposition scaffold: a biomechanical and histologic

analysis in sheep. *Journal of Shoulder and Elbow Surgery*, 31(2):402–412, feb 2022.

[179] Nadeem Siddiqui, Simran Asawa, Bhaskar Birru, Ramaraju Baadhe, and Sreenivasa Rao. PCL-Based Composite Scaffold Matrices for Tissue Engineering Applications. *Molecular Biotechnology*, 60(7):506–532, 2018.

[180] Takashi Hoshiba, Chiaki Yoshikawa, and Keita Sakakibara. Characterization of Initial Cell Adhesion on Charged Polymer Substrates in Serum-Containing and Serum-Free Media. *Langmuir*, 34(13):4043–4051, apr 2018.

[181] Guobao Wei and Peter X. Ma. Polymeric biomaterials. In *Tissue Engineering Using Ceramics and Polymers*, pages 32–51. Woodhead Publishing, jan 2007.

[182] Deepak Gupta, Atul Kumar Singh, Neelakshi Kar, Ashwin Dravid, and Jayesh Bellare. Modelling and optimization of NaOH-etched 3-D printed PCL for enhanced cellular attachment and growth with minimal loss of mechanical strength. *Materials Science and Engineering C*, 98:602–611, may 2019.

[183] Justin L. Brown, Sangamesh G. Kumbar, and Brittany L. Banik. *Bio-Instructive Scaffolds for Musculoskeletal Tissue Engineering and Regenerative Medicine*. Elsevier Inc., nov 2016.

[184] Stefano Testa, Marco Costantini, Ersilia Fornetti, Sergio Bernardini, Marcella Trombetta, Dror Seliktar, Stefano Cannata, Alberto Rainer, and Cesare Gargioli. Combination of biochemical and mechanical cues for tendon tissue engineering. *Journal of Cellular and Molecular Medicine*, 21(11):2711–2719, 2017.

[185] William Okech and Catherine K. Kuo. Informing stem cell-based tendon tissue engineering approaches with embryonic tendon development. *Advances in Experimental Medicine and Biology*, 920:63–77, 2016.

[186] Alex Lopez Marquez, Iván Emilio Gareis, Fernando José Dias, Christoph Gerhard, and María Florencia Lezcano. How Fiber Surface Topography Affects Interactions between Cells and Electrospun Scaffolds: A Systematic Review, jan 2022.

[187] Ravi Sinha, Nico Verdonschot, Bart Koopman, and Jeroen Rouwkema. Tuning Cell and Tissue Development by Combining Multiple Mechanical Signals. *Tissue Engineering Part B: Reviews*, 23(5):494–504, 2017.

[188] Zhonggang Feng, Yu Tateishi, Yasutomo Nomura, Tatsuo Kitajima, and Takao Nakamura. Construction of fibroblast-collagen gels with orientated fibrils induced by static or dynamic stress: Toward the fabrication of small tendon grafts. *Journal of Artificial Organs*, 9(4):220–225, 2006.

[189] Chiara Rinoldi, Marco Costantini, Ewa Kijeńska-Gawrońska, Stefano Testa, Ersilia Fornetti, Marcin Heljak, Monika Ćwiklińska, Robert Buda, Jacopo Baldi, Stefano Cannata, Jan Guzowski, Cesare Gargioli, Ali Khademhosseini, and Wojciech Swieszkowski. Tendon Tissue Engineering: Effects of Mechanical and Biochemical Stimulation on Stem Cell Alignment on Cell-Laden Hydrogel Yarns. *Advanced Healthcare Materials*, 1801218:1–10, 2019.

[190] O. Friedrich, D. Schneidereit, Y. A. Nikolaev, V. Nikolova-Krstevski, S. Schürmann, A. Wirth-Hücking, A. L. Merten, D. Fatkin, and B. Martinac. Adding dimension to cellular mechanotransduction: Advances in biomedical engineering of multiaxial cell-stretch systems and their application to cardiovascular biomechanics and mechano-signaling. *Progress in Biophysics and Molecular Biology*, 130:170–191, 2017.

[191] A. S.T. Smith, S. Passey, L. Greensmith, V. Mudera, and M. P. Lewis. Characterization and optimization of a simple, repeatable system for the long term

in vitro culture of aligned myotubes in 3D. *Journal of Cellular Biochemistry*, 113(3):1044–1053, 2012.

[192] Lishu Feng, Yimei Zhang, Xiaoxing Kou, Ruili Yang, Dawei Liu, Xuedong Wang, Yang Song, Haifeng Cao, Danqing He, Yehua Gan, and Yanheng Zhou. Cadherin-11 modulates cell morphology and collagen synthesis in periodontal ligament cells under mechanical stress. *The Angle Orthodontist*, 00(00):193–199., 2016.

[193] Abigail R. Raveling, Sophia K. Theodossiou, and Nathan R. Schiele. A 3D printed mechanical bioreactor for investigating mechanobiology and soft tissue mechanics. *MethodsX*, 5:924–932, jan 2018.

[194] Manuela Teresa Raimondi, Matteo Laganà, Claudio Conci, Michele Crestani, Alessia Di Giancamillo, Francesca Gervaso, Daniela Deponti, Federica Boschetti, Michele M. Nava, Chiara Scandone, Cinzia Domeneghini, Alessandro Sannino, and Giuseppe M. Peretti. Development and biological validation of a cyclic stretch culture system for the ex vivo engineering of tendons. *International Journal of Artificial Organs*, 41(7):400–412, 2018.

[195] Yvonne Reinwald, Katherine H.L. Leonard, James R. Henstock, Jonathan P. Whiteley, James M. Osborne, Sarah L. Waters, Philippe Levesque, and Alicia J. El Haj. Evaluation of the Growth Environment of a Hydrostatic Force Bioreactor for Preconditioning of Tissue-Engineered Constructs. *Tissue Engineering Part C: Methods*, 21(1):1–14, 2015.

[196] Jonathan A. Kluge, Gary G. Leisk, Robyn D. Cardwell, Alexander P. Fernandes, Michael House, Andrew Ward, A. Luis Dorfmann, and David L. Kaplan. Bioreactor system using noninvasive imaging and mechanical stretch for biomaterial screening. *Annals of Biomedical Engineering*, 39(5):1390–1402, 2011.

[197] Colin Y.L. Woon, Armin Kraus, Shyam S. Raghavan, Brian C. Pridgen, Kai Megerle, Hung Pham, and James Chang. Three-Dimensional-Construct Bioreactor Conditioning in Human Tendon Tissue Engineering. *Tissue Engineering Part A*, 17(19-20):2561–2572, 2011.

[198] Marcus Stoffel, Wolfgang Willenberg, Marzieh Azarnoosh, Nadine Fuhrmann-Nelles, Bei Zhou, and Bernd Markert. Towards bioreactor development with physiological motion control and its applications. *Medical Engineering and Physics*, 39:106–112, 2017.

[199] Peter A. Galie and Jan P. Stegemann. Simultaneous Application of Interstitial Flow and Cyclic Mechanical Strain to a Three-Dimensional Cell-Seeded Hydrogel. *Tissue Engineering Part C: Methods*, 17(5):527–536, 2011.

[200] Wolfgang Willenberg, Marzieh Azarnoosh, Marcus Stoffel, and Bernd Markert. Experimental and numerical investigation of tendons and tendon cells. *Pamm*, 16(1):113–114, 2016.

[201] Jonathan A. Kluge, Gary G. Leisk, Robyn D. Cardwell, Alexander P. Fernandes, Michael House, Andrew Ward, A. Luis Dorfmann, and David L. Kaplan. Bioreactor system using noninvasive imaging and mechanical stretch for biomaterial screening. *Annals of Biomedical Engineering*, 39(5):1390–1402, 2011.

[202] Zhi Yong Zhang, Swee Hin Teoh, Erin Yiling Teo, Mark Seow Khoon Chong, Chong Woon Shin, Foo Toon Tien, Mahesh A. Choolani, and Jerry K.Y. Chan. A comparison of bioreactors for culture of fetal mesenchymal stem cells for bone tissue engineering. *Biomaterials*, 31(33):8684–8695, 2010.

[203] T. Takebe, S. Kobayashi, H. Kan, H. Suzuki, Y. Yabuki, M. Mizuno, T. Adegawa, T. Yoshioka, J. Tanaka, J. Maegawa, and H. Taniguchi. Human elastic cartilage engineering from cartilage progenitor cells using rotating wall vessel

bioreactor. In *Transplantation Proceedings*, volume 44, pages 1158–1161. Elsevier, may 2012.

[204] Eijiro Maeda, Yasufumi Hagiwara, James H-c Wang, and Toshiro Ohashi. A new experimental system for simultaneous application of cyclic tensile strain and fluid shear stress to tenocytes in vitro. *Biomedical Microdevices*, 15(6):1067–1075, 2013.

[205] Fiona E Freeman, Jessica Schiavi, Meadhbh A Brennan, Peter Owens, Pierre Layrolle, and Laoise McNamara. Mimicking the Biochemical and Mechanical Extracellular Environment of the Endochondral Ossification Process to Enhance the In Vitro Mineralization Potential of Human MSCs. *Tissue Engineering Part A*, 23(Cmi):ten.TEA.2017.0052, 2017.

[206] Tae Yun Kang, Jung Min Hong, Bum Jin Kim, Hyung Joon Cha, and Dong Woo Cho. Enhanced endothelialization for developing artificial vascular networks with a natural vessel mimicking the luminal surface in scaffolds. *Acta Biomaterialia*, 9(1):4716–4725, 2013.

[207] Dongeun Huh, Benjamin D. Matthews, Akiko Mammoto, Martin Montoya-Zavala, Hong Yuan Hsin, and Donald E. Ingber. Reconstituting organ-level lung functions on a chip. *Science*, 328(5986):1662–1668, 2010.

[208] Ekta Pandey, Keerti Srivastava, Saurabh Gupta, Suravi Srivastava, and Nidhi Mishra. Some Biocompatible Materials Used in Medical Practices-a Review. *International Journal of Pharmaceutical Sciences and Research IJPSR*, 7(7):2748–2755, 2016.

[209] Pierre-Alexis Mouthuy, Sarah Snelling, Rafael Hostettler, Alona Kharchenko, Sarah Salmon, Alan Wainman, Jolet Mimpen, Claudia Paul, and Andrew Carr.

Humanoid robots to mechanically stress human cells grown in soft bioreactors. *Communications Engineering*, 1(1):1–11, 2022.

[210] Amra Secerovic, Aapo Ristaniemi, Shangbin Cui, Zhen Li, Astrid Soubrrier, Mauro Alini, Stephen J Ferguson, Gilles Weder, Sarah Heub, Diane Ledroit, and Sibylle Grad. Toward the Next Generation of Spine Bioreactors: Validation of an Ex Vivo Intervertebral Disc Organ Model and Customized Specimen Holder for Multiaxial Loading. *ACS Biomaterials Science and Engineering*, 8(9):3969–3976, 2022.

[211] Cody Fell, Trent L. Brooks-Richards, Maria A. Woodruff, and Mark C. Allenby. Soft pneumatic actuators for mimicking multi-axial femoropopliteal artery mechanobiology. *Biofabrication*, 14(3), 2022.

[212] Jungwook Paek, Joseph W. Song, Ehsan Ban, Yuma Morimitsu, Chinedum O. Osuji, Vivek B. Shenoy, and Dan Dongeun Huh. Soft robotic constrictor for in vitro modeling of dynamic tissue compression. *Scientific Reports*, 11(1):16478, dec 2021.

[213] Fionnuala Connolly, Conor J. Walsh, and Katia Bertoldi. Automatic design of fiber-reinforced soft actuators for trajectory matching. *Proceedings of the National Academy of Sciences of the United States of America*, 114(1):51–56, 2017.

[214] Ellen T. Roche, Markus A. Horvath, Isaac Wamala, Ali Alazmani, Sang Eun Song, William Whyte, Zurab Machaidze, Christopher J. Payne, James C. Weaver, Gregory Fishbein, Joseph Kuebler, Nikolay V. Vasilyev, David J. Mooney, Frank A. Pigula, and Conor J. Walsh. Soft robotic sleeve supports heart function. *Science Translational Medicine*, 9(373):1–12, 2017.

[215] Jaehong Lee, Stephan J. Ihle, Guglielmo Salvatore Pellegrino, Hwajoong Kim, Junwoo Yea, Chang Yeop Jeon, Hee Chang Son, Chaewon Jin, Daniel Eberli, Florian Schmid, Byron Llerena Zambrano, Aline F. Renz, Csaba Forró, Hongsoo Choi, Kyung In Jang, Roland Küng, and Janos Vörös. Stretchable and suturable fibre sensors for wireless monitoring of connective tissue strain. *Nature Electronics*, 4(4):291–301, 2021.

[216] Yuxin Liu, Jinxing Li, Shang Song, Jiheong Kang, Yuchi Tsao, Shucheng Chen, Vittorio Mottini, Kelly McConnell, Wenhui Xu, Yu Qing Zheng, Jeffrey B.H. Tok, Paul M. George, and Zhenan Bao. Morphing electronics enable neuromodulation in growing tissue. *Nature Biotechnology*, 38(9):1031–1036, 2020.

[217] Clementine M. Boutry, Levent Beker, Yukitoshi Kaizawa, Christopher Vassos, Helen Tran, Allison C. Hinckley, Raphael Pfattner, Simiao Niu, Junheng Li, Jean Claverie, Zhen Wang, James Chang, Paige M. Fox, and Zhenan Bao. Biodegradable and flexible arterial-pulse sensor for the wireless monitoring of blood flow. *Nature Biomedical Engineering*, 3(1):47–57, 2019.

[218] Clementine M. Boutry, Yukitoshi Kaizawa, Bob C. Schroeder, Alex Chortos, Anaïs Legrand, Zhen Wang, James Chang, Paige Fox, and Zhenan Bao. A stretchable and biodegradable strain and pressure sensor for orthopaedic application. *Nature Electronics*, 1(5):314–321, 2018.

[219] Pierre-Alexis Mouthuy and Andrew Carr. Growing tissue grafts on humanoid robots : A future strategy in regenerative medicine? *Science Robotics*, 2(4):1–3, 2017.

[220] Moloud Baghbadorani, Ashkan Bigham, Mohammad Rafienia, and Hossein Salehi. In vitro Studies of Polycaprolactone Nanofibrous Scaffolds Contain-

ing Novel Gehlenite Nanoparticles. *Journal of Medical Signals and Sensors*, 11(2):131–137, apr 2021.

[221] David L. Butler, Edward S. Grood, Frank R. Noyes, Ronald F. Zernicke, and Kim Brackett. Effects of structure and strain measurement technique on the material properties of young human tendons and fascia. *Journal of Biomechanics*, 17(8):579–596, 1984.

[222] Andrew S. LaCroix, Sarah E. Duenwald-Kuehl, Roderic S. Lakes, and Ray Vanderby. Relationship between tendon stiffness and failure: A metaanalysis. *Journal of Applied Physiology*, 115(1):43–51, jul 2013.

[223] H. G. Marques, C. Maufroy, A. Lenz, K. Dalamagkidis, and U Culha. 6th International Symposium on Adaptive Motion of Animals and Machines (AMAM 2013), Darmstadt, Germany, March 11-14, 2013 (Technique Universitaet Darmstadt, 2013).

[224] Akhilandeshwari Ravichandran, Yuchun Liu, and Swee Hin Teoh. Bioreactor design towards generation of relevant engineered tissues: Focus on clinical translation. *Journal of Tissue Engineering and Regenerative Medicine*, 12:e7–e22, 2018.

[225] Renwang Sheng, Yujie Jiang, Ludvig J Backman, Wei Zhang, and Jialin Chen. The Application of Mechanical Stimulations in Tendon Tissue Engineering. *Stem Cells International*, 2020:1–14, 2020.

[226] Muhammad Shakeel, Paul C. Matthews, Richard S. Graham, and Sarah L. Waters. A continuum model of cell proliferation and nutrient transport in a perfusion bioreactor. *Mathematical Medicine and Biology*, 30(1):21–44, 2013.

[227] Michael J. Osiecki, Sean D.L. McElwain, and William B. Lott. Modelling mesenchymal stromal cell growth in a packed bed bioreactor with a gas permeable wall. *PLoS ONE*, 13(8):1–34, 2018.

[228] James C.Y. Dunn, Wan Yin Chan, Vittorio Cristini, J. S. Kim, John Lowengrub, Shivani Singh, and Benjamin M. Wu. Analysis of cell growth in three-dimensional scaffolds. *Tissue Engineering*, 12(4):705–716, 2006.

[229] Paul Thevenot, Ashwin Nair, Jagannath Dey, Jian Yang, and Liping Tang. Method to analyze three-dimensional cell distribution and infiltration in degradable scaffolds. *Tissue Engineering - Part C: Methods*, 14(4):319–331, 2008.

[230] Gayathri Subramanian, Mostafa Elsaadany, Callan Bialorucki, and Eda Yildirim-Ayan. Creating homogenous strain distribution within 3D cell-encapsulated constructs using a simple and cost-effective uniaxial tensile bioreactor: Design and validation study. *Biotechnology and Bioengineering*, 114(8):1878–1887, 2017.

[231] Qinggong Tang, CHhrlotte Piard, Jonathan Lin, Kai Nan, Ting Guo, John Caccamese, John Fisher, and Yu Chen. Imaging stem cell distribution, growth, migration, and differentiation in 3-D scaffolds for bone tissue engineering using mesoscopic fluorescence tomography. *Physiology & behavior*, pages 257–265, 2018.

[232] Limin Wang, Kiran Seshareddy, Mark L Weiss, and Michael S Detamore. Effect of initial seeding density on human umbilical cord mesenchymal stromal cells for fibrocartilage tissue engineering. *Tissue Engineering - Part A*, 15(5):1009–1017, 2009.

[233] Alejandro J Almarza and Kyriacos A Athanasiou. Effects of initial cell seeding density for the tissue engineering of the temporomandibular joint disc. *Annals of Biomedical Engineering*, 33(7):943–950, 2005.

[234] Lucy A. Bosworth, Sarah R. Rathbone, and Sarah H. Cartmell. Optimizing attachment of human mesenchymal stem cells on poly(ϵ-caprolactone) electrospun yarns. *Journal of Visualized Experiments*, 2015(98):1–7, 2015.

[235] R. E. Abhari, P. A. Mouthuy, A. Vernet, J. E. Schneider, C. P. Brown, and A. J. Carr. Using an industrial braiding machine to upscale the production and modulate the design of electrospun medical yarns. *Polymer Testing*, 69(May):188–198, 2018.

[236] B. Saad and U.W. Suter. Biodegradable Polymeric Materials. In *Encyclopedia of Materials: Science and Technology*, pages 551–555. Elsevier, jan 2001.

[237] L. A. Bosworth, S. R. Rathbone, R. S. Bradley, and S. H. Cartmell. Dynamic loading of electrospun yarns guides mesenchymal stem cells towards a tendon lineage. *Journal of the Mechanical Behavior of Biomedical Materials*, 39:175–183, 2014.

[238] Erica L. Scheller, Nancy Troiano, Joshua N. Vanhoutan, Mary A. Bouxsein, Jackie A. Fretz, Yougen Xi, Tracy Nelson, Griffin Katz, Ryan Berry, Christopher D. Church, Casey R. Doucette, Matthew S. Rodeheffer, Ormond A. MacDougald, Clifford J. Rosen, and Mark C. Horowitz. Use of osmium tetroxide staining with microcomputerized tomography to visualize and quantify bone marrow adipose tissue in vivo. *Methods in Enzymology*, 537:123–139, 2014.

[239] Mark Müller, Melanie A. Kimm, Simone Ferstl, Sebastian Allner, Klaus Achterhold, Julia Herzen, Franz Pfeiffer, and Madleen Busse. Nucleus-specific X-ray stain for 3D virtual histology. *Scientific Reports*, 8(1):1–10, 2018.

[240] Madleen Busse, Mark Müller, Melanie A. Kimm, Simone Ferstl, Sebastian Allner, Klaus Achterhold, Julia Herzen, and Franz Pfeiffer. Three-dimensional virtual histology enabled through cytoplasm-specific X-ray stain for microscopic and nanoscopic computed tomography. *Proceedings of the National Academy of Sciences of the United States of America*, 115(10):2293–2298, 2018.

[241] Michael J. Osiecki, Thomas D. Michl, Betul Kul Babur, Mahboubeh Kabiri, Kerry Atkinson, William B. Lott, Hans J. Griesser, and Michael R. Doran. Packed bed bioreactor for the isolation and expansion of placental-derived mesenchymal stromal cells. *PLoS ONE*, 10(12):1–18, 2015.

[242] Archana M. Navale and Archana N. Paranjape. Glucose transporters: physiological and pathological roles. *Biophysical Reviews*, 8(1):5–9, mar 2016.

[243] Alexei Vazquez, Jiangxia Liu, Yi Zhou, and Zoltán N. Oltvai. Catabolic efficiency of aerobic glycolysis: The Warburg effect revisited. *BMC Systems Biology*, 4(1):1–9, may 2010.

[244] Avi Flamholz, Rob Phillips, and Ron Milo. The quantified cell. *Molecular Biology of the Cell*, 25(22):3497–3500, 2014.

[245] Alice Limonciel, Lydia Aschauer, Anja Wilmes, Sinikka Prajczer, Martin O. Leonard, Walter Pfaller, and Paul Jennings. Lactate is an ideal non-invasive marker for evaluating temporal alterations in cell stress and toxicity in repeat dose testing regimes. *Toxicology in Vitro*, 25(8):1855–1862, 2011.

[246] Stephen Britland, Oliver Ross-Smith, Humzah Jamil, Annie G. Smith, Kath Vowden, and Peter Vowden. The lactate conundrum in wound healing: Clinical and experimental findings indicate the requirement for a rapid point-of-care diagnostic. *Biotechnology Progress*, 28(4):917–924, 2012.

[247] S. R. McKeown. Defining normoxia, physoxia and hypoxia in tumours - Implications for treatment response. *British Journal of Radiology*, 87(1035), mar 2014.

[248] Colleen M Snyder and Navdeep S Chandel. Mitochondrial regulation of cell survival and death during low-oxygen conditions. *Antioxidants and Redox Signaling*, 11(11):2673–2683, 2009.

[249] Douglas S. Steinbrech, Michael T. Longaker, Babak J. Mehrara, Pierre B. Saadeh, Gyu S. Chin, Rene P. Gerrets, Dorothy C. Chau, Norman M. Rowe, and George K. Gittes. Fibroblast response to hypoxia: The relationship between angiogenesis and matrix regulation. *Journal of Surgical Research*, 84(2):127–133, 1999.

[250] Bin Zhao, Hao Guan, Jia Qi Liu, Zhao Zheng, Qin Zhou, Jian Zhang, Lin Lin Su, and Da Hai Hu. Hypoxia drives the transition of human dermal fibroblasts to a myofibroblast-like phenotype via the TGF-β1/Smad3 pathway. *International Journal of Molecular Medicine*, 39(1):153–159, jan 2017.

[251] Rachel H Coy, Owen R Evans, James B Phillips, and Rebecca J Shipley. An integrated theoretical-experimental approach to accelerate translational tissue engineering. *Journal of Tissue Engineering and Regenerative Medicine*, 12(1):e53–e59, 2018.

[252] S L Waters, L J Schumacher, and A. J. El Haj. Regenerative medicine meets mathematical modelling: developing symbiotic relationships. *npj Regenerative Medicine*, 6(1), 2021.

[253] Natalie C. Pearson, Rebecca J. Shipley, Sarah L. Waters, and James M. Oliver. Multiphase modelling of the influence of fluid flow and chemical concentration

on tissue growth in a hollow fibre membrane bioreactor. *Mathematical Medicine and Biology*, 31(4):393–430, 2014.

[254] R. J. Shipley, A. J. Davidson, K. Chan, J. B. Chaudhuri, S. L. Waters, and M. J. Ellis. A strategy to determine operating parameters in tissue engineering hollow fiber bioreactors. *Biotechnology and Bioengineering*, 108(6):1450–1461, 2011.

[255] Michael J. Osiecki, Sean D.L. McElwain, and William B. Lott. Modelling mesenchymal stromal cell growth in a packed bed bioreactor with a gas permeable wall. *PLoS ONE*, 13(8):1–34, 2018.

[256] Francesco Coletti, Sandro Macchietto, and Nicola Nlvassore. Mathematical modelling of three-dimensional cell cultures in perfusion bioreactors. Part II. *Computer Aided Chemical Engineering*, 21(C):1699–1704, 2006.

[257] Lauren Hyndman, Sean McKee, Nigel J Mottram, Bhumika Singh, Steven D Webb, and Sean McGinty. Mathematical modelling of fluid flow and solute transport to define operating parameters for in vitro perfusion cell culture systems. *Interface Focus*, 10(20190045), 2020.

[258] Jared W. Allen and Sangeeta N. Bhatia. Formation of steady-state oxygen gradients in vitro: Application to liver zonation. *Biotechnology and Bioengineering*, 82(3):253–262, may 2003.

[259] Myat Noe Hsu, Guo Dong Sean Tan, Marshella Tania, Erik Birgersson, and Hwa Liang Leo. Computational fluid model incorporating liver metabolic activities in perfusion bioreactor. *Biotechnology and Bioengineering*, 111(5):885–895, may 2014.

[260] Natalie C. Pearson, Sarah L. Waters, James M. Oliver, and Rebecca J. Shipley. Multiphase modelling of the effect of fluid shear stress on cell yield and distri-

bution in a hollow fibre membrane bioreactor. *Biomechanics and Modeling in Mechanobiology*, 14(2):387–402, 2015.

[261] COMSOL Multiphysics® v. 5.6. www.comsol.com. COMSOL AB, Stockholm, Sweden.

[262] Sebastian Prill, Magnus S. Jaeger, and Claus Duschl. Long-term microfluidic glucose and lactate monitoring in hepatic cell culture. *Biomicrofluidics*, 8(3):1–9, 2014.

[263] Trenton L. Place, Frederick E. Domann, and Adam J. Case. Limitations of oxygen delivery to cells in culture: An underappreciated problem in basic and translational research. *Free Radical Biology and Medicine*, 113(October):311–322, 2017.

[264] Johannes Schindelin, Ignacio Arganda-Carreras, Erwin Frise, Verena Kaynig, Mark Longair, Tobias Pietzsch, Stephan Preibisch, Curtis Rueden, Stephan Saalfeld, Benjamin Schmid, Jean-Yves Tinevez, Daniel James White, Volker Hartenstein, Kevin Eliceiri, Pavel Tomancak, and Albert Cardona. Fiji: an open-source platform for biological-image analysis. *Nature Methods*, 9(7):676–682, jul 2012.

[265] Don W. Green and Robert H. Perry. *Perry's Chemical Engineers' Handbook, Eighth Edition*. McGraw-Hill Education, 2008.

[266] C. Kleinstreuer and S. S. Agarwal. Analysis and simulation of hollow-fiber bioreactor dynamics. *Biotechnology and Bioengineering*, 28(8):1233–1240, aug 1986.

[267] Girish Pattappa, Hannah K. Heywood, Joost D. de Bruijn, and David A. Lee. The metabolism of human mesenchymal stem cells during proliferation and differentiation. *Journal of Cellular Physiology*, 226(10):2562–2570, oct 2011.

[268] Davod Mohebbi-Kalhori, Amin Behzadmehr, Charles J Doillon, and Afra Hadjizadeh. Computational modeling of adherent cell growth in a hollow-fiber membrane bioreactor for large-scale 3-D bone tissue engineering. *Journal of Artificial Organs*, 15(3):250–265, 2012.

[269] Jorun Øyaas, Ivar Storrø, Hallvard Svendsen, and David W Levine. The effective diffusion coefficient and the distribution constant for small molecules in calcium-alginate gel beads. *Biotechnology and Bioengineering*, 47(4):492–500, 1995.

[270] Foucher; Christopher D. and Tubben Robert E. Lactic acidosis, jul 2005.

[271] Feng Zhao, Pragyansri Pathi, Warren Grayson, Qi Xing, Bruce R. Locke, and Teng Ma. Effects of oxygen transport on 3-D human mesenchymal stem cell metabolic activity in perfusion and static cultures: Experiments and mathematical model. *Biotechnology Progress*, 21(4):1269–1280, jan 2008.

[272] Danilo Donato, Ilaria E. De Napoli, and Gerardo Catapano. Model-based optimization of scaffold geometry and operating conditions of radial flow packed-bed bioreactors for therapeutic applications. *Processes*, 2(1):34–57, jan 2014.

[273] Philip K. Maini, D. L.Sean McElwain, and David I. Leavesley. Traveling Wave Model to Interpret a Wound-Healing Cell Migration Assay for Human Peritoneal Mesothelial Cells. *Tissue Engineering*, 10(3-4):475–482, 2004.

[274] Saheli Sarkar, Bethany L Bustard, Jean F Welter, and Harihara Baskaran. Combined experimental and mathematical approach for development of microfabrication-based cancer migration assay. *Annals of Biomedical Engineering*, 39(9):2346–2359, 2011.

[275] Narges Abdian, Payam Ghasemi-Dehkordi, Morteza Hashemzadeh-Chaleshtori, Mahbobe Ganji-Arjenaki, Abbas Doosti, and Beheshteh Amiri. Comparison of

human dermal fibroblasts (HDFs) growth rate in culture media supplemented with or without basic fibroblast growth factor (bFGF). *Cell and Tissue Banking*, 16(4):487–495, 2015.

[276] Marina Campolo, Francesco Curcio, and Alfredo Soldati. Minimal perfusion flow for osteogenic growth of mesenchymal stem cells on lattice scaffolds. *AIChE Journal*, 59(8):3131–3144, 2013.

[277] Deborah Schop, Frank W Janssen, Linda D.S. Van Rijn, Hugo Fernandes, Rolf M Bloem, Joost D. De Bruijn, and Riemke Van Dijkhuizen-Radersma. Growth, metabolism, and growth inhibitors of mesenchymal stem cells. *Tissue Engineering - Part A*, 15(8):1877–1886, 2009.

[278] G. A. Ateshian, K. D. Costa, and C. T. Hung. A theoretical analysis of water transport through chondrocytes. *Biomechanics and Modeling in Mechanobiology*, 6(1-2):91–101, jan 2007.

[279] CP Ng, B Hinz, and M Swartz. Contribution of interstitial fluid flow to fibroblast alignment and differentiation. *Wound Repair and Regeneration*, 13(Project 73948):23–a23, 2004.

[280] Michael Lavagnino, Steven P Arnoczky, Eugene Kepich, Oscar Caballero, and Roger C. Haut. A finite element model predicts the mechanotransduction response of tendon cells to cyclic tensile loading. *Biomechanics and Modeling in Mechanobiology*, 7(5):405–416, 2008.

[281] S Han, S. J. Gemmell, K. G. Helmer, P Grigg, J. W. Wellen, A. H. Hoffman, and C. H. Sotak. Changes in ADC Caused by Tensile Loading of Rabbit Achilles Tendon: Evidence for Water Transport. *Journal of Magnetic Resonance*, 144(2):217–227, jun 2000.

[282] Anna F. Europa, Anshu Gambhir, Peng Cheng Fu, and Wei Shou Hu. Multiple steady states with distinct cellular metabolism in continuous culture of mammalian cells. *Biotechnology and Bioengineering*, 67(1):25–34, 2000.

[283] Abdullah Al-Ani, Derek Toms, Douglas Kondro, Jarin Thundathil, Yang Yu, and Mark Ungrin. Oxygenation in cell culture: Critical parameters for reproducibility are routinely not reported. *PLoS ONE*, 13(10):e0204269, oct 2018.

[284] Frederick Domann and Place. Prolyl-hydroxylase 3: evolving roles for an ancient signaling protein. *Hypoxia*, 1:13–27, oct 2013.

[285] Maija Hirsilä, Peppi Koivunen, Volkmar Günzler, Kari I. Kivirikko, and Johanna Myllyharju. Characterization of the human prolyl 4-hydroxylases that modify the hypoxia-inducible factor. *Journal of Biological Chemistry*, 278(33):30772–30780, aug 2003.

[286] Dominic Ehrismann, Emily Flashman, David N. Genn, Nicolas Mathioudakis, Kirsty S. Hewitson, Peter J. Ratcliffe, and Christopher J. Schofield. Studies on the activity of the hypoxia-inducible-factor hydroxylases using an oxygen consumption assay. *Biochemical Journal*, 401(1):227–234, jan 2007.

[287] Peppi Koivunen, Maija Hirsilä, Kari I. Kivirikko, and Johanna Myllyharju. The length of peptide substrates has a marked effect on hydroxylation by the hypoxia-inducible factor prolyl 4-hydroxylases. *Journal of Biological Chemistry*, 281(39):28712–28720, sep 2006.

[288] Min Liang, Hannah R. Cornell, Nasim Zargar Baboldashti, Mark S. Thompson, Andrew J. Carr, and Philippa A. Hulley. Regulation of Hypoxia-Induced Cell Death in Human Tenocytes. *Advances in Orthopedics*, 2012:1–12, 2012.

[289] Yun Bai, Murray Moo-Young, and William A. Anderson. A mechanistic model for gas–liquid mass transfer prediction in a rocking disposable bioreactor. *Biotechnology and Bioengineering*, 116(8):1986–1998, 2019.

[290] A. N. Rao, M. N. Avula, and D. W. Grainger. 3.34 Biomaterials Challenges in Continuous Glucose Monitors In Vivo. *Comprehensive Biomaterials II*, pages 755–770, jan 2017.

[291] Maarten Sonnaert, Ioannis Papantoniou, Frank P. Luyten, and Jan Schrooten. Quantitative Validation of the Presto Blue™ Metabolic Assay for Online Monitoring of Cell Proliferation in a 3D Perfusion Bioreactor System. *Tissue Engineering - Part C: Methods*, 21(6):519–529, 2015.

[292] Abbott. ARCHITECT Concentrated Glucose Reaction Kit Manual 3L82-41. Technical report, 2017.

[293] Katrin Pontius, Daria Semenova, Yuliya E. Silina, Krist V. Gernaey, and Helena Junicke. Automated Electrochemical Glucose Biosensor Platform as an Efficient Tool Toward On-Line Fermentation Monitoring: Novel Application Approaches and Insights. *Frontiers in Bioengineering and Biotechnology*, 8(May):1–15, 2020.

[294] Rebecca L. Dahlin, F. Kurtis Kasper, and Antonios G. Mikos. Polymeric nanofibers in tissue engineering. *Tissue Engineering - Part B: Reviews*, 17(5):349–364, jul 2011.

[295] W. Janvikul, P. Uppanan, B. Thavornyutikarn, W. Kosorn, and P. Kaewkong. Effects of surface topography, hydrophilicity and chemistry of surface-treated PCL scaffolds on chondrocyte infiltration and ECM production. *Procedia Engineering*, 59:158–165, 2013.

[296] Seyed Mohammad Amin Haramshahi, Shahin Bonakdar, Mehdi Moghtadaei, Khorshid Kamguyan, Esben Thormann, Sara Tanbakooei, Sara Simorgh, Peiman Brouki-Milan, Naser Amini, Noorahmad Latifi, Mohammad Taghi Joghataei, Ali Samadikuchaksaraei, Majid Katebi, and Mansoureh Soleimani. Tenocyte-imprinted substrate: A topography-based inducer for tenogenic differentiation in adipose tissue-derived mesenchymal stem cells. *Biomedical Materials (Bristol)*, 15(3), 2020.

[297] Alex Lopez Marquez, Iván Emilio Gareis, Fernando José Dias, Christoph Gerhard, and María Florencia Lezcano. How Fiber Surface Topography Affects Interactions between Cells and Electrospun Scaffolds: A Systematic Review. *Polymers*, 14(1):209, 2022.

[298] Behnam Liaghat, Søren T. Skou, Jens Søndergaard, Eleanor Boyle, Karen Søgaard, and Birgit Juul-Kristensen. A randomised controlled trial of heavy shoulder strengthening exercise in patients with hypermobility spectrum disorder or hypermobile Ehlers-Danlos syndrome and long-lasting shoulder complaints: study protocol for the Shoulder-MOBILEX study. *Trials*, 21(1):1–18, dec 2020.

[299] Peter Malliaras, Renea Johnston, Gabriele Street, Chris Littlewood, Kim Bennell, Terry Haines, and Rachelle Buchbinder. The Efficacy of Higher Versus Lower Dose Exercise in Rotator Cuff Tendinopathy: A Systematic Review of Randomized Controlled Trials. *Archives of Physical Medicine and Rehabilitation*, 101(10):1822–1834, oct 2020.

[300] Behnam Liaghat, Søren T Skou, Jens Søndergaard, Eleanor Boyle, Karen Søgaard, and Birgit Juul-Kristensen. Short-term effectiveness of high-load compared with low-load strengthening exercise on self-reported function in patients

with hypermobile shoulders: a randomised controlled trial. *Br J Sports Med*, 0:1–10, 2022.

[301] Josh Naunton, Gabrielle Street, Chris Littlewood, Terrence Haines, and Peter Malliaras. Effectiveness of progressive and resisted and non-progressive or non-resisted exercise in rotator cuff related shoulder pain: a systematic review and meta-analysis of randomized controlled trials. *Clinical Rehabilitation*, 34(9):1198–1216, sep 2020.

[302] Hiroki Miyamoto, Mitsuhiro Aoki, Egi Hidaka, Mineko Fujimiya, and Eiichi Uchiyama. Measurement of strain and tensile force of the supraspinatus tendon under conditions that simulates low angle isometric elevation of the glenohumeral joint: Influence of adduction torque and joint positioning. *Clinical Biomechanics*, 50:92–98, dec 2017.

[303] Zymo Research, RNA Clean and Concentrator Kit-5.

[304] Philippe Favre, Marco Senteler, Jasmin Hipp, Simon Scherrer, Christian Gerber, and Jess G. Snedeker. An integrated model of active glenohumeral stability. *Journal of Biomechanics*, 45(13):2248–2255, 2012.

[305] Naomi Oizumi, Shigeru Tadano, Youichi Narita, Naoki Suenaga, Norimasa Iwasaki, and Akio Minami. Numerical analysis of cooperative abduction muscle forces in a human shoulder joint. *Journal of Shoulder and Elbow Surgery*, 15(3):331–338, 2006.

[306] Yaping Wang, Jingrong Wang, Rui Gao, Xiang Liu, Zujian Feng, Chuangnian Zhang, Pingsheng Huang, Anjie Dong, Deling Kong, and Weiwei Wang. Biomimetic glycopeptide hydrogel coated PCL/nHA scaffold for enhanced cranial bone regeneration via macrophage M2 polarization-induced osteoimmunomodulation. *Biomaterials*, 285:121538, jun 2022.

[307] Nae Gyune Rim, Ji Hye Lee, Sung In Jung, Bu Kyu Lee, Chun Ho Kim, and Heungsoo Shin. Modulation of osteogenic differentiation of human mesenchymal stem cells by poly[(L-lactide)-co-(ϵ-caprolactone)]/gelatin nanofibers. *Macromolecular Bioscience*, 9(8):795–804, aug 2009.

[308] Wei Fu, Zhenling Liu, Bei Feng, Renjie Hu, Xiaomin He, Hao Wang, Meng Yin, Huimin Huang, Haibo Zhang, and Wei Wang. Electrospun gelatin/PCL and collagen/PLCL scaffolds for vascular tissue engineering. *International Journal of Nanomedicine*, 9(1):2335–2344, 2014.

[309] Sarah K. Czaplewski, Tsung Lin Tsai, Sarah E. Duenwald-Kuehl, Ray Vanderby, and Wan Ju Li. Tenogenic differentiation of human induced pluripotent stem cell-derived mesenchymal stem cells dictated by properties of braided submicron fibrous scaffolds. *Biomaterials*, 35(25):6907–6917, 2014.

[310] John G. Barber, Andrew M. Handorf, Tyler J. Allee, and Wan Ju Li. Braided nanofibrous scaffold for tendon and ligament tissue engineering. *Tissue Engineering - Part A*, 19(11-12):1265–1274, jun 2013.

[311] Maria Ann Woodruff and Dietmar Werner Hutmacher. The return of a forgotten polymer - Polycaprolactone in the 21st century. *Progress in Polymer Science (Oxford)*, 35(10):1217–1256, 2010.

[312] Anuradha Subramanian, Uma Maheswari Krishnan, and Swaminathan Sethuraman. Development of biomaterial scaffold for nerve tissue engineering: Biomaterial mediated neural regeneration. *Journal of biomedical science*, 16(1):108, nov 2009.

[313] Taimoor H. Qazi, David J. Mooney, Matthias Pumberger, Sven Geissler, and Georg N. Duda. Biomaterials based strategies for skeletal muscle tissue en-

gineering: Existing technologies and future trends. *Biomaterials*, 53:502–521, 2015.

[314] Beata Zylińska, Ewa Stodolak-Zych, Aleksandra Sobczyńska-Rak, Tomasz Szponder, Piotr Silmanowicz, Mirosław Łańcut, Łukasz Jarosz, Paweł Rozański, and Izabela Polkowska. Osteochondral repair using porous three-dimensional nanocomposite scaffolds in a rabbit model. *In Vivo*, 31(5):895–903, 2017.

[315] Biswadeep Chaudhuri, Debabrata Bhadra, Lorenzo Moroni, and Krishna Pramanik. Myoblast differentiation of human mesenchymal stem cells on graphene oxide and electrospun graphene oxide-polymer composite fibrous meshes: Importance of graphene oxide conductivity and dielectric constant on their biocompatibility. *Biofabrication*, 7(1):015009, feb 2015.

[316] J. Venugopal, Y. Z. Zhang, and S. Ramakrishna. Fabrication of modified and functionalized polycaprolactone nanofibre scaffolds for vascular tissue engineering. *Nanotechnology*, 16(10):2138–2142, aug 2005.

[317] J. A. Ray, N. Doddi, D. Regula, J. A. Williams, and A. Melveger. Polydioxanone (PDA). A novel monofilament synthetic absorbable suture: J. A. Ray, N. Doddi, D. Regula, J. A. Williams and A. Melveger Surg Gynecol Obstet 153:497–506, (October), 1981. *Journal of Pediatric Surgery*, 17(2):205–206, apr 1982.

[318] Nowsheen Goonoo, Roubeena Jeetah, Archana Bhaw-Luximon, and Dhanjay Jhurry. Polydioxanone-based bio-materials for tissue engineering and drug/gene delivery applications. *European Journal of Pharmaceutics and Biopharmaceutics*, 97:371–391, 2015.

[319] Hani A. Awad, David L. Butler, Matthew T. Harris, Rania E. Ibrahim, Ying Wu, Randell G. Young, Sudha Kadiyala, and Gregory P. Boivin. In vitro characterization of mesenchymal stem cell-seeded collagen scaffolds for tendon repair:

Effects of initial seeding density on contraction kinetics. *Journal of Biomedical Materials Research*, 51(2):233–240, 2000.

[320] Rita I. Issa, Brandon Engebretson, Laurence Rustom, Peter S. McFetridge, and Vassilios I. Sikavitsas. The effect of cell seeding density on the cellular and mechanical properties of a mechanostimulated tissue-engineered Tendon. *Tissue Engineering - Part A*, 17(11-12):1479–1487, jun 2011.

[321] Robabeh Gharaei, Giuseppe Tronci, Robert P.W. Davies, Caroline Gough, Reem Alazragi, Parikshit Goswami, and Stephen J. Russell. A structurally self-assembled peptide nano-architecture by one-step electrospinning. *Journal of Materials Chemistry B*, 4(32):5475–5485, aug 2016.

[322] Shannon Y. Wu, Won Kim, and Thomas J. Kremen. In Vitro Cellular Strain Models of Tendon Biology and Tenogenic Differentiation. *Frontiers in Bioengineering and Biotechnology*, 10(February):1–15, 2022.

[323] Armin Kraus, Colin Woon, Shyam Raghavan, Kai Megerle, Hung Pham, and James Chang. Co-culture of human adipose-derived stem cells with tenocytes increases proliferation and induces differentiation into a tenogenic lineage. *Plastic and Reconstructive Surgery*, 132(5):754e–766e, nov 2013.

[324] Yiwei Qiu, Xiao Wang, Yaonan Zhang, Andrew J. Carr, Liwei Zhu, Zhidao Xia, and Afsie Sabokbar. Development of a refined tenocyte differentiation culture technique for tendon tissue engineering. *Cells Tissues Organs*, 197(1):27–36, 2013.

[325] Jeffrey P. Brown, Thomas V. Galassi, Matteo Stoppato, Nathan R. Schiele, and Catherine K. Kuo. Comparative analysis of mesenchymal stem cell and embryonic tendon progenitor cell response to embryonic tendon biochemical and mechanical factors. *Stem Cell Research and Therapy*, 6(1):1–8, may 2015.

[326] Brian A. Pryce, Spencer S. Watson, Nicholas D. Murchison, Julia A. Staverosky, Nicole Dünker, and Ronen Schweitzer. Recruitment and maintenance of tendon progenitors by TGF signaling are essential for tendon formation. *Development*, 136(8):1351–1361, 2009.

[327] Chih Hao Chiu, Poyu Chen, Alvin Chao Yu Chen, Yi Sheng Chan, Kuo Yao Hsu, Higashikawa Rei, and Kin Fong Lei. Real-Time Monitoring of Ascorbic Acid-Mediated Reduction of Cytotoxic Effects of Analgesics and NSAIDs on Tenocytes Proliferation. *Dose-Response*, 17(1):1–9, jan 2019.

[328] R. C. Poulsen, H. J. Knowles, A. J. Carr, and P. A. Hulley. Cell differentiation versus cell death: Extracellular glucose is a key determinant of cell fate following oxidative stress exposure. *Cell Death and Disease*, 5(2), feb 2014.

[329] Christina N. M. Ryan and Dimitrios i. Zeugolis. Engineering the Tenogenic Niche In Vitro with Microenvironmental Tools. *Advanced Therapeutics*, 3(2):1900072, feb 2020.

[330] Ting Yang, Yue Huang, Zhiqiang Han, Huitao Liu, Rui Zhang, and Yuming Xu. Novel disposable flexible bioreactor for Escherichia coli culture in orbital shaking incubator. *Journal of Bioscience and Bioengineering*, 116(4):452–459, 2013.

[331] Wanlu Zhao, Jinwei Yang, Yuhao Kang, Kaiyan Hu, Mingyue Jiao, Bing Zhao, Yanbiao Jiang, Chen Liu, Fengxing Ding, Bo Yuan, Bin Ma, Kai Zhang, Antonios G. Mikos, and Xingdong Zhang. Animal Models of Rotator Cuff Injury and Repair: A Systematic Review. *Tissue Engineering - Part B: Reviews*, 28(6):1258–1273, dec 2022.